0 8 SEP 1999

BIAXIAL FAILURE ANALYSIS OF GRAPHITE REINFORCED POLYIMIDE COMPOSITES

FINAL REPORT
APRIL 1995 - JULY 1999

PRINCIPAL INVESTIGATOR:
M. S. KUMOSA*

CONTRIBUTORS:
K. SEARLES**, G. ODEGARD*, V. THIRUMALAI and J. MCCARTHY

*CENTER FOR ADVANCED MATERIALS AND STRUCTURES
DEPARTMENT OF ENGINEERING
UNIVERSITY OF DENVER
2390 SOUTH YORK, DENVER, CO 80208

**DEPARTMENT OF MATERIALS SCIENCE AND ENGINEERING
OREGON GRADUATE INSTITUTE OF SCIENCE & TECHNOLOGY
P.O. BOX 91000, PORTLAND, OREGON

19990927 048

REPORT DOCUMENTATION PAGE

AFRL-SR-BL-TR-99-

• 0226

1. AGENCY USE ONLY *(Leave blank)*	2. REPORT DATE	3. REPORT
	September 1999	FINAL TECHNICAL REPORT 1 Jul 96 - 30 Jun 99

4. TITLE AND SUBTITLE
BIAXIAL FAILURE ANALYSIS OF GRAPHITE REINFORCED POLYIMIDE COMPOSITES

5. FUNDING NUMBERS
F49620-96-1-0314

6. AUTHOR(S)
M. KUMOSA, K. SEARLES, G. ODEGARD, V. THIRUMALAI, AND J. MCCARTHY

61102F
2302/BS

7. PERFORMING ORGANIZATION NAME(S) AND ADDRESS(ES)
UNIVERSITY OF DENVER
DEPARTMENT OF ENGINEERING
2390 SOUTH YORK
DENVER, CO 80208

8. PERFORMING ORGANIZATION REPORT NUMBER

9. SPONSORING/MONITORING AGENCY NAME(S) AND ADDRESS(ES)
AIR FORCE OFFICE OF SCIENTIFIC RESEARCH (AFOSR)
801 N. RANDOLPH STREET, ROOM 732
ARLINGTON, VA 22203-1977

10. SPONSORING/MONITORING AGENCY REPORT NUMBER

11. SUPPLEMENTARY NOTES

12a. DISTRIBUTION AVAILABILITY STATEMENT
APPROVED FOR PUBLIC RELEASE, DISTRIBUTION UNLIMITED

12b. DISTRIBUTION CODE

13. ABSTRACT *(Maximum 200 words)*

Comprehensive macro and micro failure analyses of unidirectional and woven graphite/polyimide composites subjected to biaxial shear dominated loading conditions have been performed in this research. The composites have been tested using the biaxial Iosipescu and 10o off-axis tests at room and elevated temperatures. Particular attention has been given to the evaluation of the shear strength properties of graphite/polyimide fabric composites (8 harness satin) as a function the biaxial loading conditions and temperature. Fully non-linear finite element computations of the Iosipescu and 10o off-axis tests have been performed considering the effects of material non-linearity, geometric non-linearity and the effect of specimen sliding within the Iosipescu fixtures. This research resulted in six journal publications and four conference presentations. The abstracts of the journal papers are presented below and the most important findings/accomplishments are briefly described.

14. SUBJECT TERMS

15. NUMBER OF PAGES
236

16. PRICE CODE

17. SECURITY CLASSIFICATION OF REPORT	18. SECURITY CLASSIFICATION OF THIS PAGE	19. SECURITY CLASSIFICATION OF ABSTRACT	20. LIMITATION OF ABSTRACT
UNCLASSIFIED	UNCLASSIFIED	UNCLASSIFIED	

Objectives

This research contributes to the understanding of micro- and macro-failure mechanisms in quasi-isotropic (fabric) graphite reinforced composites based on PMR-15 and Avimid-R polyimide resins tested under biaxial, shear dominated stress conditions over a temperature range of -50°C to 315°C.

Introduction

Comprehensive macro and micro failure analyses of unidirectional and woven graphite/polyimide composites subjected to biaxial shear dominated loading conditions have been performed in this research. The composites have been tested using the biaxial Iosipescu and 10° off-axis tests at room and elevated temperatures. Particular attention has been given to the evaluation of the shear strength properties of graphite/polyimide fabric composites (8 harness satin) as a function the biaxial loading conditions and temperature. Fully non-linear finite element computations of the Iosipescu and 10° off-axis tests have been performed considering the effects of material non-linearity, geometric non-linearity and the effect of specimen sliding within the Iosipescu fixtures. This research resulted in six journal publications and four conference presentations. The abstracts of the journal papers are presented below and the most important findings/accomplishments are briefly described. Full copies of the journal papers are attached to this report.

Accomplishments/New   Findings

I. Numerical Analysis of Biaxial Unidirectional and Fabric Iosipescu Specimens

Several issues regarding the application of the shear and biaxial Iosipescu tests for the shear and biaxial strength characterization of unidirectional and fabric composite materials were addressed in the following three publications:

1

1. M. Kumosa and T. Han, Non-Linear Finite Element Analysis of Iosipescu Specimens, Composites Science and Technology, Vol. 59 (1999) pp. 561-573.

In this paper the effects of specimen sliding within the biaxial Iosipescu fixture and geometric non-linearity on the mechanical response of isotropic, composite and adhesively bonded isotropic and composite Iosipescu specimens subjected to shear under small displacement conditions have been modeled by non-linear finite element techniques. The mechanical response of the specimens to external loads has been modeled by assuming different friction coefficients between the loading blocks of the Iosipescu fixture and the specimens. It has been shown that the sliding of the specimen within the fixture in conjunction with geometric non-linearity (large specimen deformation) can affect, for some specimen geometries, the load/displacement diagrams and internal stress distributions in the gage sections of the Iosipescu specimens. These effects are especially strong in the case of adhesively bonded Iosipescu specimens with either isotropic or composite adherends. However, for 0° unidirectional graphite/epoxy composite Iosipescu specimens subjected to small shear loadings the effects of specimen sliding and geometric non-linearity on the load/displacement diagram and internal stresses appear to be negligible.

2. G. Odegard, K. Searles and M. Kumosa, A Critical Examination of the Iosipescu Shear Test as Applied to 0° Unidirectional Composite Materials, Mechanics of Composite Materials and Structures, Vol. 6 (1999) pp. 229-256.

Several issues regarding the application of the shear and biaxial Iosipescu tests for the shear strength characterization of unidirectional composite materials are addressed in this article. First, the non-linear effects of specimen sliding and geometric non-linearity on the mechanical response of 0° standard unidirectional graphite/polyimide Iosipescu specimens with different loading conditions and loading block geometries have been investigated. Second, an attempt has been made to improve the Iosipescu shear test to eliminate normal compressive stresses in the specimen gauge section and at the same time prevent axial splitting. Finally, several Iosipescu shear and biaxial experiments have been performed to select proper specimen geometry and loading conditions for the shear strength measurements of unidirectional composites.

The non-linear effects are examined with respect to various coefficients of friction, displacements, loading angles, and fixtures (biaxial with short and modified biaxial with long loading blocks) using non-linear finite element techniques. It is shown that the effect

of non-linearity is small on the stresses at the center of the standard Iosipescu specimen, but significant for the stresses near the notch root up to 2 mm applied displacements. In some cases, significant differences in the stresses calculated for different coefficients of friction have been observed. All of these results are somewhat consistent for both fixtures, but with the stress components σ_x, σ_y and σ_{xy} significantly lower in the standard Iosipescu specimens tested in the fixture with the long blocks. Numerical load/displacement diagrams show that specimen sliding and geometric non-linearity have a negligible effect on reaction forces in the biaxial fixture, and a significant effect on the reaction forces in the modified biaxial fixture. Since the various combinations of the loading conditions evaluated in this study do not eliminate transverse compressive stresses in the gauge section of the standard Iosipescu specimens, a major improvement to the Iosipescu shear test has been proposed. Using the optimized specimen geometry subjected to biaxial shear/tension loading conditions, a state of almost pure shear stress can be generated in 0° unidirectional composite Iosipescu specimens without the possibility of axial splitting along the fibers at the roots of the notches. However, it is shown in the experimental part of this study that for the optimized Iosipescu specimen, crushing at the inner loading blocks can significantly affect the shear intralaminar failure process. Only by reducing the cross-sectional area of the optimized Iosipescu specimen can the effect of crushing on the failure process be reduced, without, however, high quality shear stress fields present in the gauge section at failure.

3. G. Odegard, K. Searles and M. Kumosa, Non-Linear Analysis of Woven Fabric-Reinforced Graphite/PMR-15 Composites under Shear-Dominated Biaxial Loads, Mechanics of Composite Materials and Structures (April 1999), submitted for publication.

An elastic-plastic, time-independent, macroscopic, homogenous model of 8-harness satin woven graphite/PMR-15 composite material has been developed that predicts the non-linear response of the material subjected to shear-dominated biaxial loads. The model has been used to determine the response of woven composite off-axis and Iosipescu test specimens in non-linear finite analyses using multi-linear averaging techniques. The numerically calculated response of the specimen was then compared to experimentally obtained data. It has been shown that the numerically calculated stress-strain diagrams of the off-axis specimens are very close to the experimentally obtained curves. It has been shown that the

3

numerically determined shear stress-strain and load-displacement curves of the woven Iosipescu specimens are close to the experimentally obtained curves up to the point of significant interlaminar damage initiation and propagation. The results obtained in this study clearly demonstrate that the non-linear material behavior of the graphite/polyimide woven composites subjected to shear-dominated biaxial loading conditions cannot be ignored and should be considered in any stress analysis. The linear-elastic approach grossly overestimates the loads and stresses at failures of these materials in the off-axis and Iosipescu tests. It can be assumed that the same discrepancies will arise in the numerical analysis of the woven composites tested under other biaxial shear-dominated loading conditions using other biaxial test methods.

II. Failure Investigation of Graphite/Polyimide fabric Composites at Room and Elevated Temperatures

Shear and biaxial shear-dominated experiments using the biaxial Iosipescu and 10° off-axis tests have been performed in order to determine the biaxial shear dominated strength properties of 8 harness satin graphite/polyimide composites at room and elevated temperatures.

1. K. Searles, J. McCarthy and M. Kumosa, An Image Analysis Technique for Evaluating Internal Damage in Graphite/Polyimide Fabric Composites, Composites Science and Technology, Vol. 58 (1998) pp. 1607-1619.

The purpose of this paper is to suggest a possible technique for evaluating internal damage in fabric-reinforced composite materials. The technique presented in this work is based on capturing and performing a qualitative analysis of scanning electron microscope images of damage from planar specimen slices (serial sections) and then reassembling the slices in three-dimensional space. This method has been applied to evaluating damage in graphite-fabric/PMR-15 Iosipescu specimens tested in shear. Three-dimensional damage maps have been presented and the extent of damage through the thickness of a graphite-fabric/PMR-15 Iosipescu specimen has been determined. The same approach could be used for the evaluation of internal damage in other composite systems.

4

2. K. Searles, G. Odegard, M. Castelli, and M. Kumosa, Failure Investigation of Graphite Polyimide Fabric Composites at Room and Elevated Temperatures using the Biaxial Iosipescu Test, Journal Composite Materials (1999) in press.

The biaxial and modified biaxial Iosipescu shear test methods were applied to determine the shear dominated, biaxial mechanical response of graphite/PMR-15 and graphite/Avimid-R woven fabric composites at room and elevated temperatures. Three different composite architectures were examined: T650-35 warp-aligned, 8 harness satin fabric in a PMR-15 matrix, T650-35 warp-aligned, 8 HS fabric in an Avimid-R matrix and T650-35 0°/90° 8HS fabric in an Avimid-R matrix. Several biaxial Iosipescu tests were performed at room temperatures under shear, shear-tension, and shear-compression loading conditions to characterize damage and obtain biaxial, shear dominated failure properties. Shear tests were also conducted at elevated temperatures approaching 316°C to determine the effects of temperature on the shear strengths of the composite investigated. Within this investigation, it was found that graphite/Avimid-R was more resistant to biaxial, shear dominated failure at room temperature in comparison to graphite/PMR-15. However, the graphite/PMR-15 composite system exhibited better shear strength properties at elevated temperatures above 232°C. It was found that the effect of compression along the notch root axis generated by the loading blocks did not affect the loads at failure.

III. Evaluation of the Elastic Properties of 8 Harness Satin Composites

1. K. Searles, G. Odegard and M. Kumosa, Micro- and Mesomechanics of 8-Harness Satin Woven Fabric Composites: I - Evaluation of Elastic Behavior, Mechanics of Composite Materials and Structures (August 1999) submitted for publication.

In part I of this two-part paper, simplified two-dimensional micromechanics and mesomechanics models have been introduced to predict the elastic behavior of 8 harness satin woven fabric composites. The woven warp and fill tows were independently treated as unidirectional composites and composite cylinder assemblage (CCA) theory was adopted to predict tow elastic properties from constituent fiber and matrix properties. Since evaluation of woven lamina stiffness requires an accurate description of tow geometry, a method was also developed to describe arbitrary tow geometries by mathematically fitting cubic splines and/or polynomials to micrographs of composite cross-sections. Finally, classical lamination theory was introduced to determine the overall elastic behavior of an n-layer composite laminate, assuming the woven lamina was a modified, two-layer laminate.

The simplified mechanics model was evaluated using results from numerical strain energy and equivalent force approaches and results from a series of experimental Iosipescu shear tests and off-axis tensile tests on T650-35 (3k), 8HS woven graphite-PMR-15 composites. Issues regarding exclusion of a matrix layer in the simplified 2-layer laminate analysis were addressed in the strain energy analysis of an idealized 3-D representative volume element. The mechanics model was found adequate in estimating the lower bounds of 8HS woven fabric composite elastic properties. The model also provided a reasonable estimation of symmetric cross-ply composite properties.

Personnel Supported in this Project

Three graduate students were supported in this project. Mr. V. Thirumalai was supported by AFSOR (F49620-95-1-0250) in the Department of Materials Science and Engineering at the Oregon Graduate Institute of Science and Technology between March 15, 1995 and September 30, 1995. Mr. K. Searles was fully supported by AFOSR in the Department of Materials Science and Engineering at the Oregon Graduate Institute of Science & Technology between November 1, 1995 and March 31, 1999 (F49620-95-1-0250 and F49620-96-1-0314). Kevin Searles should graduate with Ph. D. in September 1999. Mr. G. Odegard, a graduate student in the Department of Engineering at DU, has been involved in this project (F49620-96-1-0314) since February 1997. He has been supported jointly by the National Science Foundation and the AFOSR grant between September 1, 1997 and August 1999. Mr. Odegard will graduate in 2000.

Interactions/Transitions

This study was performed in close collaboration with the NASA Lewis (Glenn) Research Center (Mr. M. Castelli) and Pratt&Whitney (Mr. R. Cairo). The composite materials investigated in this project were supplied by Pratt&Whitney (Graphite/Avimid-R) and NASA Lewis (Glenn) Research Center (Graphite/ PMR-15).

COMPLETE LIST OF PUBLICATIONS

Based on the research performed in this project the following publications have been prepared:

- Journal Publications

1. K. Searles, J. McCarthy and M. Kumosa, An Image Analysis Technique for Evaluating Internal Damage in Graphite/Polyimide Fabric Composites, Composites Science and Technology, Vol. 58 (1998) pp. 1607-1619.

2. M. Kumosa and T. Han, Non-Linear Finite Element Analysis of Iosipescu Specimens, Composites Science and Technology, Vol. 59 (1999) pp. 561-573.

3. G. Odegard, K. Searles and M. Kumosa, A Critical Examination of the Iosipescu Shear Test as Applied to $0°$ Unidirectional Composite Materials, Mechanics of Composite Materials and Structures, Vol. 6 (1999) pp. 229-256.

4. K. Searles, G. Odegard, M. Castelli, and M. Kumosa, Failure Investigation of Graphite Polyimide Fabric Composites at Room and Elevated Temperatures using the Biaxial Iosipescu Test, Journal Composite Materials (1999) in press.

5. G. Odegard, K. Searles and M. Kumosa, Non-Linear Analysis of Woven Fabric-Reinforced Graphite/PMR-15 Composites under Shear-Dominated Biaxial Loads, Mechanics of Composite Materials and Structures (April 1999), submitted for publication.

6. K. Searles, G. Odegard and M. Kumosa, Micro- and Mesomechanics of 8-Harness Satin Woven Fabric Composites: I - Evaluation of Elastic Behavior, Mechanics of Composite Materials and Structures (August 1999) submitted for publication.

- Conference Proceedings/Presentations

1. M. Kumosa, K. Searles and G. Odegard, Biaxial Failure Analysis of Graphite Reinforced Polyimide Composites, in the Proceedings of the HITEMP Review, Advanced

7

High Temperature Engine Materials Technology Program, NASA Lewis Research Center, Cleveland, Ohio, April 29-30, 1997, vol. I, paper 18.

2. M. Kumosa, K. Searles, G. Odegard and M. Castelli, Biaxial In-Plane Testing of High Temperature Graphite/Polyimide Fabric Composites, in the Proceedings of the HIGH TEMPLE Workshop XVIII, January 20 - January 22, 1998, Hilton Resort, Hilton Head Island, South Carolina.

3. K. Searles and M. Kumosa, Analysis of Nonlinear Behavior in 8-Harness Satin Woven Fabric Composites Subjected to In-Plane Biaxial Shear Deformation, Proc. of the High Temple Workshop XIX, February 1-4, 1999, Denver, Colorado, pp. X1-X25

4. G. Odegard, M. Kumosa and M. Castelli, Shear Dominated Biaxial Elastic-Plastic Analysis of Unidirectional Graphite/PMR-15 Composites at Room and Elevated Temperatures, Proc. of the High Temple Workshop XIX, February 1-4, 1999, Denver, Colorado, pp. M1-M15.

PII: S0266-3538(97)00227-3

AN IMAGE ANALYSIS TECHNIQUE FOR EVALUATING INTERNAL DAMAGE IN GRAPHITE-FABRIC/POLYIMIDE COMPOSITES

K. Searles,[a] J. McCarthy[a] & M. Kumosa[b]*

[a]*Materials Microanalysis Laboratories, Department of Materials Science and Engineering, Oregon Graduate Institute of Science and Technology, PO Box 91000, Portland, OR 97291-1000, USA*
[b]*Center for Advanced Materials and Structures, Department of Engineering, University of Denver, 2390 South York, Denver, CO 80208, USA*

Abstract

The purpose of this paper is to suggest a possible technique for evaluating internal damage in fabric-reinforced composite materials. The technique presented in this work is based on capturing and performing a qualitative analysis of scanning electron microscope (SEM) images of damage from planar specimen slices (serial sections) and then reassembling the slices in three-dimensional space. This method has been applied to evaluating damage in graphite-fabric/PMR-15 Iosipescu specimens tested in shear. Three-dimensional damage maps have been presented and the extent of damage through the thickness of a graphite-fabric/PMR-15 Iosipescu specimen has been determined. The same approach could be used for the evaluation of internal damage in other composite systems. © 1998 Elsevier Science Ltd. All rights reserved

1 INTRODUCTION

The present work is concerned with developing acceptable imaging techniques for determining the extent of in-plane and through-thickness damage in Iosipescu composite specimens tested under shear dominated, biaxial loading conditions. Although restricted to woven-fabric graphite/PMR-15 composites in this paper, the imaging techniques could also be generalized to include other composite systems.

The Iosipescu test,[1] originally intended for measuring the elastic shear properties of isotropic metals, was subsequently extended by Walrath and Adams[2,3] to include composite materials. This method has evolved into one of the more popular tests for the shear characterization of composite materials because of the simple loading configurations, specimen geometries and lower specimen preparation costs. The fixture used in this analysis (Fig. 1) is a modification based upon the

*To whom correspondence should be addressed.

traditional Iosipescu shear test[3] and the Arcan in-plane stress method.[4] It was designed by Broughton et al.[5,6] with the capability of determing failure properties for a plethora of composite systems tested in pure shear and a biaxial combination of shear/tension or shear/compression (Fig. 1(b)). The fixture consists of two stainless steel halves, each 100 mm wide. One half of the fixture displaces downward while the other is fixed. Four loading blocks, two on each side are symmetrically offset relative to the specimen centerline (notch–root axis) and generate uniform, biaxial, shear dominated stress fields at the specimen center. The loading blocks are fixed to disks which house the double edge-notched beam specimen (Fig. 2) and are indexed according to relative angle of the applied load. Each index represents a 5° increment with the total maximum rotational range being ±45° shear/tension (− or clockwise) or shear/compression (+ or counter-clockwise). The holes in the center of each rotating disk allow for strain gage attachment, acoustic emission waveguides and viewing during testing. Previous analyses have adopted the fixture for obtaining mixed mode failure properties unidirectional graphite/epoxy, Ti/SiC composites and teak wood.[5–9]

2 POTENTIAL FAILURE MECHANISMS

Recently, the biaxial failure properties of quasi-isotropic graphite/polyimide, textile structural composite Iosipescu specimens have been investigated by using the biaxial Iosipescu method at room temperature.[10,11] The composite systems, fabricated at the NASA Lewis Research Center, met the following specifications:

Fabric:	T650-35, 8-harness satin cloth
Ply Layup:	16-ply with floating undulations (warp-aligned)
Matrix:	PMR-15
Q and R:	Ultrasonic inspection
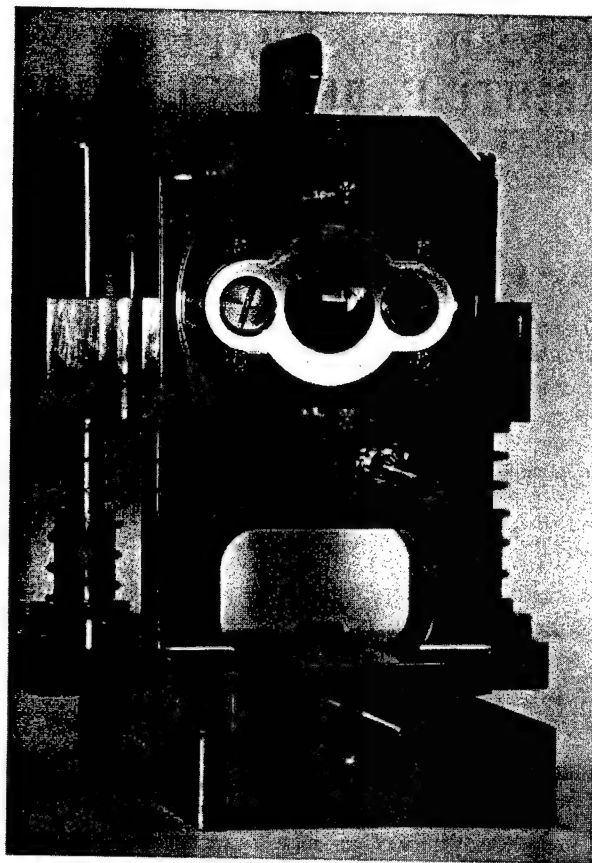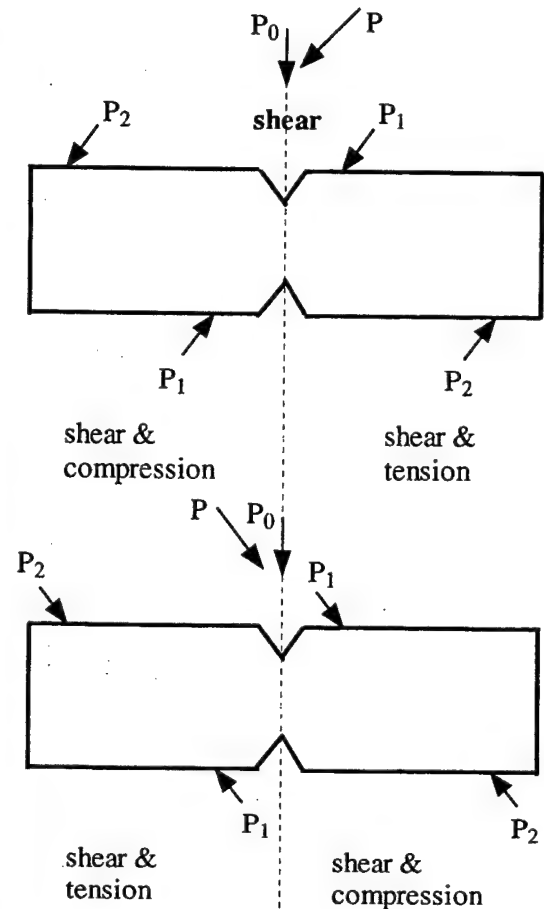
Fig. 1. (a): Biaxial Iosipescu test fixture; (b) Iosipescu specimen under in-plane biaxial stress state—(a) counter-clockwise rotation, (b) clockwise rotation.

After testing several Iosipescu specimens in shear, shear/compression and shear/tension,[10] it was noted that the failure process was significantly different in comparison to previously reported failure mechanisms observed in either isotropic materials or unidirectional composites.[5–9] Moreover, the mechanical response of the Iosipescu specimens appeared to be dependent on the external biaxial loading conditions.

2.1 Failure of unidirectional Iosipescu specimens

For 0° unidirectional specimens (fibers oriented along the long axis of the Iosipescu specimen), failure under all loading conditions, either shear or biaxial, occurs as a result of axial splits initiated at the roots of the notches.[5–9] These splits form parallel to the fibers and propagate on one side of the notch tip away from the nearest loading point. The split formation is always manifested by two successive drops on the load displacement diagram. Unidirectional composite specimens with 90° fibers (fibers oriented along the notch root axis) always fail catastrophically. For all loading angles, cracks originate at the notch root and propagate in an unstable manner parallel to the fibers.

The failure process in both 0° and 90° oriented unidirectional Iosipescu specimens can be easily determined since the failure of the specimens is usually through the thickness and the cracks are visible on the specimen surface. For the fabric composites, the failure process is much more complex and can vary through the thickness. In this case, the failure characteristics cannot be determined by examining the specimen surface only, therefore a detailed analysis of damage through the specimen thickness is required.

It has also been reported[12] that cross-ply graphite/epoxy laminates tested in shear using the traditional Iosipescu method failed in a stable manner. The failure was associated with large damage zones developed in the gage sections of the specimens. It is feasible to assume, at this point, that failure characteristics of the graphite/PMR-15 woven fabric will resemble those observed in the cross-ply specimens subjected to shear.

2.2 Failure of graphite-fabric/PMR-15 iosipescu specimens

The load/displacement diagrams for the graphite/PMR-15 Iosipescu specimens tested in shear as well as
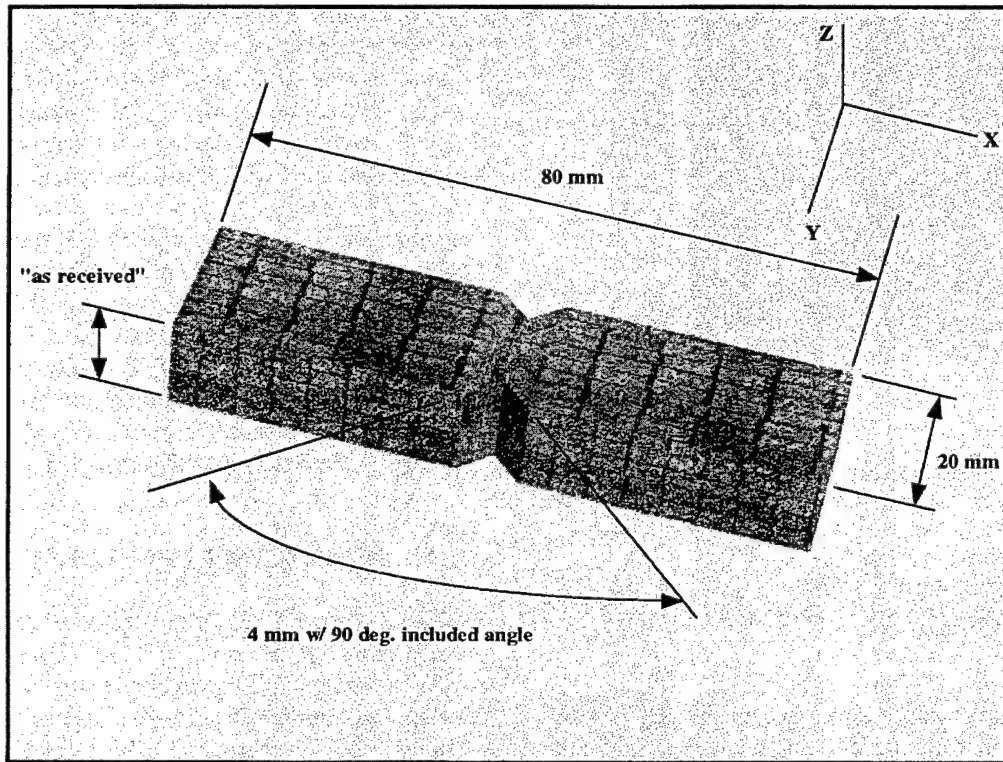
Fig. 2. Schematic of Iosipescu specimens suitable for testing in the biaxial Iosipescu fixture.
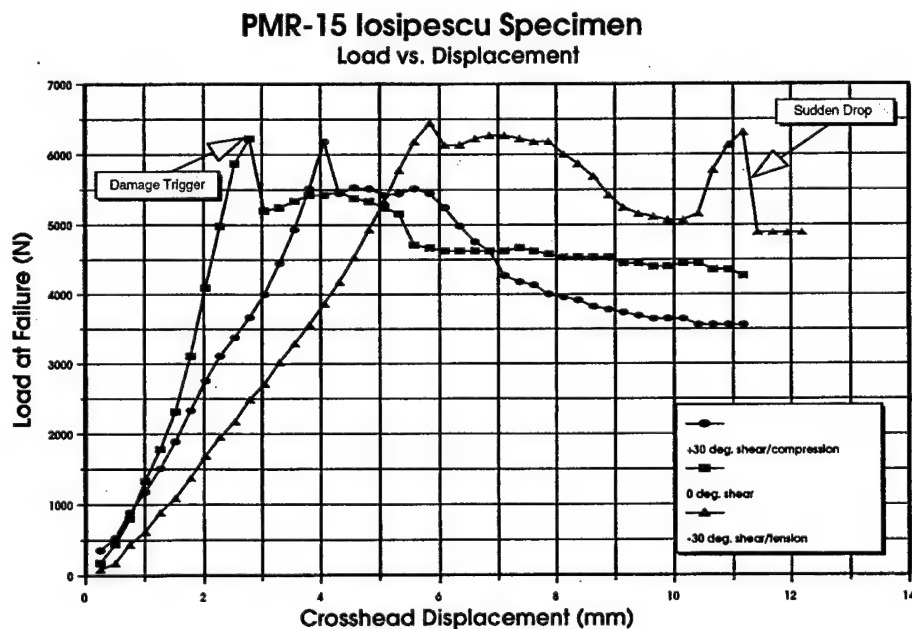

Fig. 3. Load/displacement diagrams for graphite/PMR-15 Iosipescu specimens tested under shear and biaxial, shear dominated loading conditions.

shear/tension and shear/compression are shown in Fig. 3. The curves presented in Fig. 3 exhibit a maximum load followed by a sudden drop. This phenomenon was observed for all specimens tested in this study. The results also reveal a general trend towards stability of the process after the initial 'damage trigger' as compared to graphite/epoxy laminates. Specimens tested under shear/tension loading conditions were the only exceptions to those observations. Here, the tests resulted in a significant increase in load for very high displacements followed by another 'trigger'. In all cases, this process repeated itself 2 to 3 times.
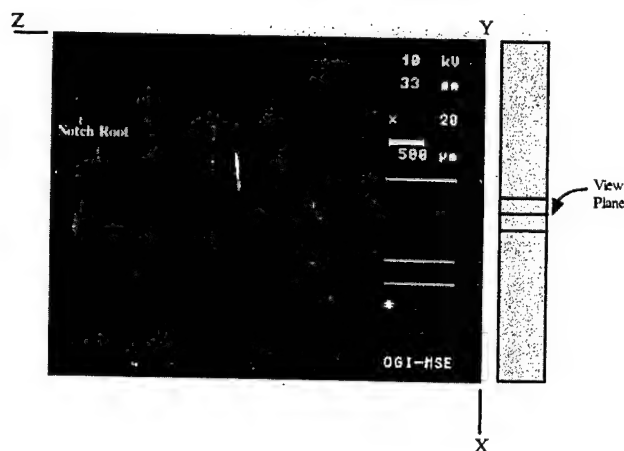
Fig. 4. Scanning electron microscope micrograph of cracking within the notch root as viewed looking from the top.

The tested specimens were examined and the most important **surface** features of their damage zones were determined:

1. Large damage zones developed in the gage section of the specimens were observed. The zones consisted of multiple surface cracks (Fig. 4). It was almost impossible to determine the mode of failure most prevalent i.e. intralaminar, interlaminar or translaminar.
2. The damage zones were associated with significant and permanent out-of-plane deformations (bulging) on the surfaces of the specimens (see Fig. 5). It seems that the specimen surface bulging developed just before the 'damage trigger'.
3. The damage zone morphology was almost identical for all loading angles. It appears, however, that damage zone size was slightly smaller in those samples tested in shear/compression in comparison to the zones developed under biaxial shear/tension loading conditions.
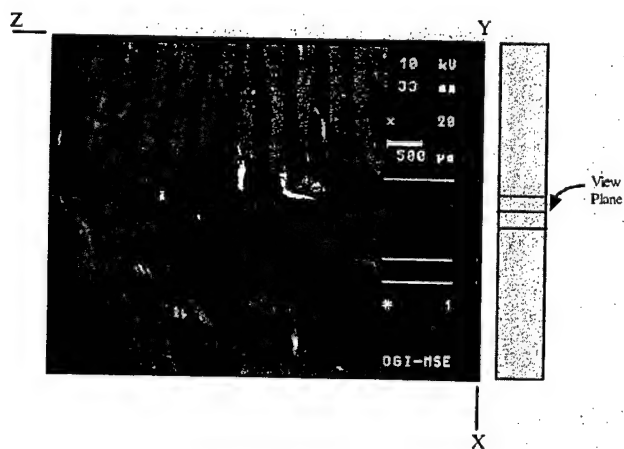

Fig. 5. Scanning electron microscope micrograph showing the out-of-plane deformation and internal cracking.

2.3 A need for refined image analysis techniques

In order to thoroughly evaluate the damage zone development and mode or modes of failure most prevalent in the graphite/PMR-15 Iosipescu specimens under shear dominated, biaxial loading conditions, we need to evaluate the damage not only on the specimen surface, but also within the specimen. This requires an acceptable method for specimen dissection and image reconstruction. Typical methods currently in use rely on scanning electron microscope (SEM) backscatter techniques, texture or 'rug' mapping, stereo pairs, z-projections, mesh generation and solid modeling. The method proposed in this paper will combine several of those ideas and yield an outcome with potentially more useful information regarding the initiation and development of damage in the specimens through their thickness.

3 IMAGE ANALYSIS PROCEDURE

The experimental procedure followed in this investigation was to capture and perform a qualitative analysis of SEM images from planar specimen slices (serial sections), reassemble the slices in 3-dimensional space and visualize the net volumetric effects of damage.

One graphite/PMR-15 Iosipescu specimen tested in shear was analyzed. The load/displacement diagram for this particular specimen is shown in Fig. 3. The internal damage in the gage section of the shear tested specimen was investigated.

3.1 Specimen preparation

Following mechanical testing, the central section of the 80 mm×20 mm specimen was removed along the SEM cutting planes (see Fig. 6) via a Buehler Isomet low speed saw. All cuts were made using a diamond tip circular blade and copious amounts of fluid. Once the central section was removed, the surface of the sample was saturated with Gatan G-60 quartz-crystalline epoxy under 45 psi of pressure. The epoxy has a fairly low viscosity, needs to be temperature cured and is capable of making sub-micron adhesive joints.

After 24 h of pressurization and curing, the specimen was placed in a 2·5 in diameter container and hard mounted with specimen preparation epoxy. This allowed for stable mounting in the SEM and safer handling during polishing with lapping disks. The encapsulated section necessitated the need for a special holder capable of indexing up an equidistant value after each slice removal in order to maintain the appropriate working distance in the SEM.

3.2 Image capturing

The hard mount was initially polished until the top planar surface of the specimen section was exposed. This was designated as the z-axis reference surface and tagged index-00. Two sets of three locator holes were used to mark the regions of interest (ROIs). One of the
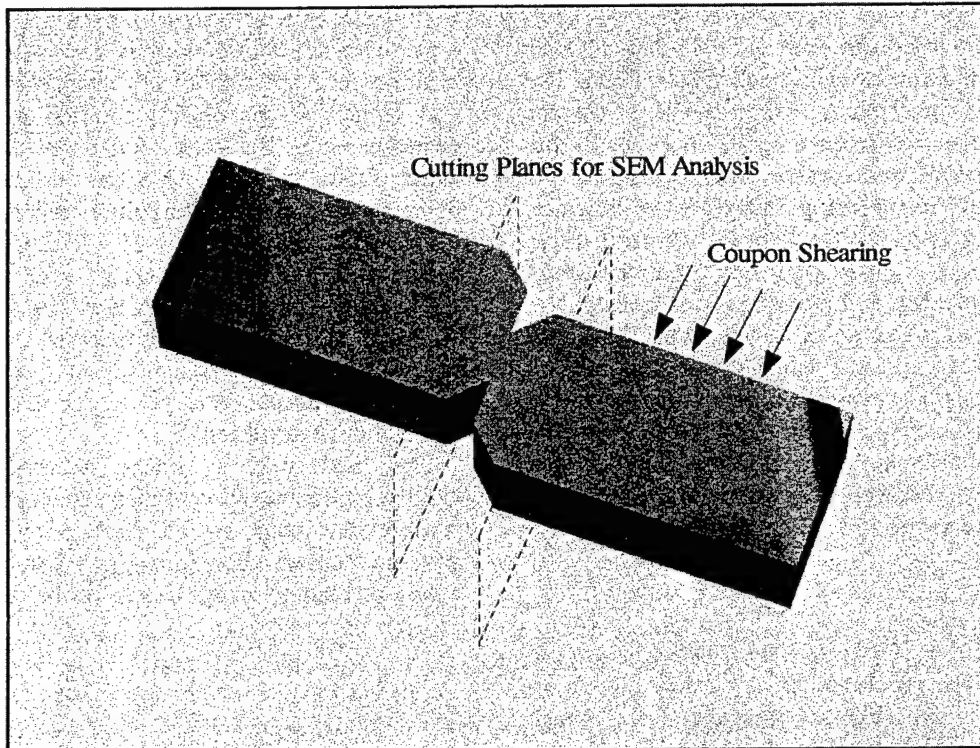
Fig. 6. Schematic showing the orientation of cutting planes for removing a sample section for analysis.
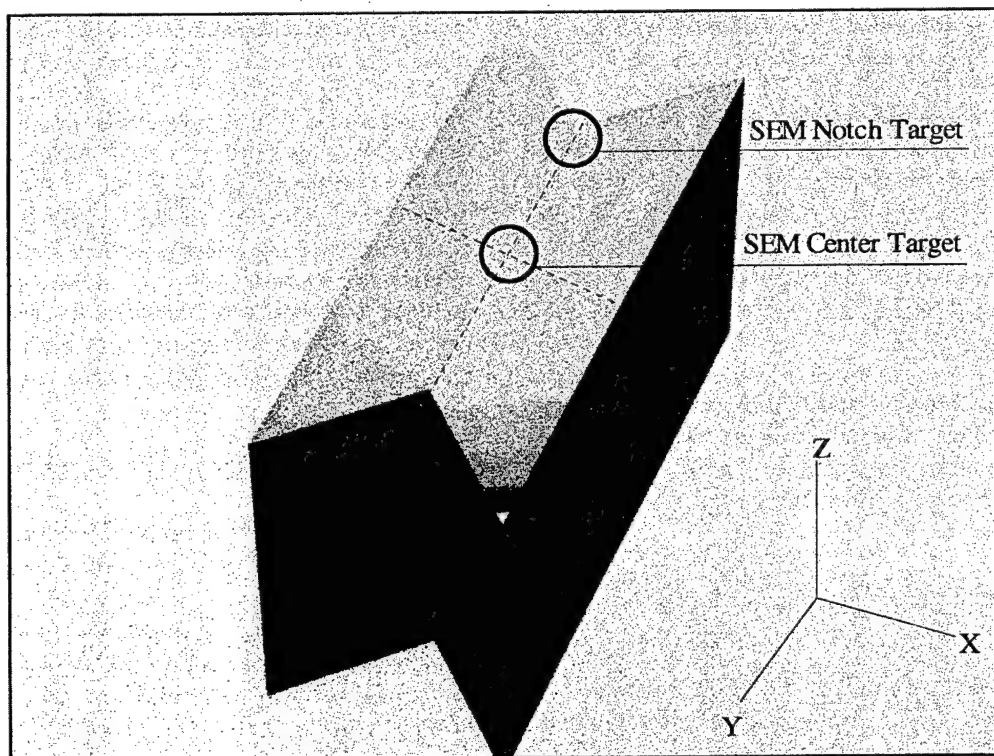

Fig. 7. Removed section showing notch and center target locations and orientation.

hole sets was located at the section center and the other set was located at the top notch as shown in Fig. 7. The holes served to define x–y planes by which sequential slices could be accurately aligned in the SEM.

After exposing index-00, the section was sputtered with approximately 150 Å of Au–Pd deposit from a Technics Hummer II D.C. Sputtering System. This was done to prevent localized charging and poor image

sampling during the image capturing process. All images were captured using the Zeiss Model 960 analytical scanning electron microscope in backscatter mode. The working distance was fixed at 16 mm, the beam current was 20 kV and the maximum magnification set by the screen capture board and locator hole separation was 45×. Subsequent to capturing index-00, a 350 μm ± 25 μm slice was removed to expose the next layer (index-01) and each exposed layer was again saturated with epoxy. Capturing and polishing was consecutive through index-04. At this point, it was stopped because symmetry along the mid-line was assumed and ensuing indexes would mirror previous indexes.

The entire specimen preparation and image capturing processes were subsequently repeated using an untested sample in order to determine the effect of the specimen preparation process on the damage initiation in the composite.

3.3 Image processing

Subsequent to capturing each index, two-dimensional damage maps were generated on a 120 MHz Pentium PC using the public domain program NIH Image (developed at the US National Institutes of Health and available on the Internet at http://rsb.info.nih.gov/ nih-image/). Indexes 00–04 were treated separately for both the center target and the notch target. A low-pass smoothing filter was applied in conjunction with a 3×3 median (rank) filter to each index and threshold was manually adjusted. This established a perimeter outline for each area of detected damage, i.e. determined via contrast changes. For this analysis, 3×3 smoothing kernels of the form:

$$\begin{bmatrix} 1 & 1 & 1 \\ 1 & 1 & 1 \\ 1 & 1 & 1 \end{bmatrix} \quad \text{or} \quad \begin{bmatrix} 1 & 1 & 1 \\ 1 & 4 & 1 \\ 1 & 1 & 1 \end{bmatrix}$$

were assumed to remove noise from one-dimensional or two-dimensional signals while preserving image information content. According to Bovik et al.,[13] the two-dimensional median filter may be defined as follows:

$$\hat{X}_{i,j} = \text{median}\{X_{i',j'} : (i',j') \epsilon W(i,j)\}$$

where $W(i,j)$ reflects centering of the filter window at image coordinates (i,j). Essentially, each pixel within a 3×3 neighborhood was replaced with a median value or all nine pixels were sorted and the center replaced with a median from the neighborhood. Application included median, multi-pass prefiltering to suppress noise, improve thresholding and yield a consistent estimation of edges.

Once edge detection was complete, the maps were stacked in order and averaged, resulting in two-dimen-

sional composite skeletons for each target. At this point, a partial quantitative analysis was made regarding the location and significance of damage and each outline was tagged as an object, counted and analyzed to determine area fractions of damage as a function of depth from index-00 (section surface). All tagged objects were analyzed using the public domain program UTHSCSA Image Tool 1·25 (developed at the University of Texas Health Science Center at San Antonio, TX and available from the Internet by anonymous FTP at maxrad6.uthscsa.edu). Important characteristics of interest were the number of objects per index, the area of each object in square pixels, the mean area size (X) and standard deviation (σ).

The final step in image processing procedures involved creating three-dimensional projections from manipulated image stacks. Each index was re-sampled and one of two sharpening 3×3 spatial convolutions was implemented using the kernels below:

$$\begin{bmatrix} -1 & -1 & -1 \\ -1 & 9 & -1 \\ -1 & -1 & -1 \end{bmatrix} \quad \text{or} \quad \begin{bmatrix} -1 & -1 & -1 \\ -1 & 12 & -1 \\ -1 & -1 & -1 \end{bmatrix}$$

A stack averaging plug-in was used on each of the index windows for a given target, producing a new image which was a pixel-by-pixel average of all index windows input into the stack. Each stack was processed into a surface using 3D View 1·00 (a public domain package available via http://physics.usyd.edu.au//mathewa/, developed as an add-on to NIH Image, by I. Huxley at the Physical Optics Dept, School of Physics, University of Sydney). According to Huxley, the program uses the *autofocus* method, finding surface heights from maximum intensity points in each column of pixels. In this analysis, surfaces were rendered for comparison from center and notch targets for both untested and mechanically tested Iosipescu sections.

4 IMAGE ANALYSIS RESULTS AND DISCUSSION

Figures 8 and 9 present two-dimensional damage maps for the shear tested graphite/polyimide Iosipescu specimen. The shaded areas shown in these maps represent damage generated at the specimen center (Fig. 8) and an area very close to the notch root (Fig. 9), respectively. Each map denotes an approximate area on the specimen of 9 mm². Below each pixel-by-pixel averaged composite map a profile plot is presented showing the relative pixel contrast intensities by average gray values as a function of image width. The profile plot illustrates where the majority of cracks is distributed across each map and gives an indication of the size of cracks compared to the width of the map. From these maps, the location and magnitude of damage in the examined areas can be estimated.
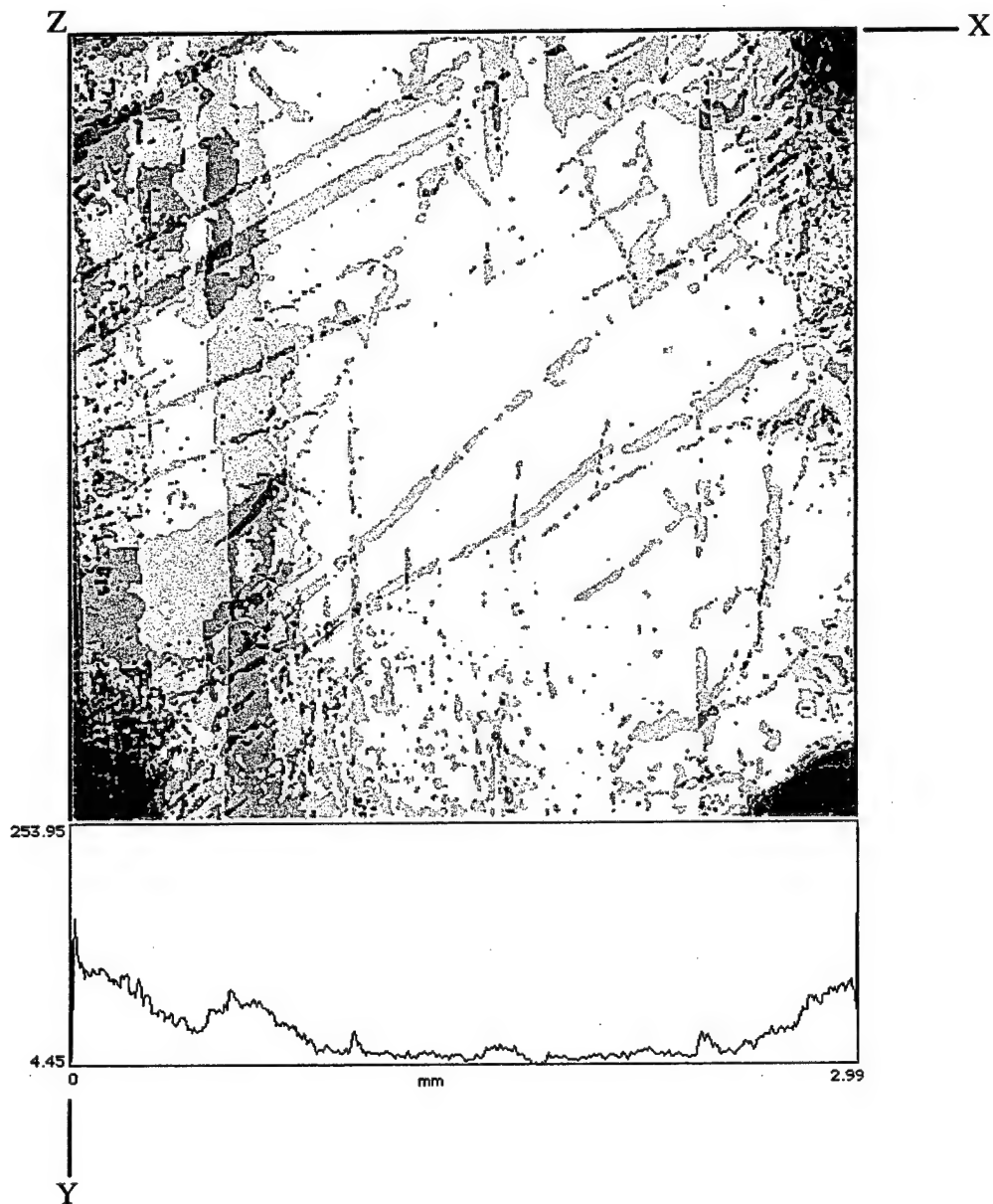
Fig. 8. Two-dimensional map and corresponding profile plot of damaged material center target.

After the shear test, the examination of the specimen surface revealed that the fiber bundles were reoriented with respect to their initial orientations.[10] Before the test, the bundles were oriented along both the long axis of the specimen and the notch root axis. Due to the large shear stresses generated during the Iosipescu shear test, bundle rotation took place in the middle portion of the specimen with the final bundle orientation being approximately 45° with respect to the notch root axis.

It is quite possible that the diagonal shaded areas shown on each map represent a combination of intralaminar failures at the fiber bundle-matrix interfaces and failure at weave (warp/fill) undulations or 'crimps'.

Very little cracking is evident in the longitudinal direction (direction parallel to the long axis of the specimen). Vertical cracks (damage zones) dictated by much larger areas seem to represent the interlaminar failure process between the layers. It is possible that one or several of the vertical cracks could be associated with the load-drops shown in Fig. 3. It is assumed that the shearing process forces the bundles to rotate and fail at the undulations as progressive intralaminar damage develops.

Simultaneously, the ends of the specimen move toward the center and kinking occurs. At some critical point during the loading process, interlaminar cracks develop and propagate, allowing the specimen to bulge outward from the centerline as shown in Fig. 5. If the fracture toughness of the interfaces between the layers is low, some of the interlaminar cracks can propagate catastrophically along the specimen causing the load drops.
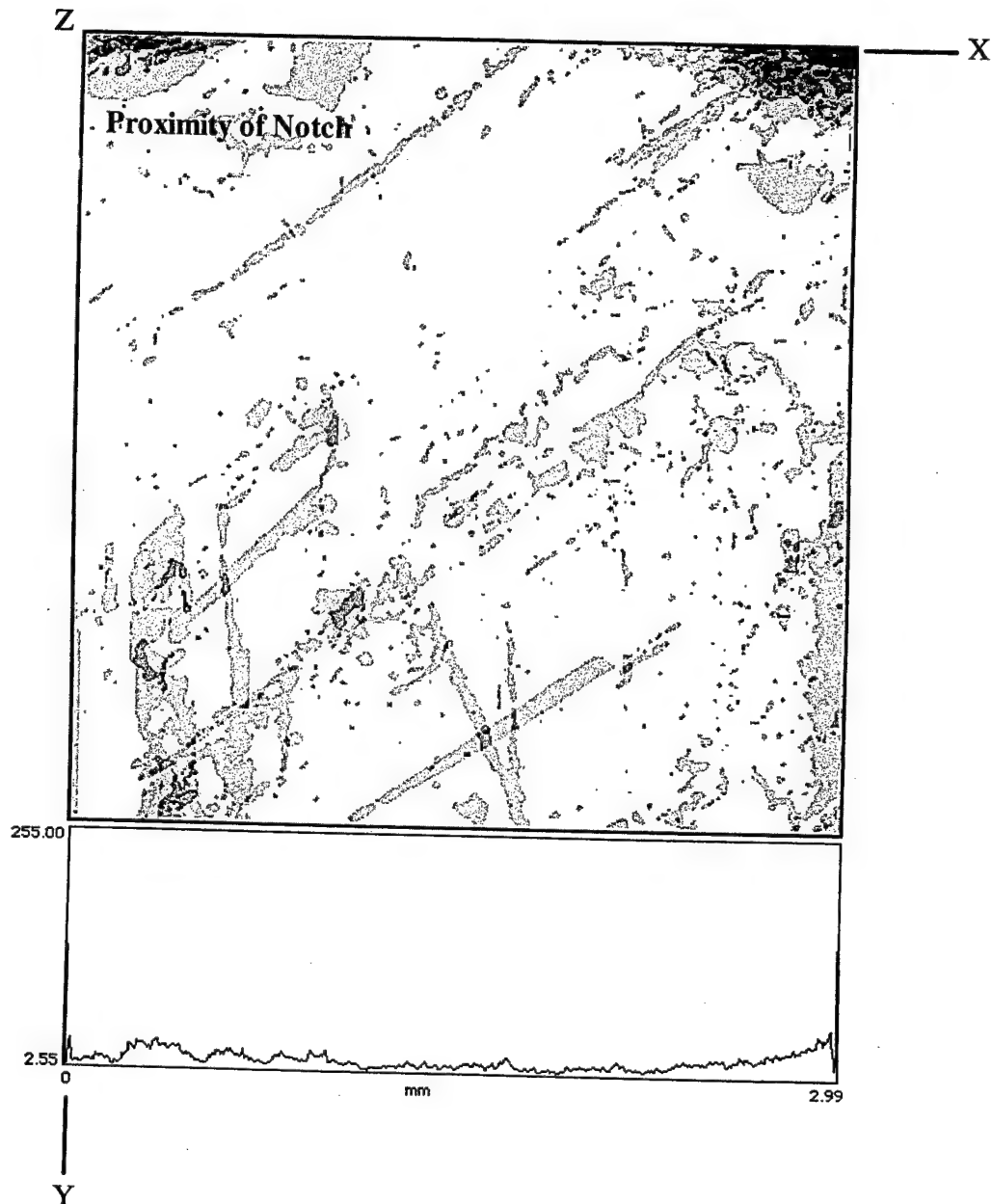
Fig. 9. Two-dimensional map and corresponding profile plot of damaged material notch target.

Since it is possible that damage could be induced into the specimen during the specimen preparation process, an untested specimen was also subjected to the polishing and epoxy curing procedure. Figures 10 and 11 represent untested (virgin) specimen center and notch target maps derived using the same techniques as previously mentioned. The differences between tested and untested center target maps are obvious as are the differences between tested and untested notch maps. The darker areas located on the maps for the untested targets most likely represent undulation resin pockets or in situ manufacturing voids. No visible damage to the composite caused by the specimen preparation process can be observed in Figs 10 and 11.

An important observation can be made by comparing the damage maps presented in Figs 8 and 9.

It is obvious that the amount of damage generated in the specimen center is significantly higher in comparison with the area close to the notch root. Therefore, it can be concluded that the specimen developed large shear stresses at its center without any stress concentrations present at the roots of the notches. This effect will most likely be observed in the specimens tested under the biaxial shear/tension and shear/compression loading conditions.

Damage area fractions represent the ratio of crack-inclusive areas to the total area. In this study, all images captured retained a 230 400 square pixel area or
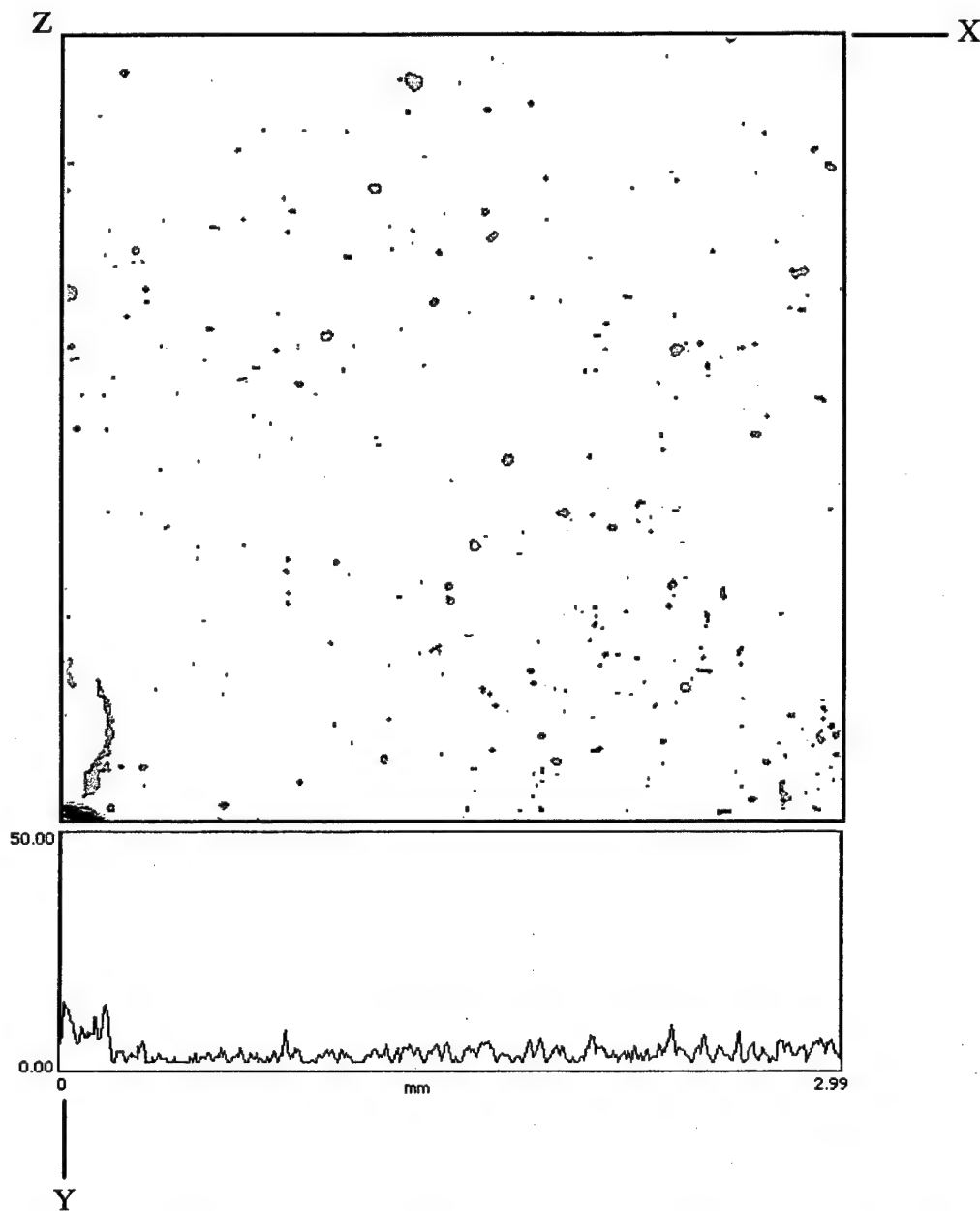
Fig. 10. Two-dimensional map and corresponding profile plot of untested material center target.

480×480 resolution. Figure 12 illustrates the difference between the center and notch target measured damage as a function of depth from the surface. Clearly, damage accumulated near the Iosipescu specimen upper notch is less significant compared to the center. Also, the notch target area fraction oscillates between 3 and 4%, while the center target area fraction progresses from 8 to 12·5%. It appears that the shear initiated, catastrophic failure (the load drop in Fig. 3) may originate near the specimen centerline and propagate outwards through the thickness and the specimen length. Figure 13 compares respective targets in the untested material, showing ranges from 0·3 to 0·68%. These results seem reasonable and tend to enforce the belief that polishing does

not significantly alter the state of the material after testing.

Figure 14 shows the projected three-dimensional reconstruction of the center and notch SEM targets from an assembly of index pairs 00–04. It can be seen from these figures that damage near the notch is not as pronounced and the majority of cracks follow diagonals similar to patterns where the warp/fill undulations are located. The projections give the illusion of transparency, but they actually represent a compilation of depth and intensity maps derived from the two-dimensional crack-laden stack averages. The darker corner areas are portions of the holes used to align each image from surface to sub-surface in sequence.
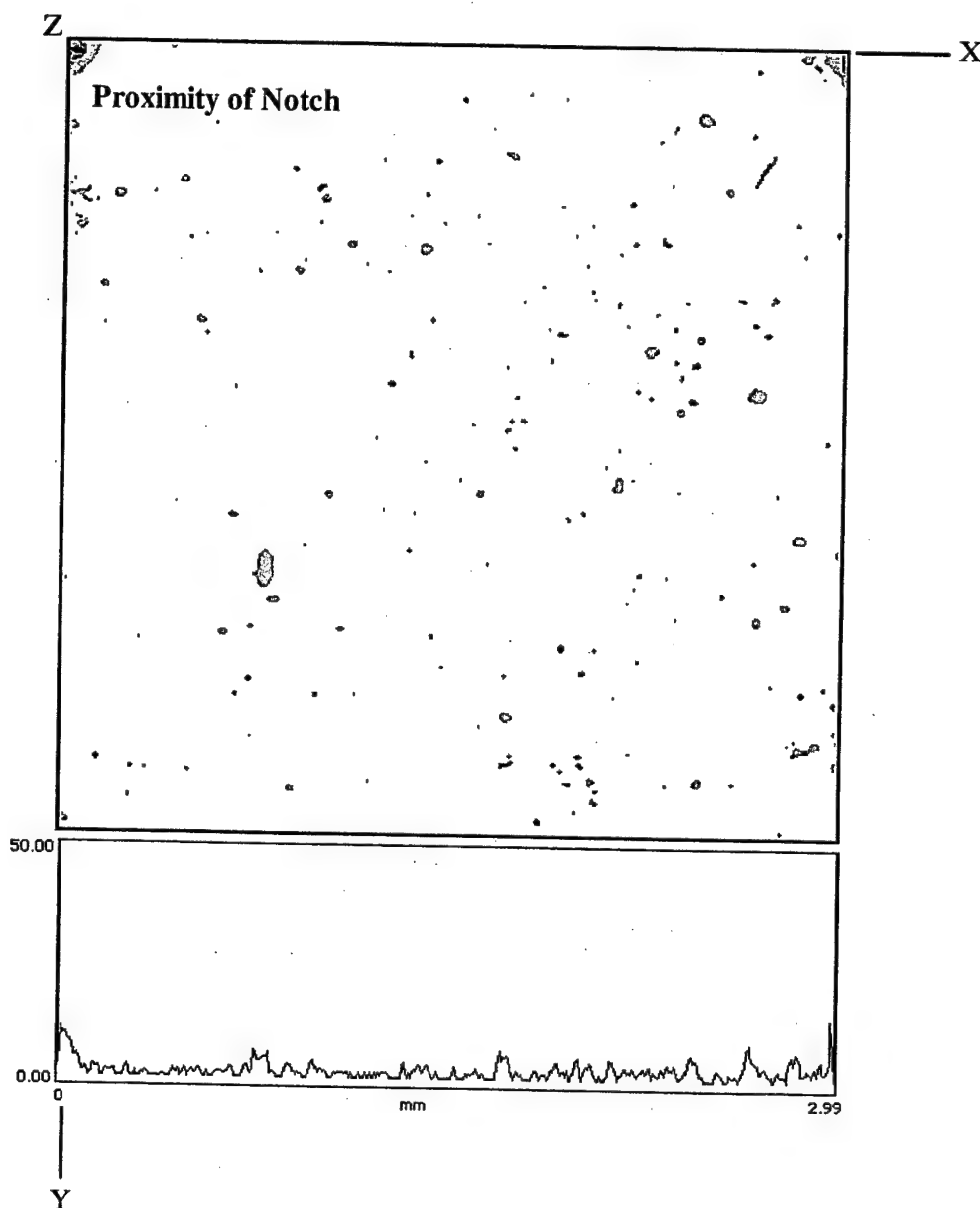
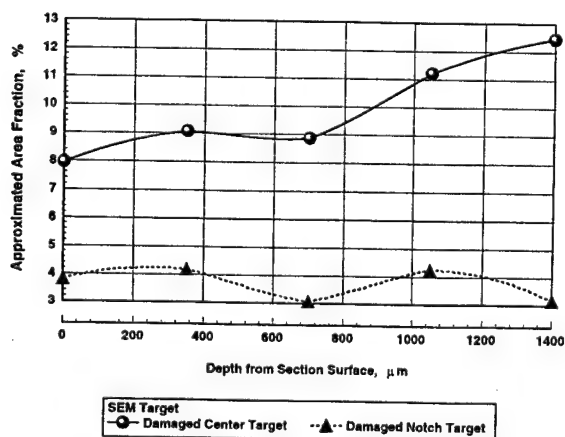**Fig. 11.** Two-dimensional map and corresponding profile plot of untested material notch target.

Fig. 12. Approximated area fraction as a function of depth from the specimen surface for both damaged material targets.
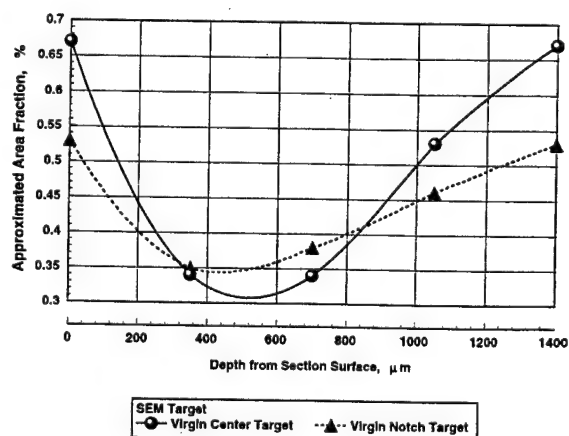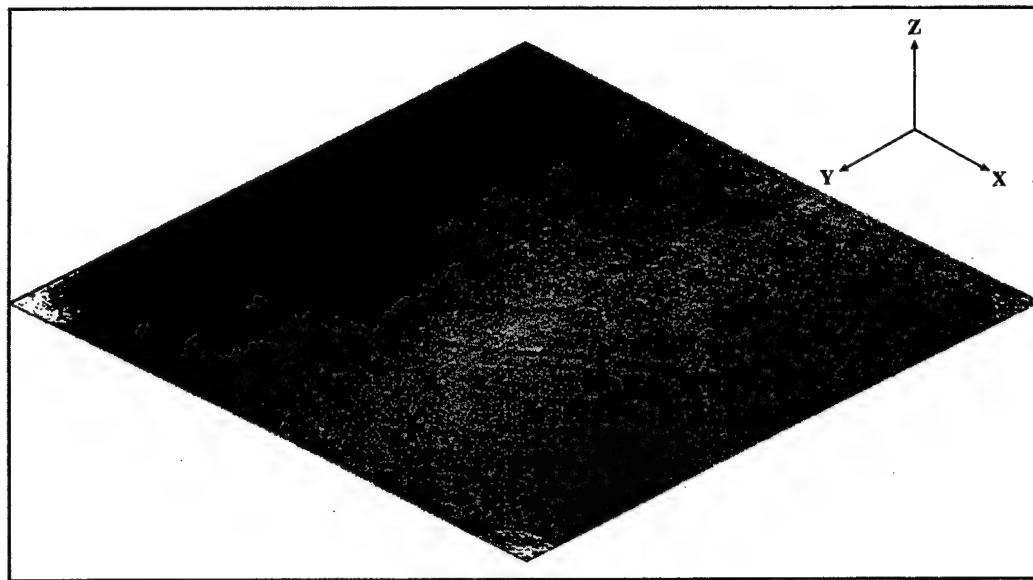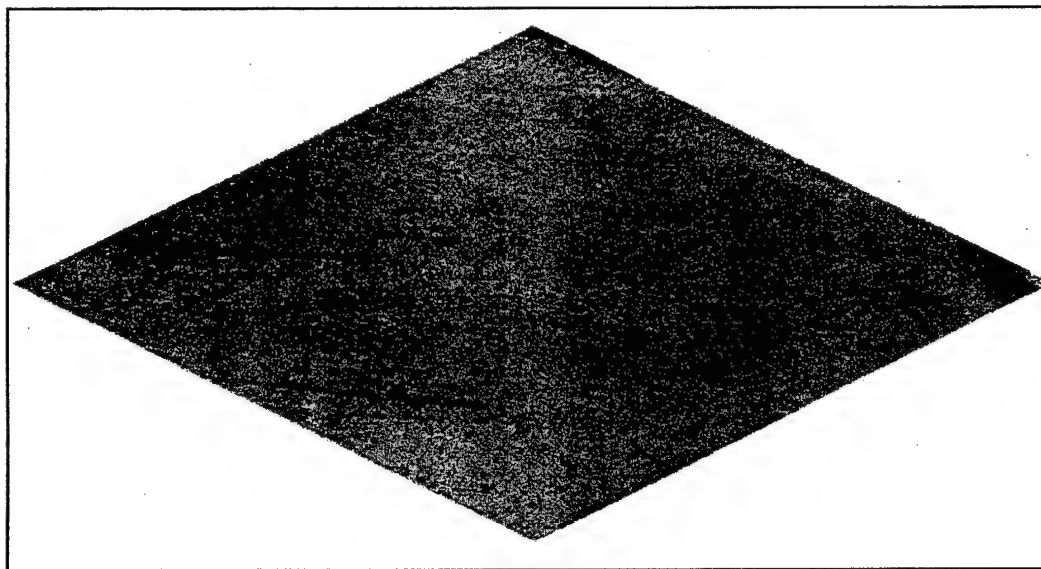

Fig. 13. Approximated area fraction as a function of depth from the specimen surface for both untested material targets.

(a)

(b)

Fig. 14. Reconstructed three-dimensional projections of damaged material targets created from intensity and depth maps: (a) center target, (b) notch target.

Finally, Fig. 15 shows 3-D projections of untested material assembled in the same manner as previously described. It should be noted that the regularly shaped flaws are indicative of resin rich pockets, voids or imaging aberrations and show no propensity towards the initiation of crack sites during the specimen preparation process.

5 CONCLUSIONS

The following conclusions can be drawn from the results presented in this study:

1. The proposed image analysis technique can be successfully applied to investigate damage initiation and development in woven textile composites. Three-dimensional damage maps for a shear tested Iosipescu woven textile composite specimen have been generated. It has been shown that the specimen preparation process does not alter the state of damage intact after testing.

2. It appears that for 8-harness woven textile composites such as graphite/PMR-15, the presence of relatively sharp notches in the Iosipescu specimens does not affect the failure process. It has been found that the majority (50% more) of damage

(a)

(b)
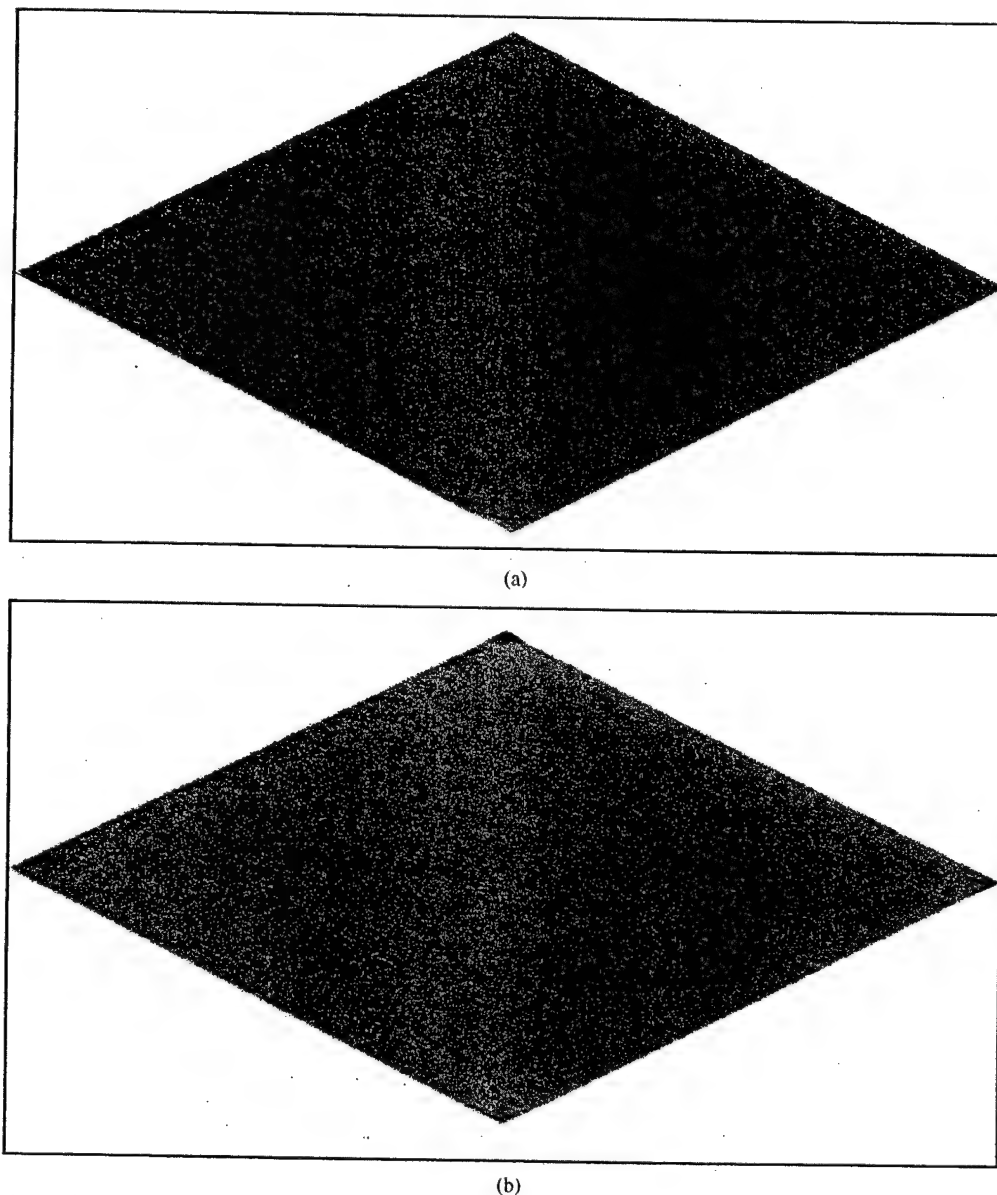
Fig. 15. Reconstructed three-dimensional projections of untested material targets created from intensity and depth maps: (a) center target, (b) notch target.

occurs in the central area of the specimen gage section. No significant damage has been detected at the roots of the notches. Therefore, it can be concluded that for this particular composite system, the Iosipescu shear test provides a uniform stress field in the gage section of the specimen.

3. From damage area fraction results, the number and size of internal cracks have been determined through the specimen thickness. The amount of damage increases as a function of the sub-surface depth and it is believed that this behavior is parabolic in nature with the maximum amount of damage occurring in the vicinity of the specimen mid-line. This seems to fit the explanation for the symmetrical out-of-plane deformation or bulging on the front and back side of the specimen.

ACKNOWLEDGEMENTS

REFERENCES

1. Iosipescu, N., New accurate procedure for single shear testing of metals. *J. Mater.*, 1967, **2**(1), 537–566.
2. Walrath, D. E. and Adams, D. F., The Iosipescu shear test as applied to composite materials. *Exp. Mech.*, 1983, **23**(1), 105–110.

3. Adams, D. F. and Walrath, D. E., Further development of the Iosipescu shear test method. *Exp. Mech.*, 1983, **27**(2), 113–119.

4. Arcan, M., Hashin, Z. and Voloshin, A., A method to produce plane-stress states with applications to fiber reinforced materials. *Exp. Mech.*, 1978, **13**(3), 141–146.

5. Broughton, W. R., Kumosa, M. and Hull, D., Analysis of the Iosipescu shear test as applied to unidirectional carbon fiber reinforced composites. *Compos. Sci. Technol.*, 1990, **38**, 299–325.

6. Broughton, W. R. Shear properties of unidirectional carbon fiber composites. Ph. D. thesis, Cambridge University, UK, 1989.

7. Bansal, A. and Kumosa, M., Experimental and analytical studies of failure modes in Iosipescu specimens under biaxial loadings. *J. Compos. Mater.*, 1995, **29**(3), 334–358.

8. Balakrishnan, M. V., Bansal, A. and Kumosa, M., Biaxial testing of unidirectional carbon/epoxy composites using the biaxial Iosipescu test fixture. *J. Compos. Mater.*, 1997, **31**(5), 486.

9. Balakrishnan, M. V., Application of the biaxial Iosipescu test fixture for the mechanical characterization of unidirectional composites. M. S. thesis, Graduate Institute of Science and Technology, Portland, OR, 1995.

10. Kumosa, M., Searles, K. and Thirumalai, V., *Biaxial Failure Analysis of Graphite Reinforced Polyimide Composites*. Annual Progress Report to the Air Force Office of Scientific Research, Department of Materials Science and Engineering. Oregon Graduate Institute of Science and Technology, 1995, pp. 1–80.

11. Kumosa, M., Searles, K. and Odegard, G., Biaxial failure analysis of graphite reinforced polyimide composites. *HITEMP Review, Advanced High Temperature Engine Materials Technology*, Vol. 1: *Overviews*, Fan/Compressor Materials–PMCs, ppr 18, pp. 1–11.

12. Hollman, K., *In-Plane Shear Failure Analysis of Notched Composites*. Department of Aeronautical Structures and Materials, The Royal Institute of Technology, Stockholm, 1990, pp. 1–39.

13. Bovik, A., Huang, T. and Munson Jr, D., The effect of median filtering on edge estimation and detection. *IEEE Transactions on Pattern Analysis and Machine Intelligence*, 1987, **9**(2), 181–193.

Non-linear finite-element analysis of Iosipescu specimens

M. Kumosa*, Y. Han

Center for Advanced Materials and Structures, Department of Engineering, University of Denver, 2450 South Gaylord Street, Denver, CO 80208, USA

Abstract

In this paper the effects of specimen sliding within the biaxial Iosipescu fixture and geometric non-linearity on the mechanical response of isotropic, composite and adhesively bonded isotropic and composite Iosipescu specimens subjected to shear under small displacement conditions have been modeled by non-linear finite-element techniques. The mechanical response of the specimens to the external applied loads has been modeled by assuming different friction coefficients between the loading blocks of the Iosipescu fixture and the specimens. It has been shown that the sliding of the specimen within the fixture in conjunction with geometric non-linearity (large specimen deformation) can affect, for some specimen geometries, the load/displacement diagrams and internal stress distributions in the gage sections of the Iosipescu specimens. These effects are especially strong in the case of adhesively bonded Iosipescu specimens with either isotropic or composite adherends. However, for 0° unidirectional graphite/epoxy composite Iosipescu specimens subjected to small shear loadings the effects of specimen sliding and geometric non-linearity on the load/displacement diagram and internal stresses appear to be negligible. © 1999 Elsevier Science Ltd. All rights reserved.

1. Introduction

In the traditional Iosipescu shear test [1], isotropic, composite or adhesively bonded Iosipescu specimens are loaded by the application of two counteracting moments produced by two force couples (see Fig. 1). A means of applying a shear loading to the specimen was proposed for the first time by Adams and Walrath [2]. The first Wyoming Iosipescu fixture designed by Adams and Walrath was later redesigned in order to reduce large compressive stresses generated in the gage section of Iosipescu specimens [3,4]. The Iosipescu specimen loaded in the modified Wyoming fixture has become one of the most popular test methods for the shear characterization of composite materials. The Iosipescu shear test was significantly modified a few years ago at the University of Cambridge by Broughton et al. [5]. In their biaxial Iosipescu test fixture Iosipescu specimens can be tested not only in shear but also under either shear/tension or shear/compression loading conditions (see Fig. 2) [5,9]. Various biaxial shear dominated stress states can be generated by rotating the specimens within the biaxial Iosipescu fixture. The first version of the biaxial Iosipescu fixture [5,9] was based on the loading block configuration very similar to the original Wyoming

design [2]. Recently, the biaxial Iosipescu fixture has been modified [10] by introducing new loading blocks, that are very similar to the modified Wyoming design.

Despite the fact that the Iosipescu shear-test method is now ASTM Standard D 5379 [11], the proper numerical solutions of internal stresses in the shear Iosipescu specimens, taking into account the effects of specimen sliding and geometric non-linearity caused by large specimen deformations within various Iosipescu fixtures, are not available. In a series of papers we would like to present comprehensive numerical studies of the effects of sliding and geometric non-linearity on the mechanical response of various Iosipescu specimens subjected to either shear or biaxial loading conditions. In this paper, these effects are discussed with respect to isotropic, unidirectional composites and adhesively bonded Iosipescu specimens subjected to relatively small shear deformations (less than 1 mm). The type of loading investigated in this study simulated the original design of the Wyoming fixture [2] and the biaxial Iosipescu fixture [5,9] as far as the loading block configuration is concerned. The influence of different loading block geometries, including the loading conditions recommended by the ASTM standard, and biaxial shear-dominated loads on the stresses and strains in the Iosipescu specimen will be discussed in our subsequent papers [12,13].

* Corresponding author.

$w = 80 \, mm$ $h = 20 \, mm$ $t = 5 \, mm$ $b = 8 \, mm$ $\alpha = 90°$ $l = 10 \, mm$

pressures P_1 and P_2: $\dfrac{P_1}{P_2} = \dfrac{w-l}{b+l}$ fixture force load: $F = (P_1 - P_2) \, l \, t$
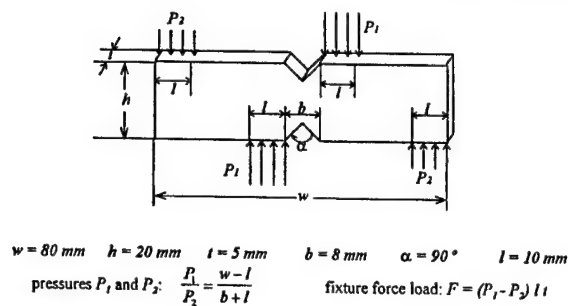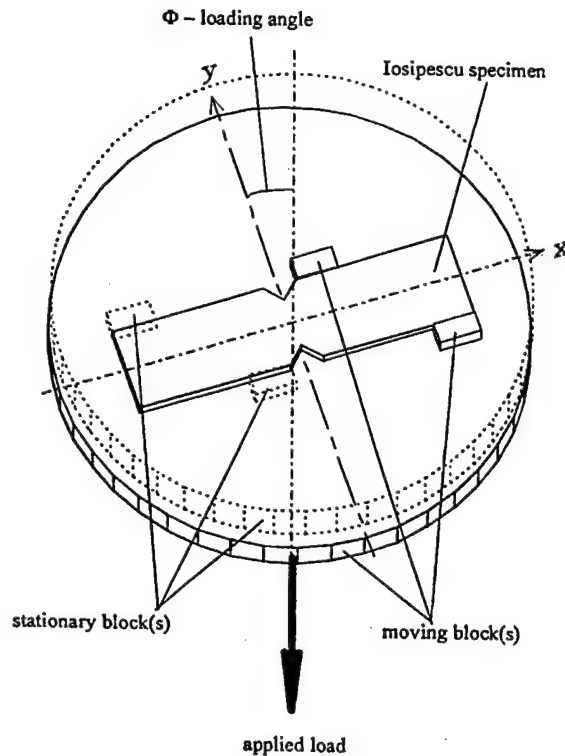
Fig. 1. Iosipescu shear test.

Fig. 2. Biaxial loading conditions in the biaxial Iosipescu fixture.

The effect of specimen sliding within the shear Iosipescu fixture was investigated for the first time by Ho et al. [14]. In their finite-element analysis, 0° and 90° unidirectional graphite/epoxy Iosipescu specimens were analyzed with the assumption that the specimens were loaded in pure shear in the fixture recommended by the ASTM standard (the modified Wyoming design).

The authors have drawn the following conclusions based on their non-linear finite-element simulations of the mechanical response of the specimens to shear:

(a) (a) The coefficient of friction between the loading blocks and the 0° and 90° unidirectional graphite/epoxy specimens were 0.3 and 0, respectively. The effect of frictional forces on the test section shear stress was negligible for 0° and 90° specimens.

(b) (b) The effect of geometric non-linearity due to the change of specimen geometry on the shear response of 0° and 90° specimen was negligible.

(c) (c) The only significantly contributing factor to the non-linear response of the composite Iosipescu specimens to shear was the non-linear material behavior.

In the numerical analyses performed by Ho et al. [14], the non-linear shear-stress/strain response of a unidirectional graphite/epoxy composite was modeled by assuming different friction coefficients between the loading blocks of their Iosipescu fixture and the specimens as well as the non-linear constitutive equations. The simulated shear-stress/strain curves were subsequently compared to the experimentally determined shear-stress/strain diagrams. If the simulated and experimental curves did not agree, small modifications to the coefficient of friction and the constitutive equations were made. It is difficult to believe that the friction coefficient determined numerically for the 90° specimen could be zero. The numerically determined shear response of the specimens depended on both the assumed friction coefficients and the constitutive equations. Most likely the constitutive equations used in the analysis were not strictly accurate. It can be expected that the friction coefficient of the 90° specimen is higher than for the 0° oriented fibers since the fibers cut perpendicular to the specimen/loading block frictional interface must increase the resistance to sliding of the specimen in comparison with the specimen with the fibers parallel to this interface.

During the Iosipescu test large compressive stresses develop in the specimens near the loading blocks. These stresses, in some cases, can cause severe crushing of a composite, thus modifying the frictional properties of the interface during the experiment. It is possible that the friction coefficient at the loading block/specimen interface will change significantly, especially for large load values. Moreover, the friction coefficient at the loading block/specimen interface can vary with temperature in the high-temperature testing of polymer-matrix composites [15]. In addition, large specimen deformations can occur when graphite/polyimide specimens are tested to failure under either shear or biaxial-shear-dominated loading conditions. Obviously, these effects should be less pronounced in the standard Iosipescu shear test, since the loading blocks in the fixture recommended by the standard are much longer in comparison with the loading blocks used in the original Wyoming design, and the biaxial Iosipescu fixture. Nevertheless, the effects of specimen sliding and geometric non-linearity on the internal stresses in the Iosipescu specimens need to be better understood if the proper failure analysis of composites is to be performed using either the standard shear test or the biaxial Iosipescu test methods.

2. Finite element computations

An attempt was made in this study to evaluate separately the effects of specimen sliding and geometric non-linearity (due to the change of specimen geometry) on the global mechanical response and internal stresses of various metal and composite Iosipescu specimens subjected to shear under the conditions of small applied displacements. The non-linear material behavior has not been considered in this research.

2.1. Specimen geometry and boundary conditions

Five different Iosipescu specimens were analyzed in this study (Fig. 3). The internal stresses and the global deformations for an isotropic (aluminum) Iosipescu specimen (Fig. 3(a)) were numerically determined as a function of different friction coefficients between the loading blocks of the Iosipescu fixture and the specimen. The recently suggested adhesively bonded Iosipescu specimen [16] [17] [18] was also investigated with isotropic (Fig. 3(b), aluminum) and unidirectional graphite/epoxy composite (Fig. 3(c)) adherends. In addition, unidirectional graphite/epoxy Iosipescu specimens were modeled with the fiber orientation either parallel to the long axis of the specimen (0° orientation, Fig. 3(d)) or to the notch root axis (90° orientation, Fig. 3(e)). The specimens were numerically loaded assuming the following boundary conditions:

(1) Displacement boundary conditions for the linear elastic model with zero friction (Fig. 4(a)). The right-side of the specimen is loaded by prescribed vertical displacements (u_y) on the loading blocks whereas the loading blocks on the left-side of the specimen are constrained against any vertical displacements (u_y). This model assumes free axial movement of the specimen
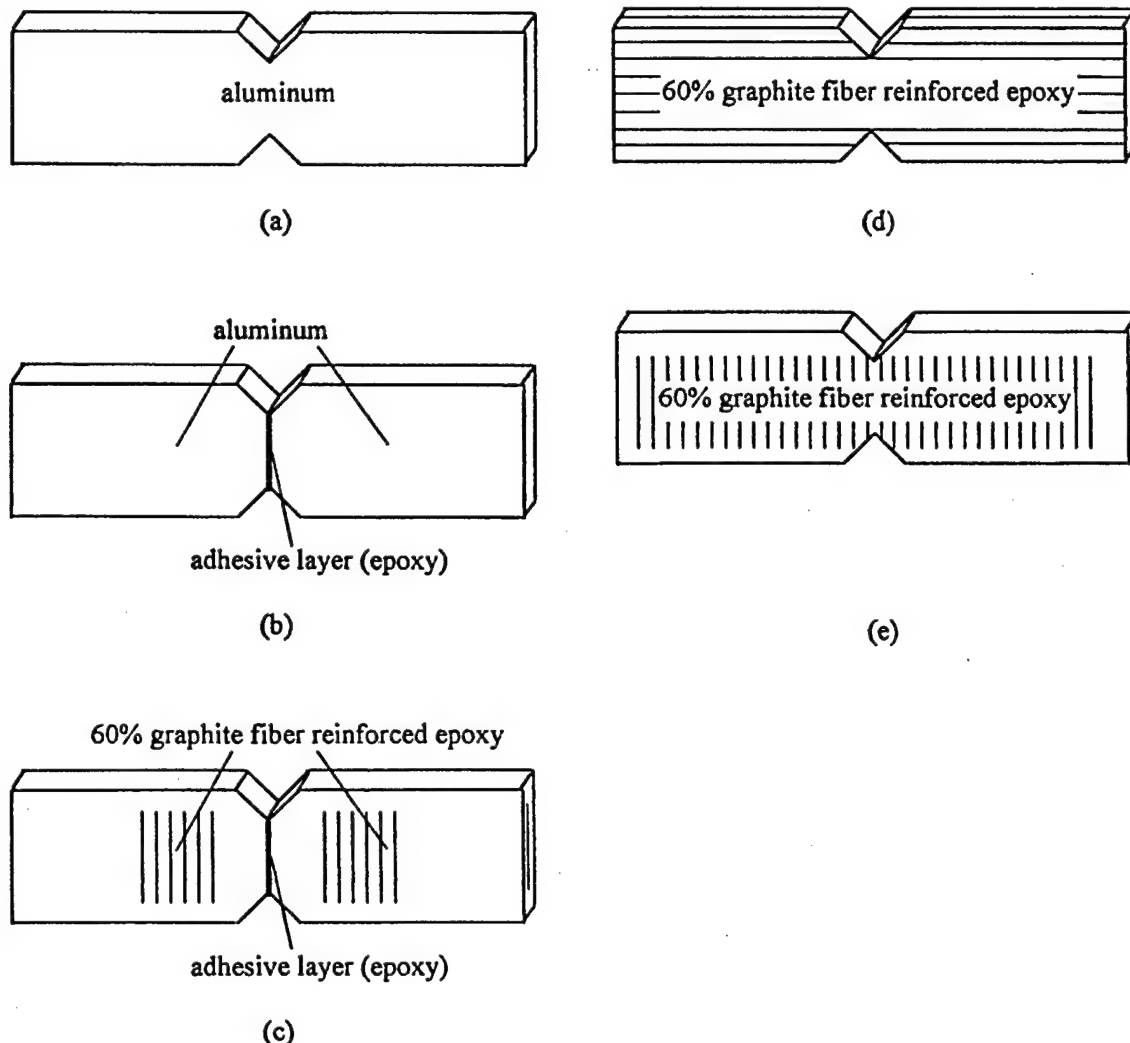

Fig. 3. Various Iosipescu specimens: (a) isotropic aluminum specimen; (b) adhesively bonded specimen with aluminum adherends; (c) adhesively bonded specimen with unidirectional graphite/epoxy adherends; (d) unidirectional 0° fiber oriented specimen; and (e) unidirectional 90° fiber oriented specimen.
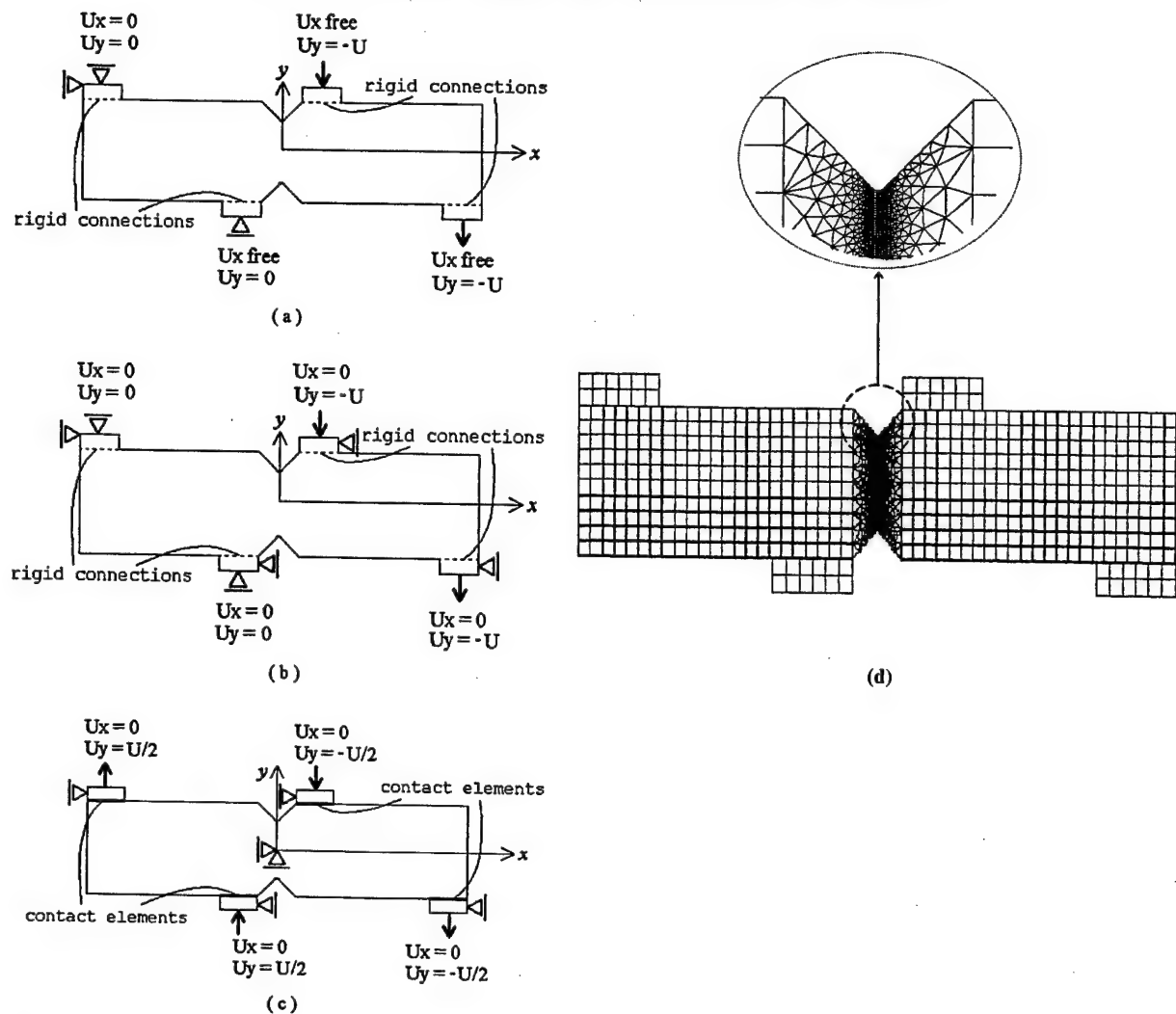
Fig. 4. Displacement boundary conditions used in the finite element analyses: (a) linear elastic model with zero friction; (b) linear elastic model with infinite friction; (c) non-linear model with specimen sliding along the loading blocks and geometric non-linearity; and (d) finite element representation of the adhesive bonded and unidirectional composite Iosipescu specimens.

along x together with the loading blocks, which are perfectly bonded to the specimen.

(2) Displacement boundary conditions for the linear elastic model with infinite friction (Fig. 4(b)). In this model the right-side of the specimen is loaded by prescribed displacements (u_y) on the loading blocks with the blocks constrained against the movement along x (by assuming $u_x = 0$). The loading blocks on the left-side of the specimen are fully constrained against any translation movements (u_x and $u_y = 0$). Similar to the previous case, contact elements were not used, with the blocks perfectly bonded to the specimen.

(3) Displacement boundary conditions with contact elements between the specimen and the loading blocks (Fig. 4(c)). In this model, the specimen center is constrained against the vertical and horizontal displacements (u_x and $u_y = 0$). The blocks on the right-side of the specimen have prescribed displacements of $-u/2$

whereas the blocks on the opposite side of the specimen are loaded by the positive displacements of the same magnitude. Thus, the total prescribed displacement acting on the specimen is equal to u. Using these boundary conditions the effect of specimen rotation (biaxial shear dominated loading generated by the biaxial fixture) can also be investigated with sliding and geometric non-linearity [21].

In the above models the loading blocks were assumed to be linear elastic and made out of steel. The dimensions of the blocks were 10 mm in length and 5 mm in height. The thickness of the specimen was assumed to be 1 mm. The material properties of the Iosipescu specimens investigated in this study are listed in Table 1. The finite element computations were performed using ANSYS 5.2 [19].

In the finite element computations two dimensional representations of the Iosipescu specimens were

Table 1
Material properties used in the finite element computation

	Aluminum	60% unidirectional graphite/epoxy	Epoxy adhesive	Steel loading blocks
Young's modulus (MPa)	$E = 70000$	$E_{11} = 212000$ $E_{22} = 7240$	$E = 3500$	$E = 400000$
Shear modulus (MPa)	$G_{12} = 26316$	$G_{12} = 4070$	$G_{12} = 1259$	$G_{12} = 154000$
Poisson's ratio	$v = 0.33$	$v_{12} = 0.33$ $v_{21} = 0.082$	$v = 0.39$	$v = 0.30$

constructed (see Fig. 4(d)) using six-node triangular and eight-node quadrilateral isoparametric elements. The frictional interfaces between the loading blocks and the specimens were modeled using two dimensional point-to-surface contact elements. Along the specimen to fixture contact regions, Coulomb friction was assumed. The loading procedure was divided into 10 load steps. For each load step, the relative displacements prescribed on the loading blocks were increased by 0.1 mm. At the end of the last load step, a total loading of 1 mm was applied. For each load step, the SRSS (the square root of the sum of squares) of the imbalance forces was calculated. The force convergence criterion was assumed with the SRSS of the imbalance forces smaller than 0.1% of the SRSS of the loading forces. The maximum prescribed displacement of 1 mm was chosen since the failure of the investigated composites and adhesively bonded composite systems could occur at this load level [5,7,16].

3. Results and discussion

3.1. Specimen sliding and reaction forces at the loading blocks

A comprehensive study of specimen deformations within both the biaxial and modified Wyoming Iosipescu shear fixtures has been performed by K. Searles, Y. Han and M. Kumosa [20,21,23]. In this paper, a short description of the specimen deformations in the biaxial Iosipescu fixture loaded in shear is presented. It should be mentioned here that the biaxial Iosipescu fixture has significantly shorter blocks than the modified Wyoming fixture. The non-linear analysis performed by Ho et al. [14] was based on the modified Wyoming fixture with significantly longer loading blocks. Therefore, the conclusion from their study may not be applicable to the case of the biaxial Iosipescu fixture. It can be speculated that the effects of specimen sliding and geometric non-linearity on the stress distributions in the Iosipescu specimens can be significantly dependent on the loading block geometries. The non-linear effects should be more pronounced in the cases when short loading blocks are used. This problem has been recently studied by Odegard et al. [23].

The reactions on the inner and outer loading blocks for the isotropic aluminum Iosipescu specimen for a

$P1x = 0$ $P1y = 15662 N$

(a)

$P2x = 0$ $P2y = -3039 N$

(b)

Fig. 5. Reaction forces and specimen deformation at the inner (a) and outer (b) loading blocks from the linear model with zero friction for the isotropic (aluminum) Iosipescu specimen loaded in shear by a prescribed displacement of 1 mm.

prescribed displacement of 1 mm are shown for the linear elastic case with zero friction (Fig. 5) and the non-linear case with a friction coefficient of 0.3 and geometric non-linearity assumed (Fig. 6). The specimen sliding at the inner and outer loading blocks is also illustrated in Fig. 6 for the non-linear case. Obviously,

$P1x = 1776\,N$ $Ply = 15347\,N$
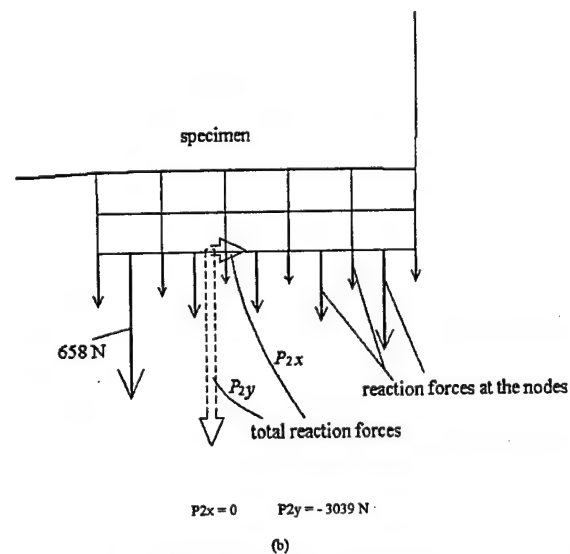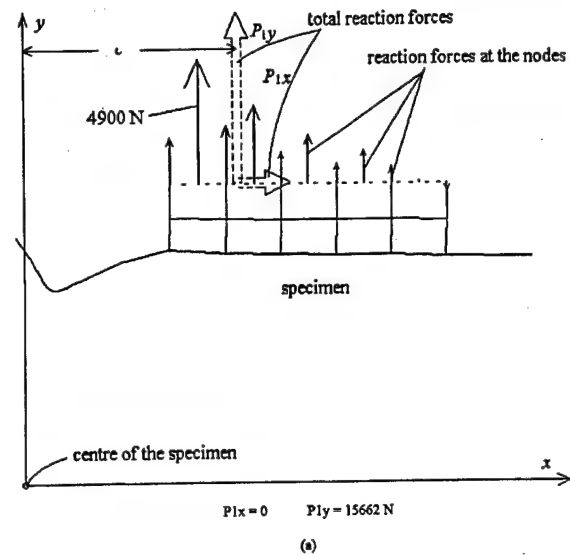
(a)

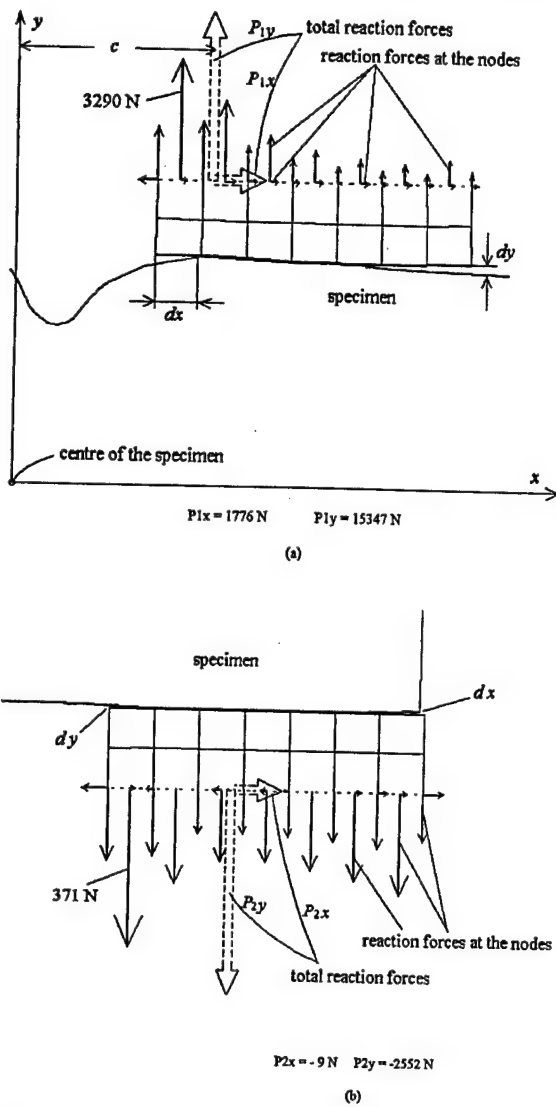$P2x = -9\,N$ $P2y = -2552\,N$

(b)

Fig. 6. Reaction forces and specimen deformation at the inner (a) and outer (b) loading blocks from the non-linear model with sliding and geometric non-linearity for the isotropic (aluminum) specimen loaded by a displacement of 1 mm with a friction coefficient of 0.3.

no sliding of the specimen along the loading blocks was observed in the linear case since the loading blocks were bonded to the specimen allowing the movements of the specimen with the loading blocks along the x axis. It can be seen in Fig. 6(a) and (b) that the movement of the specimen along the inner loading blocks (dx) is in the direction away from the center of the fixture whereas the specimen sliding along the outer blocks is toward the center. These directions of sliding were observed for all the specimens considered in this study. However, the movement of the specimen at the inner and outer loading blocks is strongly dependent on the type of loading [20]. It can also be seen in Fig. 6(a) that the specimens can separate from the inner loading blocks creating a gap (dy) which is again strongly dependent on the magnitude and type of loading (shear, shear/tension, shear/compression). The separation of the specimen from the

loading blocks during the test reduces the contact area between the blocks and specimen, thus significantly affecting the distribution and magnitude of the reaction forces.

The reaction forces on the loading blocks affect the stress conditions in the Iosipescu specimens. Since horizontal constrains on the loading blocks for the linear case with zero friction were not imposed, no shear reactions were observed at the inner and outer loading blocks. In the non-linear case, however, both the normal and shear reaction forces develop at the inner and outer loading blocks and are strongly dependent on the magnitude and type of loading, as well as the specimen configuration. It is important to note that the total reaction force P_{1y} on the inner loading block, obtained by integrating the nodal reaction forces, moves slightly towards the specimen center (distance c in Figs. 5a and 6a) with a decrease in the friction coefficient for the same magnitude of the shear load applied to the specimen. The position of the total reaction force P_{2y} does not change significantly with the friction coefficient assumed at the interface.

The normal and shear reactions on the loading blocks can be used to determine the global loads on the Iosipescu specimens for different prescribed displacements and friction coefficients. By summing up the reaction forces P_{1x}, P_{1y}, P_{2x} and P_{2y}, the magnitude and direction of the global reaction force P can be established. Obviously, for the non-linear cases the direction of P does not coincide with the direction of the applied load, which in shear is along the notch root axis. However, the vertical component of P will represent the total load on the specimen for a given prescribed displacement. Then, the load/displacement diagrams can be determined for various specimen configurations, loading conditions and the frictional properties of the loading block/specimen interfaces with and without geometric non-linearities considered.

3.2. Numerical load/displacement diagrams

Fig. 7(a)–(e) present the loading diagrams for the isotropic aluminum (Fig. 7(a)), adhesively bonded aluminum/epoxy (Fig. 7(b)), adhesively bonded unidirectional composite (Fig. 7(c)) and unidirectional graphite epoxy/epoxy Iosipescu specimens with the 0° (Fig. 7(d)) and 90° (Fig. 7(e)) fiber orientations, respectively. The diagrams were computed for the two linear elastic models (zero and infinite friction) and the non-linear models with different friction coefficients (with and without geometric non-linearity). In Fig. 7 only the results obtained for a friction coefficient of 0.3 are shown.

It can be seen in Fig. 7(a) that for the aluminum specimen the load/displacement diagram obtained from the linear elastic model, with zero friction, is very similar to
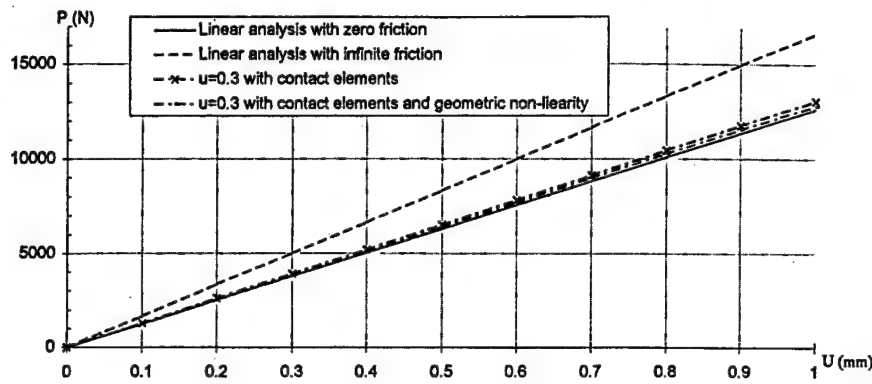
(a)
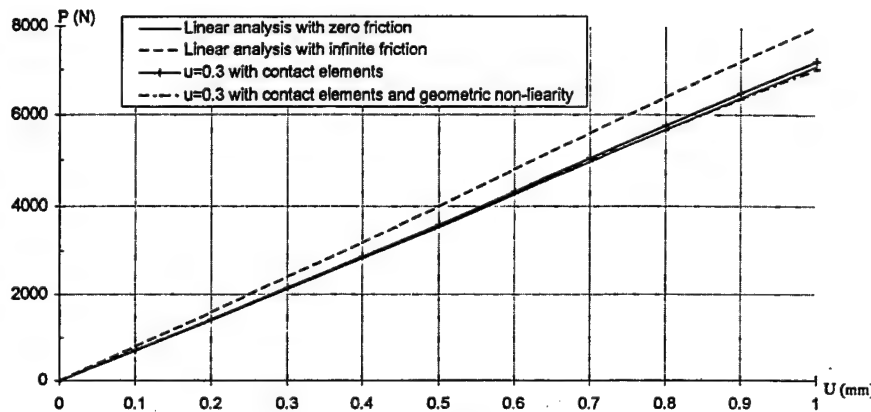
(b)
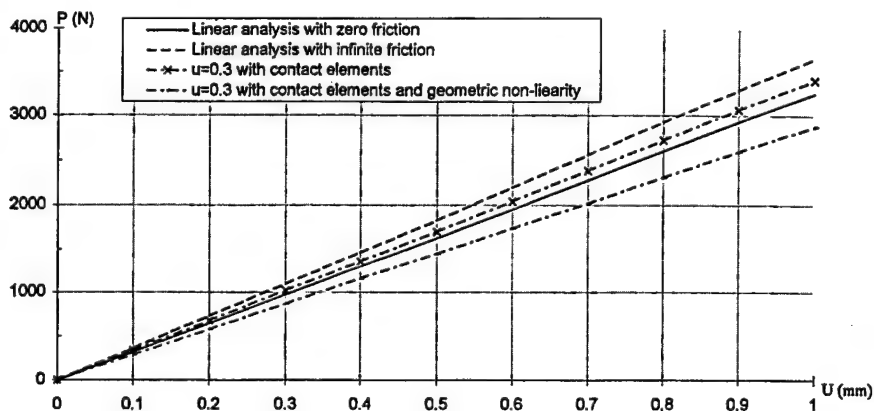
(c)

Fig. 7. Load/displacement diagrams of various Iosipescu specimens determined from four different models: (a) aluminum specimen; (b) adhesively bonded specimen with aluminum adherends; (c) adhesively bonded specimen with unidirectional composite adherends; (d) unidirectional 0° graphite/epoxy specimen; and (e) unidirectional 90° graphite/epoxy specimen.

the diagrams from the non-linear models. It can also be noticed that the effect of geometric non-linearity on the non-linear results is almost negligible. However, there is a significant difference between the load displacement diagrams obtained from the linear (infinite friction) and non-linear finite element computations. Similar observations can be made by examining Fig. 7(b), (d) and (e)

which represent the mechanical response of the adhesively bonded aluminum specimen and the unidirectional graphite/epoxy with the 0° and 90° fiber orientations. The effect of geometric non-linearity and sliding appear to be more pronounced in the case of the adhesively bonded composite specimen with the unidirectional graphite/epoxy adherends (see Fig. 7(c)).

(d)

(e)

Fig. 7 cont.

Under the same loading conditions the epoxy/aluminum specimen shows smaller effect of large deformations that the specimen with the unidirectional composite adherends (fibers parallel to the interfaces). Most likely, the higher stiffness of the epoxy/aluminum specimen along the long axis of the specimen in comparison with the composite specimen prevented specimen sliding along the loading blocks.

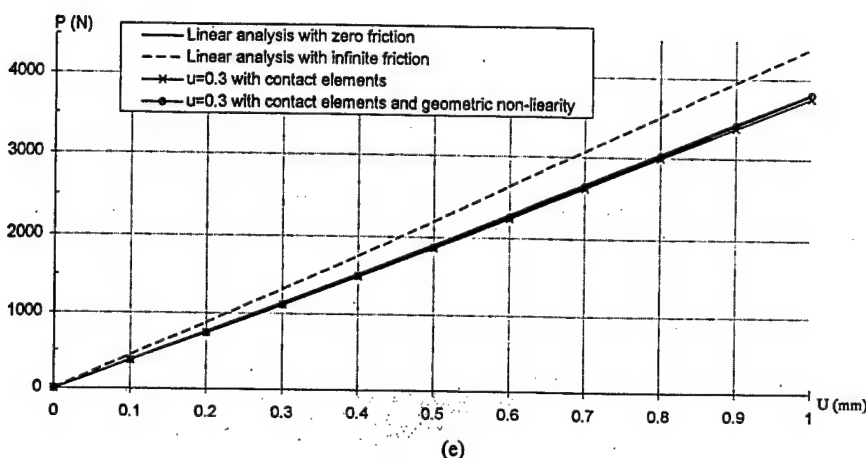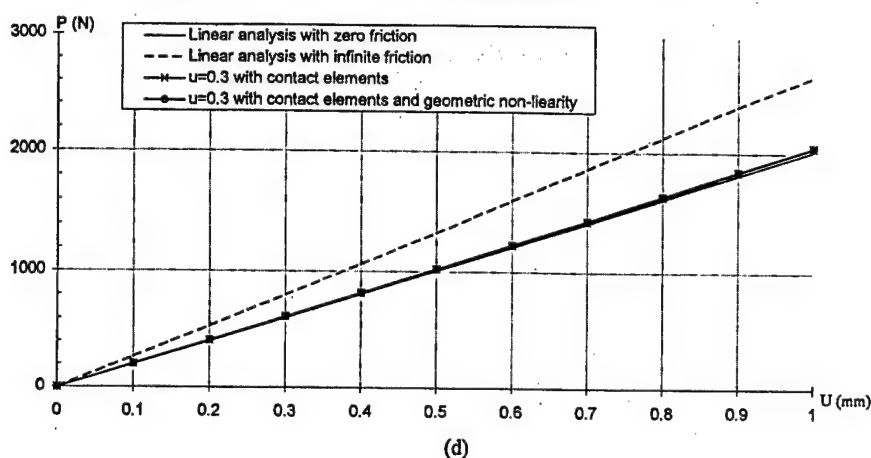The total reaction forces for a prescribed displacement of 1 mm for the linear and non-linear models of the above five different geometries of the Iosipescu specimens are presented in Fig. 8(a)–(e). These figures illustrate even better the effect of different boundary conditions and the frictional properties of the loading block/specimen interface on the total reaction forces of the specimens investigated. The data shown in Fig. 8(a) clearly demonstrate that the effect of geometric non-linearity for the aluminum specimen is almost negligible. The reaction forces are very similar for the models with contact elements analyzed with and without geometric non-linearity for different friction coefficients. Moreover, the linear elastic model with zero friction gave very similar results of the global reaction forces in comparison with the non-linear models. It can be

expected that in the actual Iosipescu shear experiment the friction coefficient between the aluminum specimen and the steel loading blocks will be somewhere between 0.1 and 0.3. Therefore, the simple linear elastic model will certainly provide very accurate estimates of the load/displacement curve for this particular specimen. The total reaction force acting on the specimen modeled with infinite friction is significantly higher than the loads obtained from the zero friction linear model and the non-linear models.

The results obtained from the computations of the total reaction forces of the adhesively bonded aluminum/epoxy Iosipescu specimen (Fig. 8(b)) show very similar trends. Again, for this particular specimen, the non-linear computations of the load/displacement diagrams are not necessary since the linear elastic model with zero friction provides very similar estimates of the total reaction force. Similar to the previous diagram for the friction coefficients ranging from 0.1 to 0.3 the total load on the specimen determined from the linear elastic model with zero friction is between the loads from the non-linear models analyzed with and without geometric non-linearity.

The effect of geometric non-linearity on the load/displacement diagram for the adhesively bonded unidirec-
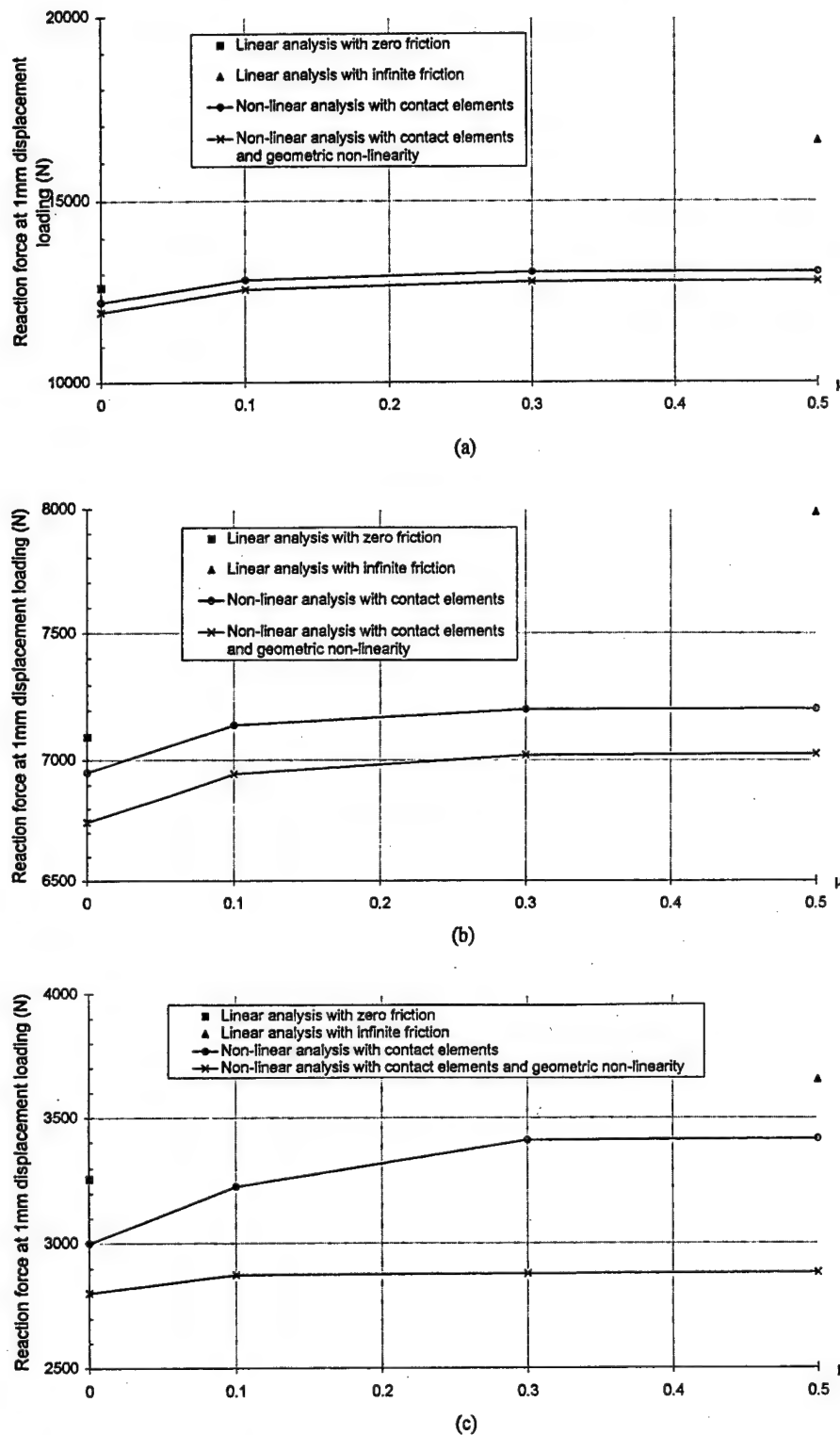
Fig. 8. The effect of different friction coefficients at the loading blocks on the total reaction forces determined from the linear and non-linear models for a prescribed displacement of 1 mm for (a) aluminum specimen, (b) adhesively bonded specimen with aluminum adherends, (c) adhesively bonded specimen with unidirectional composite adherends, (d) unidirectional 0° graphite/epoxy specimen, and (e) unidirectional 90° graphite/epoxy specimen.

tional graphite epoxy Iosipescu specimen is significantly stronger in comparison with the previous specimens (see Fig. 8(c)). In this case the total loads for a prescribed displacement of 1 mm determined from the non-linear models with geometric non-linearity are significantly lower than the loads determined from both the linear elastic model with zero friction and the non-linear models when geometric non-linearity was not assumed.
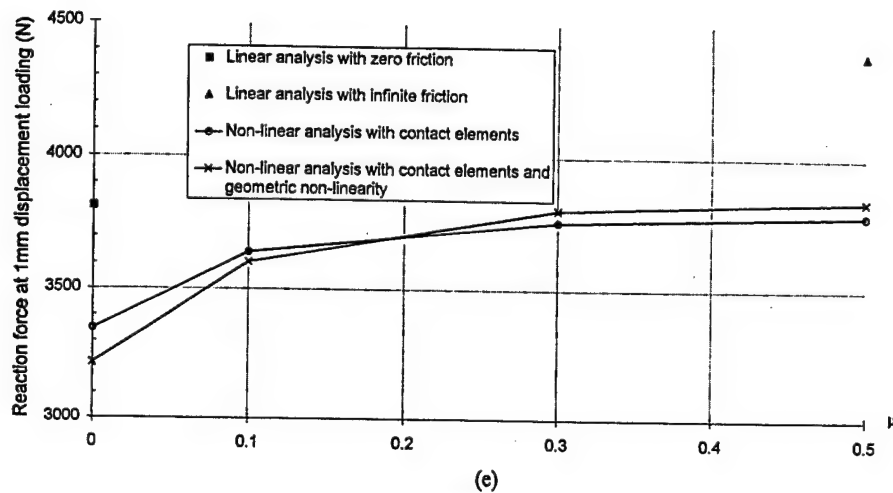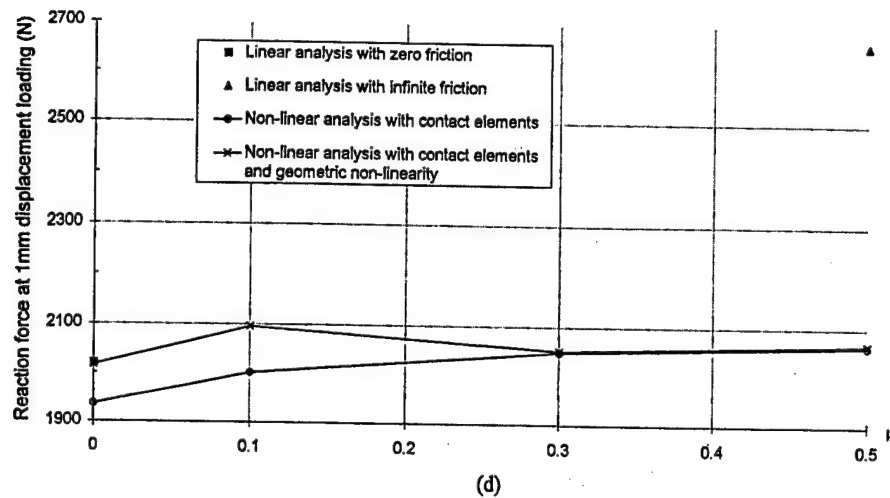
Fig. 8. cont.

Obviously, this type of specimen must be modeled assuming both the effect of specimen sliding along the loading blocks and geometric non-linearity if the proper evaluation of the load/displacement diagram is required. The linear elastic model with zero friction will not be accurate.

For the unidirectional graphite/epoxy composite specimens for both the 0° and 90° fiber orientations the effects of specimen sliding and the geometric non-linearity seem to be insignificant, similar to the first two cases (see Fig. 8(d) and (e)). It appears that for these two specimens the load/displacement curves can be modeled using the linear elastic model with zero friction providing that the prescribed displacements are relatively low (lower than 1 mm).

Despite the fact that the numerical models used in this analysis assume relatively short loading blocks, following the original Wyoming design of the Iosipescu shear fixture, the effect of specimen sliding and geometric non-linearity on the load displacement diagrams of the Iosipescu specimens loaded up to 1 mm displacement is almost insignificant for the aluminum as well as the 0° and 90° unidirectional graphite/epoxy Iosipescu specimens in comparison with the linear elastic model with zero friction. For the adhesively bonded composite specimen with the fibers oriented along the notch root axis and a thin adhesive layer placed between the roots of the notches there is a very small difference, almost insignificant, between the loads calculated using the non-linear model with sliding and without geometrical non-linearity. However, the combined effect of sliding and geometric non-linearity on the load displacement diagram is significant. Thus, for accurate simulation of shear behavior of the adhesively bonded composite Iosipescu specimen, a more complex non-linear model is needed.

3.3. Stresses at the center of the Iosipescu specimens

Since the combined effect of specimen sliding within the Iosipescu shear fixture and the change in specimen geometry can affect the mechanical shear response of some Iosipescu specimens in this section, the internal stresses at the specimen center of the five different

Table 2
Stresses at the center of various Iosipescu specimens for a displacement of 1 mm and different friction coefficients

	Linear model with $\mu=0$	Linear model with $\mu=\infty$	Non-linear model with contact elements				Non-linear model with contact elements and geometric non-linearity			
			$\mu=0$	$\mu=0.1$	$\mu=0.3$	$\mu=0.5$	$\mu=0$	$\mu=0.1$	$\mu=0.3$	$\mu=0.5$
(a) Aluminium specimen										
σ_{xx}	58.068	−976.48	18.556	−36.314	−59.83	−61.376	48.192	−1.0884	−22.994	−24.773
σ_{yy}	−576.51	−290.57	−516.08	−586.51	−609.07	−610.05	−483.93	−557.3	−580.75	−582.12
σ_{xy}	−962.5	−1254.7	−950.89	−992.39	−1009.3	−1010.2	−934.32	−978.65	−995.94	−997.16
(b) Aluminium adherends and epoxy adhesive										
σ_{xx}	14.128	−161.58	4.6646	−38.587	−53.984	−54.988	245.81	211.55	199.42	198.39
σ_{yy}	−15.557	−91.562	−16.374	−35.315	−41.857	−42.249	−90.411	−116.68	−126.29	−126.99
σ_{xy}	−568.5	−639.48	−559.17	−573.99	−579	−579.28	−535.49	−553.07	−559.84	−560.29
(c) 60% graphite/epoxy adherends and epoxy adhesive (fibers parallel to the interfaces)										
σ_{xx}	4.0531	−44.867	−2.8707	−21.315	−34.081	−35.008	42.539	39.517	39.241	39.103
σ_{yy}	0.83285	−21.063	−1.1306	−9.7647	−15.832	−16.245	−11.646	−14.767	−15.033	−15.146
σ_{xy}	−275.29	−308.48	−254.91	−273.38	−288.08	−288.69	−238.3	−244.59	−245.09	−245.28
(d) 60% graphite/epoxy specimen with horizontal fibers										
σ_{xx}	17.268	30.294	15.967	13.26	12.854	13.801	18.042	14.543	14.035	15.068
σ_{yy}	−75.775	−82.937	−71.627	−74.276	−75.49	−75.382	−76.399	−80.028	−76.483	−76.388
σ_{xy}	−128.96	−173.69	−124	−128.42	−131.69	−132.76	−129.28	−135	−132.57	−133.68
(e) 60% graphite/epoxy specimen with vertical fibres										
σ_{xx}	4.9614	−53.318	−3.3682	−23.775	−31.26	−33.571	−20.913	−90.809	−126.97	−134.92
σ_{yy}	−27.094	−152.35	−4.8755	−61.677	−83.024	−88.545	17.79	0.87297	−6.8798	−9.1512
σ_{xy}	−344.01	−394.42	−305.12	−330.08	−339.99	−342.42	−293.63	−326.69	−343.23	−346.39

specimen configurations will be evaluated. The normal and shear stresses are listed in Table 2 for the two linear models (with zero and infinite friction) and the non-linear models with sliding and with and without geometric non-linearity considered. For the aluminum specimen (Table 2(a)) the effect of sliding and the change in specimen geometry appears to be negligible as far as the shear and the normal stress σ_y along the notch root axis are concerned. The normal stress σ_x, however, seems to be significantly affected by these two factors. The normal stresses σ_x at the specimen center are positive for the linear case and the non-linear models with zero friction whereas for the non-linear cases with the friction coefficients at the specimen/loading block interfaces higher than zero the stresses are negative. This means that the non-linear effects modify the nature of the normal stresses along the long axis of the aluminum specimens making them compressive.

The stress distributions at the center of the adhesively bonded composite Iosipescu specimens are very strongly influenced by the specimen sliding and geometric non-linearity effects. For the specimen with the aluminum adherends the magnitudes of the tensile stress σ_x and the compressive stress σ_y increase dramatically in the non-linear models with large deformations. The linear model with zero friction predicted an almost pure shear stress field at the specimen center. It is obvious that the linear model cannot be used to accurately determine the stresses for this specimen geometry. Similar observations can be made when comparing the stresses at the center of the adhesively bonded specimen with the composite adherends. Also, in this case the normal stresses are altered by the non-linear effects.

For the unidirectional composite Iosipescu specimen with the 0° fiber orientation the shear and normal stresses at the specimen center obtained from the non-linear models are almost the same in comparison with the stresses from the linear model with zero friction. Most likely the high stiffness of the specimen in the direction of the fibers prevented significant sliding of the specimen, thus reducing the effect of both sliding and geometric non-linearity on the stress state in the specimen gage section. It is important to note that specimen sliding and geometric non-linearity do not reduce the high compressive stress σ_y induced by the loading blocks. These stresses can only be significantly reduced by using different loading blocks (i.e. the ASTM Standard) and by rotating Iosipescu specimens within the biaxial fixture [10].

It can be seen in Table 2(e) that the non-linear effects modify the stresses at the specimen center for the 90° fiber orientation differently in comparison with the previous case. For this specimen both σ_x and σ_y are significantly altered by the movement of the specimen within the fixture. It is important to notice that the combined effect of sliding and geometric non-linearity

on the normal stresses are especially strong. The normal stress σ_x becomes compressive, especially for high friction coefficients whereas the normal stress along the notch root axis is either positive or negative depending on the friction coefficient. For both the 0° and 90° specimens the shear stresses at the specimen center from the non-linear models are very similar to the stresses from the linear model with zero friction.

The numerical results presented in this paper strongly suggest that the effects of both specimen sliding and geometric non-linearity are small and can be ignored in the finite element computations of 0° unidirectional graphite/epoxy Iosipescu specimens tested in shear in the biaxial Iosipescu fixture with short loading blocks for relatively small applied displacements (similar to the observations made in Ref. [14] with respect to the non-linear behavior of unidirectional Iosipescu specimens tested in shear with long blocks). However, the non-linear effects will have a strong influence on the stress distributions in the 90° specimens. For both 0° and 90° fiber orientations the load/displacement diagrams are not significantly affected by geometric non-linearity and specimen sliding. These effects will be smaller in the standard Iosipescu fixture [20] which has significantly longer blocks in comparison with the block configuration based on the original Wyoming design and the biaxial Iosipescu fixture. However, for such composite materials as fabric graphite/polyimide [15,22] failure can occur at much higher displacements. In this case specimen sliding and geometric non-linearity cannot be ignored since the specimens will be significantly deformed at failure in any fixture.

4. Conclusions

The effects of specimen sliding and geometric non-linearity on the mechanical response of various Iosipescu specimens subjected to shear in the biaxial Iosipescu fixture have been investigated using non-linear finite-element methods. It has been shown that in general the combined effect of specimen sliding and geometric non-linearity on the load/displacement diagrams of the Iosipescu specimens analyzed in this study is small, and can be ignored. However, the stress distributions at the center of the specimens can be significantly altered by the non-linear effects. Significant changes in the stress distributions at the specimen center have been observed for adhesively bonded and 90° graphite/epoxy Iosipescu specimens. For 0° graphite/epoxy specimens the influence of specimen sliding and geometric non-linearity on the stress state at the specimen center is almost negligible. In this case the non-linear in-plane shear response of the specimen can only be attributed to the material non-linear behavior.

Acknowledgements

References

[1] Iosipescu N. New accurate procedure for single shear testing of metals. Journal of Materials 1967;2:537–66.

[2] Adams DF, Walrath DE. Composite Materials: Testing and Design (Sixth Conference) ASTM STP 787. In: Daniel IM, editor. American Society for Testing and Materials. Philadelphia, PA, 1982:19–33.

[3] Adams DF, Walrath DE. Further development of the Iosipescu shear test method. Experimental Mechanics 1987;27(2):537–766.

[4] Adams DF, Walrath DE. Current status of the Iosipescu shear test method. J. Composite Materials 1987;21(6):494–507.

[5] Broughton WR, Kumosa M, Hull D. Analysis of the Iosipescu shear test as applied to unidirectional carbon-fiber reinforced composites. Composites Science and Technology 1990;38:299–325.

[6] Sukumar N, Kumosa M. Finite element analysis of axial splits in composite Iosipescu specimens. Int. Journal of Fracture 1993;62(1):55–85.

[7] Bansal A, Kumosa M. Experimental and analytical studies of failure modes in Iosipescu specimens under biaxial loadings. Journal of Composite Materials 1995;29:334–58.

[8] Bansal A, Kumosa M. Application of the biaxial Iosipescu method to mixed-mode fracture of unidirectional composites. Int Journal of Fracture 1995;71:131–50.

[9] Balakrishnan MV, Bansal A, Kumosa M. Biaxial testing of unidirectional carbon-epoxy composites using biaxial Iosipescu test fixture. J. Composite Materials 1997;31(5):486–508.

[10] Kumosa M, Searles K, Odegard G, Han T. Biaxial Failure Analysis of Graphite Reinforced Polyimide Composites, Annual Report to the Air Force Office of Scientific Research, Department of Engineering, University of Denver, 1997.

[11] Standard test method for shear properties of composite materials by the V-notched beam method, ASTM Standard D 5379-93, Amer. Soc. Test. and Mat., Philadelphia, PA, 1993.

[12] Searles K, Kumosa M. Non-Linear Finite Element Computations of Biaxial Graphite/Polyimide Fabric Iosipescu Specimens, to be published.

[13] Odegard G, Searles K, Kumosa M. Non-Linear Finite Element Analysis of Biaxial Unidirectional Composite Iosipescu Specimens, to be published.

[14] Ho H, Morton J, Farley GL. Non-linear numerical analysis of the Iosipescu specimen for composite materials. Composites Science and Technology 1994;50:355–65.

[15] Kumosa M, Searles K, Odegard G. Biaxial failure analysis of graphite reinforced polyimide composites. Proceedings of the HITEMP Review, Advanced High Temperature Engine Materials Technology Program, vol. I, paper 18. NASA Lewis Research Center, Cleveland, Ohio, 1997;29–30.

[16] Ding S. Mixed Mode Failure Analysis of Adhesively Bonded Composite Systems using the Modified Iosipescu Test Method, Ph.D. Thesis, Oregon Graduate Institute of Science and Technology, 1995.

[17] Ding S, Erdinc I, Buchholz F-G, Kumosa M. Optimization of the adhesive joint Iosipescu specimen for pure shear test. International Journal of Fracture 1996;76:1–20.

[18] Han Y, Kumosa M. Adhesively bonded composite Iosipescu specimens without singular stress fields. Mechanics of Composites Materials and Structures 1998;5(2):127–51.

[19] ANSYS Engineering System, User's Manual for Version 5.2, Swanson Analysis System Inc., 1995.

[20] Kumosa M, Searles K. Biaxial Failure Analysis of Graphite Reinforced Polyimide Composites, Annual Report to the Air Force Office of Scientific Research, University of Denver, 1996.

[21] Han Y. Finite Element Analyses of Advanced Composite Structures, M.S. Thesis, Department of Engineering, University of Denver, 1997.

[22] Searles K, McCarthy J, Kumosa M. An image analysis technique for evaluating internal damage in graphite/polyimide composites. Composites Science and Technology, in press.

[23] Odegard G, Searles K, Kumosa M. A critical examination of the Iosipescu shear test as applied to 0° unidirectional composite materials. Journal of Mechanics of Composite Materials and Structures, 1998, in press.

Critical Examination of the Iosipescu Shear Test as Applied to 0° Unidirectional Composite Materials

G. ODEGARD

Center for Advanced Materials and Structures, Department of Engineering,
University of Denver, Denver, Colorado, USA

K. SEARLES

Department of Materials Science and Engineering, Oregon Graduate Institute
of Science & Technology, Portland, Oregon, USA

M. KUMOSA

Center for Advanced Materials and Structures, Department of Engineering,
University of Denver, Denver, Colorado, USA

ABSTRACT

Several issues regarding the application of the shear and biaxial Iosipescu tests for the shear strength characterization of unidirectional composite materials are addressed in this article. First, the nonlinear effects of specimen sliding and geometric nonlinearity on the mechanical response of 0° standard unidirectional graphite/polyimide Iosipescu specimens with different loading conditions and loading block geometries have been investigated. Second, an attempt has been made to improve the Iosipescu shear test to eliminate normal compressive stresses in the specimen gauge section and at the same time prevent axial splitting. Finally, several Iosipescu shear and biaxial experiments have been performed to select proper specimen geometry and loading conditions for the shear strength measurements of unidirectional composites.

The nonlinear effects are examined with respect to various coefficients of friction, displacements, loading angles, and fixtures (biaxial with short and modified biaxial with long loading blocks) using nonlinear finite-element techniques. It is shown that the effect of nonlinearity is small on the stresses at the center of the standard Iosipescu specimen, but significant for the stresses near the notch root up to 2 mm applied displacements. In some cases, significant differences in the stresses calculated for different coefficients of friction have been observed. All of these results are somewhat consistent for both fixtures, but with the stress components σ_x, σ_y, and σ_{xy} significantly lower in the standard Iosipescu specimens tested in the fixture with the long blocks. Numerical load/displacement diagrams show that specimen sliding and geometric nonlinearity have a negligible effect on reaction forces in the biaxial fixture, and a significant effect on the reaction forces in the modified biaxial fixture. Since the various combinations of the loading conditions evaluated in this study do not eliminate transverse compressive stresses in the gauge section of the standard Iosipescu specimens, a major improvement to the Iosipescu shear test has been proposed. Using an optimized specimen geometry

subjected to biaxial shear/tension loading conditions, a state of almost uniform pure shear stress can be generated in 0° unidirectional composite Iosipescu specimens without the possibility of axial splitting along the fibers at the roots of the notches. However, it is shown in the experimental part of this study that for the optimized Iosipescu specimen, crushing at the inner loading blocks can significantly affect the shear intralaminar failure process. Only by reducing the cross-sectional area of the optimized Iosipescu specimen can the effect of crushing on the failure process be reduced without, however, high-quality shear stress fields present in the gauge section at failure.

In 1967 Iosipescu developed a method to measure the shear strength of metals by applying two counteracting moments produced by two force couples onto the Iosipescu specimen (Figure 1) [1]. Adams and Walrath first applied the test to composite materials in the first Wyoming Iosipescu fixture [2, 3]. The original design of the fixture was then modified to reduce large compressive stresses generated in the gauge section of the specimen [4, 5]. The modified Wyoming Iosipescu shear test has become one of the most popular test methods for the shear characterization of composite materials, and has become the standard (ASTM D 5379) [6]. In 1990 Broughton, Kumosa, and Hull introduced the biaxial Iosipescu fixture, which allows the testing of Iosipescu specimens not only in shear, but also under biaxial shear/tension or shear/compression loading conditions (Figure 2) [7]. Various biaxial stress states can be created by rotating the specimen and the loading blocks within the fixture [8–11]. The original biaxial Iosipescu fixture contained short loading blocks similar to the original Wyoming Iosipescu fixture. In 1997 Kumosa et al. [12] introduced the modified biaxial Iosipescu fixture, which features new loading geometries that are very similar to those used in the modified Wyoming fixture [4, 5] and ASTM standard [6]. Another shear characterization test that is similar to the biaxial Iosipescu test is the Arcan shear test [13]. Despite some apparent advantages of the Arcan test over the biaxial Iosipescu shear test associated with the loading of the specimen, there are disadvantages to this test that exclude it from use in many research projects associated with the shear characterization of composite materials. The Arcan test requires a very complicated specimen geometry, and the specimen preparation process is very time consuming and expensive. Furthermore, the Arcan test requires bonding between the specimen and fixture, which might become a problem when testing unidirectional composite materials at elevated temperatures.

The first study of specimen sliding and geometric nonlinearities within the modified Wyoming Iosipescu fixture was performed by Ho, Morton, and Farley [14]. In their analysis the nonlinear effects were investigated in 0° and 90° unidirectional composite Iosipescu
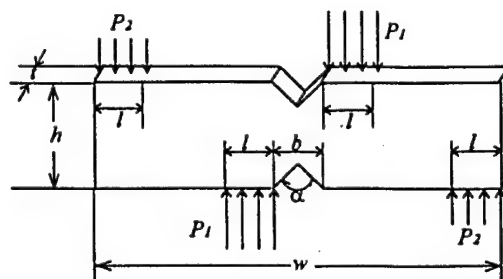
$w = 80\,mm \quad h = 20\,mm \quad t = 5\,mm \quad b = 8\,mm \quad \alpha = 90° \quad l = 10\,mm$

Figure 1. *Iosipescu shear test.*
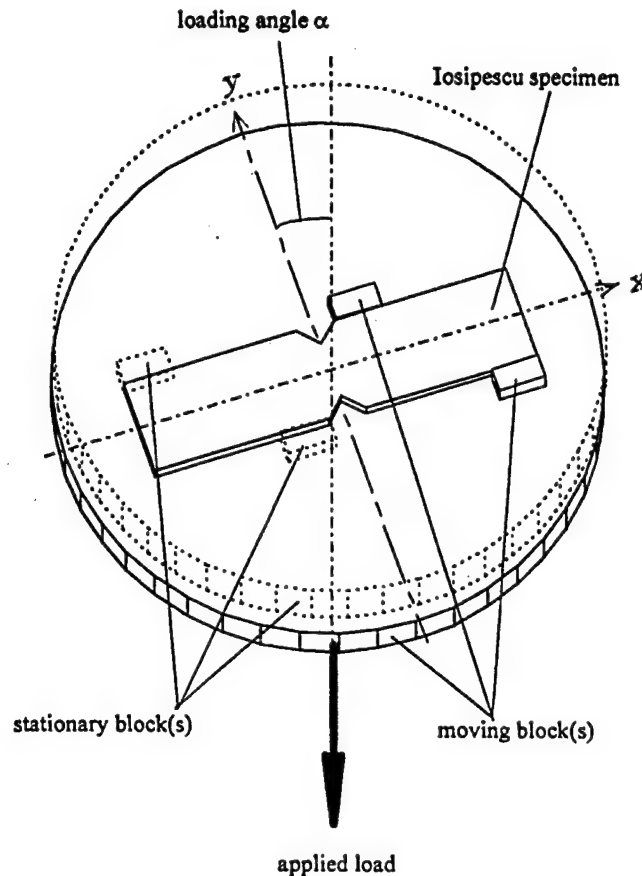
Figure 2. *Biaxial loading conditions in the biaxial Iosipescu fixture.*

specimens subjected only to shear. Recently, Kumosa and Han studied the combined effect of specimen sliding and geometric nonlinearity on the load/displacement diagrams and internal stresses of isotropic, composite, and adhesively bonded isotropic and composite Iosipescu specimens subjected to shear under small displacement conditions using nonlinear finite element techniques [15, 16]. They showed, by using linear and nonlinear models with varying coefficients of friction, that for some specimen geometries the load/displacement diagrams and internal stress distributions in the gauge section of the specimen were affected by sliding and geometric nonlinearity. Specifically, for the adhesively bonded and 90° unidirectional graphite/epoxy specimens, significant changes in the stress distributions did occur. For the 0° graphite/epoxy and isotropic specimens, the effects of specimen sliding and geometric nonlinearity on the load displacement diagrams and the stresses at the specimen center were almost negligible for displacements up to 1 mm. In the study performed by Kumosa and Han the effect of sliding and geometric nonlinearity on the stresses near the notch roots was not investigated. Moreover, only the biaxial Iosipescu fixture was considered, with loading blocks significantly shorter than the blocks recommended by the ASTM standard.

In the first part of this study, the effects of specimen sliding and geometric nonlinearity on internal stresses and load/displacement diagrams were investigated with respect to 0° unidirectional graphite/polyimide Iosipescu specimens with various coefficients of friction, displacements, loading angles, and fixtures. The effect of material nonlinearity on the mechanical response of the specimens was not considered. A similar analysis will be presented for graphite/polyimide fabric composite Iosipescu specimens in another article [17]. In the second part, an optimized Iosipescu test has been developed that creates a

high-quality shear stress field by almost eliminating the transverse compressive stress σ_y along the notch root axis in 0° unidirectional composites. The new design incorporates a new specimen configuration (based on the flat-bottomed notch specimen developed by Adams and Lewis [18]) and another modification of the loading block geometries with the specimen loaded in shear/tension.

The purpose of this study was to optimize the Iosipescu test in order to eliminate undesirable normal stresses in the specimen gauge section which might affect the intralaminar failure process. Despite the popularity of the Iosipescu test, this test is certainly not straightforward. If we examine the standard we find that the determination of shear failure in 0° unidirectional composite Iosipescu specimens is not clear. The standard says "in [0] specimens tested in the 1–2 plane, a visible crack develops at the notch root, causing a small load drop prior to ultimate failure. The small load drop accompanying the notch root crack is not considered the failure load; rather the load that accompanies failure in the test section shall be used as the failure load." The problem is that the standard does not indicate which failure in the test section should be considered as the shear failure. If the intralaminar shear cracks formed along the notch root axis are considered as the shear failure, the formation of these cracks is still going to be affected by the compressive transverse stresses perpendicular to the fibers caused by the loading blocks. An attempt has been made in this research to optimize the Iosipescu specimen geometry in such a way that the axial splitting at the notch root is prevented and any damage formed along the notch root axis will be caused by shear only, without any transverse normal stresses. The following issues have been addressed in this article:

What are the effects of specimen sliding and geometric nonlinearity on the stresses in the 0° standard Iosipescu specimens tested under biaxial shear dominated loads with short and long loading blocks

How to prevent axial splitting and promote intralaminar failure due to shear only along the notch root axis

How to eliminate transverse compressive stresses in the gauge section

Effect of specimen crushing by the loading blocks on the intralaminar shear failure process in the gauge section.

§1. FINITE-ELEMENT ANALYSIS

The effects of specimen sliding and geometric nonlinearity were determined numerically for unidirectional graphite/polyimide Iosipescu specimens under various loading conditions. The stresses at the center of the specimen and near the notch root surface as well as the load/displacement diagrams were determined as a function of coefficients of friction, displacements, loading angles, and fixtures (biaxial and modified biaxial). The finite-element models used in this study are two-dimensional (having a thickness of unity, i.e., 1 mm) and analyzed using ANSYS 5.2 [19] (with isoparametric 6- and 8-node elements). Material properties for the composite system and the loading blocks are given in Table 1. The properties for the graphite/polyimide composite system, along with the strength properties mentioned later in the article, were provided by the NASA Lewis Research Center. The stiffness and strength properties of unidirectional graphite/polyimide composites are very similar to those of unidirectional graphite/epoxy composites. Therefore, the results given in this article for graphite/polyimide composites are applicable to graphite/epoxy composites.

For the linear elastic model, displacement boundary conditions with zero friction were applied (Figure 3a). The right side of the specimen was loaded by prescribed vertical displacements (u_y) on the loading blocks. The loading blocks on the left side of the specimen

Table 1

Mechanical properties of the graphite/polyimide composite, steel loading blocks, and glass/epoxy composite

	Unidirectional Graphite/Polyimide	Steel Loading Blocks	Unidirectional Glass/Epoxy
Young's modulus (GPa)	$E_x = 129.6$ $E_y = 8.6$	$E = 200.0$	$E_x = 40.0$ $E_y = 10.0$
Shear modulus (GPa)	$G_{xy} = 4.3$	$G = 75.0$	$G_{xy} = 4.5$
Poisson's ratio	$\nu_{xy} = 0.25$	$\nu = 0.33$	$\nu_{xy} = 0.27$

were constrained against any vertical displacements. A single constraint against horizontal displacements was placed on the left side of the specimen in order to prevent rigid-body motion. This model assumes free axial movement of the specimen and loading blocks, which are perfectly bonded together, along the x direction [15].

For the nonlinear models, displacement boundary conditions with contact elements between the specimen and the loading blocks were applied (Figure 3b) [15]. The specimen center was constrained against vertical and horizontal displacements (u_x and $u_y = 0$). The blocks on the right side of the specimen had prescribed displacements of $u/2$ and the blocks on the opposite side were loaded by a negative displacement of the same magnitude. Thus, the total prescribed displacement acting on the specimen is equal to u. For nonzero
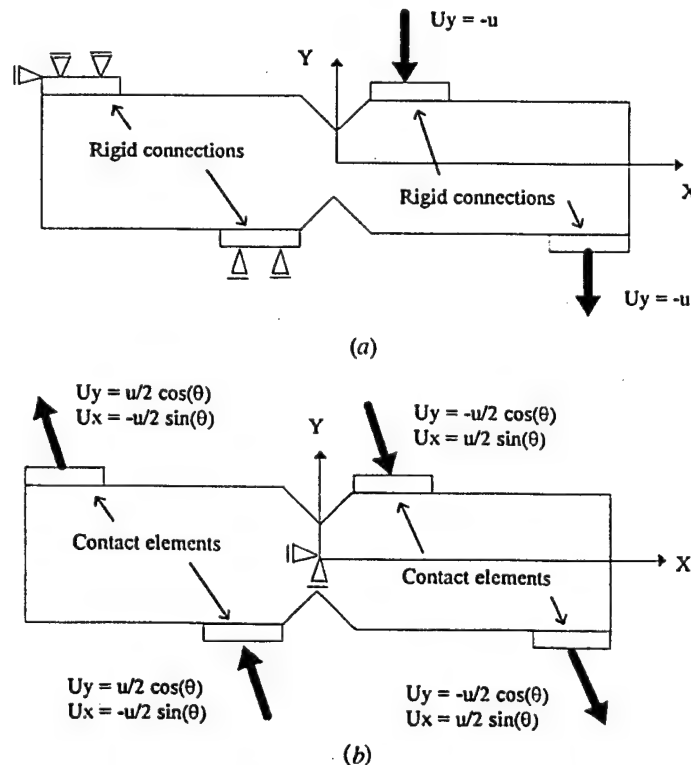

Figure 3. *Displacement boundary conditions for (a) the linear elastic model and (b) the nonlinear model with contact elements.*

loading angles (θ), the prescribed displacements were broken up into x and y components, generating biaxial shear-dominated loading conditions [15].

Three different loading block geometries were considered. In Section 2 the standard Iosipescu specimens are modeled together with the loading blocks in the biaxial (short blocks) and modified biaxial Iosipescu (long blocks) fixtures. In Section 3.2 the effect of another loading block geometry on the mechanical response of a flat-bottomed notch Iosipescu specimen is discussed.

When a specimen is tested in the biaxial and ASTM standard fixtures, undesired compressive stresses along the notch root axis may cause inaccuracies in the shear strength measurement. These stresses will be reduced, but not eliminated, by using the modified biaxial fixture design, thus allowing a more uniform shear stress state to exist along the notch root axis of the Iosipescu specimens [4, 5, 12]. It might be possible for the compression generated by the loading blocks to be completely eliminated if the modified biaxial Iosipescu fixture is used under shear/tension loading conditions. Searles and Kumosa [17] and Searles et al. [20] have shown recently that introducing a biaxial state of stress coupled with the use of the modified biaxial loading blocks entirely eliminates the σ_y compressive stresses along the notch root axis for fabric composites. Thus, an attempt was made to demonstrate the same effect for 0° unidirectional composites. Rotation of the specimen into shear/tension might move the compressive stress fields, which are generated by the loading blocks, away from the center of the specimen. In order to examine this prediction, a numerical comparison between the biaxial Iosipescu loading blocks and the modified biaxial Iosipescu loading blocks with respect to the other parameters in this article was performed.

For all numerical models, the loading blocks were assumed to be linear elastic and made out of steel. The blocks have a height of 2.5 mm. The loading blocks in the original biaxial Iosipescu fixture are 10 mm in length [7] (see Figure 4a). In the modified biaxial Iosipescu fixture the inner and outer loading blocks are 30.9 and 25.4 mm in length, respectively [12] (see Figure 4b). These loading blocks are very similar to the blocks recommended by the ASTM standard [6].

The coefficients of friction between the loading blocks and the Iosipescu specimen are not known a priori. Moreover, the frictional properties of the specimen/loading block interfaces may vary as a function of the applied load. Therefore, different friction coefficients were assumed. The effect of specimen sliding along the loading blocks was modeled using two-dimensional point-to-surface contact elements with Coulomb friction assumed. For the linear model, $\mu = 0$ was assumed since the specimen and loading blocks are free to move in the x direction [15]. For the nonlinear models with sliding and sliding with geometric nonlinearity the coefficients of friction were $\mu = 0.0$, 0.3, and 0.5. These values were chosen due to their reasonable approximations of the possible friction coefficients between polymer–matrix unidirectional composites and steel loading blocks.

In the analysis performed by Kumosa and Han [15], small displacement conditions (up to 1.0 mm) were assumed for the Iosipescu specimens loaded in shear in the biaxial Iosipescu fixture. Even though some unidirectional specimens may fail in shear at displacements below 1.0 mm [7, 9, 21], larger displacements must be considered for the specimens subjected to biaxial loading conditions [9]. Therefore, the models used here had displacements of 0.5, 1.0, 1.5, and 2.0 mm in order to cover the entire range of displacements at failure for unidirectional 0° Iosipescu specimens tested under shear and biaxial shear-dominated loading conditions. These displacements were applied to both the linear elastic and the nonlinear models with and without geometric nonlinearity. For the nonlinear models, the total displacements were divided into 10 substeps. This decreases the error that could occur with a single load increment in a nonlinear analysis [19].

Short loading blocks

(a)

Long loading blocks

(b)
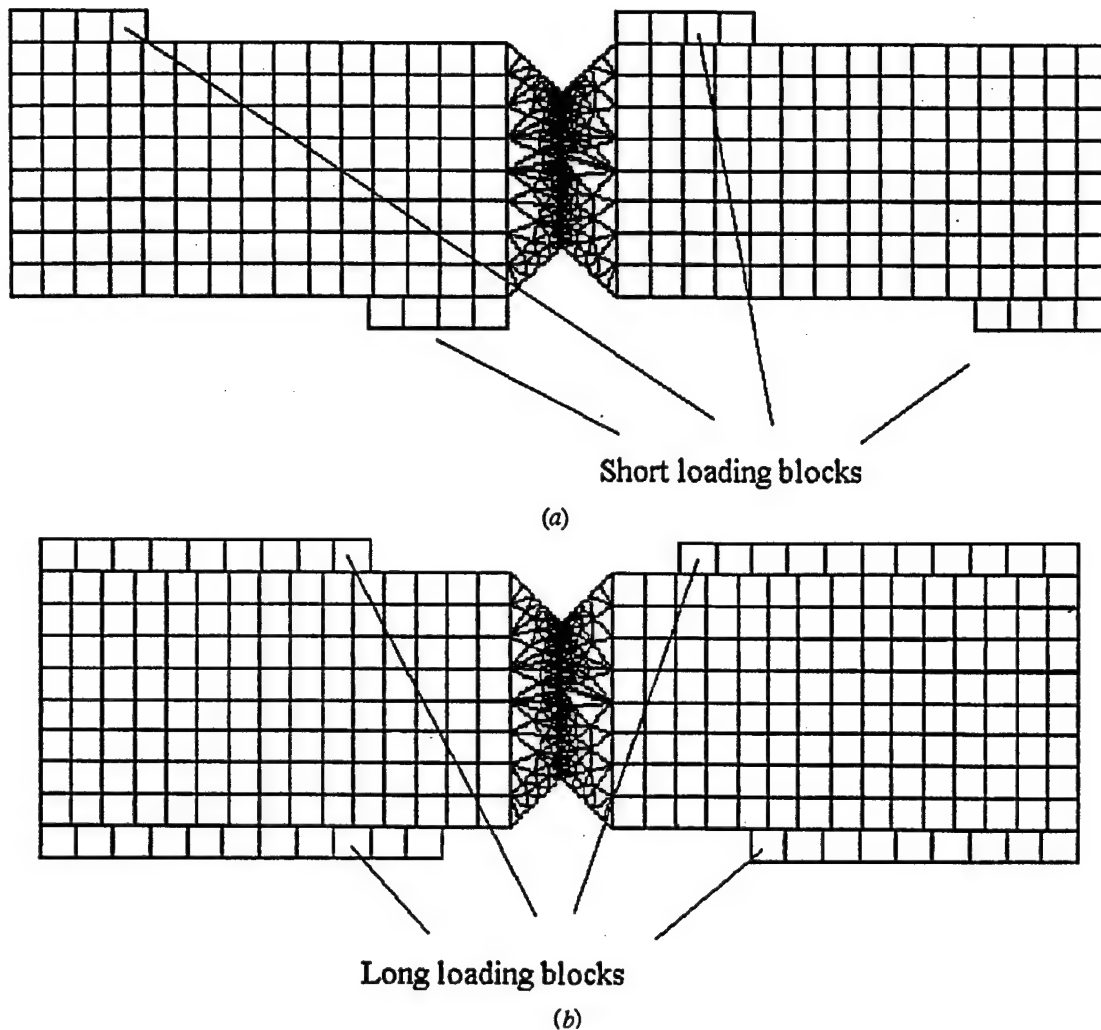
Figure 4. *Finite-element mesh for (a) the biaxial Iosipescu specimen and (b) the modified biaxial Iosipescu specimen.*

§2. RESULTS AND DISCUSSION

2.1. *Stresses at the center of the standard Iosipescu specimen*

One way to monitor the effects of specimen sliding and geometric nonlinearity on the mechanical response of Iosipescu specimens is to compute the internal stresses at the center of the specimen. The normal and shear stresses (σ_x, σ_y, and σ_{xy}) were found for all combinations of loading angles, coefficients of friction, displacements, and fixtures at the midpoint of the notch root axis. The results are presented in Tables 2a, 2b, and 2c.

The numerical effects of sliding can be found by comparing the linear elastic results with the nonlinear without geometric nonlinearity results (with $\mu = 0$). When the biaxial fixture is used, the difference for all three stress components over all four displacements is negligible, which agrees with the results of Kumosa and Han [15]. With the modified biaxial fixture, the difference is somewhat larger. Even though the magnitudes are relatively small, the σ_x stresses are tensile when considering the linear elastic model, and compressive with sliding assumed. For σ_y and σ_{xy}, the difference is smaller. The difference in the normal stresses along x computed from the linear model and the nonlinear model with sliding only may be due to the larger frictional forces generated with the longer loading blocks in the modified biaxial fixture.

Table 2a

Stress (σ_x in MPa) at the center of the graphite/polyimide Iosipescu specimens under various conditions

| | | | Fixture Displacement (mm) | | | | | | | |
| | | | Biaxial (Short) Loading Blocks | | | | Modified Biaxial (Long) Loading Blocks | | | |
	θ (Deg)	μ	0.5	1.0	1.5	2.0	0.5	1.0	1.5	2.0
Linear	0	0	12.5	25.0	37.5	50.0	5.4	10.8	16.2	21.6
Nonlinear with sliding	0	0	10.4	22.3	34.1	46.0	−2.2	−3.9	−5.9	−13.0
		0.3	10.1	22.3	33.6	45.4	−3.5	−6.4	−9.1	−17.3
		0.5	10.5	23.3	34.7	47.0	−3.6	−6.5	−9.3	−17.7
	20	0	9.8	20.6	31.4	42.2	−2.1	−3.9	−5.9	−7.9
		0.3	14.4	30.1	45.7	60.9	3.2	6.8	10.3	13.2
		0.5	16.1	33.6	51.1	67.8	5.1	10.8	16.3	20.7
	−20	0	9.8	21.1	32.4	43.6	−2.2	−4.6	−7.7	−11.3
		0.3	1.9	5.9	10.0	16.2	−10.3	−20.8	−30.6	−40.5
		0.5	1.8	5.5	8.7	13.4	−12.1	−24.3	−37.0	−48.5
Nonlinear with sliding and geometric nonlinearity	0	0	10.7	24.0	37.8	52.7	−2.3	−4.2	−6.7	−12.4
		0.3	10.6	24.1	38.6	54.2	−3.4	−6.2	−8.9	−16.8
		0.5	11.0	24.9	39.9	55.7	−3.5	−6.2	−9.0	−16.7
	20	0	10.1	22.4	35.0	48.3	−2.2	−4.1	−6.6	−9.4
		0.3	14.8	32.0	49.8	68.0	3.2	6.9	10.3	12.2
		0.5	16.5	35.7	55.3	75.3	5.2	10.9	16.3	20.6
	−20	0	10.2	22.5	35.8	49.7	−2.2	−4.8	−8.2	−12.2
		0.3	2.5	7.8	14.4	24.5	−10.2	−20.4	−30.2	−39.5
		0.5	2.4	7.3	13.1	21.6	−12.0	−23.9	−36.0	−47.1

Table 2b

Stress (σ_y in MPa) at the center of the graphite/polyimide Iosipescu specimens under various conditions

		Fixture Displacement (mm)							
		Biaxial (Short) Loading Blocks				Modified Biaxial (Long) Loading Blocks			
θ (Deg)	μ	0.5	1.0	1.5	2.0	0.5	1.0	1.5	2.0
Linear	0	0	−50.0	−100.0	−150.0	−200.0	−13.5	−26.9	−40.4	−53.9
Nonlinear with sliding	0	0	−44.6	−93.7	−142.9	−192.0	−11.9	−25.3	−38.8	−58.7
		0.3	−45.8	−95.5	−145.9	−196.6	−13.2	−28.0	−43.2	−63.0
		0.5	−45.7	−95.3	−145.7	−196.3	−13.3	−28.1	−43.4	−63.3
	20	0	−42.2	−87.4	−132.9	−179.2	−11.0	−23.5	−35.9	−48.8
		0.3	−40.8	−85.0	−129.2	−174.4	−9.9	−21.1	−32.3	−44.2
		0.5	−40.4	−84.3	−128.2	−173.0	−9.5	−20.4	−31.2	−42.8
	−20	0	−42.1	−88.1	−134.6	−180.9	−10.9	−25.1	−44.2	−67.0
		0.3	−45.5	−95.9	−144.9	−194.0	−14.3	−31.5	−52.3	−77.2
		0.5	−45.5	−96.1	−145.5	−195.5	−15.0	−33.1	−54.7	−79.7
Nonlinear with sliding and geometric nonlinearity	0	0	−44.5	−93.5	−142.6	−191.6	−11.3	−23.0	−33.4	−46.3
		0.3	−45.7	−95.9	−146.2	−196.2	−12.6	−25.5	−36.9	−51.4
		0.5	−45.7	−95.8	−145.9	−195.9	−12.7	−25.5	−37.0	−51.5
	20	0	−42.0	−87.9	−133.2	−179.0	−10.5	−21.4	−31.1	−40.1
		0.3	−40.7	−85.4	−129.2	−173.7	−9.4	−19.0	−27.4	−35.3
		0.5	−40.3	−84.8	−128.1	−172.5	−9.0	−18.3	−26.3	−33.7
	−20	0	−42.0	−87.9	−134.6	−180.9	−10.4	−22.6	−38.5	−57.1
		0.3	−46.1	−96.0	−145.5	−194.6	−13.8	−29.2	−46.9	−66.7
		0.5	−46.1	−96.2	−146.2	−196.5	−14.5	−30.7	−49.0	−69.2

Table 2c

Stress (σ_{xy} in MPa) at the center of the graphite/polyimide Iosipescu specimens under various conditions

	θ (Deg)	μ	Fixture Displacement (mm)							
			Biaxial (Short) Loading Blocks				Modified Biaxial (Long) Loading Blocks			
			0.5	1.0	1.5	2.0	0.5	1.0	1.5	2.0
Linear	0	0	−82.7	−165.3	−248.0	−330.6	−69.2	−138.4	−207.5	−276.7
Nonlinear with sliding	0	0	−76.5	−157.1	−239.0	−320.9	−51.8	−106.3	−161.8	−224.5
		0.3	−79.2	−162.3	−246.7	−331.2	−55.5	−113.4	−172.8	−237.3
		0.5	−79.3	−162.7	−247.1	−331.8	−55.8	−114.0	−173.7	−238.6
	20	0	−72.2	−147.3	−223.7	−302.1	−48.6	−99.5	−151.0	−203.6
		0.3	−73.0	−149.3	−226.8	−305.5	−49.8	−101.9	−154.4	−207.9
		0.5	−73.7	−150.6	−228.8	−308.0	−50.5	−103.3	−156.5	−210.6
	−20	0	−72.0	−147.2	−223.8	−301.0	−48.3	−101.3	−160.4	−223.0
		0.3	−74.6	−153.4	−231.5	−310.1	−51.6	−107.2	−167.5	−231.8
		0.5	−74.6	−153.5	−231.9	−311.5	−52.6	−109.5	−170.6	−235.4
Nonlinear with sliding and geometric nonlinearity	0	0	−76.7	−157.8	−240.5	−323.9	−51.5	−104.9	−158.6	−216.1
		0.3	−79.4	−163.3	−249.0	−335.5	−55.1	−112.1	−169.2	−231.2
		0.5	−79.5	−163.6	−249.5	−336.0	−55.4	−112.7	−170.2	−232.4
	20	0	−72.2	−148.3	−225.6	−304.7	−48.3	−98.3	−148.2	−198.4
		0.3	−73.1	−150.1	−228.2	−308.1	−49.4	−100.5	−151.2	−201.9
		0.5	−73.8	−151.5	−230.1	−310.3	−50.1	−101.9	−153.2	−204.6
	−20	0	−72.1	−147.9	−225.3	−304.0	−48.0	−99.6	−156.9	−217.6
		0.3	−75.3	−154.6	−234.5	−315.3	−51.4	−106.2	−165.4	−227.5
		0.5	−75.3	−154.8	−235.2	−317.0	−52.4	−108.6	−168.4	−231.5

The effects of geometric nonlinearity can be determined by comparing the two nonlinear models. In general, when specimen sliding is coupled with geometric nonlinearity, the difference compared to the assumption of specimen sliding without geometric nonlinearity is found to be negligible, even for relatively large displacements. Geometric nonlinearity does not noticeably affect the stresses at the center in the 0° unidirectional Iosipescu specimens loaded in both fixtures. This also agrees very well with the results of Ho et al. [14] and Kumosa and Han [15].

The effects of the change in coefficient of friction on the stresses at the center for the zero loading angle (in shear) are negligible. However, when the specimen is loaded under either shear/tension or shear/compression, there is a significant change in the normal stress, σ_x, as the coefficient of friction increases. This may be due to the increased component of displacement in the x direction of the loading blocks as the fixture is rotated. As this happens, the frictional forces change in magnitude in the x direction, thus forcing σ_x in the center of the specimen to be more sensitive to the coefficient of friction.

There is a very large difference in the internal stresses at the specimen center obtained from the models with the biaxial and modified biaxial loading blocks. Clearly, the magnitudes of the stresses are lower for nearly all of the combinations of loading conditions when the modified biaxial fixture is used. More important, the ratio of σ_y to σ_{xy} decreases with the use of the modified biaxial fixture (from 50–60% to 15–25%) for the same loading conditions. However, the ratio of σ_x to σ_{xy} is approximately the same. By moving the compressive fields caused by the loading blocks away from the test section of the specimen, the transverse compressive stresses were reduced (as predicted by Adams and Walrath [4, 5]).

It can be seen from the results presented in Table 2*b* that the compressive stresses σ_y do not reduce to zero for any loading angles for a unidirectional graphite/polyimide Iosipescu specimen loaded in the modified biaxial fixture. Obviously, the same applies to the biaxial fixture. To examine this effect further, an additional calculation of the stresses was performed with $\mu = 0.3$, $u = 2.0$ mm, and $\alpha = 40°$ (shear/tension). The stresses are $\sigma_x = 21.7$ MPa, $\sigma_y = -24.4$ MPa, and $\sigma_{xy} = -158.3$ MPa. Even for this large loading angle, the compressive stress is significant. Therefore, it is not possible to improve the quality of the shear stress field by significantly reducing the compressive stresses at the center of the 0° unidirectional specimen with the current test fixtures and the standard Iosipescu specimen geometry. In order to achieve this, additional modifications to the Iosipescu test are required. This will be discussed further in Section 3.2.

2.2. *Stresses near the notch root of the standard Iosipescu specimen*

The stress components σ_y and σ_{xy} must be zero at the free edge of the notch root, where the slope of the radius is zero in the x–y plane. Numerically, the stresses only come close to zero, due to the difficulty of placing a node (on which the forces are calculated) as close as possible to the very bottom of the notch root radius. It was found that σ_y and σ_{xy} are significantly large very close to (but not on) the notch root. The three components of stress were calculated approximately 0.002 mm away from the notch root along the notch root axis (Tables 3*a*, 3*b*, and 3*c*). Clearly, these stresses are not equal to the stresses at the center of the specimen, therefore a uniform state of stress does not exist along the test section of the specimen, which is not surprising. This has been shown by many researchers in the past (e.g., [7]) by performing linear elastic finite-element computations of the Iosipescu shear test.

It can be clearly seen that the assumption of sliding between the specimen and the loading blocks affects the stresses near the notch root significantly. Only σ_y and σ_{xy} generated

Table 3a

Stress (σ_x in MPa) near the notch root of the graphite/polyimide Iosipescu specimens under various conditions

	θ (Deg)	μ	Biaxial (Short) Loading Blocks				Modified Biaxial (Long) Loading Blocks			
			0.5	1.0	1.5	2.0	0.5	1.0	1.5	2.0
Linear	0	0	−42.3	−84.5	−126.8	−169.1	−9.5	−18.9	−28.4	−37.9
Nonlinear with sliding	0	0	−83.2	−189.5	−293.1	−388.8	100.7	195.1	287.1	88.3
		0.3	−166.1	−337.9	−525.7	−706.7	−0.3	−5.0	−6.0	−270.0
		0.5	−157.9	−315.8	−501.3	−670.2	−5.5	−13.8	−22.1	−296.3
	20	0	−79.6	−177.6	−268.9	−362.6	94.8	182.1	267.4	348.3
		0.3	44.0	73.1	107.9	131.4	225.0	444.5	661.0	862.9
		0.5	83.3	152.1	228.1	288.1	269.4	533.8	795.2	1,030.4
	−20	0	−79.9	−179.7	−276.4	−373.6	95.2	128.3	58.6	−93.5
		0.3	−415.3	−840.5	−1,232.8	−1,535.3	−203.6	−460.1	−757.9	−1,118.8
		0.5	−418.6	−857.1	−1,288.9	−1,663.2	−267.7	−590.2	−988.6	−1,398.9
Nonlinear with sliding	0	0	8.1	196.0	591.6	1,183.1	138.9	353.7	647.8	871.2
and geometric		0.3	−68.8	61.5	412.7	981.2	44.6	180.5	416.4	516.2
nonlinearity		0.5	−60.1	79.9	442.1	1,015.4	40.3	175.6	405.3	508.8
	20	0	1.8	161.5	502.3	1,029.9	128.4	321.2	582.6	909.2
		0.3	126.9	420.9	902.4	1,544.9	261.5	594.8	999.5	1,452.6
		0.5	167.1	503.0	1,029.0	1,705.0	306.3	685.9	1137.8	1,642.7
	−20	0	1.3	160.2	500.5	1,025.4	128.4	277.8	420.2	581.4
		0.3	−329.5	−468.4	−379.0	11.3	−163.6	−290.9	−356.7	−352.5
		0.5	−332.7	−485.6	−434.0	−125.8	−226.6	−414.2	−563.1	−605.5

Fixture Displacement (mm)

Table 3b

Stress (σ_y in MPa) near the notch root of the graphite/polyimide Iosipescu specimens under various conditions

	θ (Deg)	μ	Fixture Displacement (mm)							
			Biaxial (Short) Loading Blocks				Modified Biaxial (Long) Loading Blocks			
			0.5	1.0	1.5	2.0	0.5	1.0	1.5	2.0
Linear	0	0	−1.8	−3.5	−5.3	−7.0	−1.0	−1.9	−2.9	−3.9
Nonlinear with sliding	0	0	−6.0	−12.9	−19.7	−26.4	1.0	1.8	2.5	−4.2
		0.3	−8.1	−16.6	−25.6	−34.4	−1.5	−3.2	−4.8	−13.0
		0.5	−7.9	−16.1	−25.0	−33.6	−1.6	−3.4	−5.2	−13.7
	20	0	−5.7	−12.0	−18.3	−24.6	1.0	1.7	2.3	2.8
		0.3	−2.8	−6.2	−9.5	−13.1	4.0	7.8	11.5	14.8
		0.5	−1.9	−4.3	−6.7	−9.5	5.0	9.8	14.6	18.6
	−20	0	−5.7	−12.1	−18.6	−25.0	1.0	0.3	−3.2	−9.0
		0.3	−13.7	−28.1	−41.6	−53.1	−6.2	−13.8	−22.7	−33.5
		0.5	−13.8	−28.5	−43.0	−56.2	−7.7	−17.0	−28.3	−40.1
Nonlinear with sliding and geometric nonlinearity	0	0	−2.0	3.7	17.7	38.9	2.5	7.6	15.5	22.7
		0.3	−3.8	0.8	14.5	36.2	0.2	3.7	10.6	15.8
		0.5	−3.6	1.3	15.2	37.0	0.1	3.6	10.4	15.7
	20	0	−2.1	2.5	14.5	33.4	2.2	6.8	13.7	22.8
		0.3	0.8	8.4	23.2	43.8	5.3	12.9	22.8	34.1
		0.5	1.7	10.3	25.9	47.0	6.3	14.9	25.7	38.0
	−20	0	−2.2	2.5	14.5	33.3	2.2	5.8	10.2	16.3
		0.3	−10.1	−12.0	−4.6	13.3	−4.7	−7.5	−7.6	−4.5
		0.5	−10.1	−12.4	−5.8	10.4	−6.2	−10.5	−12.5	−10.4

Table 3c

Stress (σ_{xy} in MPa) near the notch root of the graphite/polyimide Iosipescu specimens under various conditions

| | θ (Deg) | μ | Fixture Displacement (mm) | | | | | | | |
| | | | Biaxial (Short) Loading Blocks | | | | Modified Biaxial (Long) Loading Blocks | | | |
			0.5	1.0	1.5	2.0	0.5	1.0	1.5	2.0
Linear	0	0	−202.3	−404.6	−606.9	−809.2	−139.3	−278.5	−417.8	−557.0
Nonlinear with sliding	0	0	−233.8	−484.1	−736.9	−990.0	−125.2	−258.1	−393.3	−553.4
		0.3	−241.7	−498.4	−758.9	−1,020.3	−134.7	−276.8	−422.2	−585.9
		0.5	−241.9	−499.1	−759.6	−1,021.4	−135.3	−278.0	−424.2	−588.7
	20	0	−220.7	−452.9	−688.3	−929.3	−117.2	−241.3	−366.6	−494.9
		0.3	−221.1	−455.0	−691.7	−932.2	−119.0	−244.9	−371.5	−501.1
		0.5	−222.2	−457.4	−695.3	−936.8	−120.3	−247.5	−375.4	−506.1
	−20	0	−220.4	−454.0	−691.4	−929.9	−116.5	−247.5	−399.1	−563.6
		0.3	−230.1	−477.9	−721.6	−967.5	−127.2	−266.7	−422.0	−592.2
		0.5	−230.1	−478.2	−723.5	−972.2	−129.7	−273.1	−430.5	−601.6
Nonlinear with sliding	0	0	−231.5	−472.6	−706.0	−927.2	−122.8	−247.5	−368.0	−497.4
and geometric		0.3	−239.8	−489.9	−732.4	−962.5	−132.4	−266.8	−396.1	−539.4
nonlinearity		0.5	−240.1	−490.2	−732.7	−962.8	−133.0	−268.1	−398.3	−542.0
	20	0	−218.5	−445.3	−664.4	−876.1	−115.1	−232.1	−344.7	−453.6
		0.3	−218.4	−444.5	−660.5	−869.3	−116.4	−233.9	−345.6	−452.9
		0.5	−219.3	−446.2	−662.2	−870.5	−117.6	−236.1	−348.3	−456.0
	−20	0	−218.3	−444.2	−665.2	−877.3	−114.4	−236.7	−374.3	−520.0
		0.3	−232.1	−475.5	−712.1	−937.4	−125.8	−260.5	−406.9	−560.1
		0.5	−232.1	−476.1	−715.2	−946.3	−128.5	−267.5	−416.5	−573.2

with the modified biaxial fixture show little deviation from the stresses calculated with the linear-elastic assumption. The effect of geometric nonlinearity also has a large influence on all σ_x and σ_y stresses. The stresses are in general more sensitive to changes of the loading conditions near the notch root than in the center of the specimens, and this applies to both fixtures. Therefore, when calculating the stresses near the notch root for the 0° unidirectional Iosipescu specimens loaded either in shear or biaxial conditions, the assumption of sliding with geometric nonlinearity must be made in order to avoid large numerical inaccuracies. Based on this very important observation, it can be said that all the previous published data regarding the stress distributions near the notches of the 0° Iosipescu specimens obtained from the linear elastic models are incorrect.

The effects of changing the coefficient of friction between the loading blocks and the specimen has little significance on the stresses except on σ_x when the coefficient is adjusted from 0.0 to 0.3 in both fixtures. Again, as in the case of σ_x in the center of the specimen, the differences may be due to the resulting frictional forces on the specimen that act in the x direction. The magnitude of the frictional forces vary with the coefficient of friction and rotation. Since it was previously shown that the consideration of sliding is important near the notch root, care should be taken in choosing the friction coefficient for numerical analyses if it is below 0.3.

As is the case with the stresses at the center of the specimen, the stresses near the notch root are strongly influenced by the loading block geometry. The magnitude of nearly all of the stresses is lower when the modified biaxial fixture is used over the biaxial geometry. Also, the ratio of σ_y to σ_{xy} decreases in most cases, and the ratio of σ_x to σ_{xy} is approximately the same. As the compressive fields move away from the notch root axis, which is the case of the modified fixture, the transverse compressive stresses are reduced near the notch root.

From the results of the stresses at the center of the specimen and near the notch root, it is clear that for all of the combinations of loading conditions there does not exist a uniform state of shear stress along the notch root axis and the transverse compressive stress is nonzero in the test section of the specimen. Introducing various applied states of biaxial loading conditions (shear/tension and shear/compression) does not give the desired stress state in the test section of the unidirectional specimens. It can be therefore speculated that the presence of the compressive stresses in the gauge section of the specimen will affect modes of failure for unidirectional graphite/polyimide and graphite/epoxy composites. Moreover, the proper evaluation of the shear strengths of the composites will be possible only if a multiaxial failure criterion is used.

2.3. *Numerical load/displacement diagrams*

Numerical load/displacement diagrams were generated for the graphite/polyimide unidirectional composite specimens. As an example, the load/displacement diagrams for a zero loading angle and a coefficient of friction of 0.3 are shown in Figures 5 and 6 for the biaxial and modified biaxial fixtures, respectively. The loads were calculated by taking the sum of the reaction forces on the right side of the specimen (as in [15]), thus modeling the load read by a load cell in a mechanical testing machine.

The load/displacement curve for a specimen tested in the biaxial fixture shows an insignificant variation in response for the three assumptions of loading conditions, even at relatively high displacements. This agrees closely with the results of Kumosa and Han [15] (considering that they used different materials). For a specimen tested in the modified biaxial
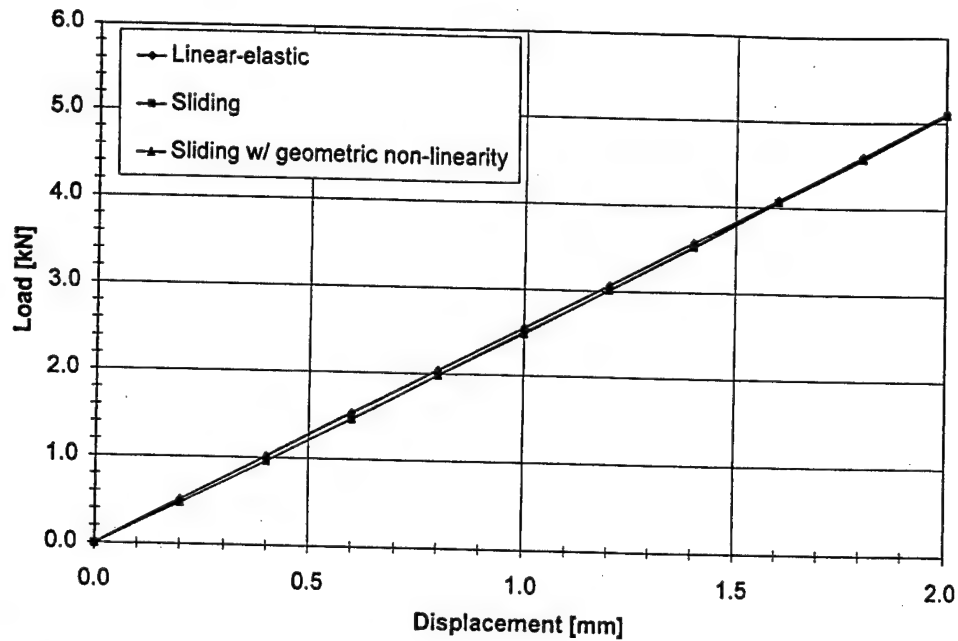
G. Odegard et al.

Figure 5. *Numerical load–displacement curve of a specimen in the biaxial Iosipescu fixture.*

fixture, the results are quite different. There is a significant reduction in the slopes of the curves when specimen sliding is assumed. The assumption of geometric nonlinearity lessens the loads further, but is significant only at large deformations. Therefore, the effects of sliding and geometric nonlinearity on the load/displacement curves will be more pronounced if the composite is tested in the modified biaxial fixture or the fixture recommended by the ASTM standard.
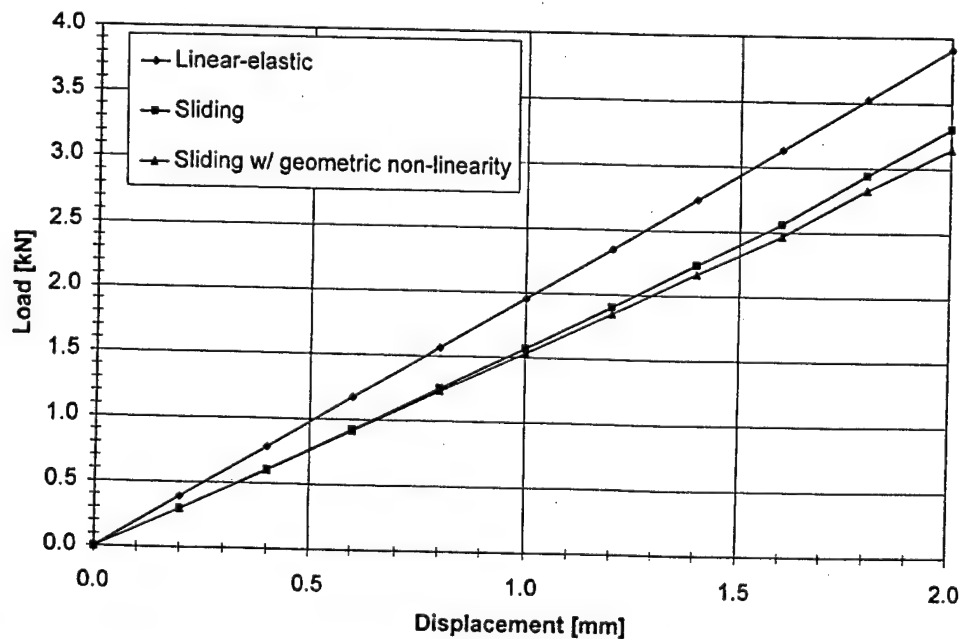
Figure 6. *Numerical load–displacement curve of a specimen in the modified biaxial Iosipescu fixture.*

§3. MODIFICATION TO THE IOSIPESCU SHEAR TEST

3.1. *Failure criterion*

It was demonstrated in the previous section that the stress distribution is nonuniform throughout the test section of Iosipescu specimens loaded with the biaxial and modified biaxial fixtures at various loading angles and using various assumptions of nonlinearity. Moreover, for all of the above loading conditions, a state of pure shear does not exist, either at the notch root or at the center of the specimens. Therefore, unidirectional glass/epoxy, graphite/polyimide, and graphite/epoxy composites with the fibers parallel to the long axis of the specimen tested in the standard Iosipescu fixture, biaxial fixture, and modified biaxial fixture will always be subjected to biaxial stresses with significant normal longitudinal and transverse stresses present. Furthermore, the presence of large transverse compressive stresses (in some cases) in the gauge section of the specimens will prevent the proper shear failure analysis of the composites. It can be assumed that the normal stresses along the fibers should not affect the modes of failure for the composites considered, since the longitudinal strengths of unidirectional composites are significantly higher than the transverse and shear strength properties. The ASTM standard [6] clearly stipulates that for a unidirectional 0° composite, the splits that are always formed at the roots of the notches should not be considered as the shear failure. The problem is that any type of shear failure (either individual intralaminar cracks [21] or interlaminar "shear" damage zones [22]) will be affected by the transverse compressive stresses in the test section.

The Tsai-Wu quadratic failure criterion may be used to approximate the failure envelope of unidirectional composites [23, 24]. Peirron and Vautrin initially suggested applying the Tsai-Wu criterion to Iosipescu specimens [25]. The criterion is described by

$$F_{xx}\sigma_x^2 + F_x\sigma_x + F_{yy}\sigma_y^2 + F_y\sigma_y + F_{xy}\sigma_x\sigma_y + F_{ss}\sigma_s^2 = 1 \tag{1}$$

X and X' are the strengths in tension and compression, respectively, along the fiber direction, and Y and Y' are the strengths perpendicular to the fiber direction. S is the in-plane (intralaminar) shear strength. The coefficients of (1) may be expresses as

$$F_{xx} = \frac{1}{XX'} \qquad F_{yy} = \frac{1}{YY'}$$

$$F_x = \frac{1}{X} - \frac{1}{X'} \qquad F_y = \frac{1}{Y} - \frac{1}{Y'} \tag{2}$$

$$F_{ss} = \frac{1}{S^2} \qquad F_{xy} = \frac{F_{xy}^*}{\sqrt{XX'YY'}}$$

where F_{xy}^* is the interaction term and is often assumed to be -0.5, as is the case here. The approximate strength values for glass/epoxy and graphite/polyimide composites are given in Table 4. The properties for the unidirectional graphite/polyimide composite are similar to the strength properties of a unidirectional graphite/epoxy composite.

It can be easily shown that the stress fields near the roots of the notches of the specimens subjected to all of the loading conditions considered in Section 2 cause the failure criterion to be exceeded long before the criterion is satisfied at the center of the specimen, even for small displacements (0.5 to 1.0 mm). Therefore, a redesign of the fixtures to minimize the shear stress concentrations and the presence of the compressive stresses near the notches would be highly beneficial. If the transverse compressive stress was reduced to zero uniformly over the notch root axis, then the failure criterion will not be necessary to extrapolate the

Table 4

*Failure properties of graphite/polyimide and
glass/epoxy composite systems (in MPa) for
use with the Tsai-Wu failure criterion*

	Unidirectional Graphite/Polyimide	Unidirectional Glass/Epoxy
X	1,300	800
X'	900	700
Y	40	35
Y'	180	120
S	80	60

shear strength from the loads associated with any type of damage generated in the gauge section (following the recommendations provided by the ASTM standard [6]). Since the normal stresses along the fibers (σ_x) will contribute a negligible amount to the composite failure in shear, their absence in the test section is not critical. It will be shown in the next section that by modifying the specimen geometry significantly and employing shear/tension loading conditions, the best-quality shear stress fields can be generated in the 0° Iosipescu specimens.

3.2. Modifications to the Iosipescu shear test

An iterative process was used to find a combination of loading angles, loading block geometries, and specimen geometries that would produce shear failure, preferably at the center of the unidirectional Iosipescu specimen, and reduce the transverse compressive stress uniformly along the notch root axis to nearly zero. As a starting point, an optimized specimen, based on the flat-bottomed notch specimen design of Adams and Lewis [18], was used in order to eliminate the two characteristic splits that occur in 0° unidirectional Iosipescu specimens. These splits are due to transverse tension near the notch roots, as investigated by many authors [26–28]. This also creates a more uniform stress field along the notch root, which can be easily shown with the finite-element method [18, 22]. Therefore, by eliminating the axial splitting in the Iosipescu specimens, more uniform (but still biaxial) stress conditions can be generated in the specimen gauge section. The flat-bottom specimen was investigated with 2-mm, 4-mm (as suggested by Adams and Lewis [18]), and 6-mm notch depths.

Rotation of the standard Iosipescu specimen into shear/tension, as shown previously, reduces the transverse compressive stresses in the test section of the specimen. However, this in turn increases the normal stress along the fibers. It was observed in this study that increasing the distance between the inner loading blocks and the center of the specimen, while keeping them flush with the ends of the specimen, and decreasing the notch depth, also decreases the transverse compressive stresses relative to the normal stresses along the fibers and shear stresses. Maintaining a notch root radius of at least 1 mm helps minimize the σ_x stress concentration at the notch roots.

The optimized Iosipescu test consists of loading blocks that are 22.5 mm long (top and bottom). The notch root angle is 90°, the notch depth is 2 mm, and the notch root radius is 1 mm (Figure 7). The specimen is 80 mm in length and 20 mm in width. The length of the flat-bottomed notches is 10 mm. The specimen is loaded in shear/tension (45°).
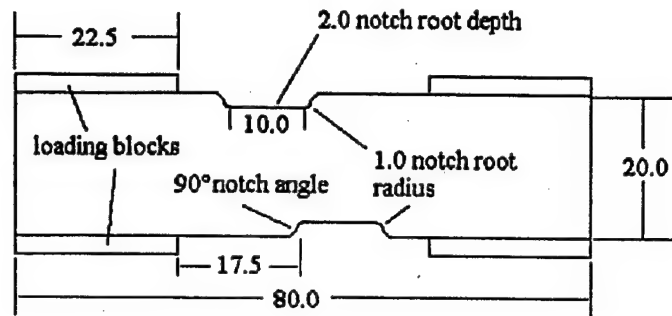
Figure 7. *Optimized Iosipescu test specimen and loading block geometry (dimensions in mm).*

A finite-element model of the above specimen (see Figure 8) was generated (with $\mu = 0.3$ and geometric nonlinearity). The stress distributions along the notch root axis in the standard Iosipescu specimen loaded in shear are presented in Figure 9 for comparison with the stresses determined from the optimized test (Figure 10). Obviously, the stresses in the gauge section are not uniform with large stress concentrations present near the notches (see Figure 9). It can be seen that the stress fields along the notch root axis in the optimized test are completely different (see Figure 10). It should be noted that the transverse compressive stresses in the optimized test are nearly zero along the notch root axis. Moreover, there is no shear stress concentration at the notches, with the shear stress reaching its maximum at the specimen center.

Plots of the failure envelopes (following the Tsai-Wu failure criterion) along the notch root axis for the standard and optimized tests are shown in Figures 11 and 12, respectively, for the material strengths listed in Table 4 (unidirectional graphite/polyimide). The envelopes presented in Figures 11 and 12 represent three different stress fields. One was obtained from the exact stresses along the notch root axis from the standard shear and optimized tests, whereas the other two were generated with σ_y set equal to zero and σ_y and σ_x set equal to zero in order to determine the influence of the normal stresses on the failure of the specimens. Figure 12 clearly indicates that in the optimized test the shear failure should occur near the center of the specimen where the shear stress is maximized and the normal stresses are minimized. There is a negligible effect of normal stresses on the shear failure

Modified long loading blocks
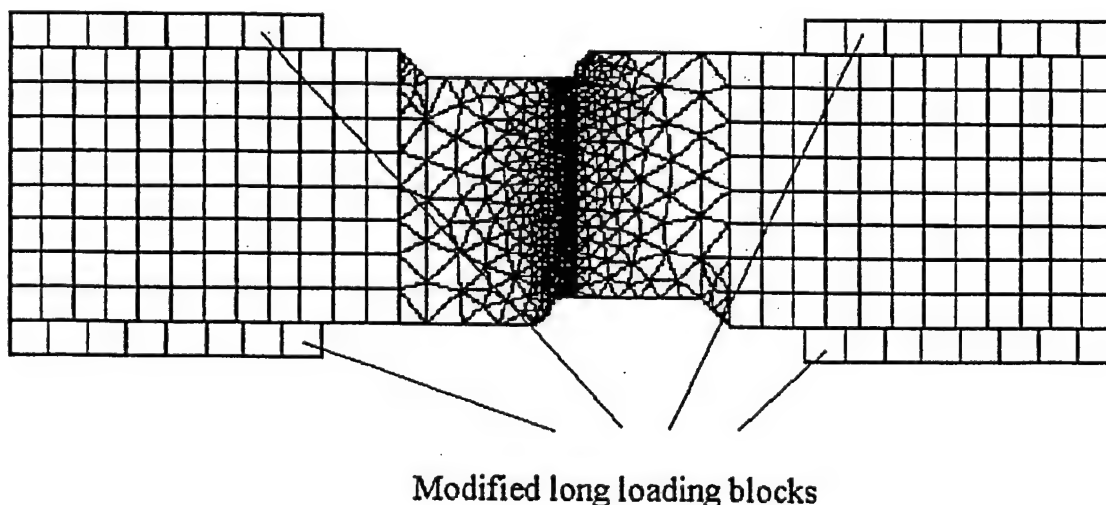
Figure 8. *Optimized Iosipescu test specimen finite-element model mesh.*

G. Odegard et al.
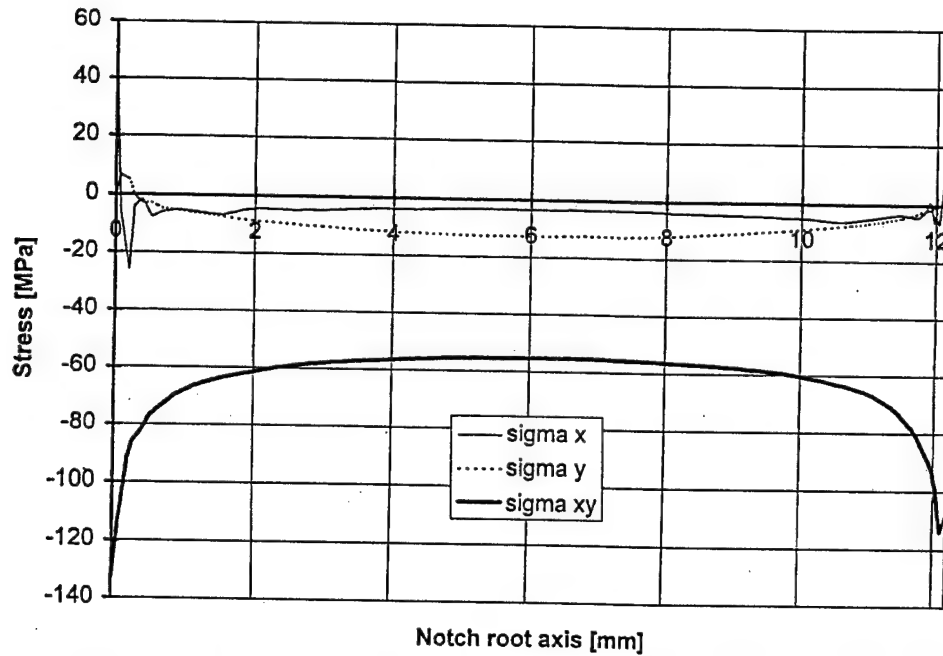
Figure 9. *Stresses along the notch root axis of the standard Iosipescu test specimen under a 0.5-mm fixture displacement.*

process. Figure 11 shows that in the standard test the failure will occur near the notch roots. Also, there is a greater effect of σ_y on the failure process at the center of the specimen. In both cases, there is no influence of the normal stresses along the fibers. Most important, the optimized Iosipescu test generates a stress field in unidirectional composites that should cause failure to occur due to shear stresses only, and the failure should occur at the center of the specimen. Therefore, by modifying the specimen geometry and the loading blocks significantly and rotating the specimen toward large shear/tension loading angles, the best-quality shear stress fields can be generated.
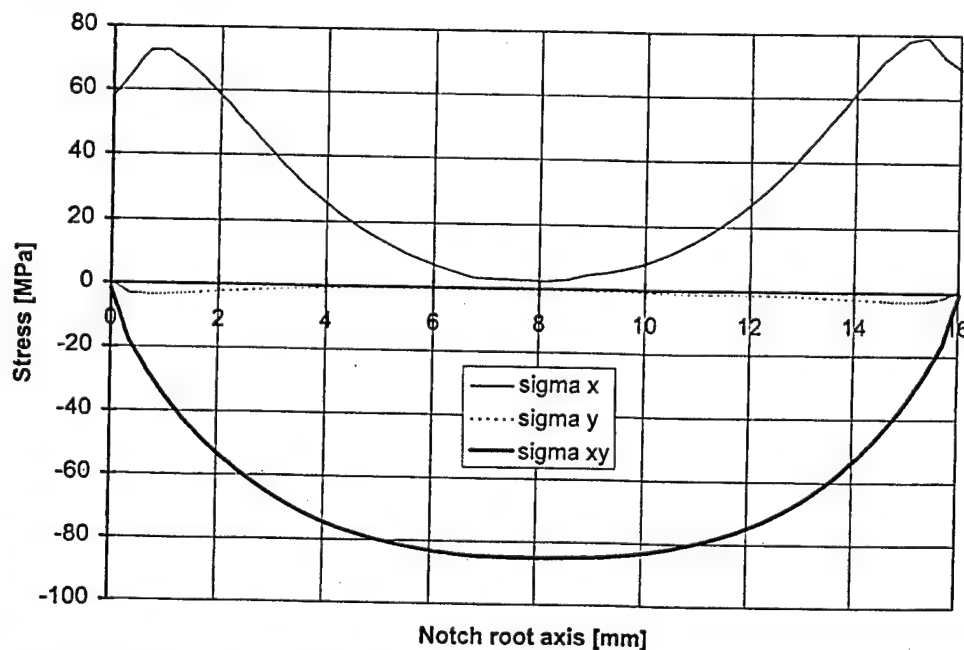
Figure 10. *Stresses along the notch root axis of the optimized Iosipescu test specimen under a 2.5-mm fixture displacement.*
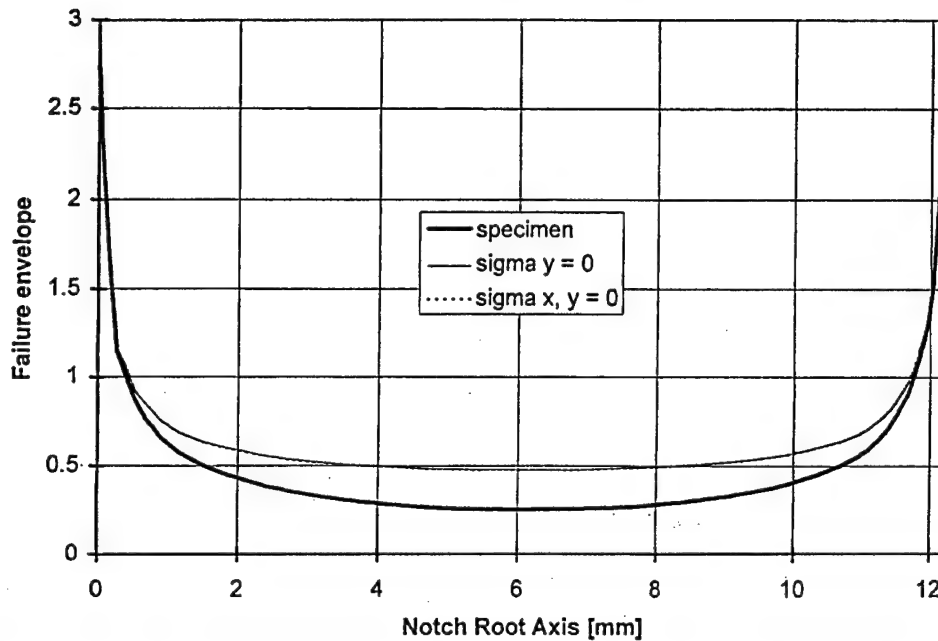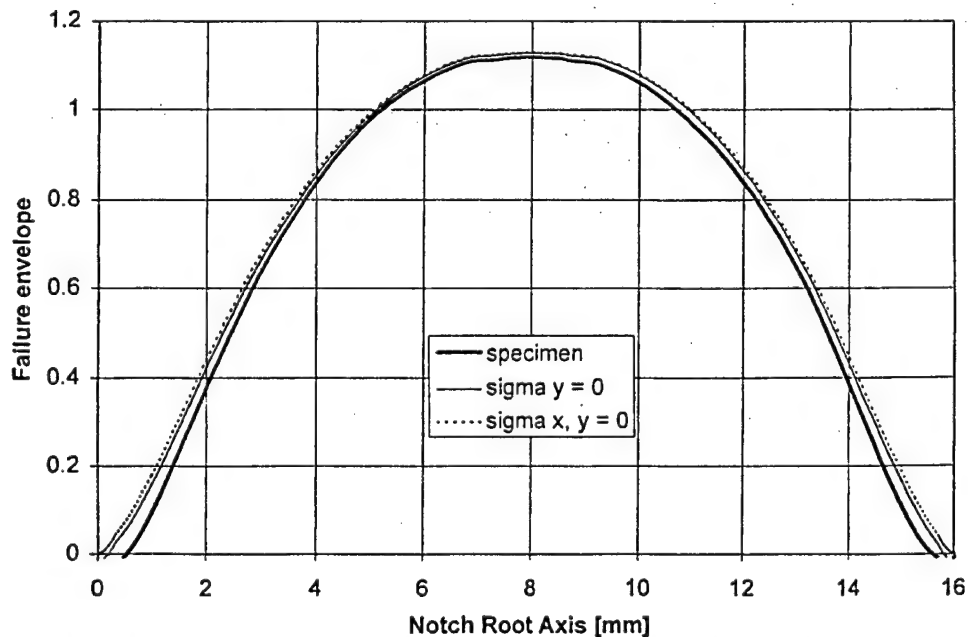
Figure 11. *Tsai-Wu failure envelope along the notch root axis of the standard Iosipescu test specimen under a 0.5-mm fixture displacement.*

In summary, the optimized "shear" test can be characterized by the following:

1. Failure of 0° unidirectional composites should occur at the specimen center.
2. Failure at the center will be due to shear only.
3. There will be no axial splitting due to transverse tension at the notch root.
4. The shear strength of the composites can be determined from the first load drop on the load/displacement curve associated with the onset of intralaminar shear damage in the gauge section of the specimen, provided the localized crushing near the loading blocks is prevented.

Figure 12. *Tsai-Wu failure envelope along the notch root axis of the optimized Iosipescu test specimen under a 2.5-mm fixture displacement.*
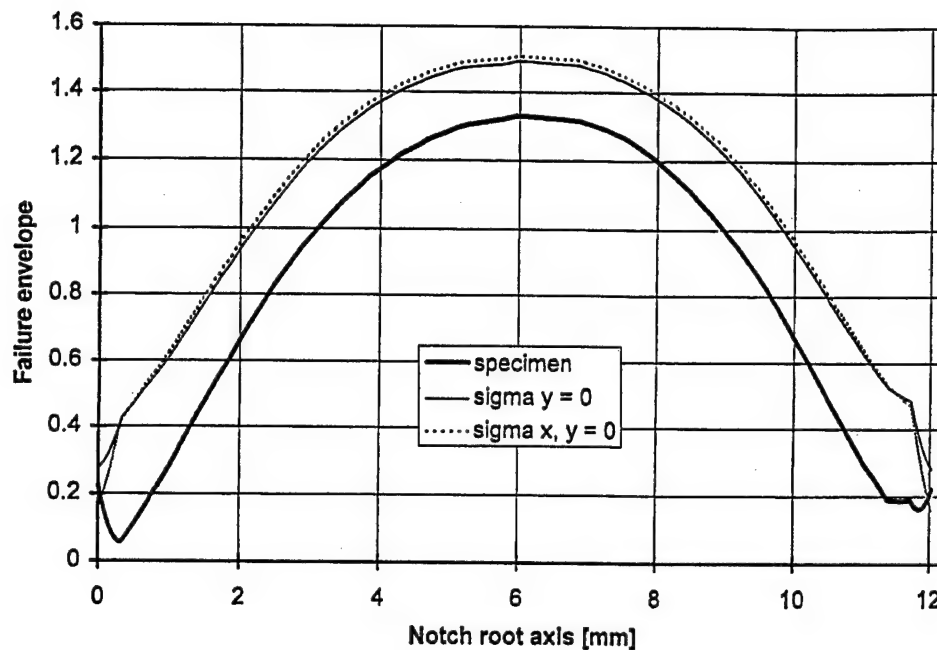
Figure 13. *Tsai-Wu failure envelope along the notch root axis of the optimized Iosipescu specimen with a notch depth of 4.0 mm under a 2.5-mm fixture displacement.*

In the flat-bottom Iosipescu specimens suggested by Adams and Lewis, the notch depth was assumed to be 4 mm. However, the above computations were performed for the specimen with 2-mm notches. The importance of reducing the notch depth in the optimized "shear" test to 2 mm will now be demonstrated. The failure envelopes for the optimized test, but with a notch depth of 4 mm, is shown in Figure 13. It can be clearly seen, by comparing Figures 12 and 13, that the effect of the transverse compressive stress along the notch root axis in the 4-mm notch specimen is significant, and a failure criterion must be used to extract the true shear strength unless the notch depth is reduced to 2 mm.

The preceding analysis was performed on graphite/polyimide unidirectional composites. In order to examine the effect of the orthotropy ratio on the stress distributions in the optimized Iosipescu specimens, the same analysis was performed on a glass/epoxy unidirectional composite, which has a much lower orthotropy ratio (strength properties may be found in Table 4). The stresses and failure envelopes using the optimized test are shown in Figures 14 and 15, respectively. Clearly, the optimized test should work just as well for glass/epoxy composites, with orthotropy ratio significantly lower than that of the unidirectional graphite/polyimide.

In order to match the shear stresses determined experimentally (the shear component of load on the fixture divided by the cross-sectional area of the specimen) with the actual shear stress in the specimen at failure, a correction factor must be used. This is due to the nonuniform shear stresses along the notch root axis. The ratio of the average shear stress to the shear stress at the center of the specimen is 57.0% for graphite/polyimide and 59.0% for glass/epoxy. The ratio for any 0° unidirectional polymer–matrix composite should be very close to these values.

§4. EXPERIMENTAL VERIFICATION

It has been shown in this article that the Iosipescu shear test can be optimized to eliminate almost entirely the presence of transverse compressive stresses in the gauge
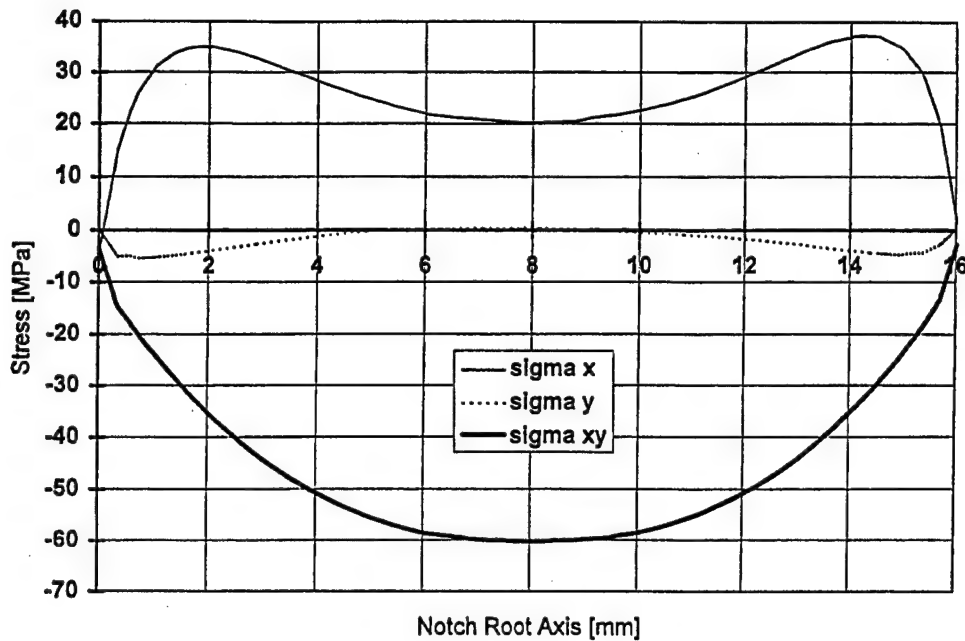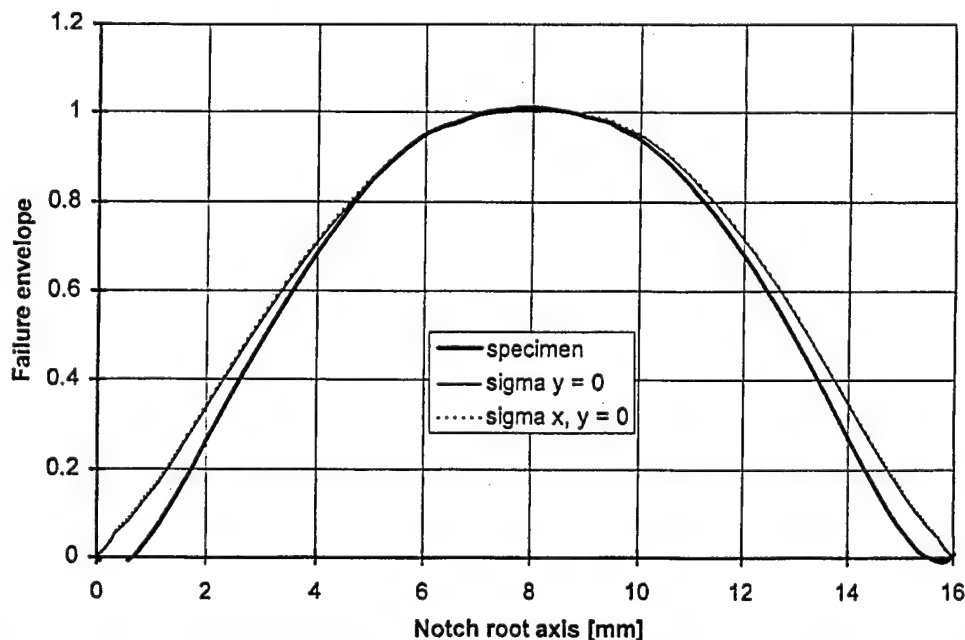
Figure 14. *Stresses along the notch root axis of a glass/epoxy optimized Iosipescu test specimen under a 2.5-mm fixture displacement.*

section of unidirectional Iosipescu specimens and at the same time prevent axial splitting. However, the nonlinear finite element results of internal stress distributions in the specimens did not take into consideration two very important factors: the effect of local crushing of the specimens underneath the inner loading blocks and the nonlinear material behavior. The effect of material nonlinearity on the stresses in unidirectional Iosipescu specimens will be discussed in a subsequent article [29]. Since the numerical results presented in this article look very promising, an attempt was made to verify the numerical work presented

Figure 15. *Tsai-Wu failure envelope along the notch root axis of a glass/epoxy optimized Iosipescu test specimen under a 2.5-mm fixture displacement.*

above experimentally. In particular, the effect of specimen crushing on the intralaminar failure process in a unidirectional glass/epoxy Iosipescu specimens was investigated.

Four Iosipescu specimen geometries were tested in order to determine experimentally the proper specimen geometry for initiating intralaminar damage in the gauge section. The specimens were 0° unidirectional E-glass/epoxy with the volume fraction of fibers approximately 0.55 (per volume). Since unidirectional glass fiber/epoxy composites are transparent materials, the initiation and development of intralaminar damage in the specimen gauge sections and crushing underneath the loading blocks could be easily monitored optically (unlike in unidirectional graphite fiber composites). The loading blocks used in these tests had rounded corners to reduce the stress concentrations in the specimens at the loading block–specimen interfaces.

The first set of specimens (three specimens) had the standard ASTM geometry tested with the long loading blocks in shear. The load–displacement diagrams obtained from these tests exhibited the typical features associated with this type of testing, e.g., load drops caused by the axial splitting and the nonlinear behavior at higher loads. The intralaminar damage in the gauge section, reported in [22] and [26], never occurred, since the specimens developed significant crushing underneath the loading blocks at loads very close to the loads for the onset of splitting. The nonlinear behavior of the load–displacement curves was associated with the rapid development of the crush zones at the inner loading blocks. Therefore, this geometry clearly cannot be used to determine the strength of the composite without considering the effect of crushing at loading blocks on the failure process.

In the next set of experiments three flat-bottom Iosipescu specimens with 4-mm notches (as recommended by Adams and Lewis [18]) were tested in shear. In this case, the specimen geometry prevented the axial splitting along the fibers. However, similar to the previous experiments, the three specimens developed significant crushing before any intralaminar cracking in the gauge section occurred. Again, the observed significant nonlinear behavior of the load–displacement curves at higher loads could be attributed primarily to the significant crushing of the composite at the inner loading blocks. Therefore, this geometry cannot be recommended for the shear strength characterization of unidirectional composites without considering the effect of crushing on the intralaminar failure process in the gauge section.

It has been shown in Section 3.2 that the flat-bottom Iosipescu specimen with 2-mm notches exhibits the highest-quality shear stress field in the gauge section when loaded under shear/tension with the transverse compressive stresses almost entirely eliminated. According to the numerical predictions, this specimen should fail in the middle of the test section, and the failure should be due to shear only. Two specimens were tested, and both behaved the same way. Significant crushing of the composite underneath of the loading blocks developed before any intralaminar failure could be observed in the gauge section. Despite the presence of a pure shear stress field in the test section of the specimen, this geometry cannot be recommended for the shear strength characterization of unidirectional composites.

Since the optimized Iosipescu specimens with 2-mm and 4-mm notches developed significant crushing before any visible intralaminar damage along the notch root axis could be detected, the flat-bottom Iosipescu specimens with 6-mm notches were tested. It was hoped that by reducing the test-section area, the stresses in the gauge section could be increased relative to the compressive stresses at the loading blocks. In all three trials, intralaminar damage in the gauge section and crushing were initiated simultaneously. Furthermore, the damage in the center propagated from the notch root at the center of the specimen within seconds. The simultaneous development of the intralaminar damage and crushing associated with the onset of significant nonlinearity of the load–displacement curve. The
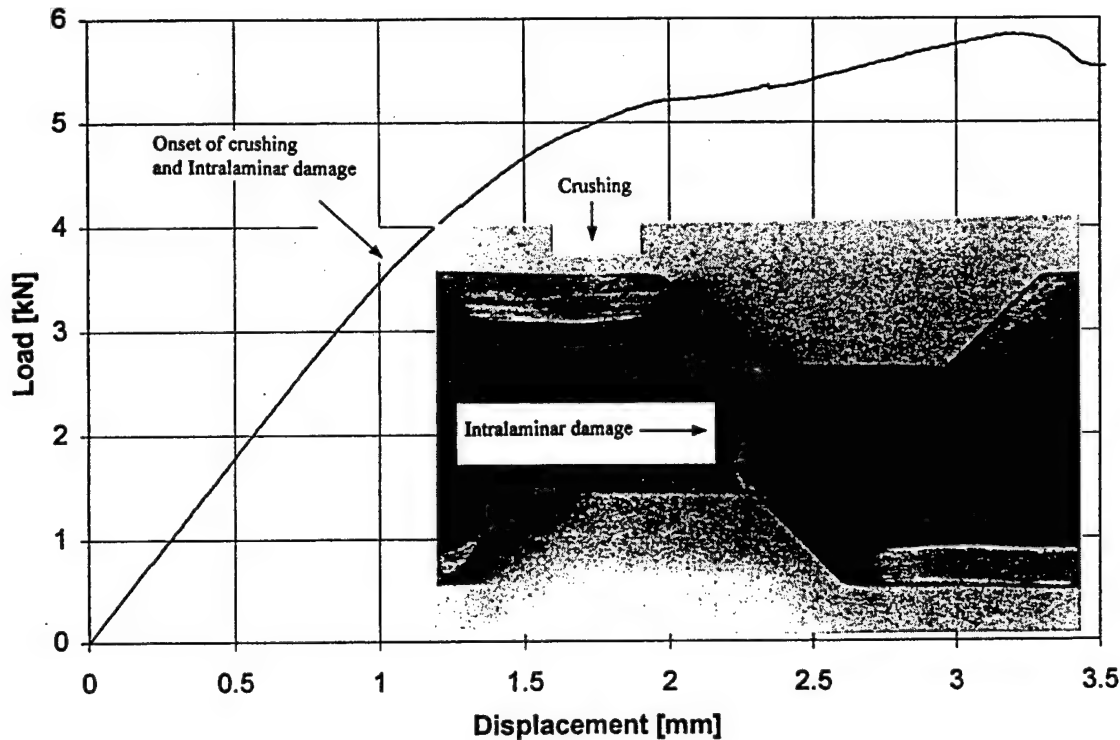
Figure 16. *Experimental load–displacement curve for glass/epoxy flat-bottomed Iosipescu specimen with 6-mm notches.*

load–displacement diagram and the flat-bottom specimen tested are presented in Figure 16. The stress distributions along the notch root axis in the Iosipescu specimen with 6-mm notches and the failure envelopes are shown in Figures 17 and 18, respectively. It can be seen that for this specimen geometry the stress field in the gauge section is biaxial, with a large contribution of normal stresses. The shear strength of the composite was subsequently obtained using the multiaxial failure criterion and was found to be 105 MPa (at the center of the specimen). However, the failure most likely did not initiate at the specimen center. Similar shear stress distributions, with the maximum shear at the specimen center, have been found for the standard Iosipescu specimens with the 90° fiber orientation tested in shear [22]. For this fiber orientation the initiation of specimen failure was also observed at the notch root, despite the fact the shear stress was maximum at the specimen center. Therefore, there is an obvious discrepancy between the numerical predictions and the actual failure mode in the flat-bottom specimen with 6-mm notches. Most likely the nonlinear material behavior, neglected in this research, will make the shear stress field along the notch root axis less concentrated and more uniform. Therefore, the obtained shear strength of the composite determined based on the linear elastic computations is significantly overestimated. This could be another example of the incorrect application of linear elastic finite element models for the failure analysis of composite materials tested in the Iosipescu shear test. The effect of material nonlinearity on the failure process in unidirectional Iosipescu specimens will be discussed in another article [29].

In graphite/polymer unidirectional Iosipescu specimens, crushing at the loading blocks cannot be easily observed since those materials are not transparent. Therefore, the effect of crushing on the shear strength measurements of the composites has been often neglected. It can be assumed that even if cracks on the specimen surface underneath the loading blocks are not observed, significant material crushing can still occur inside the specimen. However,
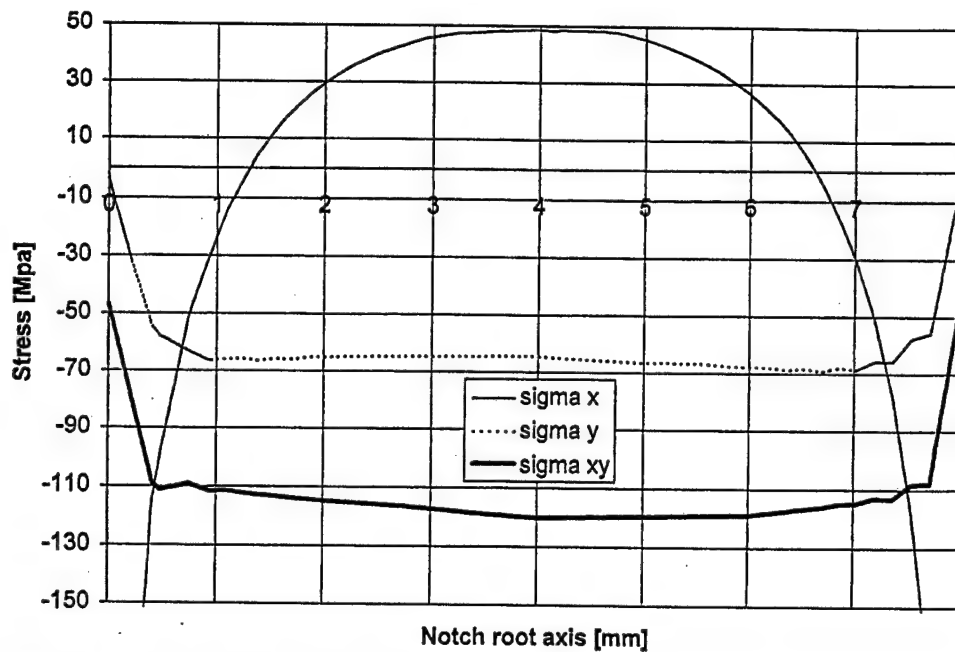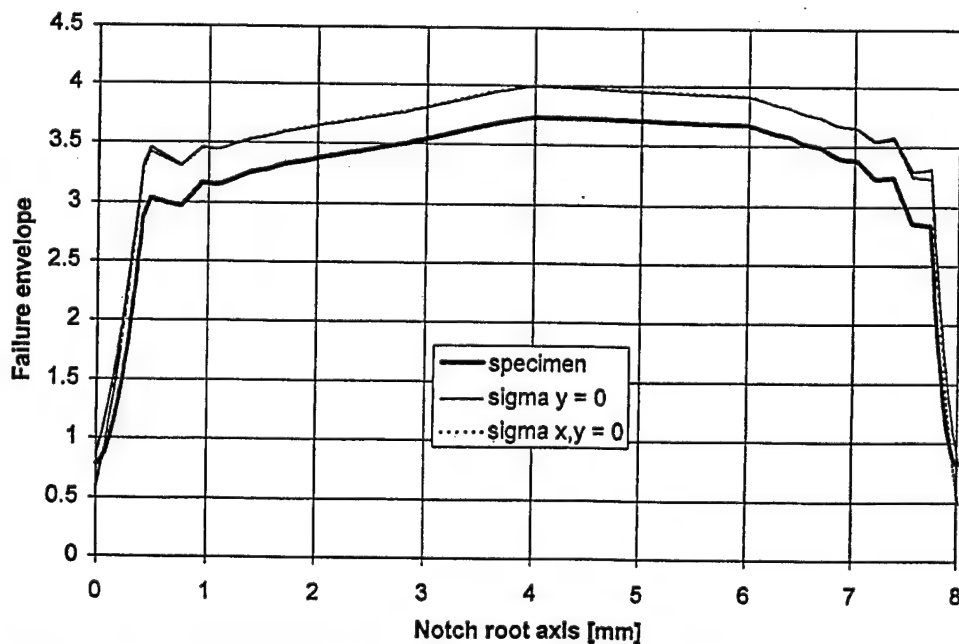
G. Odegard et al.

Figure 17. *Stresses along the notch root axis of a glass/epoxy flat-bottomed Iosipescu specimen with 6-mm notches under a 1.0-mm fixture displacement.*

this type of damage cannot be detected optically in unidirectional graphite/polyimide and graphite/epoxy specimens. In the experiments performed in this study, significant damage was detected in the specimens underneath the inner loading blocks long before any surface cracks could be detected along the specimen edges. Therefore, any assumptions about the presence (or lack thereof) of crushing made based purely on optical observation of the specimen edges underneath the loading blocks is invalid. Both material nonlinearity and

Figure 18. *Tsai-Wu failure envelope along the notch root axis of a glass/epoxy flat-bottomed Iosipescu specimen with 6-mm notches under a 1.0-mm fixture displacement.*

the local crushing at the loading blocks must affect the stress distributions in unidirectional 0° Iosipescu specimens at failure, and at the same time, the shear strength determination.

It has been shown in this research that even if the specimen geometry is optimized in order to eliminate undesirable normal stresses in the gauge section, crushing of the specimens at the inner loading blocks can create severe experimental difficulties, leading to the incorrect interpretation of experimental results obtained from the Iosipescu tests. Obviously, the effect of crushing on the failure process in the Iosipescu specimens will be significantly more pronounced if the specimens are tested with the short loading blocks. In this case, the concentration of the compressive stresses in the specimens underneath the loading blocks is significantly higher in comparison with the long blocks used in the experimental part of this research.

§5. CONCLUSION

The effects of specimen sliding and geometric nonlinearity on the mechanical response of 0° unidirectional graphite/polyimide standard Iosipescu specimens subjected to the biaxial shear-dominated loading conditions in the biaxial and modified biaxial fixtures have been investigated using nonlinear finite element methods. It has been shown that the effects of sliding are small, in some cases negligible, and the effects of geometric nonlinearity are always negligible for stresses at the center of the standard Iosipescu specimen tested up to 2 mm. The stresses near the notch root change significantly for both assumptions of nonlinearity. Variations in the coefficient of friction in some cases have a significant influence on σ_x, but have very little effect on σ_y and σ_{xy} in the center of the specimen and near the notch roots. The use of the modified biaxial loading blocks over the biaxial loading blocks has the same effect on all of the stresses along the notch root. The magnitude of all of the stresses decreases, and the ratio of σ_y to σ_{xy} decreases.

Neither set of loading blocks under the investigated conditions can induce failure due to shear only in the standard Iosipescu specimen, even if the specimen is rotated within the biaxial fixture. The optimized Iosipescu test, the flat-bottom specimen with 2-mm notches, might eliminate this problem by forcing the specimen to fail due to shear stresses only at the center of the specimen. Also, the optimized specimen eliminates characteristic axial splitting initiating at the notch roots and associated load drops on the load–displacement curves. However, for this specimen geometry, local crushing at the loading blocks affects the intralaminar failure process in the gauge section in the shear strength determination. Only in the flat-bottom Iosipescu specimen with 6-mm notches crushing occurs simultaneously with the rapid development of intralaminar damage along the notch root axis. In this case, however, the stress field in the gauge section is biaxial.

REFERENCES

[1] N. Iosipescu, New Accurate Procedure for Single Shear Testing of Metals, *J. Mater.*, vol. 2, no. 3, pp. 537–566, 1967.

[2] D. F. Adams and D. E. Walrath, Composite Materials: Testing and Design (Sixth Conference), ASTM STP 787, I. M. Daniel (ed.), pp. 19–33, American Society for Testing and Materials, Philadelphia, 1982.

[3] D. F. Adams and D. E. Walrath, The Iosipescu Shear Test as Applied to Composite Materials, *Exp. Mech.*, vol. 23, no. 1, pp. 105–110, 1983.

[4] D. F. Adams and D. E. Walrath, Further Developments of the Iosipescu Shear Test Method, *Exp. Mech.*, vol. 27, no. 2, pp. 113–119, 1987.

[5] D. F. Adams and D. E. Walrath, Current Status of the Iosipescu Shear Test Method, *J. Composite Mater.*, vol. 21, no. 6, pp. 494–507, 1987.

[6] Standard Test Method for Shear Properties of Composite Materials by the V-Notched Beam Method, ASTM Standard D 5379-93, American Society for Testing and Materials, Philadelphia, May 1993.

[7] W. R. Broughton, M. Kumosa, and D. Hull, Analysis of the Iosipescu Shear Test as Applied to Unidirectional Carbon-Fiber Reinforced Composites, *Composites Sci. Technol.*, vol. 38, pp. 299–325, 1990.

[8] N. Sukumar and M. Kumosa, Finite Element Analysis of Axial Splits in Composite Iosipescu Specimens, *Int. J. Fracture*, vol. 62, no. 1, pp. 55–85, 1993.

[9] A. Bansal and M. Kumosa, Experimental and Analytical Studies of Failure Modes in Iosipescu Specimens under Biaxial Loadings, *J. Composite Mater.*, vol. 29, pp. 334–358, 1995.

[10] A. Bansal and M. Kumosa, Application of the Biaxial Iosipescu Method to Mixed-Mode Fracture of Unidirectional Composites, *Int. J. Fracture*, vol. 71, pp. 131–150, 1995.

[11] M. V. Balakrishnan, A. Bansal, and M. Kumosa, Biaxial Testing of Unidirectional Carbon-Epoxy Composites using Biaxial Iosipescu Test Fixture, *J. Composite Mater.*, vol. 31, no. 5, pp. 486–508, 1997.

[12] M. Kumosa, K. Searles, G. Odegard, and Y. Han, Biaxial Failure Analysis of Graphite Reinforced Polyimide Composites, Annual Report to the Air Force Office of Scientific Research, Department of Engineering, University of Denver, September 1997.

[13] M. Arcan, Z. Hashin, and A. Voloshin, A Method to Produce Uniform Plane-Stress States with Application to Fiber Reinforced Materials, *Composites Sci. Technol.*, vol. 38, pp. 141–146, 1978.

[14] H. Ho, J. Morton, and G. L. Farley, Non-linear Numerical Analysis of the Iosipescu Specimen for Composite Materials, *Composites Sci. Technol.*, vol. 50, pp. 355–365, 1994.

[15] M. Kumosa and Y. Han, Non-linear Finite Element Analysis of Iosipescu Specimens, *Composites Sci. Technol.*, in press, 1998.

[16] Y. Han and M. Kumosa, Adhesively Bonded Composite Iosipescu Specimens without Singular Stress Fields, *Mech. Composite Mater. Struct.*, vol. 5, no. 2, pp. 127–151, 1998.

[17] K. Searles and M. Kumosa, Non-linear Finite Element Computations of Biaxial Graphite/Polyimide Fabric Iosipescu Specimens, to be published, 1998.

[18] D. Adams and E. Lewis, Experimental Strain Analysis of the Iosipescu Shear Test Specimen, *Exp. Mech.*, vol. 35, no. 4, pp. 352–360, 1995.

[19] ANSYS Engineering System, User's Manual for Version 5.2, Swanson Analysis System, 1995.

[20] K. Searles, G. Odegard, M. Castelli, and M. Kumosa, Failure Investigation of Graphite-Polyimide Fabric Composites at Room and Elevated Temperatures using the Biaxial Iosipescu Test, *J. Composite Mater.*, in press, 1998.

[21] S. Ding, Mixed Mode Failure Analysis of Adhesively Bonded Composite Systems using the Modified Iosipescu Test Method, Ph.D. thesis, Oregon Graduate Institute of Science & Technology, Portland, OR, April 1995.

[22] M. Kumosa and D. Hull, Mixed-Mode Fracture of Composites using Iosipescu Shear Test, *Int. J. Fracture*, vol. 35, pp. 83–102, 1987.

[23] S. W. Tsai and E. M. Wu, A General Theory of Strength for Anisotropic Materials, *J. Composite Mater.*, vol. 5, pp. 58–80, 1971.

[24] S. W. Tsai, A Survey of Macroscopic Failure Criteria for Composite Materials, *J. Reinforced Plastics Composites*, vol. 3, pp. 40–62, 1984.

[25] F. Pierron and A. Vautrin, Measurement of the in-Plane Shear Strength of Unidirectional Composites with the Iosipescu Test, *Composites Sci. Technol.*, vol. 57, no. 12, pp. 1653–1660, 1997.

[26] J. A. Barnes, M. Kumosa, and D. Hull, Theoretical and Experimental Evaluation of the Iosipescu Shear Test, *Composites Sci. Technol.*, vol. 28, no. 4, pp. 251–269, 1987.

[27] J. Morton, H. Ho, M. Y. Tsai, and G. L. Farley, An Evaluation of the Iosipescu Specimen for Composite Materials Shear Property Measurement, *J. Composite Mater.*, vol. 26, no. 5, pp. 708–750, 1992.

[28] M. J. Pindera, P. Ifju, and D. Post, Iosipescu Shear Characterization of Polymeric and Metal Matrix Composites, *Exp. Mech.*, vol. 30, no. 1, pp. 101–108, 1990.

[29] G. Odegard and M. Kumosa, Elasto-Plastic Analysis of the Iosipescu Shear Test, *J. Composite Mater.*, in press, 1998.

Failure Investigation of Graphite/Polyimide Fabric Composites at Room and Elevated Temperatures Using the Biaxial Iosipescu Test

K. SEARLES

Department of Materials Science and Engineering
Oregon Graduate Institute of Science and Technology

G. ODEGARD AND M. KUMOSA*

Department of Engineering
University of Denver
2450 S. Gaylord St.
Denver, CO 80208

M. CASTELLI

NASA Lewis Research Center

ABSTRACT: The biaxial and modified biaxial Iosipescu shear test methods were applied to determine the shear dominated, biaxial mechanical response of graphite/PMR-15 and graphite/Avimid-R woven fabric composites at room and elevated temperatures. Three different composite architectures were examined: T650-35 warp-aligned, 8-harness satin (8HS) fabric in a PMR-15 matrix, T650-35 warp-aligned, 8HS fabric in an Avimid-R matrix and T650-35 0°/90°, 8HS fabric in an Avimid-R matrix. Several biaxial Iosipescu tests were performed at room temperature under shear, shear-tension, and shear-compression loading conditions to characterize damage and obtain biaxial, shear dominated failure properties. Shear tests were also conducted at elevated temperatures approaching 316°C to determine the effects of temperature on the shear strengths of the composites investigated. A nonlinear finite element analysis is briefly introduced to evaluate the effects of specimen sliding and geometric nonlinearities on the stress and strain distributions in the biaxial Iosipescu specimens. In addition, the effects of different loading block geometries on the stress distribution in the Iosipescu specimens subjected to biaxial loads were also investi-

*Author to whom correspondence should be addressed.

1

gated. Within this investigation, it was found that graphite/Avimid-R was more resistant to biaxial, shear dominated failure at room temperature in comparison to graphite/PMR-15. However, the graphite/PMR-15 composite system exhibited better shear strength properties at elevated temperatures above 232°C. It was also found that the effect of compression along the notch root axis generated by the loading blocks did not affect the loads at failure.

INTRODUCTION

HIGH TEMPERATURE POLYMERS and polymer matrix composites (PMC's) are finding increasing use in the aerospace and electronics industries. At the present time, PMC's account for about 4% by weight of commercial aircraft and about 10% of military aircraft. Current predictions are that, within the next decade, up to 65% of new commercial and military aircraft could be polymer composites. Advanced thermosetting polymer composites such as cloth based, graphite reinforced polyimides, have become highly relevant in the realm of reduced weight at high temperature applications [1]. These composites possess exceptional specific properties, are stable to temperatures as high as 360°C and effectively translate stiff, strong yarns into stiff, strong composites. The 8H woven architecture also exhibits good conformability (drape) over complex surfaces. However, conformability and resistance to shear and shear dominated, biaxial in-plane loading conditions tend to be inversely related.

For successful application of graphite/polyimide composites, it is essential to have a reliable database of material properties and a comprehensive understanding of fracture and failure behavior, especially at elevated temperatures. A major limitation of many fiber-polymer composite systems is the inability of these materials to resist intralaminar and interlaminar damage initiation and propagation under biaxial, shear dominated in-plane monotonic and cyclic loading conditions. The primary purpose of this research is to experimentally investigate the in-plane shear and biaxial response of 8HS woven graphite/polyimides as a function of temperature and characterize the damage development through novel application of image analysis techniques. Secondly, this research addresses the effects of specimen sliding, geometric nonlinearities and the geometry of the loading blocks on the stress distributions in the graphite/polyimide Iosipescu specimens tested in the biaxial and modified biaxial Iosipescu fixtures.

EXPERIMENTAL MECHANICS OF WOVEN FABRICS

From an experimental viewpoint, uniaxial tensile and compressive properties of advanced woven composites may be readily obtained by employing standardized tests such as unnotched tension or compression tests. In most cases, interpretation is straightforward and the values obtained are fairly accurate with minimal data scattering. There are, of course, exceptions subject to interpretation as in cases involving grip failures and slippage, buckling or crushing. Conversely, obtaining ac-

curate information on in-plane shear behavior can be quite complicated and cumbersome. Interpretation of material response to shear dominated, biaxial loading conditions at elevated temperatures can prove to be even more difficult.

A great deal of time, effort and understanding have been invested to establish the guidelines and best known methods (BKM's) for conducting shear tests on polymer matrix composite materials. Currently, there are only a few tests available for the shear characterization of these materials. The most commonly applied testing methods include the two and three-rail test, cross-beam sandwich test, picture frame panel test, thin-walled torsion tube test, 10° off-axis test, ±45° off-axis tensile test, slotted tensile test and the Iosipescu test. In several of these tests, end-constraint effects, buckling and bending moments introduce errors in the measured elastic properties. Of these tests, the Iosipescu method is most likely the best and least expensive available test.

Iosipescu Testing of Fabrics

The Iosipescu shear test, which was originally intended for determining shear properties of metals [2], was first applied to composite materials by Walrath and Adams [3–5]. With the efforts of Adams, Walrath and Slepetz et al. [6] the Iosipescu specimen geometry and loading have been certified through extensive investigations and finite element analysis. Based upon those investigations and more comprehensive studies [7] that include the analysis of stress distributions in the specimen as a function of geometry, a redesigned test specimen and fixture emerged from the University of Wyoming. The fixture was aptly named the modified Wyoming fixture.

Comparative studies have been made between isotropic and orthotropic materials to determine the questionable influences of geometry, loading configuration and fiber direction on the stress distribution in the specimen gage section and to understand why the shear stress field is not uniform as originally proposed by Iosipescu [2]. However, very little work has been done to further the understanding of the aforementioned influences on shear response of fabric composites, especially as a function of temperature. The major focus has been on applying uniaxial/biaxial extension and compression or off-axis tensile testing to these materials under room temperature conditions [8–11]. As exceptions, Ho et al. [12] used the Iosipescu shear test method to evaluate the in-plane shear response of AS4 and Celion carbon fiber-epoxy fabric composite materials. Woven architecture influences and materials response were quantified using conventional strain gages and Moiré interferometry. Walsh and Ochoa [13] applied the Iosipescu shear test to plain woven hybrid S-RIM composites for comparison of elastic constants predicted by original mathematical mechanics models. Ifju [14–15] abandoned the traditional Iosipescu specimen geometry altogether, opting for a compact version with u-shaped notches and a larger gage section. This combined with a newly de-

signed shear gage [16] and Moiré interferometry was shown to provide less exper-
imental scatter for shear properties of woven fabric composites.

Biaxial and Modified Biaxial Fabric Testing

In most engineering applications, composite systems are not subjected to sim-
ple states of stress, but to biaxial and triaxial loads. Only a limited few of the previ-
ously mentioned test methods can extend to include these loading conditions. The
modified Wyoming fixture is fixed and does not allow for external loading appli-
cations other than parallel to the notch root axis. Therefore, exploration of unre-
solved issues pertaining to the influence of normal and transverse stress compo-
nents on the shear stress distribution is not possible. As a result of this problem,
lengthy studies have been conducted by Broughton, Kumosa and Hull [17–19] to-
wards the development of a more refined biaxial fixture.

The biaxial Iosipescu test fixture allows for rotation of the externally applied
loads with respect to the notch root axis and is capable of measuring biaxial,
shear dominated material failure properties. It has been used for measuring
mixed-mode failure properties of unidirectional carbon/epoxy, glass/polymer,
carbon/PEEK, Ti/SiC and Teak wood [20–22]. The biaxial Iosipescu test tech-
nique is being proposed in this investigation as a successful experimental tool for
evaluating the shear dominated biaxial response of 8HS woven graph-
ite/polyimides at room and elevated temperatures. Also proposed herein is a
modified version of this fixture that loads the specimen similar to the modified
Wyoming design and allows the reduction of transverse stresses generated by the
loading blocks.

Loading Contact and Geometric Nonlinearities

It is well known that the in-plane shear response of most unidirectional compos-
ite materials is highly nonlinear, primarily due to yielding of a dominant matrix.
For brittle matrix fabric composites, such as the graphite/polyimides studied
herein, we may expect some yielding in the resin rich crimp pockets, but the re-
sponse should be more linear or bilinear until failure because of the different
microstructures of the fabric composites in comparison with unidirectional com-
posites. At elevated temperatures, the degree of nonlinearity exhibited should in-
crease as the matrix glass transition temperature is approached. However, at room
temperature it is possible that any observed deviation from linearity during an
Iosipescu test could be partially contributed to specimen-fixture contact
nonlinearities (sliding) and geometric nonlinearities. Previously, Ho et al. [23]
found these conditions not to be of significance in the shear testing of brittle matrix
graphite/epoxy unidirectional composites using the modified Wyoming fixture.

The investigation performed by Ho et al. [23] concentrated, however, on the effect of sliding and geometric nonlinearity on the stress distributions in unidirectional graphite/epoxy Iosipescu specimens subjected to relatively small deformations. Since graphite/polyimide fabric Iosipescu specimens tested under biaxial, shear dominated loading conditions fail at large applied displacements [24–25], these non-linear effects must be further investigated.

A preliminary numerical analysis from an ongoing study, supplemental to the experimental investigation of the biaxial failure properties, will be introduced to show the effects of contact and geometric nonlinearities on stress and strain distributions in a graphite-polyimide Iosipescu specimen. What is of interest is the influence of large biaxial deformations and varying contact conditions between the specimen and the loading blocks. A comparison will be made between the biaxial Iosipescu fixture with contact lengths of 10 mm and the modified biaxial Iosipescu fixture with long and short contact lengths of 31.1 mm and 25.4 mm, respectively. Although the friction coefficients at the loading block/specimen interface are not known a priori, a reasonable value of 0.3 is assumed in this analysis, since simple inclined sliding experiments produce rough approximations in the range of 0.2 to 0.4.

COMPOSITE MATERIAL ARCHITECTURES

In the experimental part of this study, three different composite systems based on woven graphite fabrics were tested. The graphite/PMR-15 composite plaques were fabricated at the NASA Lewis Research Center per the following specifications:

Fabric: T650-35, 8-harness satin cloth (V_f = 58–60% nominal)
Ply Arrangement: warp-aligned, 16-ply with floating undulations (crimps)
Matrix: PMR-15 (polymerization of monomer reactants, At. wt. = 1500)
Cure: simulated autoclave and postcure (General Electric specifications)
Q/A: C-scan (exceptional density, uniformity)
Dimensions: 305 mm × 305 mm × (4.82 – 5.15 mm)

Two slightly different graphite/PMR-15 plaques (same ply orientation) were supplied by the NASA Lewis Research Center; one plaque was 4.82 mm thick and the other plaque was 5.15 mm thick. Two graphite/Avimid-R systems with different ply orientations were also submitted by Pratt & Whitney. These plaques were fabricated at DuPont per the following specifications:

Fabric: T650-35, 8-harness satin cloth (V_f = 58–60% nominal)
Ply Arrangement: warp-aligned orientation with 10-plies
Matrix: Avimid-R (proprietary combination of dianhydride-diamine monomers)

indent 1 cm

Cure: simulated autoclave and postcure (specifications unknown)
Q/A: C-scan (exceptional density, uniformity)
Dimensions: 305 mm × 305 mm × 3.92 mm

Fabric: T650-35, 8-harness satin cloth (V_f= 58–60% nominal)
Ply Arrangement: 0°/90° orientation with 10-plies
Matrix: Avimid-R (combination of dianhydride-diamine monomers)
Cure: simulated autoclave and postcure (specifications unknown)
Q/A: C-scan (exceptional density, uniformity)
Dimensions: 305 mm × 305 mm × 3.92 mm

Approximately 55 Iosipescu specimens were processed from the 2 graphite/PMR-15 plaques and 25 specimens from each of the graphite/Avimid-R plaques. All of the specimens were selectively cut and the material inside the C-scanned edge effect boundary was examined for uniformity before being used. Each specimen blank was cut with a diamond-tipped blade and included a 2 mm allowable tolerance on all sides. The blanks were subsequently surface ground to final dimensions and the notches were machined to the desired depth using a grinding wheel dressed in the form of a v-notch with an included 90° angle (Figure 1). Special precautions were taken during the critical step of machining the notches and all operations were performed under a copious flow of water. Post-machining

4 mm w/ 90 deg. included angle and a
0.45 mm notch root radius
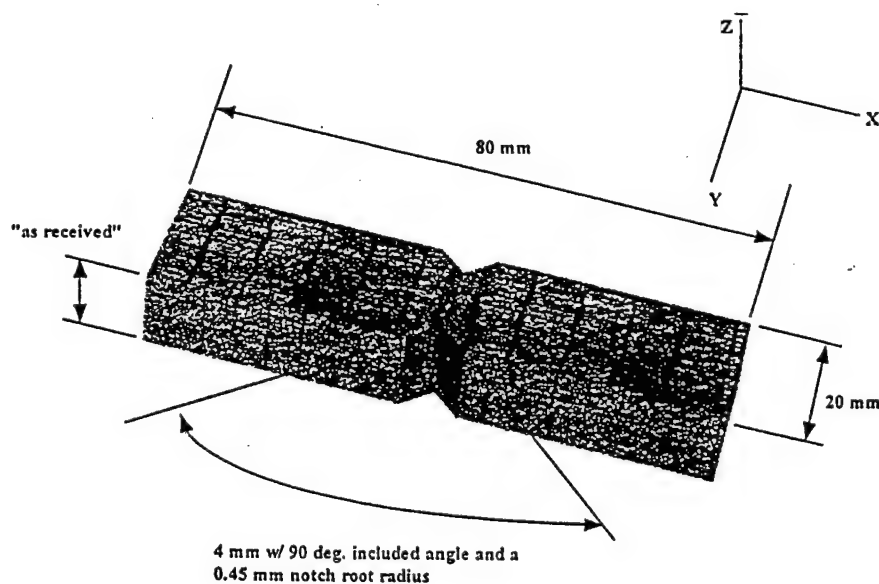
Figure 1. Iosipescu specimen geometry.

requirements included immediate specimen drying to reduce moisture absorption by the matrix and examination of machined surfaces with an optical stereoscope. In all instances, no visible damage due to machining was detected. The notch root radii of the specimens were consistently 0.45 mm.

MECHANICAL TESTING PROCEDURE

The biaxial Iosipescu test fixture employed in this study is shown in Figure 2 and has the capabilities to test composite materials in shear and combined shear-tension or shear-compression. The specimen may be rotated corresponding to a changing loading angle (α) ranging from (+40°) shear-compression to (−40°) shear-tension. Four 10 mm × 10 mm stainless steel loading blocks (in the original design of the fixture) can be adjusted to accommodate specimens as thin as 1 mm and the position of these blocks, with respect to the notch root axis, may be changed for various notch geometries. The modified version of the biaxial fixture employs significantly longer blocks with geometries similar to the modified Wyoming design and the ASTM standard (D5379/D5379M-93, Standard Test Method for Shear Properties of Composite Materials by the V-Notched Beam Method). For this study, a screw-driven Dillon Test System with a planetary gearbox and a 45 kN load capacity was used as the mechanical testing platform. An environmental chamber capable of sustaining temperatures in excess of 343°C was also incorporated into the platform. The entire system was calibrated with reference to a given monotonic compressive load at a constant displacement rate of 1.5 mm/min.

The assemblage of data acquisition components necessary for recording dynamic mechanical test data is shown schematically in Figure 3. The analog load signal (1 Vdc full scale), sensed as strain by the 45 kN load cell, was routed to a DC amplifier and raised by an order of magnitude to compliment the Measurements Group Model 2000 A/D converter range of ±10 Vdc. Measurements Group MG 2000 and National Instruments IEEE-488 GPIB software were utilized to interpret the incoming signals (channels) and dynamically display them, allowing for the capture of experimental data points. Displacements were measured with a Newport displacement transducer and the ambient lab temperature was measured using a Type-K thermocouple.

For elevated temperature testing, a second Type-K thermocouple was placed on the Iosipescu specimen to monitor surface temperature of the composite and testing was conducted only when the composite surface temperature reached a steady-state condition with no more than a ±2% drift from the target temperature. This channel was also routed into the A/D converter and displayed dynamically along with the load-displacement data. Finally, the data acquisition system was inherently capable of externally plotting load-displacement response on a Hewlett-Packard X-Y Recorder and measuring 6 individual strains produced from 2 back-to-back, 3-element rosette or Iosipescu [16] strain gages.
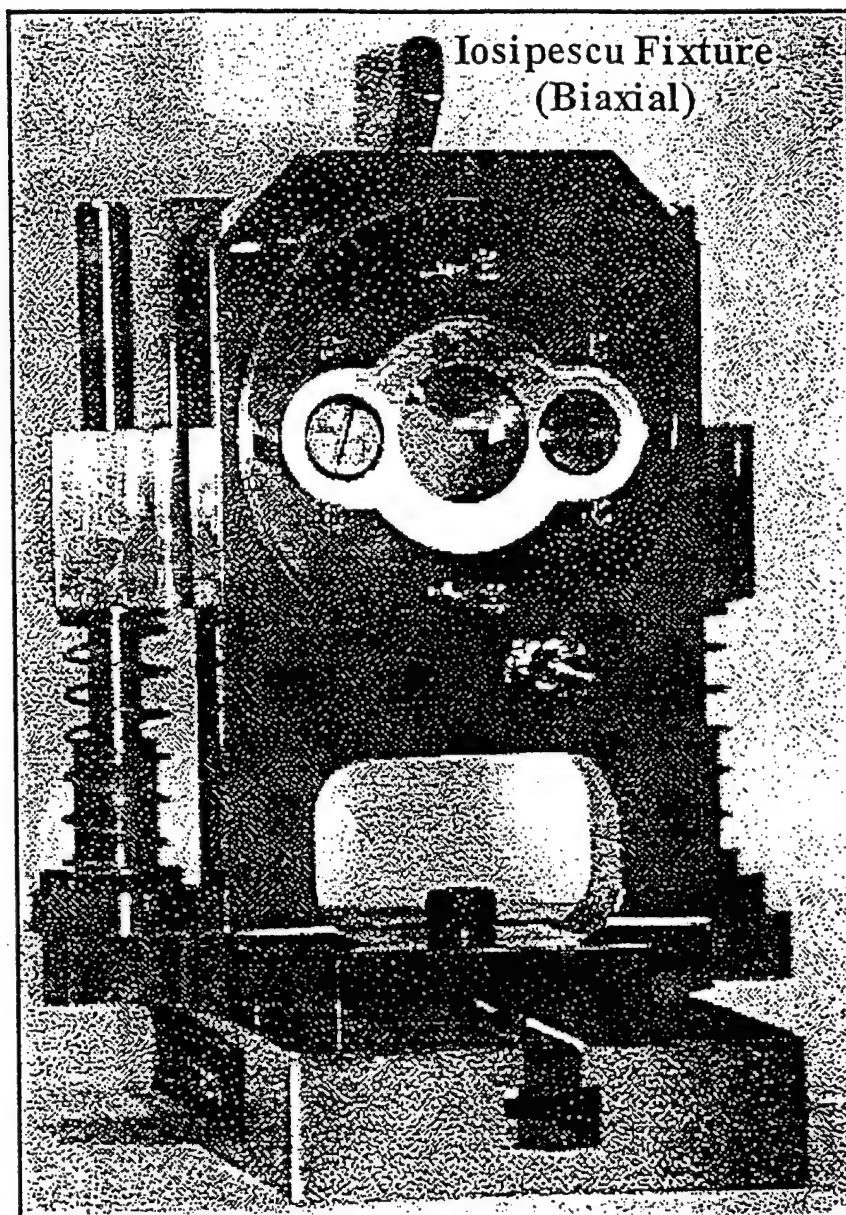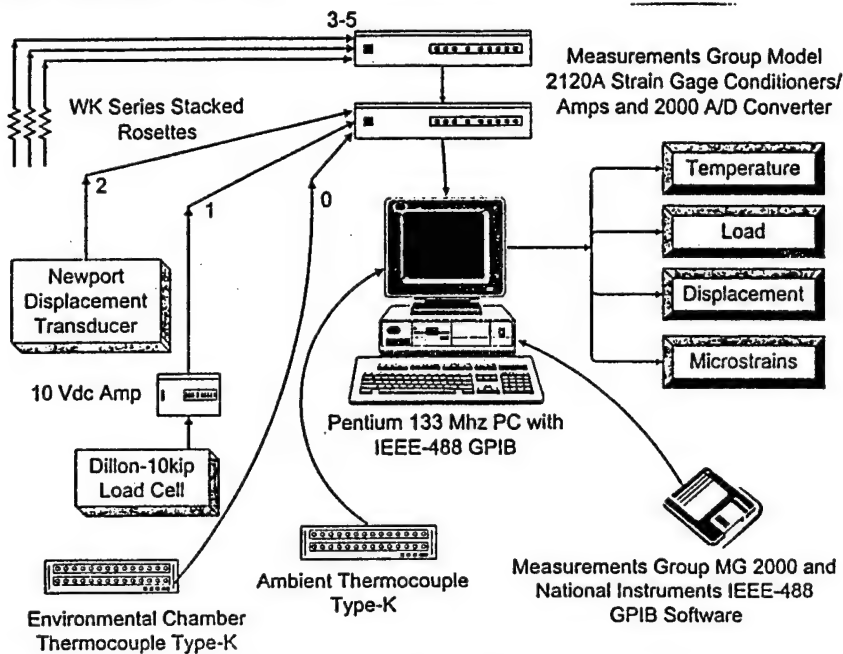
Figure 2. Biaxial Iosipescu test fixture.

Figure 3. *Schematic of high temperature experimental setup.*

Room Temperature

At room temperature (from 24°C to 27°C), 53 specimens were tested to determine the effects of loading conditions on composite shear strengths, establish the most important damage and failure mechanisms and characterize failure phenomena according to significance, whether intralaminar, interlaminar or translaminar in nature. Of the specimens tested, 19 were from the 1st PMR-15 plaque with an "as received" thickness (t_r) of 4.82 mm, 12 were from the 2nd PMR-15 plaque (t_r = 5.15 mm), 12 were from the warp-aligned Avimid-R (t_r = 3.91 mm) and 10 were from the 0°/90° Avimid-R (t_r = 3.92 mm). Several specimens were also instrumented with self-temperature compensating rosette or Iosipescu gages placed on both sides to monitor out-of-plane deformation, twisting and recording tensor strains at $\varepsilon_{\pm\theta}$ (where $\theta = 45°$ with respect to the neutral gage axis). Front and back strains were averaged to determine G_{12}. Several experiments were also conducted to determine the effect of loading block geometries, in the biaxial and modified biaxial fixtures, on the biaxial failure process at room temperature. In particular, the effect of compression generated by the loading blocks was examined for influence on the failure process.

Elevated Temperature

In addition, several shear tests were performed at elevated temperatures (up to 315°C) within the environmental chamber to compare the strength and deformation properties based on ply orientations and matrix constituents. Ten PMR-15 specimens from the 2nd plaque were reserved for these tests as were 12 warp-aligned and 0°/90° Avimid-R specimens. Strain gages were encapsulated above 260°C to avoid possible signal degradation resulting from oxidation of the Ag solder lead attachment paste and the target test temperature was maintained for a minimum of 5 minutes prior to testing to ensure a steady-state condition.

DAMAGE EVALUATION

For 0° unidirectional PMC specimens (fibers oriented along the long axis of the Iosipescu specimen), failure under all loading conditions, either shear or biaxial, occurs as a result of axial splits initiated at the roots of the notches. These splits form parallel to the fibers and propagate on one side of the notch tip away from the nearest loading point. Both split formations are always manifested by two successive drops on the load-displacement diagram. Unidirectional composite specimens with 90° fibers (fibers oriented along the notch root axis) always fail catastrophically. For all loading angles, cracks originate at the notch root and propagate in an unstable manner parallel to the fibers. The failure process in both 0° and 90° unidirectional Iosipescu specimens can be easily observed since the failure of the specimens is usually through the thickness and the cracks are visible on the specimen surface. For the fabric composites, the failure process is much more complex and can vary through the thickness. In this case, the failure characteristics cannot be determined by examining the specimen surface only, therefore a detailed analysis of damage through the specimen thickness is required.

Current methods typically relied upon for image analysis of failed specimen morphology include: SEM backscattering, texture and rugmapping, stereo pairing, z-projections, laminography and mesh generation. To supplement the mechanical testing in this investigation, a novel image analysis technique was developed to evaluate the state of damage in a shear tested graphite-polyimide specimen. This technique is based on capturing and qualitatively analyzing scanning electron microscopy (SEM) images of damage from planar 2D specimen slices (serial sections) and subsequently rendering an isosurface or 3D volume. A full description of this damage image analysis technique can be found elsewhere [26].

Image Analysis Procedure

Following mechanical testing, the gage section of an Iosipescu specimen tested in shear was removed using a Buehler Isomet, a low speed saw with a diamond tip circular blade immersed in methanol. The removed gage section was encapsulated by a low viscosity epoxy, pressurized at 310 kPa for 24 hours and temperature cured. The purpose of the encapsulation was to arrest damage associated with the mechanical test and prevent further damage caused by serial sectioning, thus mis-representing actual results. Upon curing, the encapsulated fabric artifact was placed in a fixture that permitted consistent indexing in the z-direction and stable mounting on a scanning electron microscope (SEM) stage. It was found that con-sistent indexing was critical not only for proper focus at a given working distance, but for accurate reassembly of sections as well.

The artifact was initially polished until the top surface of the gage section was exposed through the epoxy. The surface was then sputter coated with 150 Å of Au-Pd deposit from a Technics Hummer II system to prevent localized charging and poor image sampling during the capture process. Capturing and polishing were consecutive through 4 more intervals of 350 μm thickness per interval at which point the process was stopped because symmetry along the midline was as-sumed and ensuing intervals would mirror previous ones. It should be noted that this process was also repeated using an untested gage section in order to determine if encapsulation using epoxy was effective in protecting against additional damage from polishing.

RESULTS AND DISCUSSION

Room Temperature Biaxial Data

All room temperature biaxial graphite/PMR-15 specimens from the same plate tested to failure exhibited similar and quite repeatable failure characteristics. As an example, Figure 4 shows the load-displacement response for three specimens from the thinner plate tested at loading angles of 0°, +30°, and −30°, respectively. The load-displacement response is quite linear and similar for small loads, but for higher loads the response to biaxial loading conditions becomes more evident. Clearly, the slope is the highest in shear followed by shear-compression and shear-tension. Moreover, sudden drops or "triggers" are apparent upon reaching the maximum load carrying capacity of the specimens. In all cases, the specimens revealed a general trend towards stability of the failure process after this trigger. The only exceptions were tests for the shear-tension loading conditions associated with large displacements. Here, the tests resulted in a significant secondary (some-times tertiary) rise and sudden drop in load. It should be pointed out however, that the relationships between the biaxial loading conditions and the slopes might vary,
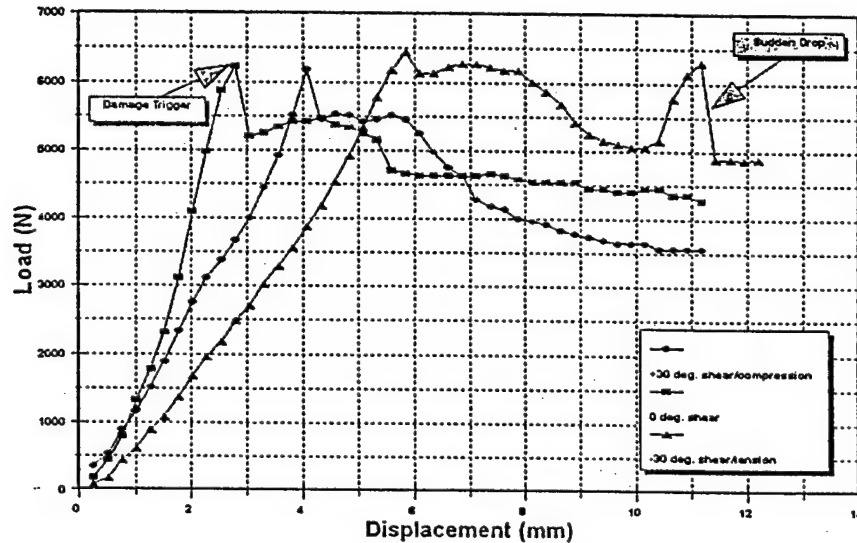
PMR-15 Iosipescu Specimen

Figure 4. *Load-displacement diagram for graphite/PMR-15 (thinner) tested in shear (0°), shear-tension (−30°) and shear-compression (+30°).*

especially for the shear-compression and shear-tension curves for small loading angles.

The mechanical response to biaxial loads of the PMR-15 specimens prepared from the thicker plate exhibited very similar behavior for low to intermediate loads. However, the load-displacement curves near the maximum loads did not show the presence of the trigger observed for the specimens cut from the thinner plate. In these cases, the loads, after reaching a maximum value, gradually decreased as a function of the applied displacement (see Figure 5).

Similar to the effect of biaxial loading conditions on the failure properties of the graphite/PMR-15, the response characteristics of the graphite/Avimid-R systems are also strongly dependent on these conditions with one exception. As shown in Figure 5, the Avimid-R systems display a distinct "knee" indicative of multiple cracking phenomena versus a sudden drop or trigger associated with large delaminations.

The shear and biaxial strengths of the composites were determined from both the loads at the onset of nonlinearity and the maximum loads on the load-displacement curves. The onset of nonlinearity was defined in this investigation as the abrupt change in the load-displacement response before a maximum load was reached. One parallel line was drawn over the linear regime and a second line was drawn tangent to the abrupt change. A third vertical line was placed at the

intersection of the first two lines and the onset was that point formed by the intersection of the vertical line with the load-displacement curve. It is believed that the onset of nonlinearity defined by this method represented significant damage development in the fabric composites.

For the majority of PMR-15 specimens cut from the thinner plate, the interpreted nonlinearity and the maximum load capacity were nearly identical (trigger). However, the load-displacement curves for the thicker PMR-15 specimens exhibited the onset of nonlinearity slightly below the maximum load. For the Avimid-R Iosipescu specimens, the onset of nonlinearity was considered to be the same point as "the knee." The shear strengths of the composites were determined from the average shear stress in the specimen gage section and defined, at this point, as the load divided by the cross-sectional area of the specimens. For the biaxial tests, the load was taken as $P_\alpha \cos (\alpha)$, where $\dot{\alpha}$ was the loading angle. The strengths of the composites in shear and the shear strengths under biaxial conditions (as a function of the loading angle) for the onset of nonlinearity and the maximum load are presented in Figures 6 and 7, respectively. The data shown in these figures was obtained from the tests in the biaxial Iosipescu fixture with the short loading blocks.

It can be seen in Figure 6 that the shear and "biaxial" shear strengths of the
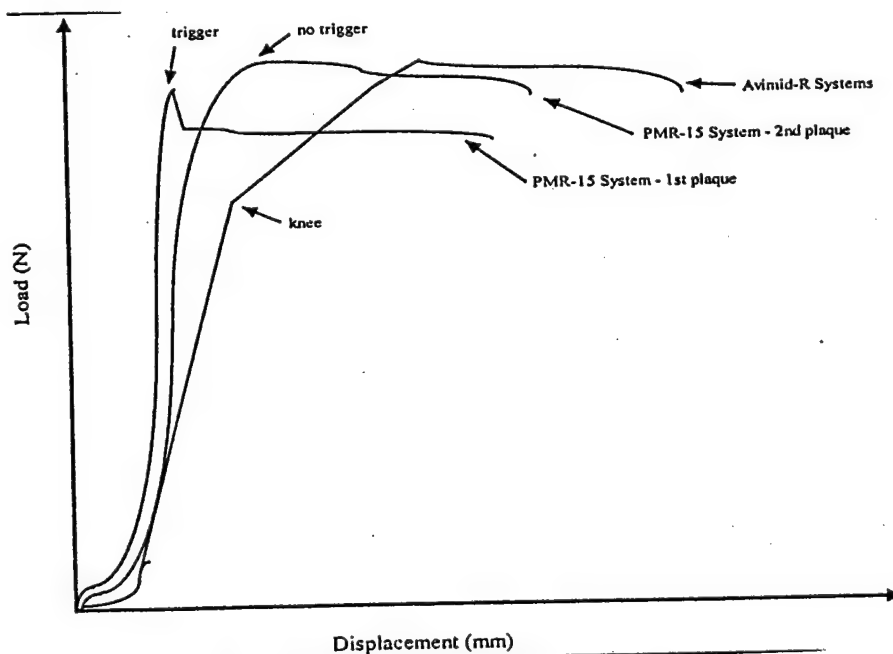
Figure 5. *Typical load-displacement diagrams for Iosipescu specimens made from both graphite/PMR-15 and graphite/Avimid-R plaques.*
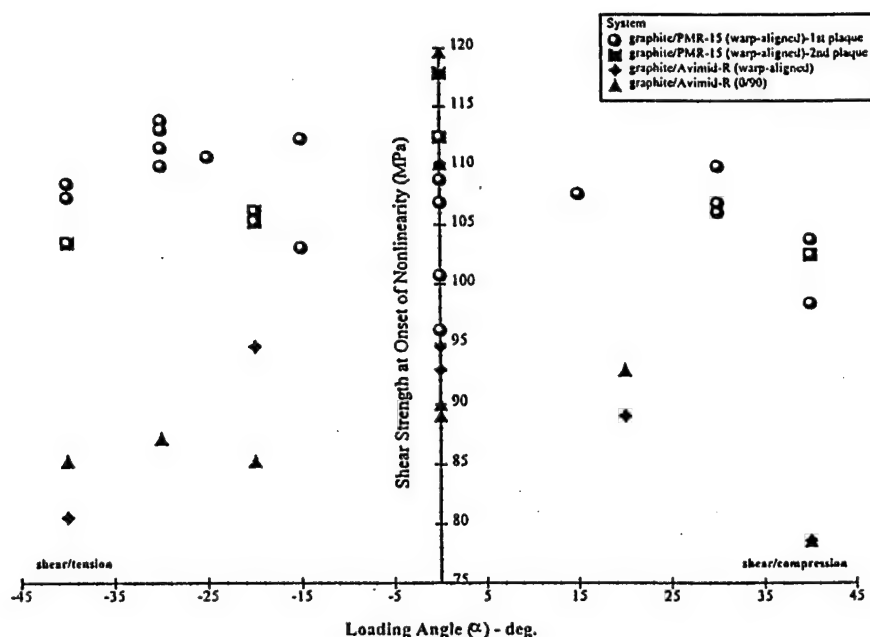
Figure 6. Shear strength data determined at the onset of nonlinearity for all composites investigated.

PMR-15 specimens established from the loads at nonlinearity are, in general, higher than the strengths of the Avimid-R systems. Moreover, there is an insignificant difference between the strengths for the PMR-15 specimens from the thicker and thinner plates. The effect of the tensile dominated loading angle on the shear strength properties of the PMR-15 composites is negligible. On the compression side, the strength is reduced, indicating that there is some influence of compression on the loads at the onset of nonlinearity for this particular composite. The data for the Avimid-R systems indicate similar trends, however, there is more scatter in the experimental results.

The shear and biaxial shear strengths of the composites established for the maximum loads shown in Figure 7 clearly demonstrate that the Avimid-R systems exhibit higher strength properties measured in shear and under biaxial conditions. The reduction in the shear strength measured under the shear-compression conditions seems to be more pronounced for the Avimid-R systems than for the PMR-15 composite. However, in all the systems, there is no effect of tension on the shear strength properties.

The average shear strengths for the PMR-15 composite (thinner plate) at the onset of nonlinearity and the maximum load, measured in shear and at room temperature are 105.1 MPa and 106.5 MPa, respectively. The same strengths for the

thicker plate are 115.2 MPa and 120.8 MPa. The shear strengths for the Avimid-R warp aligned system are 102.6 MPa and 137.5 MPa, whereas for the Avimid-R 0/90 composites, the same strengths are 100.1 MPa and 147.3 MPa. The shear stress-strain diagrams (for relatively small displacements) for the specimens from the thinner plate are shown in Figure 8 for five different loading angles. The shear strains in these specimens were measured using both Iosipescu strain gages and rosettes mounted back-to-back. A detailed description of this application of the Iosipescu gages and stacked rosettes for the shear modulus measurements in the biaxial Iosipescu test can be found in Reference [24]. Influences of specimens position, out-of-plane deformations and twisting on reliable shear strain readings were previously established.

In reference to Figure 8, the shear modulus G_{xy} is defined according to the following relationship:

$$G_{xy} = \frac{\int \tau_{xy}}{\int \gamma_{xy}} = \frac{P_\alpha \cos(\alpha)}{A \int (\varepsilon^{+45} - \varepsilon^{-45})} \tag{1}$$

where P_α is the applied load at an angle normal to the longitudinal specimen axis,
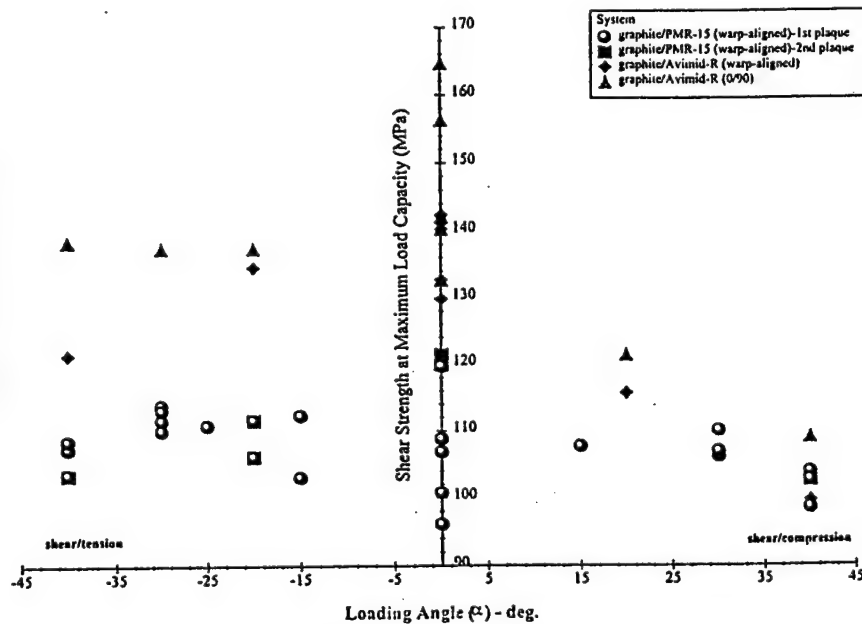
Figure 7. *Shear strength data determined at the maximum load capacity for all composites investigated.*
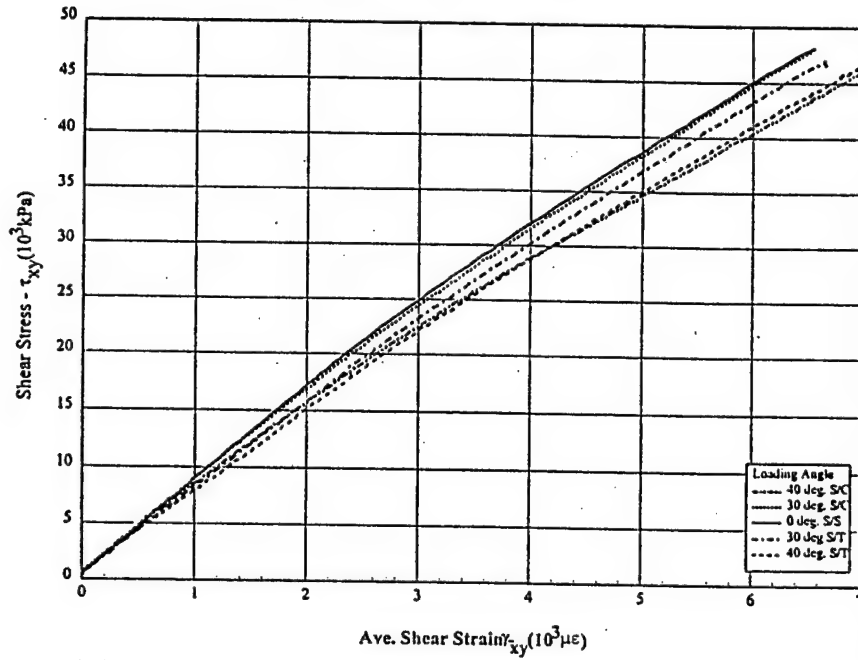
Figure 8. *Typical shear stress-strain response for graphite/PMR-15 (thinner).*

A is the cross-sectional area between the notches and ε_θ is the measured strain with respect to the neutral gage axis. It can also be deduced that the average strain measured by a strain gage of grid area ($A \times B$) can be represented as follows [27]:

$$\varepsilon^*_{45} = \frac{1}{AB} \int_{-A/2}^{A/2} \int_{-B/2}^{B/2} \varepsilon^*_{45} ds^* dt^* \tag{2}$$

where ds^* and dt^* are respective to gage coordinates corresponding to the dimensions A and B.

The shear moduli ($\alpha = 0°$) for both the thicker and thinner graphite/PMR-15 plates were determined to be 7.6 GPa and 6.3 GPa, respectively. Both the Iosipescu gages and rosettes gave very similar estimates of the shear moduli. This might suggest that the strain field in the fabric Iosipescu specimen is fairly uniform along the notch root axis, otherwise the strains and thus, the moduli obtained from using two completely different gage geometries would yield totally different shear moduli estimates. Since the Iosipescu gages measure the average strain along the entire notch root axis, whereas the small-element rosettes measure the strain only at the specimen center, any nonuniform strain distribution would be reflected by obvious differences in measurements.

As of this writing, a viable explanation cannot be given as to why the biaxial

shear-compression, stress-strain response supersedes that of biaxial shear-tension as shown previously in Figure 8. Since shear strength of the PMR-15 system is predominantly dictated by the properties of the matrix and imposed by resin rich undulations in the woven geometry, it is expected that introduction of a tensile component should result in a sharper slope than introduction of a compressive component. However, as observed, this was not the case, speculatively due to shear and compression-coupled bundle locking influences on load transfer to undamaged laminae. Arguably though, it is also reasonable to assume that shear and tension coupling would resist bundle movement as well, subsequent to matrix failure, resulting in a different mode of transfer. It is also possible that the effect of the out-of-plane deformations on the shear strain measurements may be dependent on the biaxial loading conditions. Therefore, the out-of-plane deformations may also affect the shear modulus measurements differently for various biaxial loading conditions. However, this behavior has not been investigated in this research.

Elevated Temperature Shear Tests

The high temperature Iosipescu shear ($a = 0°$) tests were conducted using the experimental set-up presented in Figure 3. The tests were performed on the PMR-15 composite specimens prepared from the thicker plate. The effect of high temperature on the shear strength properties of the thinner plate was not evaluated due to an insufficient number of specimens available for the high temperature research. The high temperature shear tests were also performed on the Avimid-R (both the warp aligned and 0°/90°) composite systems. The high temperature experiments were conducted using the biaxial Iosipescu fixture with the short loading blocks. The effect of different loading block geometries on the high temperature shear strength properties was not examined again due to an insufficient number of specimens.

As an example a set of shear stress-displacement curves for the PMR-15 specimens obtained at various temperatures is shown in Figure 9 whereas the curves for the Avimid-R specimens (warp aligned) are presented in Figure 10. The curves for the Avimid-R specimens (0°/90°) exhibited very similar behavior. It can be seen in these diagrams that both the loads at the onset of nonlinearity and the maximum loads are significantly affected by temperature. Clearly, the influence of temperature on the shear strength properties of the Avimid-R composites is stronger than for the PMR-15 system. The shear strengths of the composites determined from the loads at the onset of nonlinearity and the maximum loads are illustrated in Figures 11 and 12, respectively. The data presented in these two figures represent the average points for each temperature. In addition, the high temperature shear strength results for the composites are listed in Table 1. As far as the shear strengths at the onset of nonlinearity are concerned, both Avimid-R composites exhibit very similar behavior. A large reduction in the shear strength with temperature was observed. The PMR-15 system also exhibited a reduction in shear
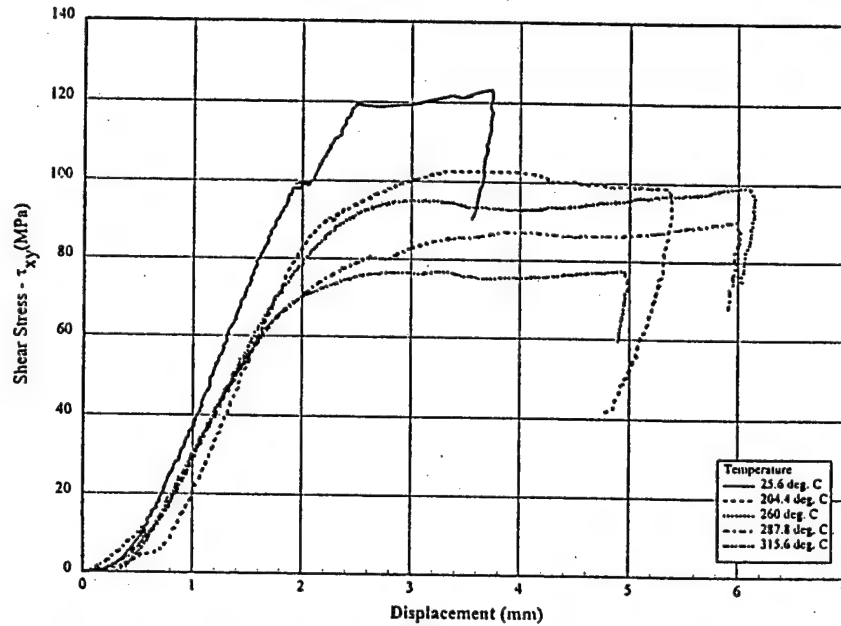
Figure 9. Shear stress-displacement diagrams for graphite/PMR-15 (thicker) obtained at various test temperatures under shear ($\alpha = 0°$) loading conditions.
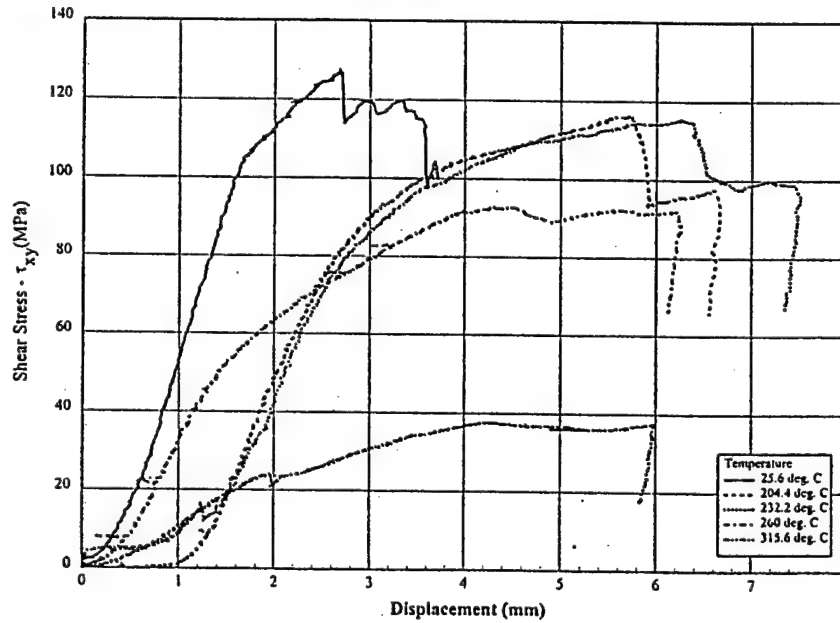

Figure 10. Shear stress-displacement diagrams for graphite/Avimid-R (warp-aligned) obtained at various test temperatures under shear ($\alpha = 0°$) loading conditions.
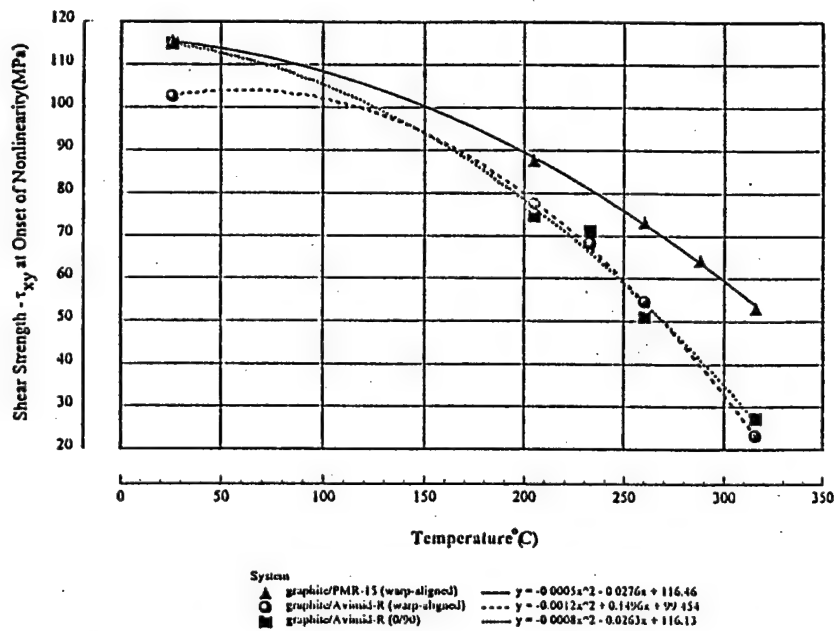
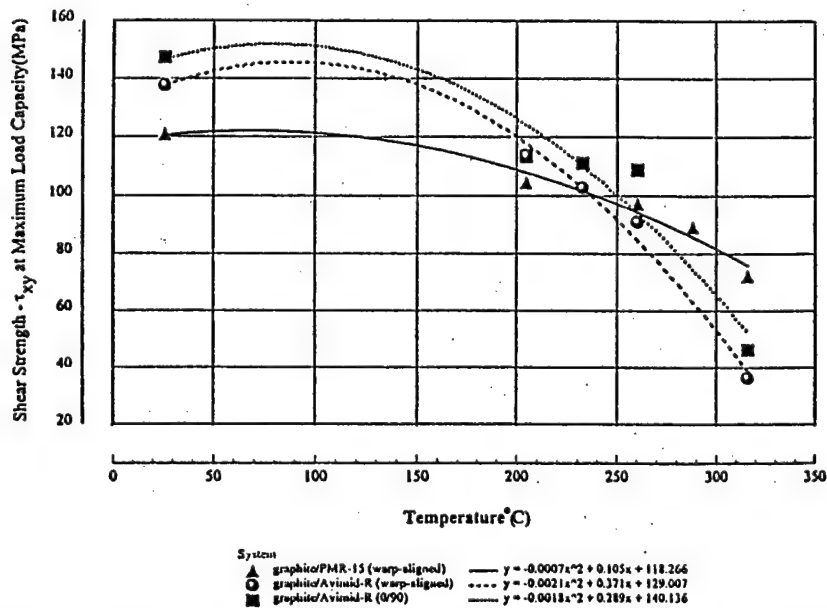**Figure 11.** *Average shear strengths at the onset of nonlinearity as a function of temperature.*

Figure 12. *Average shear strengths at maximum load capacity as a function of temperature.*

strength at high temperature, however the reduction in strength was smaller in comparison with the Avimid-R systems. The shear strengths of the composites determined from the maximum loads were also affected by temperature (see Figure 12). The data presented in Figure 12 clearly demonstrate that the shear strength of the PMR-15 system at room temperature is lower than the shear strength of the Avimid-R systems. However, at high temperatures the PMR-15 system exhibits better shear strength properties in comparison.

The shear moduli of the graphite/PMR-15 composite from the thicker plate were also measured as a function of temperature. The strains were obtained using high temperature, three element rosettes mounted on the specimens in the gage section. Typical examples of the strain-applied load relationships are presented in Figure 13. The shear moduli at room temperature (25.6°C), 204.4°C and 260°C are 6.0 GPa, 3.0 GPa and 2.8 GPa, respectively. Shear strains above 260°C were not obtained because the high temperature gage encapsulant failed and the Ag

Table 1. Room and high temperature shear strength results.

| Material	Temperature (°C)	Shear Strength at Nonlinearity (MPa)	Shear Strength at Maximum Load Capacity (MPa)
Avimid-R (warp-aligned)	24.4	109.9	143.0
Avimid-R (0/90)	24.4	109.9	164.3
Avimid-R (0/90)	24.4	119.4	156.0
PMR-15 (thicker)	26.7	117.9	121.5
PMR-15 (thicker)	204.4	96.3	111.6
PMR-15 (thicker)	204.4	81.9	100.8
PMR-15 (thicker)	204.4	84.6	101.7
Avimid-R (warp-aligned)	204.4	70.9	112.3
Avimid-R (0/90)	204.4	74.5	118.2
Avimid-R (warp-aligned)	204.4	83.9	114.7
Avimid-R (warp-aligned)	232.2	68.6	106.4
Avimid-R (0/90)	232.2	70.9	117.0
Avimid-R (warp-aligned)	232.2	67.4	108.7
PMR-15 (thicker)	260.0	87.3	102.6
PMR-15 (thicker)	260.0	66.6	93.6
PMR-15 (thicker)	260.0	65.7	95.4
Avimid-R (warp-aligned)	260.0	54.4	95.7
Avimid-R (0/90)	260.0	50.8	108.7
Avimid-R (warp-aligned)	260.0	54.4	93.4
PMR-15 (thicker)	287.8	56.7	81.0
PMR-15 (thicker)	287.8	72.0	97.2
PMR-15 (thicker)	315.6	55.8	75.6
PMR-15 (thicker)	315.6	50.4	68.4
Avimid-R (warp-aligned)	315.6	21.3	34.3
Avimid-R (0/90)	315.6	27.2	46.1
Avimid-R (warp-aligned)	315.6	24.8	37.8
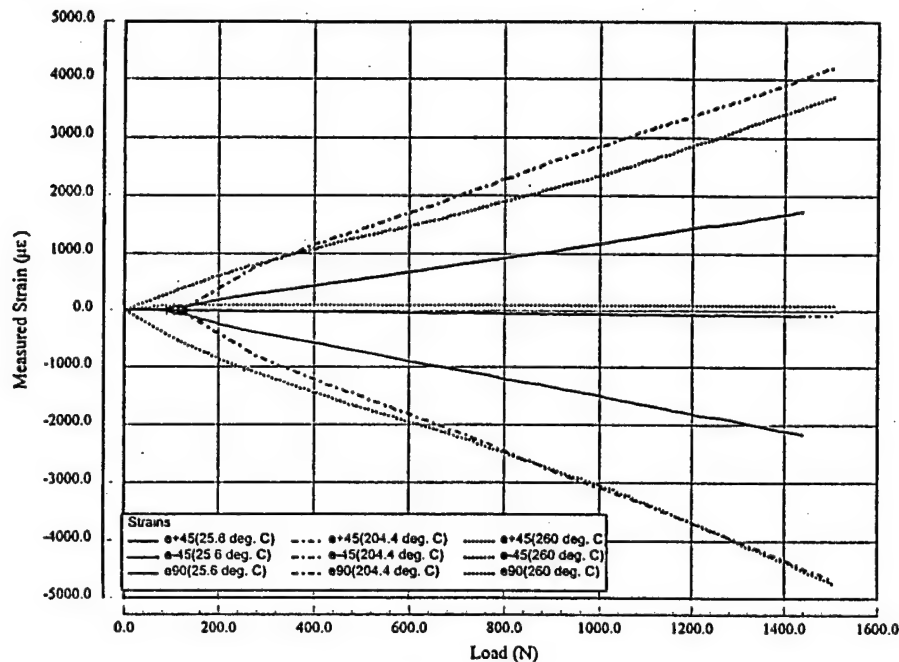
Figure 13. Typical examples of the strain-applied load relations.

gage lead solder paste oxidized, resulting in erratic strain readings. If the shear strengths of the composite for the above three temperatures (120.8 MPa, 104.7 MPa and 97.2 MPa) are compared with the shear moduli, it is evident that the reduction in the shear strength properties is significantly smaller than the reduction in the stiffness properties as a function of temperature.

In Figures 4, 9, and 10, load-displacement curves were presented for the room and elevated temperature shear and biaxial Iosipescu tests. The reason why the mechanical response of the composite as a function of temperature and loading conditions was illustrated in these diagrams in terms of the load-displacement curves instead of load-strain curves was due to severe experimental difficulties caused by the decoupling of the strain gages from the specimens at large applied displacements and elevated temperatures. Because of the out-of-plane deformation (bulging) of the specimens at high loads it was impossible to determine the complete load-strain curves under the above loading conditions.

DAMAGE AND FAILURE MECHANISMS

Room Temperature Tests

The deformation and failure processes in the graphite/PMR-15 Iosipescu speci-

mens were vastly different compared to the graphite/Avimid-R specimens. More-over, the failure process in the specimens cut from the thinner and thicker plates appeared to be different as well. There are also slight differences between these properties determined by testing the warp-aligned and 0°/90° graphite/Avimid-R specimens. As far as both PMR-15 systems are concerned, the micro-failure process starts from the initiation of interlaminar cracks with some evidence of intralaminar and translaminar cracking. This leads to the formation of large delaminations within the gage section of the Iosipescu specimens. These delaminations are especially large in the case of the specimens cut from the thinner plate. At some point, one of the interlaminar cracks propagates catastrophically along the sample, causing the trigger previously shown. These large damage zones lead to significant and permanent out-of-plane deformation (bulging) on the surfaces of the specimen. Figures 14a–14f illustrate the sequence of events leading to bulging and in-plane kinking as a specimen is loaded. This effect is more pronounced under shear-compression loading conditions since large compressive, in-plane stresses generated within the gage section will create opening displacements at the tip of an interlaminar crack, thereby making the entire failure process easier. This might explain why the maximum loads decrease as the specimens are loaded under the shear-compression loading conditions. Conversely, we can expect the process to become more difficult in shear-tension due to crack closure. The formation of the interlaminar cracks and large delaminations appear to be sig-
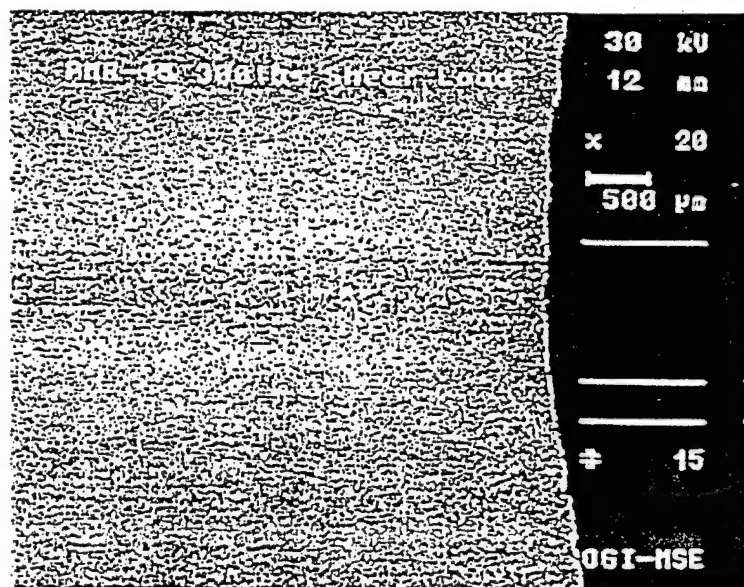

Figure 14a. Damage zone development at the notch root of graphite/PMR-15 (thinner) at 1334 N.
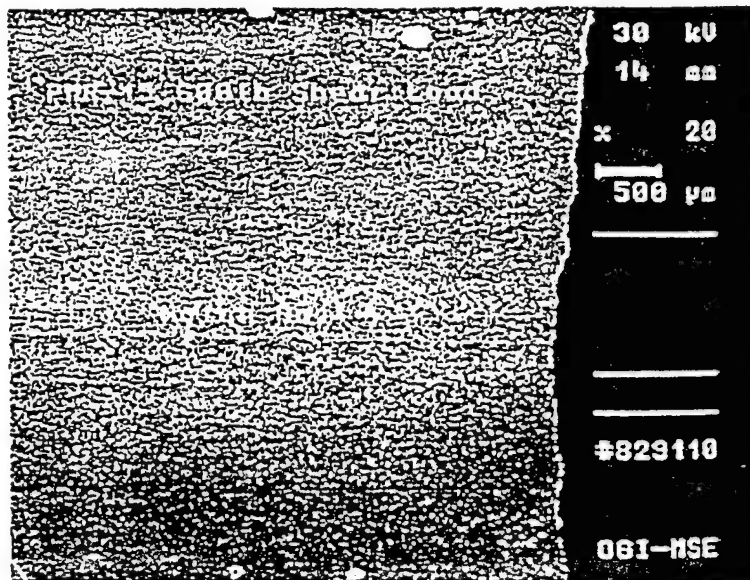
Figure 14b. Damage zone development at the notch root of graphite/PMR-15 (thinner) at 2669 N.
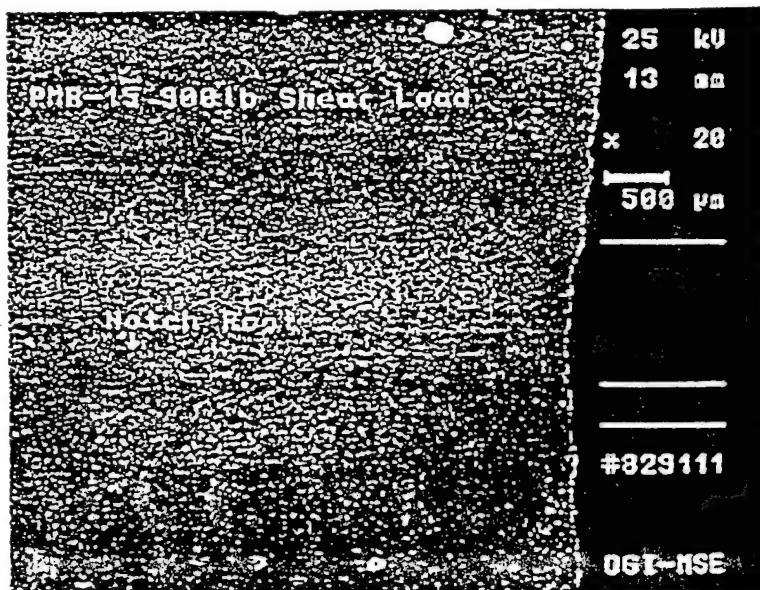

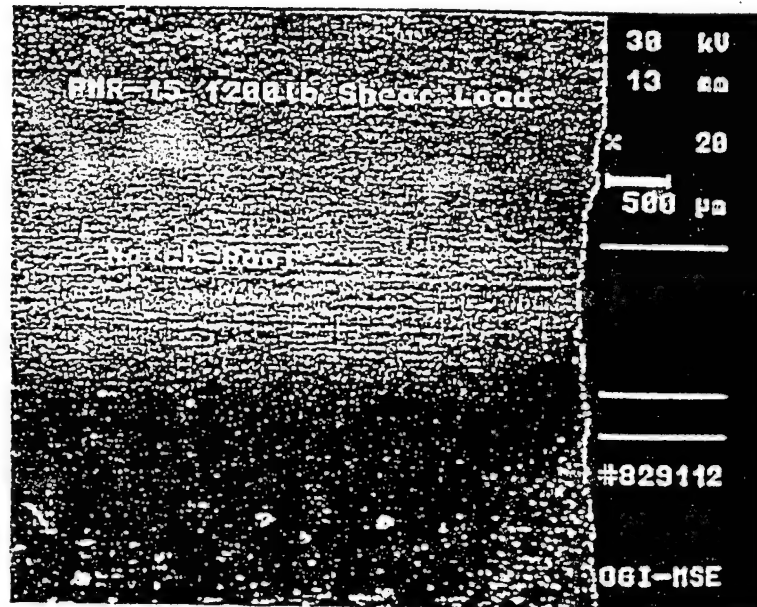*Figure 14c. Damage zone development at the notch root of graphite/PMR-15 (thinner) at 4003 N.*

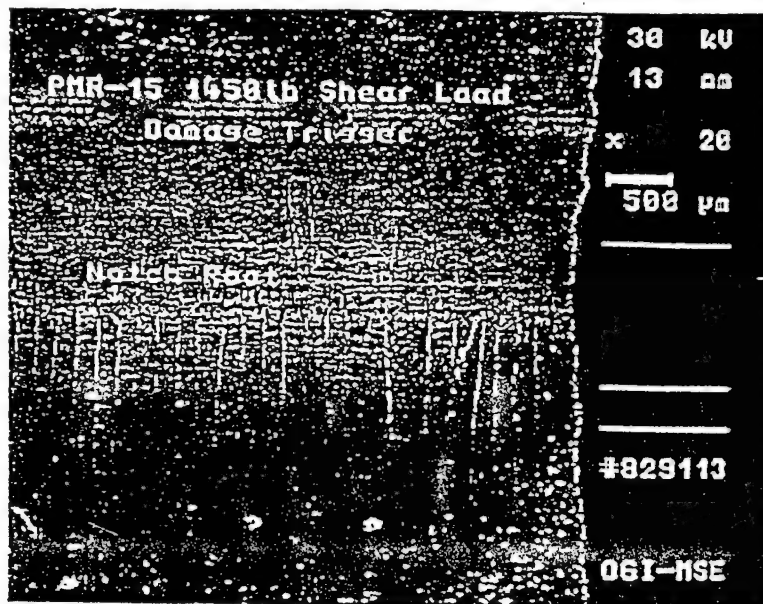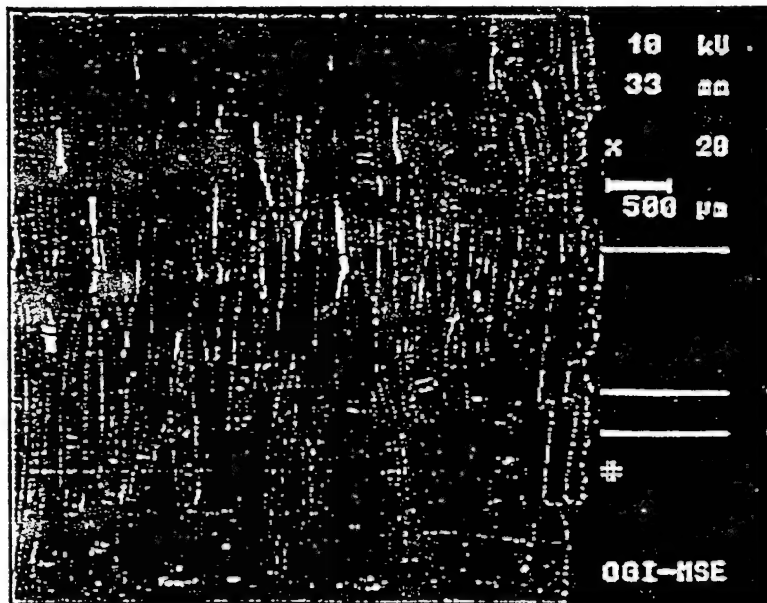*Figure 14d.* Damage zone development at the notch root of graphite/PMR-15 (thinner) at 5338 N.

Figure 14e. Damage zone development at the notch root of graphite/PMR-15 (thinner) at 6450 N.

Figure 14f. *Damage zone development at the notch root of graphite/PMR-15 (thinner) at max load.*

nificantly constrained due to perhaps significantly higher interlaminar fracture toughness properties of the material in the thicker plate. In this case, the sudden drops at the maximum loads were not observed.

The micro-failure process that determines the failure of the Avimid-R system is the formation of intralaminar cracks along the notch root axis (see Figure 15). The second mechanism is the ensuing formation of interlaminar cracks (see Figure 16). These interlaminar cracks start forming at "the knee." Since this composite appears to have very good interlaminar fracture properties (Avimid-R matrix G_{IC} = 1.0 kJ/m^2 versus PMR-15 matrix G_{IC} = 0.3 kJ/m^2), the interlaminar failure process is not as severe as exhibited by the PMR-15 system and occurs at higher loads. Therefore, it is expected that less out-of-plane deformation would be exhibited, which was the case in this investigation.

High Temperature Tests

The morphology of the damage zones in the gage sections of the Iosipescu specimens tested at high temperatures seems to be similar to the room temperature conditions. Very similar out-of-plane permanent deformations (bulging) associated with the formation of interlaminar cracks were also observed. However, it is diffi-
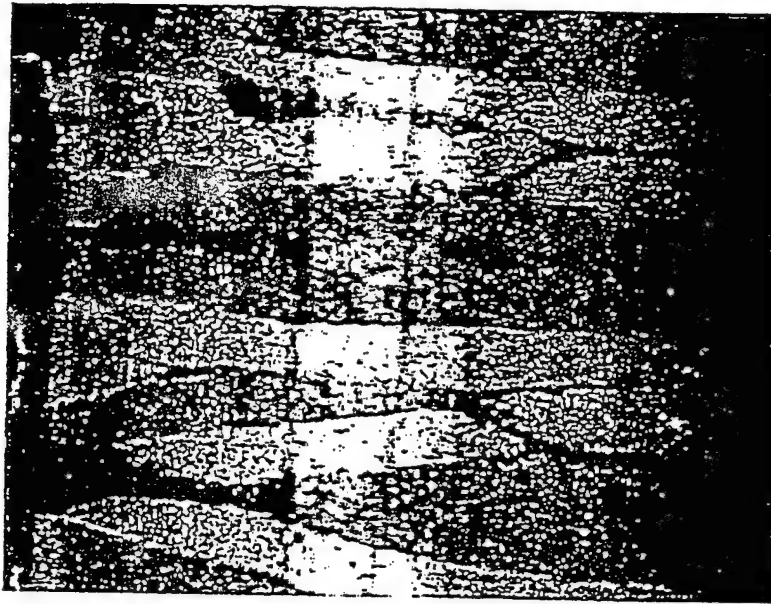
Figure 15. *Development of intralaminar cracks at the notch root in the graphite/Avimid-R composite just before the "knee."*
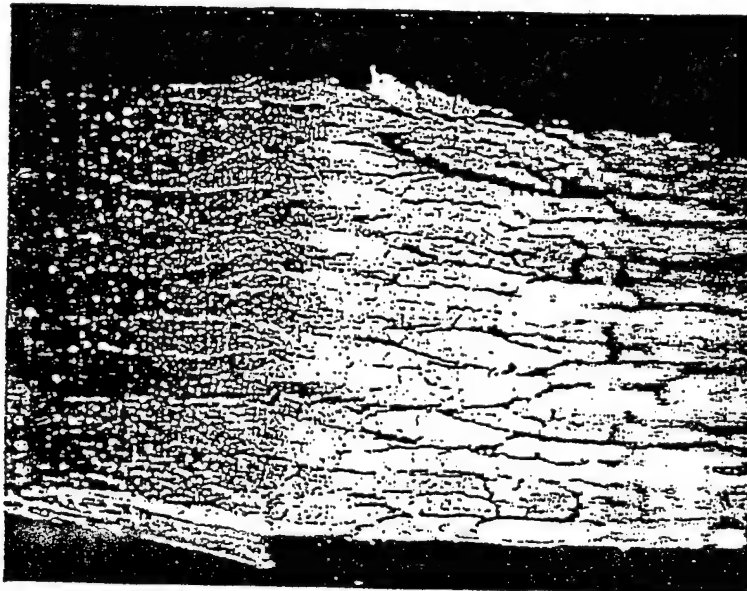

Figure 16. *Interlaminar cracking in graphite/Avimid-R near final failure.*

cult to determine at this point if the interlaminar cracking was more severe in the specimens from the high temperature experiments than in the samples tested at room temperature.

DAMAGE IMAGING

Obviously, the intralaminar and interlaminar cracks observed in both the graphite/PMR-15 and graphite/Avimid-R Iosipescu specimens tested at room temperature have to be initiated somewhere. To determine damage initiation location, an efficient method needs to be used to look beneath the specimen surface. In this investigation, individual, through-thickness slices were removed from a graphite/PMR-15 Iosipescu specimen tested in shear (from the thinner plate) and examined qualitatively for the development of damage. Two-dimensional damage maps were generated by applying a low-pass smoothing filter to SEM images of each slice in conjunction with a 3×3 median (rank) filter to establish an outline for each area of detected damage, i.e., determined via contrast changes. For this study, 3×3 kernels of the form:

$$\begin{bmatrix} 1 & 1 & 1 \\ 1 & 1 & 1 \\ 1 & 1 & 1 \end{bmatrix} \text{ or } \begin{bmatrix} 1 & 1 & 1 \\ 1 & 4 & 1 \\ 1 & 1 & 1 \end{bmatrix}$$

$$(3)$$

$$\hat{X}_{ij} = \text{median}\{X_{i'j'} : (i', j') \in W(i, j)\}$$

were assumed to remove noise from one-dimensional or two-dimensional signals while preserving image information content. The two-dimensional median filter defined in Equation (3), where $W(i,j)$ reflects centering of the filter window at image coordinates (i,j), essentially allows for sorting of a 3×3 pixel neighborhood and replacement by a median. This suppresses image noise, improves thresholding and yields a consistent estimation of crack edges.

Once edge detection was complete, each map of damage was stacked on top of another in the reverse order that each slice was removed from the specimen. Figure 17 represents a stack average of the damage removed from an area approximately 9 mm^2 at the center. This process was also applied to an untested sample to determine whether or not polishing to remove slices was responsible for some of the damage shown in the map. As Figure 18 illustrates, it is evident that mechanical polishing had little or no effect on causing significant additional damage. The darker areas located on the map mostly likely represent undulated resin-rich pockets and/or in situ manufacturing voids.
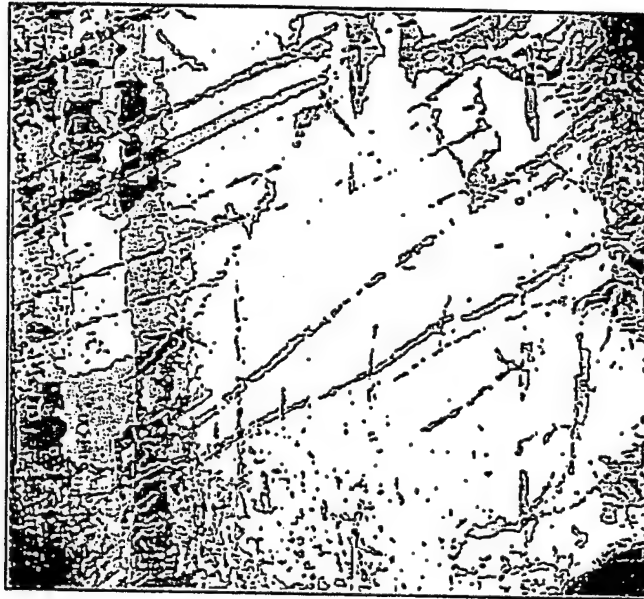
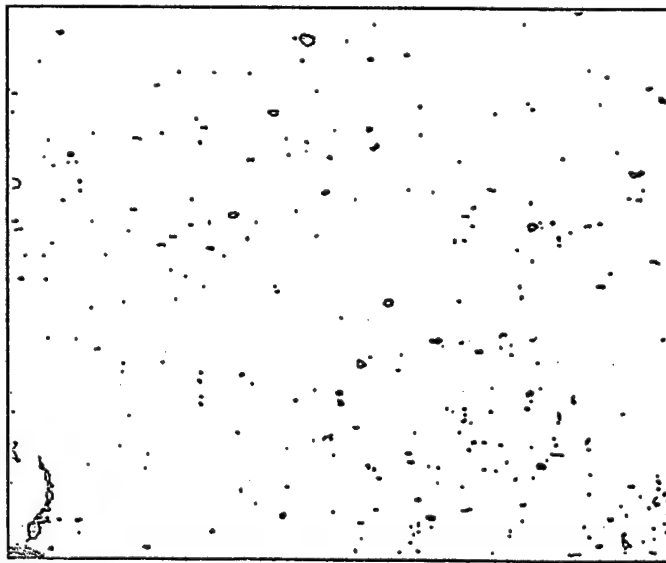**Figure 17.** Two-dimensional damage map of shear tested graphite/PMR-15 specimen center.

Figure 18. Two-dimensional damage map of untested graphite/PMR-15 specimen center.

Before shear testing occurred, the woven bundles were oriented orthogonally along both the long and notch root axes of the specimen. Due to the large shear stresses generated during the Iosipescu shear test, bundle rotation took place in the middle portion of the specimen, with the final bundle orientation being approximately 45° with respect to the notch root axis. It is quite possible that the diagonal shaded areas shown on the map in Figure 17 represent a combination of intralaminar failures at the fiber bundle-matrix interfaces and failure at weave (warp/fill) undulations or crimps. Very little cracking is evident in the direction parallel to the long axis of the specimen and vertical cracks (damage zones) dictated by much larger areas appear to represent the interlaminar failure process. It is also possible that one of the vertical cracks could be associated with triggers similar to those shown in Figure 4. Here, it is initially assumed that the shearing response forces the bundles to rotate and fail at the undulations as progressive intralaminar damage develops.

During the shearing process, the ends of the specimen simultaneously shift toward the center and kinking occurs. At some critical point, governed by the interlaminar fracture toughness, damage development and crack propagation is so catastrophic that both specimen faces bulge away from the center and the process alternates from a Mode II dominated, mixed-mode behavior to a Mode I dominated, mixed-mode behavior. This seems to be the case of the specimens from the thinner PMR-15 plate. The newly developed damage analysis technique used here can also be applied to various fabric composite systems tested in different environments.

FINITE ELEMENT COMPUTATIONS

In practice, the in-plane shear response of most composite materials exhibits severe nonlinearity. The nonlinearity is usually attributed to the plastic deformation of the matrix. However, it is possible that this response could be partly composed of the geometric nonlinearities, i.e., large rotations and displacements as well as boundary contact nonlinearities such as specimen sliding along the loading blocks in the biaxial Iosipescu fixture. These nonlinear effects could be especially well pronounced in the Iosipescu specimens tested under large displacements. Since the fabric graphite-polyimide composites investigated in this research fail at large displacements, especially under biaxial loading conditions, these nonlinear effects must be numerically investigated and their influence established on the stresses in the Iosipescu specimens and thus, the failure process of the composites.

An attempt was made in this study to evaluate the effects of specimen sliding and geometric nonlinearity (due to the change of specimen geometry) on the global mechanical response and internal stresses/strains of the graphite-polyimide Iosipescu specimens subjected to shear, shear-tension and shear-compression. The nonlinear material behavior was not considered in this research due to the lack

of appropriate constitutive equations for the materials studied. The finite element computations were conducted assuming that the specimens were loaded in the biaxial fixture with the short loading blocks and the modified fixture with the long loading blocks similar to the ASTM standard D5379/D5379M-93. The specimens were subjected to external displacements up to 3 mm. Since the failure of the specimens occurs at significantly higher displacements (up to 7 mm) for larger loading angles, the computations should have been performed with the displacements matching the experimental results. However, due to very high computation times required for convergence of these very large deformation cases, the finite element analyses in this study are restricted to prescribed displacements of 3 mm.

Two finite element models were considered. The first model is the standard linear elastic model of the Iosipescu specimen loaded by prescribed displacements [Figure 19(a)]. In this model the right side of the specimen is loaded by prescribed vertical displacements on the loading blocks, whereas the loading blocks on the left side of the specimen are constrained against any vertical displacements. This model assumes free axial movements of the specimen along x together with the loading blocks, which are perfectly bonded to the specimen. Since the loading blocks are not constrained against the movements in the x-direction this model simulates free sliding of the specimen along x with zero friction. It should be mentioned here that the linear model with the vertical prescribed displacements and vertical constraints is not suitable for the linear elastic finite element analyses of the Iosipescu specimen under biaxial loading conditions. Only the shear loading conditions can be simulated.

The other model is nonlinear with contact elements placed between the loading blocks and the specimen [Figure 19(b)]. In this model, the specimen center is constrained against vertical and horizontal displacements (u_x and u_y are zero). The blocks on the right side of the specimen have prescribed displacements of $-u/2$ whereas the blocks on the opposite side of the specimen are loaded by the positive displacements of the same magnitude. Thus, the total prescribed displacement acting on the specimen is equal to u. Using these boundary conditions, the effect of specimen rotation can be investigated with sliding and geometric nonlinearity by resolving the displacements into components [28–29].

In the above models, the thickness of the specimen was assumed to be 1 mm and the loading blocks were assumed to be homogeneous and made from steel. The material properties of the Iosipescu specimens investigated in this study are presented in Table 2. The finite element computations were performed on a dual processor, Intel Pentium Pro™, 180 MHz configuration using ANSYS 5.3 and two-dimensional FEM representations of the Iosipescu specimens were constructed using six-noded triangular and eight-noded quadrilateral isoparametric elements as shown in Figures 20(a) and 20(b). The frictional interfaces between the loading blocks and the specimen were modeled using two-dimensional point-to-surface contact pseudoelements. Along the specimen-to-fixture contact
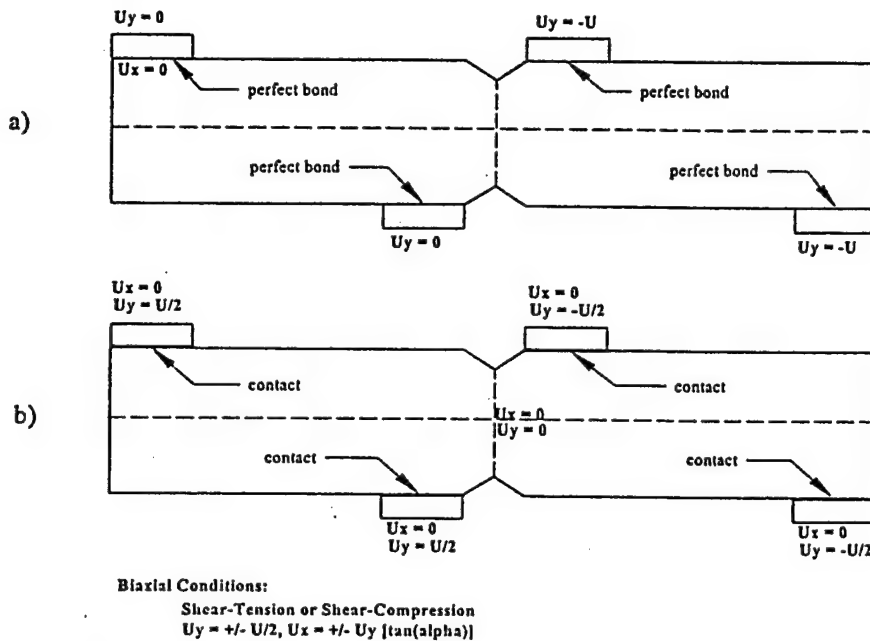
a) Uy = 0 | Ux = 0 | perfect bond | Uy = -U | perfect bond | Uy = 0 | perfect bond | perfect bond | Uy = -U

b) Ux = 0, Uy = U/2 | contact | Ux = 0, Uy = -U/2 | contact | Ux = 0, Uy = 0 | contact | contact | Ux = 0, Uy = U/2 | Ux = 0, Uy = -U/2

Biaxial Conditions:
Shear-Tension or Shear-Compression
Uy = +/- U/2, Ux = +/- Uy [tan(alpha)]

Figure 19. *Boundary conditions used in the finite element computations: (a) linear elastic case and (b) nonlinear case.*

regions, a Coulomb friction model was assumed, allowing both sticking and sliding conditions.

The numerical load-displacement diagrams for the Iosipescu specimens loaded in shear in the biaxial and modified biaxial fixtures are presented in Figure 21. The global loads were calculated from the normal and shear reactions on the loading blocks as a function of the prescribed displacement for a friction coefficient of 0.3. The mechanical response of the specimen was determined from the linear elastic finite element model with zero friction and the nonlinear model with contact elements. It can be seen that the effect of specimen sliding and geometric nonlinearities on the load displacement diagrams is almost insignificant for prescribed displacements up to 3 mm. However, this cannot be said for specimen deformation and internal stresses.

Table 2. *Elastic properties used in finite element computations.*

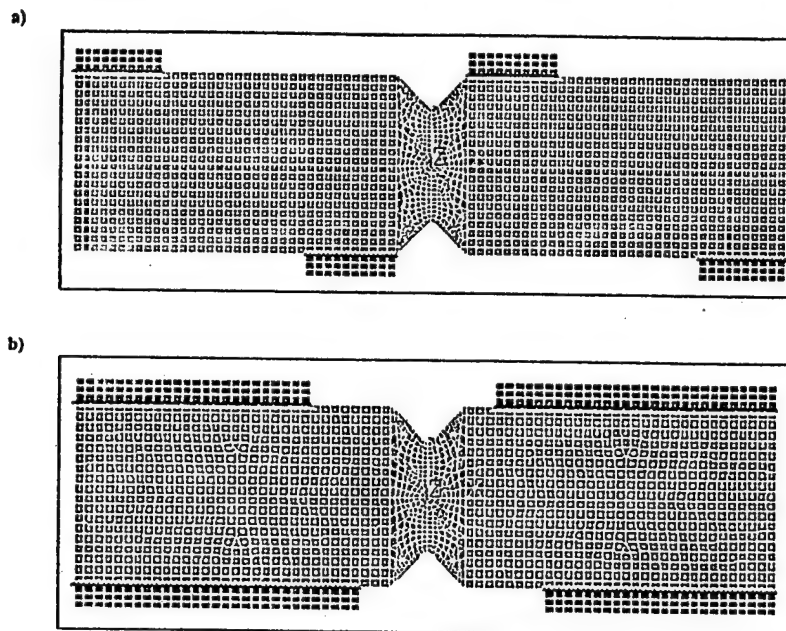| Properties	Specimen Properties				Loading Block		
Model	E_x (GPa)	E_y (GPa)	G_{xy} (GPa)	v_{xy}	E_x (GPa)	G_{xy} (GPa)	v_{xy}
Biaxial Fixture	79.0	79.0	7.50	0.15	400	400/2(1 + 0.30)	0.30
Modified Biaxial Fixture	79.0	79.0	7.50	0.15	400	400/2(1 + 0.30)	0.30

a)

b)

Figure 20. Finite element meshes of Iosipescu specimens: (a) short loading blocks (biaxial fixtures) and (b) long loading blocks (modified biaxial fixture).
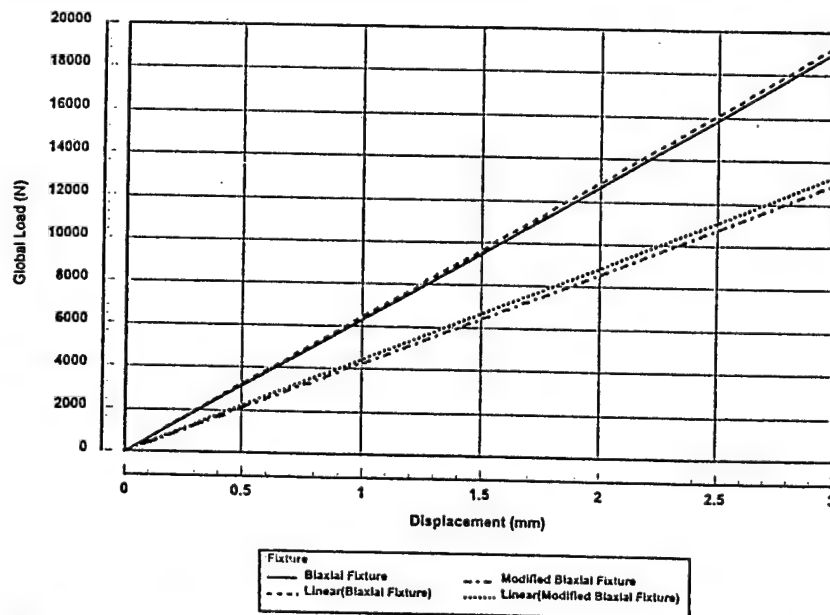

Figure 21. Simulated load-displacement diagrams for the Iosipescu specimens loaded in shear in the biaxial and modified biaxial fixtures.

Table 3. Internal stresses at specimen center.

Iosipescu Models	Displacement (mm)	Nonlinear Iosipescu Models				Linear Elastic			
		σ_X (MPa)	σ_Y (MPa)	τ_{XY} (MPa)	P/A (MPa)	σ_X (MPa)	σ_Y (MPa)	τ_{XY} (MPa)	P/A (MPa)
Biaxial Iosipescu Fixture	1	−14.5	−183.1	−500.5	−526.3	5.7	−147.2	−530.8	−557.7
	2	25.5	−430.0	−1019.4	−1073.4	11.4	−294.4	−1061.6	−1115.5
	3	116.3	−726.7	−1537.3	−1619.4	17.2	−441.6	−1592.4	−1673.1
Modified Biaxial Iosipescu Fixture	1	−22.9	−183.1	−323.7	−307.9	7.9	−27.9	−365.5	−353.1
	2	−25.3	−72.4	−648.9	−614.0	15.7	−55.8	−731.0	−706.2
	3	−16.6	−104.6	−969.2	−910.7	23.6	−83.7	−1096.5	−1059.3

In Table 3, the internal stresses at the specimen center for the two finite element models loaded in shear with 1 mm, 2 mm and 3 mm prescribed displacements are shown. In addition, the shear stresses are calculated from the global reaction force P via dividing the total global reaction by the cross-sectional area of the specimen. The nonlinear effects, sliding and geometric nonlinearities, have a marginal influence on the internal shear stresses at the specimen center for both models. However, the normal stresses, especially the tensile stress σ_{11}, seem to be significantly affected. There is good agreement between the shear stresses determined from the reaction forces and the stresses at the specimen center. It can be seen that the compression along the notch root axis σ_{22} in the biaxial fixture is high, almost 50% of the shear stress along the notch root axis. The compression is smaller in the modified biaxial model with the longer loading blocks. This is not surprising since the long loading blocks in the Iosipescu shear test, according the ASTM standard, were designed to reduce the compression caused by the loading blocks. In this case, the compression is about 10% of the shear stress. Since the failure process in the Iosipescu graphite/polyimide fabric composites is predominantly interlaminar in nature, the in-plane compression along the notch root axis would enhance the failure process. The interlaminar cracks in the specimen could initiate and propagate easier in the presence of the compression and thus reduce the loads at failure (both the loads at the onset of significant damage and the maximum loads).

It can be expected that the stresses in the Iosipescu specimen will change if the specimen is rotated either towards shear/tension or shear/compression. The numerical load-displacement diagrams, derived from the non-linear model for various loading angles, are presented for the biaxial and modified biaxial fixture in Figure 22. In addition, the internal stresses in the center of the specimens are shown in Figure 23 and Figure 24 for three different prescribed displacements (1 mm, 2 mm, and 3 mm). It is clearly evident that the loading angle affects the mechanical response of the specimen similar to the experimental results shown in Figure 4. What is more important is the fact that the stresses in the specimen loaded in the biaxial fixture with the short loading blocks are always biaxial and large compressive stresses are always present in the gage section, despite the angle of applied load. The tensile stress component σ_{11} increases only slightly if the specimen is rotated towards larger shear-tension loading angles. Moreover, the ratios of shear-tension and shear-compression seem to be unaffected by magnitude of the applied displacement.

Examination of the stresses at the specimen center, as a function of the loading angle, for a specimen loaded in the fixture with long loading blocks reveals that the normal compressive stress σ_{22} can be entirely eliminated if the specimen is loaded at an angle somewhere between 15–20° shear-tension. At this angle, the stress field in the specimen gage section is almost pure shear with only a small tensile stress component, which is almost insignificant in comparison with the shear stress. These small in-plane tensile stresses should not affect the failure process in
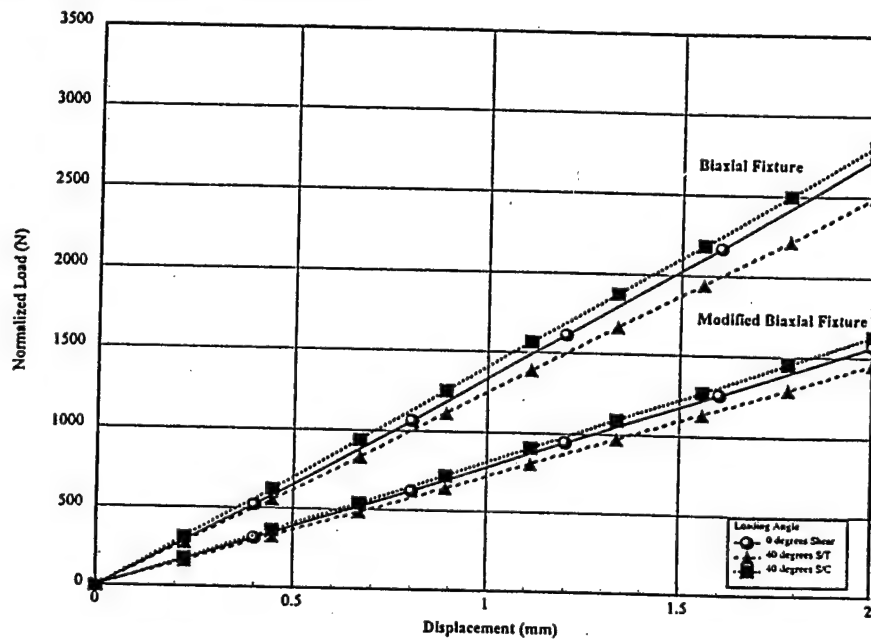
Figure 22. Simulated load-displacement diagrams of graphite/PMR-15 Iosipescu specimens under biaxial conditions.
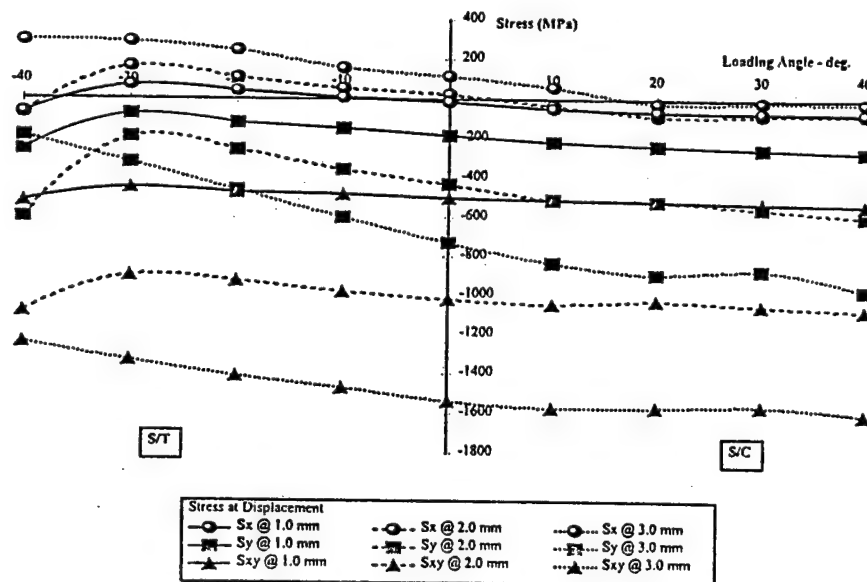

Figure 23. Stresses at specimen center from biaxial Iosipescu model as a function of the loading angle for three different displacements (1 mm, 2 mm, 3 mm).
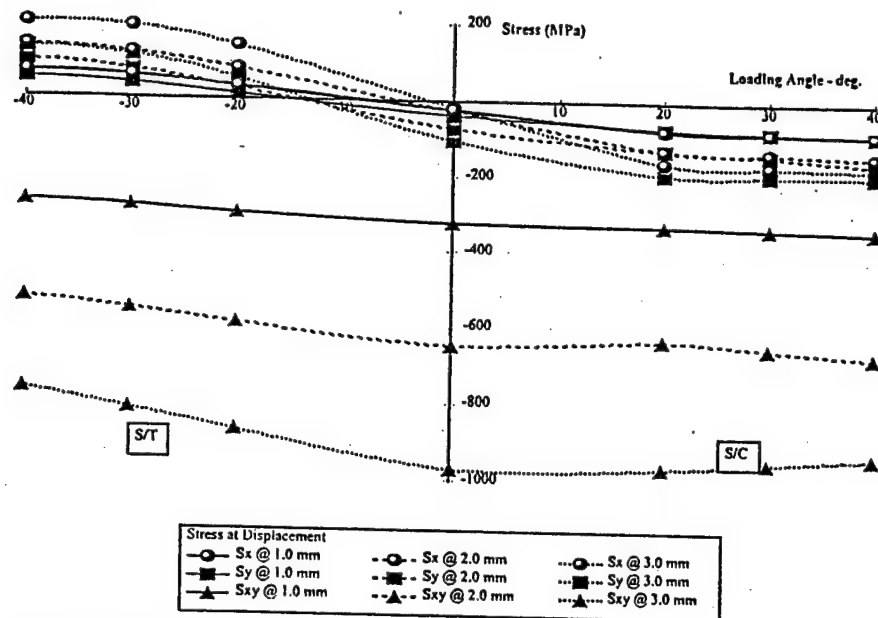
Figure 24. *Stresses at specimen center from modified biaxial Iosipescu model as a function of the loading angle for three different displacements (1 mm, 2 mm, 3 mm).*

the fabrics. Therefore, it can be concluded that by loading the specimen in the modified biaxial fixture at an angle above −15°, the specimen gage section will develop a superlative shear stress field.

It should be pointed out that the nonlinear finite element computations were restricted to 3 mm displacements. Under certain biaxial loading conditions, some of the specimens failed at displacements beyond the prescribed 3 mm. At this point, it can only be assumed that the impact of this limitation on understanding the failure process of the fabric Iosipescu specimens is trivial.

EFFECT OF THE LOADING BLOCKS ON THE FAILURE PROCESS

The biaxial Iosipescu fixture employs short loading blocks. It has been previously shown [24] that for this loading block geometry, large compressive stresses develop in the specimen gage section. It could be speculated that the in-plane compression along the notch root axis in the fabric Iosipescu specimens tested either in shear or under biaxial loading conditions might significantly affect the loads at failure and the failure modes in the composites investigated. In the previous section of this work, it was shown that the compression can be entirely eliminated by employing the new loading block geometry similar to the previously mentioned ASTM standard and by rotating the specimens towards the shear-tension loading

condition. This should produce an almost pure shear stress field in the fabric Iosipescu specimens.

Since the admixture of the old and new loading blocks allows different combinations of in-plane biaxial shear and compressive stress fields to be generated, we can now examine the effect of these different induced states of stress on the failure process in the PMR-15 and Avimid-R based composites. If the compression generated along the notch root axis by the short loading blocks was influential in promoting the failure process in the composites, both the loads at the onset of interlaminar damage and the maximum failure loads should increase when the longer loading blocks are employed. In this case (see Figure 24), the axial compression to shear ratio along the notch root axis is approximately 0.1 which is significantly smaller than the same ratio in the specimens loaded under the same conditions in the fixture with the short loading blocks (~0.5). Moreover, the loads at failure for the specimens tested in the modified biaxial Iosipescu fixture under shear/tension (with the loading angles about 15–20°) should be even higher since the stresses at the center of the specimen are almost pure shear without any compression along the notch root axis. The results presented in Table 4 clearly contradict the above speculations.

Table 4 shows that there are significant differences between the failure loads for the PMR-15 specimens from the thinner and thicker specimens shear tested in the fixture using the short loading blocks. These differences are most likely due to improved interlaminar strengths resulting from variation in the manufacturing process. However, if we compare the loads for the Iosipescu specimens made out of the same plate, the thicker one, the change in the shear loads at failure for the specimens tested with the new and old loading blocks is almost insignificant. The same statement can be made regarding the results for the Avimid-R samples tested under the same conditions. For these materials, the average load at the knee for the warp-aligned samples tested in shear with the short loading blocks is 4.56 kN and the average maximum failure load is approximately 6.45 kN. If we compare these loads with the loads for the same specimens tested in shear with the long loading blocks (4.89 kN and 6.56 kN), it can be immediately concluded that the effect of the compression on the failure loads is negligible. The same behavior was also observed for the 0°/90° specimens tested in shear with two different loading block geometries. In this case, the average loads at the knee and the average maximum failure loads for the short blocks are 4.55 kN and 6.75 kN, respectively whereas the same average loads for the specimens tested with the long blocks are 4.89 kN and 6.56 kN.

In conclusion, the failure modes and loads at failure are not affected by the compression generated by the inner loading blocks in the gage section of the specimens tested in shear. This is not surprising since the compressive strengths of graphite/polyimide fabric composites are always significantly greater than the shear strengths. It has been recently shown by Grape and Gupta [9] that the compressive

Table 4. Loads at the onset of nonlinearity and the maximum loads for the thinner and thicker Iosipescu specimens tested in shear using the biaxial and modified biaxial Iosipescu fixtures.

	Graphite/PMR-15 (4.82 mm)		Graphite/PMR-15 (5.15 mm)		Graphite/PMR-15 (5.15 mm)	
	Load at Onset of Nonlinearity	Max. Loading Capacity	Load at Onset of Nonlinearity	Max. Loading Capacity	Load at Onset of Nonlinearity	Max. Loading Capacity
	5826.9 N	5826.9 N	6947.8 N	7392.6 N	6502.9 N	7228.0 N
	5560.0 N	5560.0 N	6823.2 N	7539.4 N	7170.2 N	7895.2 N
	6182.7 N	6004.8 N	—	—	—	—
	6293.9 N	6293.9 N	—	—	—	—
Average Load	5964.8 N	5964.8 N	6885.5 N	7463.7 N	6836.6 N	7561.6 N
	Short Blocks Biaxial Fixture		Short Blocks Biaxial Fixture		Long Blocks Modified Biaxial Fixture	

strength of a graphite/polyimide fabric composite (8-harness ICI HMF-2474 carbon fiber cloth, 20 plies thick) tested under uniaxial compression at room temperature is approximately 600 MPa. Since the shear strengths of the composites investigated in this project are approximately 6 times lower than the compressive strength of the fabric investigated by Grape and Gupta, it is reasonable to assume that the compressive stress σ_{22} along the notch root axis (which is lower than the shear stress at the specimen center) does not contribute to the initiation of interlaminar damage, even if the short loading blocks are used. Therefore, the results presented in this paper regarding the shear strength properties of the PMR-15 and Avimid-R composites obtained using the biaxial Iosipescu fixture at room and high temperatures are valid and they are not affected by the compression from the loading blocks.

As shown in Figures 6 and 7, the failure process under shear-compression loading conditions at room temperature is dependent in the loading angle. Clearly, there is a general trend regarding the strength properties and the loading angle. Figures 6 and 7 indicate that the strength properties gradually decrease as the specimen is rotated towards shear-compression. Obviously, under shear-compression, the compressive stresses in the gage section of the specimens increase as the specimen is rotated towards larger loading angles (see Figures 23 and 24) regardless of the loading block geometry. This increase in compressive stresses due to specimen rotation within the fixture affects the failure process and thus the loads at failure.

CONCLUSIONS

1. The application of the biaxial Iosipescu technique has been successful in determining the biaxial shear dominated failure properties of graphite/polyimide woven composites at room and elevated temperatures. The biaxial strength properties of the graphite/PMR-15 and graphite/Avimid-R composites defined by the maximum load are different at room and elevated temperatures.

2. The shear strength of the Avimid-R system at room temperatures determined from the maximum load is higher than the shear strength of the PMR-15 composite. However, the shear strength properties of the graphite/PMR-15 composite at elevated temperatures are significantly better than the properties of the Avimid-R system.

3. It has been observed in this research that the onset of significant interlaminar damage can be associated with the formation of a knee on the load-displacement diagrams for the Avimid-R system. In the case of the PMR-15 system, the damage can be defined by the onset of nonlinearity on the load-displacement curves, which usually occurs just before the maximum load. It appears that the significant development of interlaminar damage in the PMR-15 system tested under biaxial conditions at room temperature occurs at

lower shear stresses in comparison with the Avimid-R based composite. At elevated temperatures, the interlaminar damage in the PMR-15 composite develops at a much higher level of shear stress than in the Avimid-R composite.

4. The mechanical properties and failure modes of the PMR-15 composite system tested at room temperature seem to be dependent on the manufacturing process. The Iosipescu specimens cut from the thinner plate exhibit significantly lower loads at failure in comparison with the specimens from the slightly thicker plate. It appears that the out-of-plane bulging in the thinner specimens is greater than in the thicker ones. Since the final failure of the specimens is associated with the formation of multiple interlaminar cracks, this might suggest that the interlaminar strength properties of the composites strongly depend on the manufacturing process.

5. The finite element computations of the Iosipescu specimens have shown that the specimens loaded in the biaxial Iosipescu fixture in shear develop large compressive stresses at the specimen center. This compression cannot be eliminated by rotating the specimens. For any biaxial loading conditions, the state of stress in the gage section of the specimens is always biaxial with large compressive stresses present along the notch root axis. It has been shown, however, that the compressive stresses generated by the loading blocks can be entirely eliminated if the longer loading blocks geometry is used in conjunction with specimen rotation toward the shear/tension loading condition.

6. The PMR-15 and Avimid-R composites have been tested using the biaxial and modified biaxial Iosipescu fixtures. Various biaxial shear-compression stress states in the specimens have been generated, based on the finite element computations, ranging from almost pure in-plane shear to shear-compression. It has been found that the effect of the large in-plane compressive stress generated by the loading blocks in the biaxial fixture do not affect the failure modes of the composites investigated under shear and shear-tension loading conditions. However, when the compressive stresses in specimen gage sections are increased due to rotation towards larger shear-compression loading angles, the room temperature strength properties of the composite decrease.

ACKNOWLEDGMENTS

REFERENCES

1. Meador, M. A., P. J. Cavano and D. C. Malarik. 1992. "High Temperature Polymer Matrix Composites for Extreme Environments," *HITEMP Review 1992*, 529–539.

2. Iosipescu, N. 1967. "New Accurate Procedure for Single Shear Testing of Metals," *Journal of Materials*. 2:537–566.

3. Adams, D. F. and D. E. Walrath. 1982. "Iosipescu Shear Properties of SMC Composite Materials," In *Composite Materials: Testing and Design (Sixth Conference)*, edited by I. M. Daniel, 19–33: ASTM STP 787.

4. Adams, D. F. and D. E. Walrath. 1987. "Current Status of the Iosipescu Shear Test Method," *Journal of Composite Materials*, 21:494–507.

5. Adams, D. F. and D. E. Walrath. 1987. "Further Developments of the Iosipescu Shear Test Method," *Experimental Mechanics*, 27:113–119.

6. Slepetz, J. M., T. F. Zagaeski and R. F. Novello. 1978. Report AMMRC TR 78-30. Watertown, MA: Army Materials and Mechanics Research Center.

7. Walrath, D. E. and D. F. Adams. June 1983. *Analysis of the Stress State in an Iosipescu Shear Test Specimen*. Report UWME-DR-301-102-1. Laramie, Wyoming: Department of Mechanical Engineering, University of Wyoming.

8. Owens, G. A. and S. E. Schofield. 1988. "Thermal Cycling and Mechanical Property Assessment of Carbon Fibre Fabric Reinforced PMR-15 Polyimide Laminates," *Composites Science and Technology*, 33:177–190.

9. Grape, J. A. and V. Gupta. 1995. "Failure in Carbon/Polyimide Laminates under Biaxial Compression," *Journal of Composite Materials*, 29:1850–1872.

10. Mirzadeh, F. and K. L. Reifsnider. 1992. "Micro-deformations in C3000/PMR15 Woven Composite," *Journal of Composite Materials*, 26:185–205.

11. Naik, N. K., P. S. Shembekar and M. V. Hosur. 1991. "Failure Behavior of Woven Fabric Composites," *Journal of Composites Technology & Research*, 13:107–116.

12. Ho, H., M. Y. Tsai, J. Morton and G. L. Farley. March 1994. "In-Plane Shear Testing of Graphite-Woven Fabric Composites," *Experimental Mechanics*, 45–52.

13. Walsh, T. J. and O. O. Ozden. 1996. "Analytical and Experimental Mechanics of Woven Fabric Composites," *Mechanics of Composite Materials and Structures*, 3:133–152.

14. Ifju, P. G. 1995. "Shear Testing of Textile Composite Materials," *Journal of Composites Technology & Research*, 17:199–204.

15. Ifju, P. G., P. G. Masters and W. C. Jackson. 1995. "The Use of Moiré Interferometry as an Aid to Standard Test-Method Development for Textile Composite Materials," *Composites Science and Technology*, 53:155–163.

16. Ifju, P. G. 1991. "The Shear Gage: For Reliable Shear Modulus Measurements of Composite Materials," *SEM Proceedings Conference*, 1–10, Department of Engineering Science and Mechanics.

17. Broughton, W. R. 1989. "Shear Properties of Unidirectional Carbon Fibre Composites," Ph.D. Dissertation, University of Cambridge.

18. Kumosa, M. and D. Hull. 1987. "Mixed-mode Fracture of Composites using the Iosipescu Shear Test," *International Journal of Fracture*, 35:83–102.

19. Broughton, E. R., M. Kumosa and D. Hull. 1990. "Analysis of the Iosipescu Shear Test as Applied to Unidirectional Carbon-Fiber Reinforced Composites," *Composites Science and Technology*, 38:299–325.

20. Bansal, A. and M. Kumosa. 1995. "Experimental and Analytical Studies of Failure Modes in Iosipescu Specimens under Biaxial Loadings," *Journal of Composite Materials*, 29:334–358.

21. Sukumar, N. and M. Kumosa. 1992. "Finite Element Analysis of Mixed Mode Fracture and Failure in Iosipescu Specimens," *International Journal of Fracture*, 58:177–192.

22. Bansal, A. and M. Kumosa. 1995. "Application of the Biaxial Iosipescu Method to Mixed-Mode Fracture of Unidirectional Composites," *International Journal of Fracture,* 71:131–150.

23. Ho, H., J. Morton and G. Farley. "Non-linear Numerical Analysis of the Iosipescu Specimen for Composite Materials," *Composites Science and Technology,* 50:355–365.

24. Searles, K., V. Thirumalai, M. V. Balakrishnan and M. Kumosa. 1995–1996. Annual Progress Report. "Biaxial Failure Analysis of Graphite Reinforced Polyimide Composites," Portland, OR and Denver, CO: Department of Materials Science and Engineering, Oregon Graduate Institute of Science and Technology. Center for Advanced Materials and Structures, University of Denver.

25. Kumosa, M., K. H. Searles and G. Odegard. 1997."Biaxial Failure Analysis of Graphite Reinforced Polyimide Composites," *HITEMP Review 1997,* Paper 18:1–11.

26. Searles, K., J. McCarthy and M. Kumosa. 1997. "An Image Analysis Technique for Evaluating Internal Damage in Graphite/Polyimide Fabric Composites," *Composites Science and Technology,* accepted for publication.

27. Tsai, C. L. and I. M. Daniel. 1991. "Determination of In-Plane and Out-of-Plane Shear Moduli of Composite Materials," *Experimental Mechanics,* pp. 295–299.

28. Kumosa, M. and Y. Han. "Non-Linear Finite Element Analysis of Iosipescu Specimens," submitted to *Journal of Composites Science and Technology,* Sept. 1997.

29. Han, Y. Finite Element Analyses of Advanced Composite Structures, MS Thesis, Department of Engineering, University of Denver, November 1997.

Au. updates?

Non-Linear Analysis of Woven Fabric-Reinforced Graphite/PMR-15 Composites Under Shear-Dominated Biaxial Loads

G. Odegard*, K. Searles**, and M. Kumosa*

**Center for Advanced Materials and Structures
Department of Engineering
University of Denver
2390 South York, Denver, CO 80208, USA*

***Department of Materials Science and Engineering
Oregon Graduate Institute of Science & Technology
PO Box 91000, Portland, OR 97291-1000*

Abstract

An elastic-plastic, time-independent, macroscopic, homogenous model of a 8HS woven graphite/PMR-15 composite material has been developed that predicts the non-linear response of the material subjected to shear-dominated biaxial loads. The model has been used to determine the response of woven composite off-axis and Iosipescu test specimens in non-linear finite analyses using a multi-linear averaging technique. The numerically calculated response of the specimen was then compared to experimentally obtained data. It has been shown that the numerically calculated stress-strain diagrams of the off-axis specimens are very close to the experimentally obtained curves. It has also been shown that the numerically determined shear stress-strain and load-displacement curves of the woven Iosipescu specimens are close to the experimentally obtained curves up to the point of significant interlaminar damage initiation and propagation. The results obtained in this study clearly demonstrate that the non-linear material behavior of the graphite/polyimide woven composites subjected to shear-dominated biaxial loading conditions cannot be ignored and should be considered in any stress analysis. The linear-elastic approach grossly overestimates the loads and stresses at failure of theses materials in the

off-axis and Iosipescu tests. It can be assumed that the same discrepancies will arise in the numerical analysis of the woven composites tested under other biaxial shear-dominated loading conditions using other biaxial test methods.

1. Introduction

High temperature polymer matrix composites are finding an increasing use in the electronics and aerospace industries. The main advantage of using these materials is the high specific strength that they can achieve at room and elevated temperatures (up to 670° F). One of the premier high temperature polymer resin systems is PMR-15, which is a thermosetting polyimide that is primarily used in aircraft structures. PMR-15 offers a combination of relatively good thermal-oxidative stability, processability, mechanical properties, and cost [1]. The constituent monomers are soluble in easily removed solvents such as methanol, which makes the impregnation of the fiber reinforcement relatively easy [2].

Cloth based graphite/polyimide composites effectively translate stiff, strong yarns (bundles of 10^3-10^4 fibers) into stiff, strong composites. The satin weave pattern is defined by the number of yarn widths between exchanges and these exchanges are arranged so as not to connect. The 8-Harness satin weave (8HS) has a 7-over, 1-under pattern (Figure 1). Of all 2D weave patterns, the 8HS is of particular interest since the float is long and exchanges are minimized. The 8HS woven architecture exhibits good conformability (drape) over complex surfaces. However, conformability and resistance to shear and shear-dominated biaxial in-plane loading conditions tend to be inversely related [3,4].

A major limitation of many fabric fiber/polymer matrix composite systems is the inability of these materials to resist intralaminar and interlaminar damage initiation and propagation under shear-dominated biaxial loading conditions. Since it is essential to have a reliable database of mechanical properties for the successful application of 8HS fabric Graphite/PMR-15 composites, their response to these loading conditions must be fully investigated. The purpose of this research is to quantitatively investigate the non-linear behavior (elastic-plastic) of this material under shear-dominated biaxial loading conditions using a macroscopic approach. It will be

2

assumed that the 8HS woven fabric composite is a quasi-isotropic homogeneous material. This approach will provide a model in which microscopic models may be compared to in future research. A mathematical constitutive model has been developed to represent the time independent elastic-plastic properties of this material based on the off-axis tensile tests. This model will then be applied to the numerical determination of the stresses in the off-axis and Iosipescu shear tests (both of which create a biaxial stress state in the material).

The Iosipescu shear test, which was originally intended for determining shear properties of metals [5], was first applied to composite materials by Adams and Walrath [6,7]. The original design of the fixture was then modified to reduce large compressive stresses generated in the gage section of the specimen [8,9]. The modified Wyoming Iosipescu shear test has become one of the most popular test methods for the shear characterization of composite materials, and has become an ASTM standard [10]. Since 1994, a series of papers has outlined the non-linear effects in the Iosipescu shear test that affect the shear strength determination. Ho et al. [11] showed the effects of geometric, boundary contact, and material non-linearities using non-linear finite element techniques. However, they determined the boundary contact and material non-linearities of unidirectional composites based on a non-experimental parametric study, which lead to questionable results. Kumosa and Han [12] and Odegard et al. [13] investigated the effect of boundary contact and geometric non-linearities involved in the Iosipescu shear test. In particular, Odegard and Kumosa [14] investigated the effect of material non-linearity on the mechanical behavior of unidirectional composites subjected to the Iosipescu test. They showed that the Iosipescu specimen response (load-displacement and load-strain curves) can be determined accurately only if the actual elastic-plastic properties of a unidirectional composite are experimentally determined and then used in a finite element model.

Very little research has been performed on the testing of woven fabric composites with the Iosipescu shear test [3,15]. Searles et al. [3] experimentally investigated 8HS graphite/PMR-15 composite Iosipescu specimens at room and elevated temperatures. They also introduced a finite element model of the Iosipescu specimen made of this material. The model assumed boundary contact and geometric non-linearities. The effect of material plasticity on the response of the specimens was not considered at that time due to the lack of a reliable material non-linearity

3

model. In order to accurately model the Iosipescu shear test of fabric composite specimens from a homogeneous approach, the actual macroscopic elastic-plastic properties need to be determined and used in a finite element model, as shown by Odegard and Kumosa [14] in their study of unidirectional graphite/epoxy composites subjected to the Iosipescu test.

Many researchers have successfully performed the calculation of elastic and plastic properties of unidirectional polymer matrix composites [16-18]. However, the determination of mechanical properties of woven fabric composites using experimental uniaxial/biaxial tests has been limited [19-22]. A few published attempts have been made to apply a macroscopic continuum approach to determine the plastic behavior of woven fabric composites. Vaziri *et al.* [23] suggested a plasticity model for bi-directional composite laminates that requires the knowledge of the axial and shear yield strengths, which can be difficult to define and to obtain experimentally for composite materials. Also, their model provides only a bi-linear approximation of plastic properties. Naik [24] suggested using an empirical relationship between shear stress and shear strain, however this type of approach cannot be generalized for different fiber architectures (e.g. unidirectional composites and 3-dimensional composites). The theory proposed below assumes the presence of inelastic deformation at very small shear stresses (which has been experimentally verified) instead of assuming known shear strength values. In addition, the axial strengths of the composites are unnecessary. The resulting constitutive equation in shear is a continuous power-law type curve. The assumptions used in formulating the theory proposed herein can be easily changed to describe the inelastic deformation of other fiber architectures.

In this paper, off-axis tensile testing will be used to characterize the time-independent elastic-plastic properties of the 8HS graphite/polyimide composite. These properties describe the behavior of the material under any multi-axial loading condition. Therefore, they can be directly applied (numerically or analytically) to determine the response of any structure made of this material. In the next stage, the elastic-plastic model will be applied to determine the response of the 8HS graphite/polyimide Iosipescu specimens. It is highly desirable to numerically apply this approach to the Iosipescu problem since it represents a case where the same material is subjected to shear-dominated biaxial stresses, and therefore offers an excellent opportunity to verify the plasticity model.

4

2. Plasticity Theory

Yield Function:

The theory proposed below is an extension of Hill's formulation for anisotropic plasticity [25]. Many researchers have used this type of approach to successfully model unidirectional composites [26-29]. Specifically, the approach developed by Sun and coworkers has proven to be simple and relatively accurate [14,28,30]. The mathematical theory of the plasticity for fabric composites developed in this paper employs a similar approach and is derived based on Hill's theory of an anisotropic yield function, and its modification to a plastic potential. The yield function used in this model is:

$$f(\sigma_{ij}) = \frac{a_{11}}{2}\sigma_{11}^2 + \frac{a_{22}}{2}\sigma_{22}^2 + \frac{a_{33}}{2}\sigma_{33}^2 + a_{12}\sigma_{11}\sigma_{22} + a_{13}\sigma_{11}\sigma_{33} + a_{23}\sigma_{22}\sigma_{33}$$
$$+ a_{44}\sigma_{23}^2 + a_{55}\sigma_{13}^2 + a_{66}\sigma_{12}^2 \tag{1}$$

where σ_{ij} is the stress tensor (with the 1 and 2 axes parallel to the two fiber directions) and a_{ij} is the anisotropy tensor. The flow rule that relates the plastic strain increment tensor and the stress tensor is:

$$d\varepsilon_{ij}^p = \frac{\partial f(\sigma_{ij})}{\partial \sigma_{ij}}d\lambda \tag{2}$$

where $d\varepsilon_{ij}^p$ is the plastic strain increment tensor, $d\lambda$ is a scalar value to be determined experimentally, and the yield function $f(\sigma_{ij})$ plays the role of the plastic potential. It is assumed that the graphite fibers in a woven composite prevent plastic deformation along the x_1 and x_2 axis, therefore:

$$d\varepsilon_{11}^p = d\varepsilon_{22}^p = 0$$

5

Substitution of equation 1 into 2, and using the conditions specified in equation 3 reveals:

$$a_{11} = a_{12} = a_{13} = a_{22} = a_{23} = 0$$

Assuming zero plastic dilatation:

$$a_{33} = 0$$

Equation 1 is now:

$$f(\sigma_{ij}) = a_{44}\sigma_{13}^2 + a_{55}\sigma_{23}^2 + a_{66}\sigma_{12}^2$$

Assuming that plane stress conditions exist, equation 6 becomes:

$$f(\sigma_{ij}) = a_{66}\sigma_{12}^2$$

Since a$_{66}$ is the only coefficient remaining in the above yield function, it may be arbitrarily set to unity without loss of generality.

Constitutive relationship:

Using the concept of plastic work, the scalar coefficient dλ may be given by [25]:

$$d\lambda = \frac{3}{2}\frac{\overline{d\varepsilon^p}}{\overline{\sigma}}$$

Combining with the flow rule (equation 2):

$$d\varepsilon_{ij}^{p} = \frac{3}{2}\frac{\partial f}{\partial \sigma_{ij}}\frac{d\overline{\varepsilon^{p}}}{\overline{\sigma}}$$

(9)

It can be assumed that the equivalent plastic strain is related to the equivalent stress by a power law:

$$\overline{\varepsilon^{p}} = A\overline{\sigma}^{n}$$

(10)

Differentiating equation 10 and substituting into equation 9:

$$d\varepsilon_{ij}^{p} = \frac{3}{2}\frac{\partial f}{\partial \sigma_{ij}} An\overline{\sigma}^{n-2} d\overline{\sigma}$$

(11)

Equation 11 describes the relationship between the incremental equivalent plastic strain and the incremental equivalent stress which follows the power law.

Equivalent stress and equivalent plastic strain

The equivalent stress may be defined in terms of the yield function f as [25]:

$$\overline{\sigma} = \sqrt{3f}$$

(12)

Substitution of equation 7 into 12 (and assuming $a_{66} = 1$) leads to:

$$\overline{\sigma} = \sqrt{3}\sigma_{12}$$

(13)

7

Evaluation of $d\varepsilon_{12}{}^P$ using equation 2 yields:

$$d\varepsilon_{12}^p = (2\sigma_{12})d\lambda \qquad (14)$$

Substitution of equation 8 and 13 into equation 14 and rearranging gives:

$$\overline{d\varepsilon^p} = \frac{\sqrt{3}}{3} d\varepsilon_{12}^p \qquad (15)$$

Assuming that proportional loading exists results in:

$$\overline{\varepsilon^p} = \frac{\sqrt{3}}{3} \varepsilon_{12}^p \qquad (16)$$

Evaluating equation 11 for $d\varepsilon_{12}{}^P$, assuming proportional loading, and using equation 13 yields:

$$\varepsilon_{12}^p = \left(\sqrt{3}\right)^{n+1} A\sigma_{12}^n \qquad (17)$$

Equation 17 is a constitutive relationship that may be used to characterize the plastic component of composite off-axis behavior. The plastic shear strain in equation 17 is the tensorial plastic shear strain, not the engineering plastic shear strain, $\gamma_{12}{}^P$.

Off-Axis Tests

In the off-axis test, the tensile load is applied along the long axis of the specimen, which is defined as the x-direction (σ_{xx}), and the fibers are aligned at an angle θ from the loading axis (Figure 2). A stacked rectangular three-element strain gage rosette is mounted at the center of the specimen with one gage aligned along the loading axis, another aligned 45° away from the

8

first, and the third aligned 90° from the loading axis. The material shear stress (σ_{12}) in the composite may be related to the applied tensile load (σ_{xx}) by:

$$\sigma_{12} = -\cos(\theta)\sin(\theta)\sigma_{xx} \tag{18}$$

Similarly, the total shear strain (ε_{12}^t) in the material coordinate system may be related to the strain gage strains by transforming the coordinates:

$$\varepsilon_{12}' = -\cos(\theta)\sin(\theta)\varepsilon_{xx}' + \cos(\theta)\sin(\theta)\varepsilon_{yy}' + \left[\cos^2(\theta) - \sin^2(\theta)\right]\varepsilon_{xy}' \tag{19}$$

where ε_{xx}^t is the gage aligned along the loading axis ($\varepsilon_{xx}^t = \varepsilon_{0°}^t$), ε_{yy}^t is the gage aligned transverse to the loading axis ($\varepsilon_{yy}^t = \varepsilon_{90°}^t$), and ε_{xy}^t is:

$$\varepsilon_{xy}' = \varepsilon_{45°}' - \frac{1}{2}\left(\varepsilon_{0°}' + \varepsilon_{90°}'\right) \tag{20}$$

The experimental plastic strains can be calculated by subtracting the elastic strains from the total strains. The elastic shear strain (ε_{12}^e) may be calculated as a function of shear stress (σ_{12}) using an assumed value of the shear modulus G_{12} (see Table I):

$$\varepsilon_{12}^e = \frac{\sigma_{12}}{2G_{12}} \tag{21}$$

Once the plastic tensorial shear strain is determined, the effective plastic strain for the off-axis test may be calculated using equation 16. The effective stress/effective plastic strain curves for each of the off-axis tests can be plotted together, and a power law curve can be fitted to the resulting data using equation 10. The data obtained from different off-axis conditions should be very close to each other and the fitted master curve. The constants A and n determining the

9

master curves should describe the plastic behavior of the particular fabric composite material under any plane-stress biaxial loading.

3. Experimental Setup and Results

Material

The material used in the experimental part of this study was a fabric graphite/PMR-15 composite. The specimens were machined from two composite plaques fabricated at the NASA Lewis Research Center per the following specifications:

Fabric:	T650-35, 8HS cloth (v_f = 58-60%)
Ply Arrangement:	warp-aligned, 16-ply with floating undulations (crimps)
Cure:	simulated autoclave and postcure (General Electric specifications)
Q/A:	C-scan (exceptional density, uniformity)
Dimensions:	305 mm × 305 mm × ~5 mm

All of the specimens were selectively cut and the material inside the C-scanned edge effect boundary was examined for uniformity before being used.

Off-Axis Tests

Off-axis tensile tests were performed in order to determine the elastic-plastic properties of the fabric graphite/PMR-15 composite material. The specimens were machined from the plates as described above to the dimensions recommended by ASTM D3039-76 [31] for θ = 15°, 30°, and 45° (1 each). The specimens were 220.5 mm long and 24.5 mm wide with an "as received" thickness of about 5 mm. Three-element rosette strain gages were mounted in the center of the specimen (Measurements Group WK-06-060WR-350) aligned as described above. Aluminum tabs were used at the gripped portions of the specimen to prevent specimen crushing due to the serrated (diamond-faceted) grips. A 15° tapered angle was included on the tabs to minimize stress concentrations at the tab-specimen interface. The tabs were 38 mm long, 24.5 mm wide, and 3 mm thick. A hardened steel pin was tightly placed through the tabs and the specimen in order to prevent sliding at the interface and specimen slipping. The tabs were also adhered to the

specimen using epoxy in order to eliminate rotation of the tabs about the pin. The tests were performed on a servo-hydraulic MTS 880 with hydraulic grips and a displacement rate of 0.5 mm/min. All specimens failed in the gage section away from the gripped areas.

The stress and stain data required for the determination of the master curve were obtained from three off-axis tests (one test per angle). The effective stress/effective plastic strain for each test is plotted in Figure 3 along with the fitted master curve. Clearly, a single master curve accurately describes the behavior of the fabric composite subjected to the different off-axis tests. The parameters for the master curve are $A = 5.22 \times 10^{-8}$ and $n = 2.27$. These parameters are for the unit-less tensorial shear strain and stress in MPa.

Iosipescu Shear Test

Two Iosipescu specimens were machined to the dimensions suggested by the ASTM standard [10]. The same strain gages used for the off-axis tests were mounted on both sides of both specimens to measure shear strain. The biaxial Iosipescu test fixture was used [32] with loading blocks that are the same dimensions as that suggested by the ASTM standard. The same testing machine was used as with the off-axis specimens. Load and displacement data were taken up to about 5.5 and 6.0 mm fixture displacements. However, the strain gages failed at fixture displacements of about 1.0 and 1.5 mm for the two tests. Therefore, the complete load-strain curves up to 5.5 mm displacement could not be obtained. The gages decoupled due to extensive out-of-plane deformation of the specimen surfaces in the gage sections. The shear stress was calculated by dividing the applied fixture load by the cross sectional area between the notches of the specimen. The shear strain was measured by taking the difference of the two gages mounted at 45° angles to the vertical axis on each side of the test section, and then averaging over both sides of each specimen.

11

4. Finite Element Modeling

Two non-linear finite element models (off-axis tensile test and Iosipescu shear test) were created in order to examine the effect of material non-linearity on the specimen response. Both models assumed geometric non-linearity and material non-linearity. The Iosipescu model also assumed boundary contact non-linearity between the specimen and loading blocks. The resulting numerical load-displacement and load-strain data can be directly compared to the experimental results in order to determine if the plasticity model outlined in section 2 can accurately describe the composite behavior for a shear-dominated biaxial stress state generated by two entirely different testing procedures.

Iosipescu Shear Test Model

The finite element model of the Iosipescu shear tests simulated the loading conditions of the modified Wyoming fixture and the fixture recommended by the ASTM standard. The computations were performed using ANSYS 5.4 [33]. The model is two-dimensional (having a thickness of unity, i.e. 1mm) and uses isoparametric elements with 6 and 8 nodes (PLANE2 and PLANE82, respectively). Point-to-surface contact elements (CONTAC48) were used to simulate sliding between the loading blocks and the composite specimen with a friction coefficient of $\mu =$ 0.3. This friction coefficient was chosen based on an expected value of a static friction coefficient between steel loading blocks and a graphite-reinforced polymer composite (see table I for elastic properties of the steel loading blocks and the composite material). It has been previously shown that the effect of changing the friction coefficient is negligible for unidirectional composite Iosipescu specimens within the range of 0.1 to 0.5 [13,14].

The mesh and boundary conditions used in the analysis are shown (Figure 4 a&b) with a deformed finite element representation of the specimen. The specimen center was constrained against vertical and horizontal displacements (u_x and $u_y = 0$). The blocks on the right side of the specimen had prescribed displacements of u/2 and the blocks on the opposite side were loaded by a negative displacement of the same magnitude. Thus, the total prescribed displacement acting on the specimen was equal to u. The total reactions from each node on the right loading

blocks were summed (this is equal to the load as read by a load cell in the experiment). Also, shear strains were calculated at the center of the specimen using the nodal displacements (modeling the three-element rosette strain gage).

The loading procedure for both models was divided into a minimum of 40 load steps. Each load step had a maximum of 25 equilibrium iterations, and during each iteration the SRSS (the square root of the sum of squares) of the imbalance forces were calculated. The force convergence criterion was assumed with the SRSS of the imbalance forces smaller than 0.1% of the SRSS of the loading forces.

Off-Axis Tensile Test Model

The model of the off-axis tensile test is three-dimensional and uses isoparametric 10 node tetrahedral elements (SOLID92) (see Figure 5). The off-axis specimen has one plane of symmetry in the plane of the thickness (z = 0). The gripping tab is modeled as aluminum and perfectly bonded to the composite specimen. These assumptions are consistent with the experiment (see experimental section). The assumed elastic properties can be found in Table I.

The boundary conditions used the analysis are shown in Figure 5. The backside of the specimen is constrained against displacements in the z-direction at each node in order to satisfy the conditions of a plane of symmetry. Each node on the front face of the top tab is displaced in the direction of the loading axis by u/2. The bottom tab has a negative displacement with an equal magnitude. Thus, the total prescribed displacement acting on the specimen is equal to u. The total reactions from each node on the top tab were summed and doubled (due to the plane of symmetry), which is equal to the load as read by a load cell in the experiment. A numerical strain gage was added at the center of the specimen to model a three-element rosette strain gage. The strains were calculated from the displacements at each node in the gage and averaged. The loading procedure is the same as that for the Iosipescu model.

Modeling Material Non-Linearity

Due to the current computational tools available to this research (ANSYS 5.4) there is a critical limitation to the way elastic-plastic properties of anisotropic materials can be modeled. The non-linear stress-strain curve for a composite material must be estimated with a bi-linear approximation. The slope of the first line is the elastic portion, and the slope of the second line is the plastic portion. The point were the two linear curves intersect is defined as the yield strength. This estimate must be input for the separate cases of pure axial stress along the three principal axes of the fabric composite, i.e. along each fiber direction and through the thickness of the specimen. Also, this must be input for the three cases of pure shear. Clearly, this is not strictly accurate for modeling the elastic-plastic behavior of either unidirectional or fabric composite materials since there is no sharp cutoff between the elastic and plastic portions of the stress-strain curve and the plastic stress-strain behavior of composites is not linear but follows a power law-type hardening curve.

A method was developed in this research to overcome this difficulty. The elastic-plastic stress/strain response of the fabric composite material was approximated with a multi-linear fit as input into the finite element code. The master curve was calculated for the case of pure shear, and a series of bi-linear fits was fit to this curve, then averaged to produce a multi-linear fit that estimated the master curve very closely up to a desired strain. The finite element model was solved for each bi-linear fit and the resulting load, stress, and strain values were averaged. The proposed method of multi-linear approximations is still not perfect, however, significantly better than the bi-linear approximation technique.

For the numerical models the multi-linear fits were approximated with two different estimates. The total strain range (plastic strain plus elastic strain) estimated was equal to that recorded before the strain gages failed. A combination of 4 and 6 bi-linear curves were used to average the curved line. This was done by taking 4 and 6 points along the master curve for pure shear and optimizing the 4 and 6 curves so that their average at these points was the same as the value of the curve at that point. This insured that the value of the average line closely followed the master curve line between these 4 and 6 points. At the first approximation point one of the bi-

linear lines changed its slope while the others maintained their original slope. At the next point another bi-linear line changed its slope, and the second slope of the line that changed its slope at the first approximation point was changed so that the average of all of the bi-linear fits was the same as the value at the second approximation point. For each successive point, a bi-linear fit changes to its second slope, and the second slope of the bi-linear fit that changed its slope in the previous point is adjusted to maintain the average so that it is equal to the master curve at that approximation point. Thus, with 4 and 6 approximation points there are 4 and 6 bi-linear fits, respectively. Also, for 4 and 6 approximation points there are 5 and 7 total slopes to estimate the master curve with, respectively. Since this was only done in the case of pure shear, each bi-linear fit assumed a different value of the shear modulus (the axial moduli and poison's ratio are the same as shown in Table I). Occasionally, it is impossible to maintain the average at each point, and the process must start over with different original slopes before the first approximation point for each bi-linear fit. The approximation points were concentrated at the smaller strains in order to give a better estimate of the higher amount of curvature in this range of the power law estimation for a given total strain range. Figures 6 and 7 show the master curve in pure shear with the bi-linear approximations and the average for the cases of 4 and 6 approximation points. This procedure was repeated for the case of large shear strains (as experienced by the Iosipescu specimen after the strain gage fails). The master curves in pure shear with bi-linear approximations for this case are shown in Figures 8 and 9.

Table II lists the percent errors associated with each estimation of the master curve. The error is defined as the absolute difference of the integrated areas of the master curve and the multi-linear curve generated by the averaged bi-linear approximations, and is computed analytically. The percent error is the error divided by the total area of the master curve. As expected, the approximations with 4 bi-linear fits have a higher percent error than with 6 bi-linear fits for the small and large strain cases, although they are both very small. If the bi-linear (single) approximation technique had been used these errors would have been significantly larger.

5. Results and Discussion

Numerical and Experimental Off-Axis Tests

Figures 10 to 12 present the experimental and numerical tensile stress and total tensile strain (σ_{xx} vs. ε_{xx}^t) curves for the three different off-axis tensile tests. The three numerical curves on each plot correspond to the assumption of linear-elastic material behavior and elastic-plastic behavior with 4 and 6 approximation points. Table II lists the percent error associated with each loading angle for both elastic-plastic approximation points. In this case, the error is defined as the absolute difference of the integrated areas of the experimental curve and the numerically estimated elastic-plastic curves. The percent error is defined as the error divided by the area under the experimental curve. This was calculated by fitting 6th order polynomials to each of the curves. It was observed that the error of the curve fit was insignificant compared to the errors between experimental and numerical results.

It is clear from Table II that the percent error of the elastic-plastic numerical models for both approximation points and for each loading angle is very small relative to the total area under the experimental curves. It can also be seen in Figures 10 to 12 that the elastic-plastic models predict the material behavior much more accurately than the numerical linear-elastic model. In fact, the assumption of a linear-elastic material response results in axial stresses that are about twice as large as those measured experimentally. The percent errors listed in Table II indicate that for the 45° off-axis test, the 6 point approximation generates a smaller error than the 4 point approximation, which is expected, keeping in mind that both errors are very small. For the 15° and 30° off-axis tests, the 4 point approximation actually is more accurate than the 6 point approximation. Since both errors are still relatively small, this indicates that the 4 point approximation is accurate enough to model the plastic behavior of the material, and adding more approximation points does not significantly improve the accuracy of modeling the off-axis experiment.

Numerical and Experimental Iosipescu Shear Test

Figure 13 presents the experimental and numerical shear stress/strain (τ_{xy} vs. $\gamma_{xy}{}^t$) curves for the Iosipescu shear test in the range where the experimental strain gages are valid. At higher fixture displacements, the strain gages either break or de-bond from the specimen. The shear stress τ_{xy} is computed by dividing the applied fixture load by the specimen cross-sectional area, and the total engineering shear strain is computed using the strain gages. The three numerical curves on each plot correspond to the assumption of linear-elastic material behavior and elastic-plastic behavior with 4 and 6 approximation points. Table II lists the percent error associated with the small strain case for both elastic-plastic approximation points. The percent error is defined and calculated the same way as for the off-axis experimental/numerical errors.

It is clear from Figure 13 that the elastic-plastic numerical model approximates the experiment (two experimental curves obtained from two independent Iosipescu tests) much more closely than the linear-elastic numerical model. However, the 4 approximation point elastic-plastic model slightly underestimates the experiment, whereas the 6 approximation point elastic-plastic model underestimates the experiment to a larger degree. One would expect the 6 point approximation to model the experiments more closely because the error between the master curve and the multi-linear approximation is smaller in the case of 6 points than for the approximation with 4 points. This might indicate that a proportional relationship between the input bi-linear curves (mechanical properties) and the output bi-linear curves (numerical results) does not exist. In Figures 6 and 7, it can be seen that the bi-linear curves for the 4 point approximation have a smaller range of initial and secondary slopes that are close to the averaged approximation, and the 6 point approximation curves have slopes that are relatively small and large compared to the average. Since the relationship between the input and output bi-linear curves is not proportional, this would cause the 6 point approximation to have a greater error in the final numerical calculation. From this data, it can be deduced that for the small strain numerical computation of the Iosipescu specimen the 4 approximation point technique is good enough to model the specimen behavior accurately. The accuracy would be improved if the slopes of the bi-linear curves (used as mechanical properties) have a smaller range of initial and secondary slopes.

17

Figure 14 shows the experimental and numerical shear stress/fixture displacement curves for the same experiments. Since large displacements can be monitored throughout the test (up to about 6mm) unlike the strain gages, this figure represents the entire test performed. The numerical calculations in this case correspond to the linear-elastic and the elastic-plastic with 4 and 6 approximations for large strains. Again, the shear stress is calculated by dividing the fixture load by the specimen cross-sectional area. Figure 15 is the same plot as Figure 14, but focused on the lower stress values in order to emphasize the difference between the experimental curve and elastic-plastic numerical model.

From Figure 14, it is clear that the linear-elastic approximation of the stress/displacement curves is very inadequate, and the elastic-plastic approximations are much more accurate. The two elastic-plastic approximations are very close to each other, however the same trend can be observed as described for the case of the small strains described above. The approximation that is averaged from bi-linear curves that have a larger difference in slopes tends to predict lower stresses than the approximation with bi-linear curves that have slopes closer to the averaged curve. In this case, the 6 point approximation has bi-linear slopes that are closest (Figures 8 and 9), and the stresses in the numerical Iosipescu computation are somewhat higher than those of the 4 point approximation.

It can also be observed in Figure 14 that even though the elastic-plastic numerical stress/displacement curves are much closer to the experimental curves than the linear-elastic computation, it still overestimates the experimental data significantly. A magnifications of this can be seen in Figure 15. It is evident that the approximation is relatively close to the experiment up to about 1.5 mm fixture displacements (considering that this is a numerical approximation for large strains) but deviates significantly for large displacements. Searles *et al.* [3] showed that for this same composite, interlaminar damage in the Iosipescu specimen begins to occur at a fixture load and displacement of about 100 MPa and 1.5 mm, respectively. Figure 16 (Figure 14 from *Searles et al.* [3]) shows the rapid progression of interlaminar damage that occurs at the maximum load. It can be seen in Figure 15 that the point at which the elastic-plastic estimation begins to deviate from the experiment corresponds to the rapid development of

interlaminar damage in the Iosipescu specimen caused by shear and compression from the loading blocks.

The reason why the elastic-plastic model deviates from the experiment near the maximum load is because it is characterized based on the off-axis tension tests that are effected very little by interlaminar damage. Even though interlaminar damage does occur in the off-axis tensile tests (see Figure 17), its influence on the non-linear behavior of the material is very small in a combined shear/tension stress state. From Figure 17, it is evident that even though bundle rotation occurs which causes damage, the interlaminar cracks are forced to remain closed due to extensional-bending coupling while the specimen is loaded. Since the closed cracks are parallel to the applied load, further damage propagation due to interlaminar crack growth is prevented. The out-of-plane bulging in the off-axis specimen in Figure 17 is not visible when the specimen is loaded. Upon unloading, the interlaminar cracks prevent the specimen from holding its original shape and thus bulging occurs. In the Iosipescu specimen the interlaminar damage is significant because of a shear/compression state of stress that exists in the gage section. This state of stress forces the interlaminar crack to open and propagate rapidly. Therefore, the master curve that was developed based on the off-axis tension tests does not include the information related to the interlaminar damage, and cannot properly predict non-linear behavior of the fabric Iosipescu specimens developing large interlaminar damage zones in their gage sections.

Searles *et al.* [3] assumed that the shear stress in the fabric Iosipescu specimens calculated using the applied fixture load divided by the cross-sectional area of the gage section of the specimens was similar to the actual internal shear stress in the specimen. The shear stress calculated from the linear-elastic model of the test with friction and geometric non-linearity was not used since it was suspected at that time that this could grossly overestimate the shear strength of the composite. Therefore, it was assumed that the shear stress at the point where significant non-linearity began near the maximum load (rapid interlaminar damage development and propagation) could be defined as the shear strength of the composite calculated from the load divided by the cross-sectional area. In order to investigate the validity of this assumption, the internal stresses along the notch root axis were numerically calculated for the maximum load (fixture displacement = 1.5 mm) of the Iosipescu specimen using the elastic-plastic model with

19

the 4 point approximation. Figure 18 shows the calculated internal stresses (longitudinal and transverse normal stresses σ_x and σ_y and the shear stress σ_{xy}) along the notch root axis of the specimen. It can be seen that the shear stress is very uniform along the notch root axis, and the shear stress calculated using the load/area approach is very accurate. It is also clear that not only are all three stress components relatively uniform along the notch root axis, but the normal stress components are very small with respect to the shear stress component. This means that there should be very little influence of the normal stresses on the initiation of the interlaminar damage in the composite material. The compressive stress σ_y, however, must have a strong effect on the interlaminar damage propagation. This could be the reason why the experimental load-displacement curves for the Iosipescu fabric composites at large displacements are so flat. Even relatively small compressive stresses in the gage section of the specimens will enhance the interlaminar damage propagation process.

It has been shown in this research that the apparent shear strength of the fabric composite can be defined by the maximum applied fixture load divided by the cross-sectional area. Since the normal stress components are significantly smaller than the shear stress in the gage section they should have almost no effect on the initiation of interlaminar damage which determines the strength of the composite when subjected to shear. Moreover, the shear stress field along the notch root axis appears to be very uniform with small reductions near the roots of the notches. All of this means that the use of correction factors and/or failure criteria are unnecessary, and no stress concentrations along the notch root axis need to be considered.

Conclusions

It is well known that woven fiber reinforced polymer matrix composites tend to exhibit significant material non-linearity when subjected to shear loads and negligible material non-linearity when subjected to loads parallel to the fiber reinforcement. Therefore, when numerically modeling and experimentally determining shear-dominated biaxial properties of woven composites, it is important to consider the non-linear material behavior. In this research, it has been shown that by using a time-independent, macroscopic, homogeneous plasticity model for woven fabric composites, it is possible to predict the non-linear response of these structures

20

under shear-dominated biaxial loads. Once the model has been characterized for a specific woven composite material, it can be used in a comprehensive non-linear finite element analysis to determine the mechanical response of any structure based on these materials.

A series of off-axis tests of a 8HS woven graphite/PMR-15 composite material has been performed to characterize the elastic-plastic model. It has been shown that the model can accurately predict the response of the material under axial tension/shear biaxial loading conditions in the off-axis experiments, and it can also predict the mechanical response of the woven Iosipescu specimens up to the point of significant interlaminar failure.

Using the newly developed, fully non-linear finite element model of the woven Iosipescu specimens the shear strength properties of woven composites can be experimentally determined. The shear stress calculated by taking the applied fixture load at failure and dividing by the cross-sectional area of the specimen is the same as the shear stress along the notch root axis of the specimen obtained from the non-linear analysis. The linear-elastic approach overestimates the shear strength of the composite determined from the Iosipescu test by a factor of at least three.

Acknowledgments

References

1. Meador, M.A., P.J. Cavano, and D.C. Malarik, "High Temperature Polymer Matrix Composites for Extreme Environments", *Proceedings of the Sixth Annual ASM/ESD Advanced Composites Conference*, Detroit, Michigan, October 1990, pp. 529-539

2. Vannucci, R.D., "PMR Polyimide Compositions for Improved Performance at 371°C", NASA Technical Memorandum 88942

3. Searles, K., G. Odegard, M. Castelli, and M. Kumosa, "Failure Investigation of Graphite/Polyimide Fabric Composites at Room and Elevated Temperatures Using the Biaxial Iosipescu Test", *Journal of Composite Materials,* In press.

4. Kumosa, M.S., K. Searles, G. Odegard, and T. Han, "Biaxial Failure Analysis of Graphite Reinforced Polyimide Composites", Annual report to the Air Force Office of Scientific Research, University of Denver (1997)

5. Iosipescu, N., "New Accurate Procedure for Single Shear Testing of Metals", *Journal of Materials*, Vol. 2, No. 3 (1967), pp. 537-566

6. Adams, D.F. and D.E. Walrath, Composite Materials: Testing and Design (Sixth Conference) ASTM STP 787, I.M. Daniel, ed., Philadelphia, PA: American Society for Testing and Materials, (1982), pp. 19-33

7. Adams, D.F. and D.E. Walrath, "The Iosipescu Shear Test as Applied to Composite Materials, *Experimental Mechanics*, Vol. 23, No.1 (1983), pp. 105-110

8. Adams, D.F. and D.E. Walrath, "Further Developments of the Iosipescu Shear Test Method", *Experimental Mechanics,* Vol. 27, No. 2 (1987), pp. 113-119

9. Adams, D.F. and D.E. Walrath, "Current Status of the Iosipescu Shear Test Method", *Journal of Composite Materials*, Vol. 21, No. 6 (1987), pp. 494-507.

10. Standard Test Method for Shear Properties of Composite Materials by the V-Notched Beam Method, ASTM Standard D 5379-93, American Society for Testing and Materials, Philadelphia, (1993)

11. Ho, H., J. Morton, and G.L. Farley, "Non-Linear Numerical Analysis of the Iosipescu Specimen for Composite Materials", *Composites Science and Technology*, Vol. 50 (1994), pp. 355-365

12. Kumosa, M. and Y. Han, "Non-Linear Finite Element Analysis of Iosipescu Specimens", *Composites Science and Technology*, Vol. 5 (1999), pp. 561

13. Odegard, G., K. Searles, and M. Kumosa, "A Critical Examination of the Iosipescu Shear Test as Applied to 0° Unidirectinal Composite Materials", *Mechanics of Composite Materials and Structures*, In press (1999)

14. Odegard, G. and M. Kumosa, "Elasto-Plastic Analysis of the Iosipescu Shear Test", *Journal of Composite Materials,* In press (1999)

15. Ho, H., M.Y. Tsai, J. Morton, and G.L. Farley, "In-plane Shear Testing of Graphite-Woven Fabric Composites", *Experimental Mechanics*, Vol. 34, No. 1 (1994), pp. 45-52

16. Hahn, H.T. and S.W. Tsai, "Nonlinear Elastic Behavior of Unidirectional Composite Laminae", *Journal of Composite Materials*, Vol. 7 (1973), pp. 102-118

17. Kenaga, D., J.F. Doyle and C.T. Sun, "The Characterization of Boron/Aluminum Composite in the Nonlinear Range as an Orthotrpic Elastic-Plastic Material", *Journal of Composite Materials*, Vol. 21 (1987), pp. 516-531

18. Hansen, A.C., D.M. Blackketter, and D.E. Walrath, "An Invariant-Based Flow Rule for Anisotropic Plasticity Applied to Composite Materials", *Journal of Applied Mechanics*, Vol. 58 (1991), pp. 881-888

19. Owens, G.A. and S.E. Schofield, "Thermal Cycling and Mechanical Property Assessment of Carbon Fiber Fabric Reinforced PMR-15 Polyimide Laminates", *Composites Science and Technology*, Vol. 33 (1988), pp. 177-190

20. Grape, J.A. and V. Gupta, "Failure in Carbon/Polyimide Laminates Under Biaxial Compression", *Journal of Composite Materials*, Vol. 29 (1995), pp. 1850-1872

21. Mirzadeh, F. and K.L. Reifsnider, "Micro-Deformations in C3000/PMR-15 Woven Composite", *Journal of Composite Materials*, Vol. 26 (1992), pp. 185-205

22. Naik, N.K., P.S. Shembekar, and M.V. Hosur, "Failure Behavior of Woven Fabric Composites", *Journal of Composites Technology & Research*, Vol. 13 (1991), pp. 107-116

23. Vaziri, R., M.D. Olson, and D.L. Anderson, "A Plasticity-Based Constitutive Model for Fibre-Reinforced Composite Laminates", *Journal of Composite Materials*, Vol. 25 (1991), pp. 512-535

24. Naik, R.A., "Failure Analysis of Woven and Braided Fabric Reinforced Composites", *Journal of Composite Materials*, Vol. 29 (1995), pp 2334-2363

25. Hill, R., The Mathematical Theory of Plasticity, Oxford University Press, London (1950)

26. Valliappan, S., P. Boonlaulohr, and I.K. Lee, "Non-Linear Analysis for Anisotropic Materials", *International Journal for Numerical Methods in Engineering*, Vol. 10 (1976), pp. 597-606

27. Griffin, O.H., M.P. Kamat, and C.T. Herakovich, "Three Dimensional Inelastic Finite Element Analysis of Laminated Composites", *Journal of Composite Materials*, Vol. 5 (1981), pp. 543-560

28. Sun, C.T. and J.L. Chen, "A Simple Flow Rule for Characterizing Nonlinear Behavior of Fiber Composites", *Journal of Composite Materials*, Vol. 23 (1989), pp. 1009-1020

29. Xie, M. and D.F. Adams, "A Plasticity Model for Unidirectional Composite Materials and Its Applications in Modeling Composites Testing", *Composites Science and Technology*, Vol. 54 (1995), pp. 11-21

30. Sun, C.T. and K.J. Yoon, "Characterization of Elastic-Plastic behavior of AS4/PEEK Thermoplastic Composite for Temperature Variation, *Journal of Composite Materials*, Vol. 25 (1991), pp. 1297-1313

31. Standard Test Method Tensile Properties of Fiber-Resin Composites, ASTM Standard D 3039-76, American Society for Testing and Materials (1976)

32. Broughton, W.R., M. Kumosa, and D. Hull, "Analysis of the Iosipescu Shear Test as Applied to Unidirectional Carbon-Fiber Reinforced Composites", *Composites Science and Technology*, Vol. 38 (1990), pp. 299-325

33. ANSYS Engineering System, User's Manual, Swanson Analysis System Inc. (1997)

Captions

Table I. Mechanical properties of the 8-HS woven composite material, steel loading blocks, and aluminum tabs.

Table II. Percent errors of the multi-linear approximations and the numerical results.

Figure 1. Solid model of the 8-harness satin woven architecture.

Figure 2. Off-axis tensile test with material and global coordinates shown.

Figure 3. The effective stress-effective plastic strain diagram with the experimental off-axis data and the master curve.

Figure 4. Finite element model showing (a) the boundary conditions and nodes and (b) the deformed mesh.

Figure 5. Finite element model of the off-axis test showing the mesh and the boundary conditions.

Figure 6. Shear stress-total shear strain diagram (for small strains) of the master curve, 4 bi-linear approximations, and the averaged multi-linear curve.

Figure 7. Shear stress-total shear strain diagram (for small strains) of the master curve, 6 bi-linear approximations, and the averaged multi-linear curve.

Figure 8. Shear stress-total shear strain diagram (for large strains) of the master curve, 4 bi-linear approximations, and the averaged multi-linear curve.

Figure 9. Shear stress-total shear strain diagram (for large strains) of the master curve, 6 bi-linear approximations, and the averaged multi-linear curve.

Figure 10. Axial stress-total axial strain diagram of the 15° off axis test.

Figure 11. Axial stress-total axial strain diagram of the 30° off axis test.

Figure 12. Axial stress-total axial strain diagram of the 45° off axis test.

Figure 13. Shear stress-shear strain diagram of the Iosipescu test for a small strain.

Figure 14. Shear stress-shear strain diagram of the Iosipescu test for a large strain.

Figure 15. Same as Figure 14 for small shear stresses.

Figure 16. Damage zone development at the notch root of a graphite/PMR-15 Iosipescu
specimen at (a) a load of 5338 N, (b) a load of 6450 N, and (c) the maximum
load [3].

Figure 17. Side view of a tested off-axis tensile woven graphite/PMR-15 specimen
showing the interlaminar damage.

Figure 18. Numerically determined internal stresses along the notch root axis of an
Iosipescu test specimen. Also shown is the shear stress as calculated by
dividing the numerical load by the specimen cross-sectional area.

	T650-35/PMR-15 8HS woven composite	Steel Loading Blocks	Aluminum Tabs
Axial Moduli (Gpa)	$E_{11} = E_{22} = 79$ $E_{33} = 15$	$E = 200$	$E = 74$
Shear Modulus (Gpa)	$G_{12} = 7.5$	$G = 75$	$G = 28$
Poisson's Ratio	$\nu_{12} = 0.15$	$\nu = 0.33$	$\nu = 0.33$

Table I

approximation points	Master Curve Error		Experimental/Numerical Error			
	small strain	large strain	15 degree off-axis	30 degree off-axis	45 degree off-axis	Iosipescu small strain
4	1.26 %	1.62 %	1.53 %	0.81 %	10.48 %	8.15%
6	0.34 %	0.53 %	4.01%	2.01%	3.57%	22.40%

Table II

FIGURE 1

FIGURE 2

FIGURE 3

loading blocks

(a)

(b)
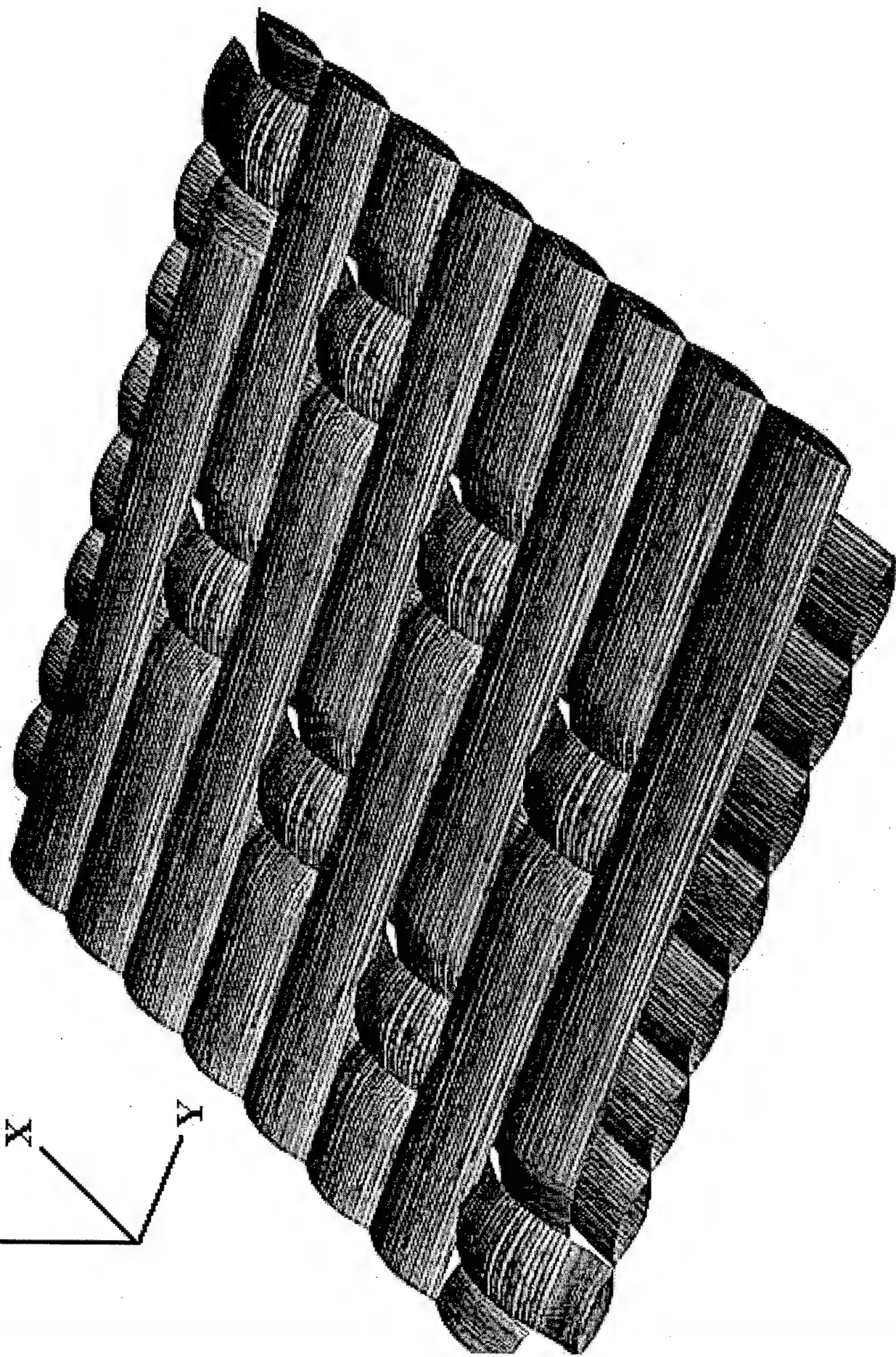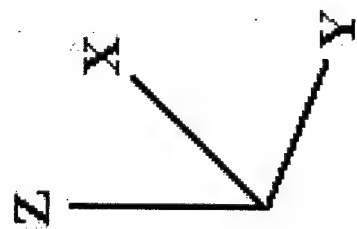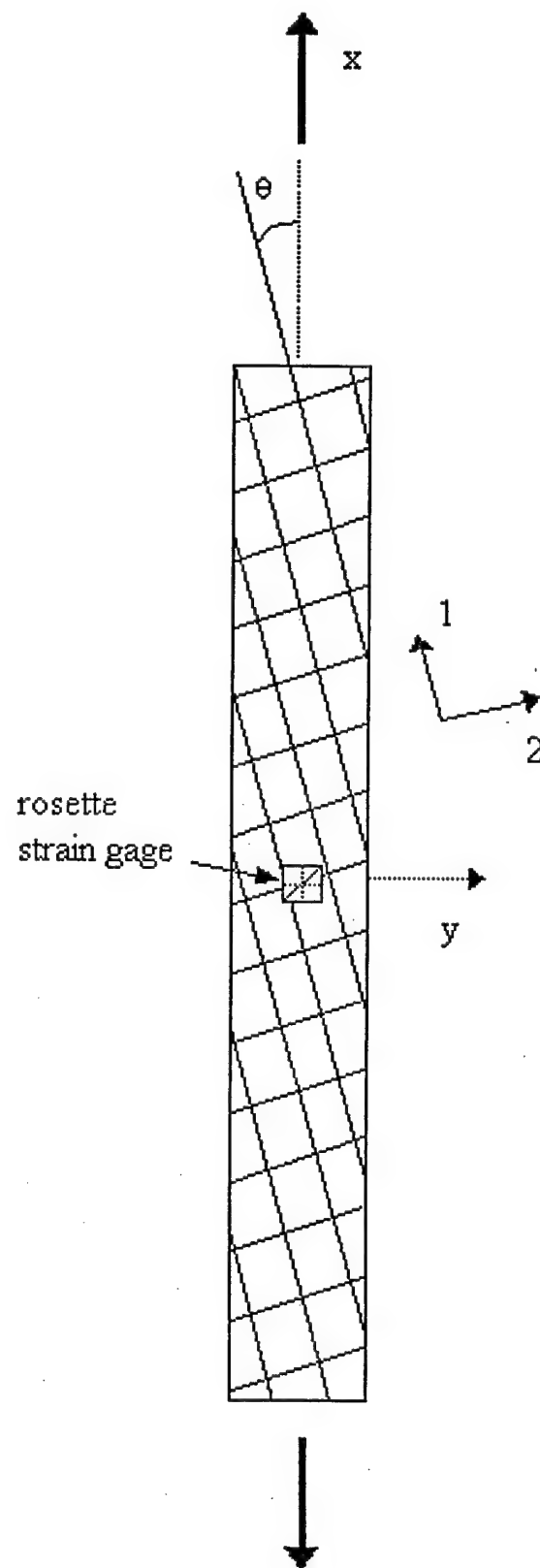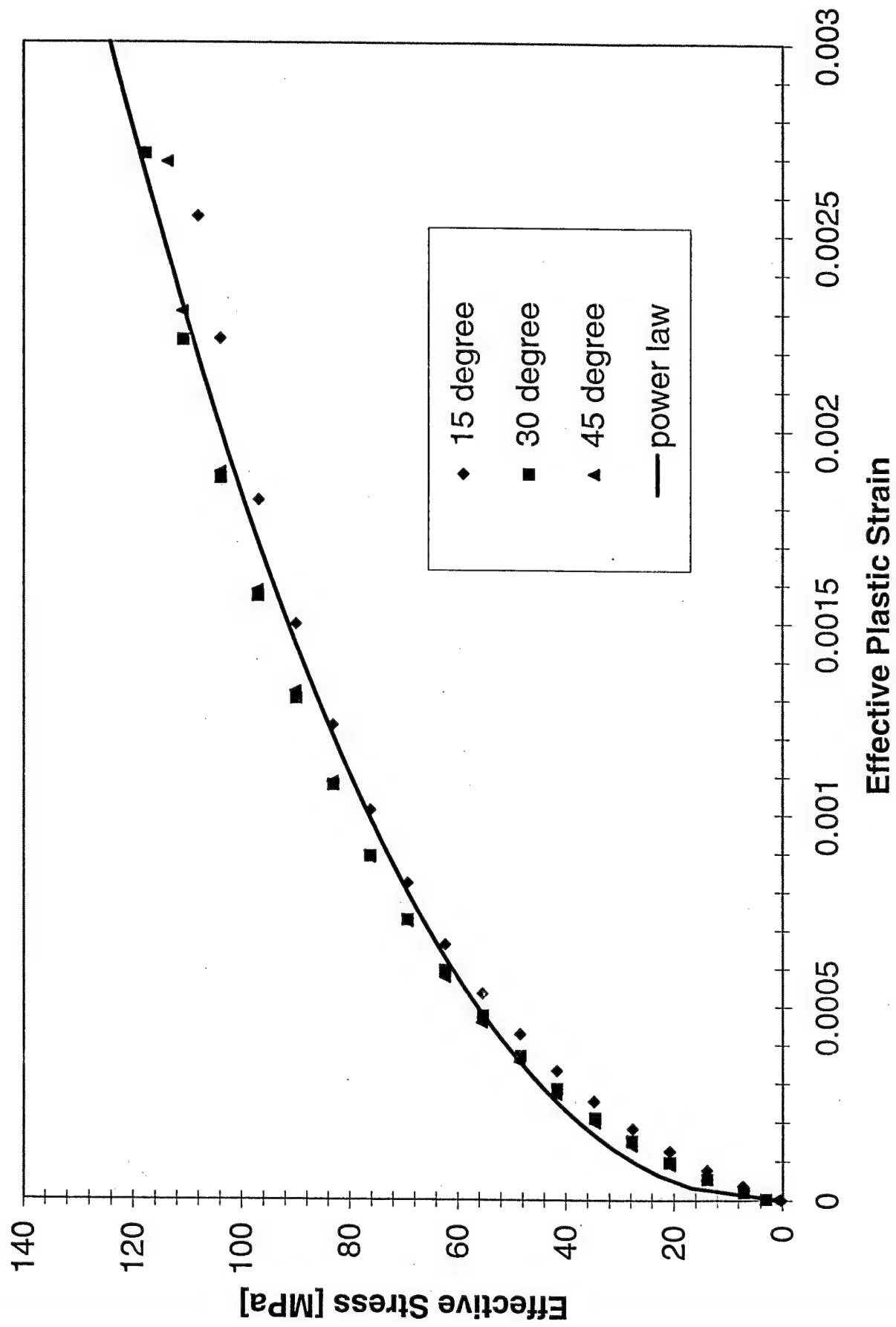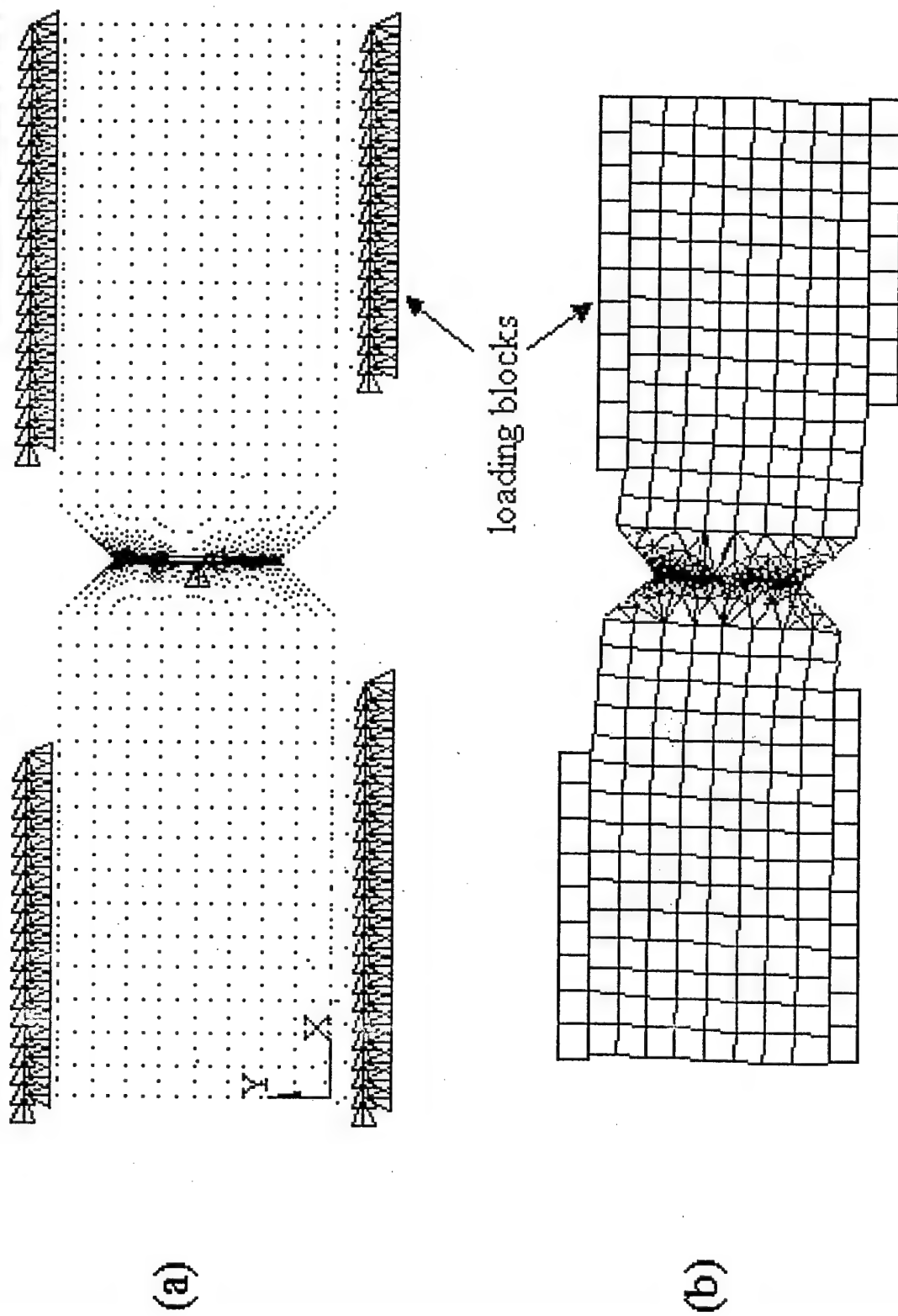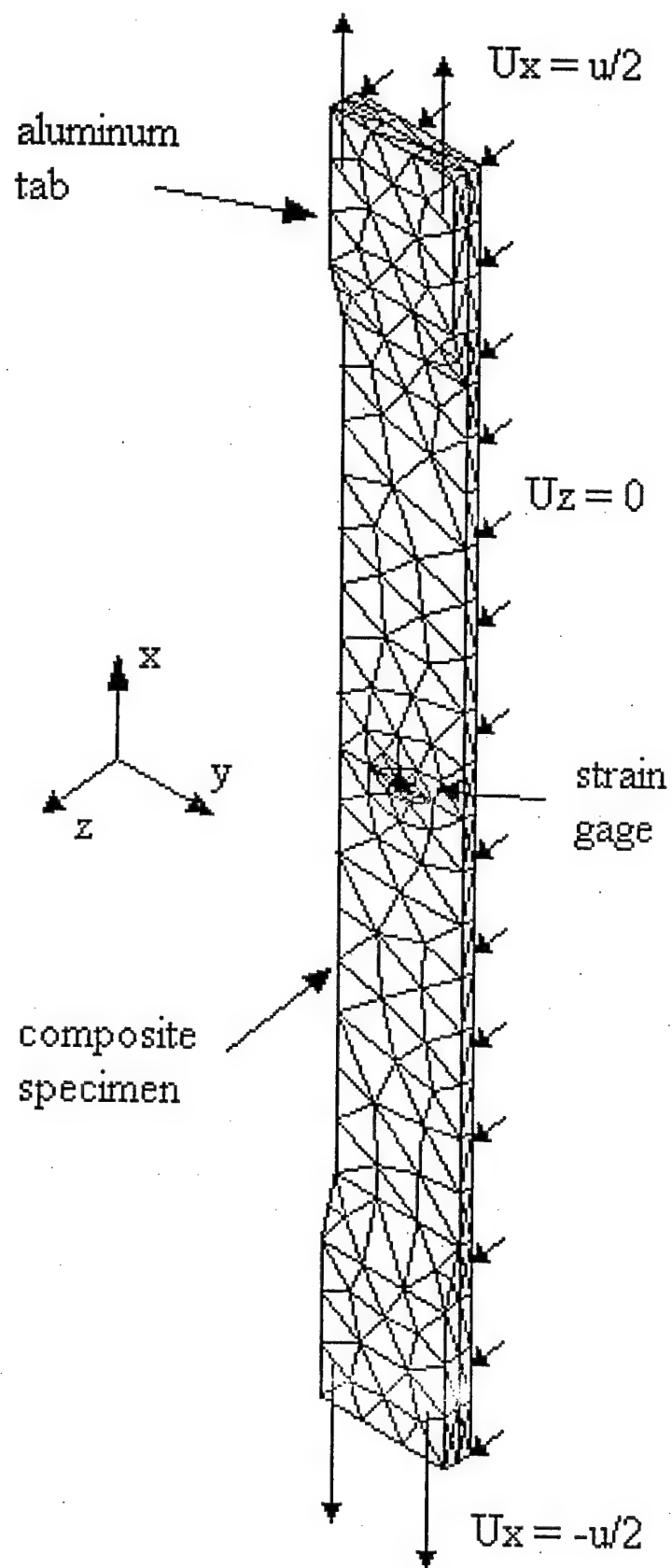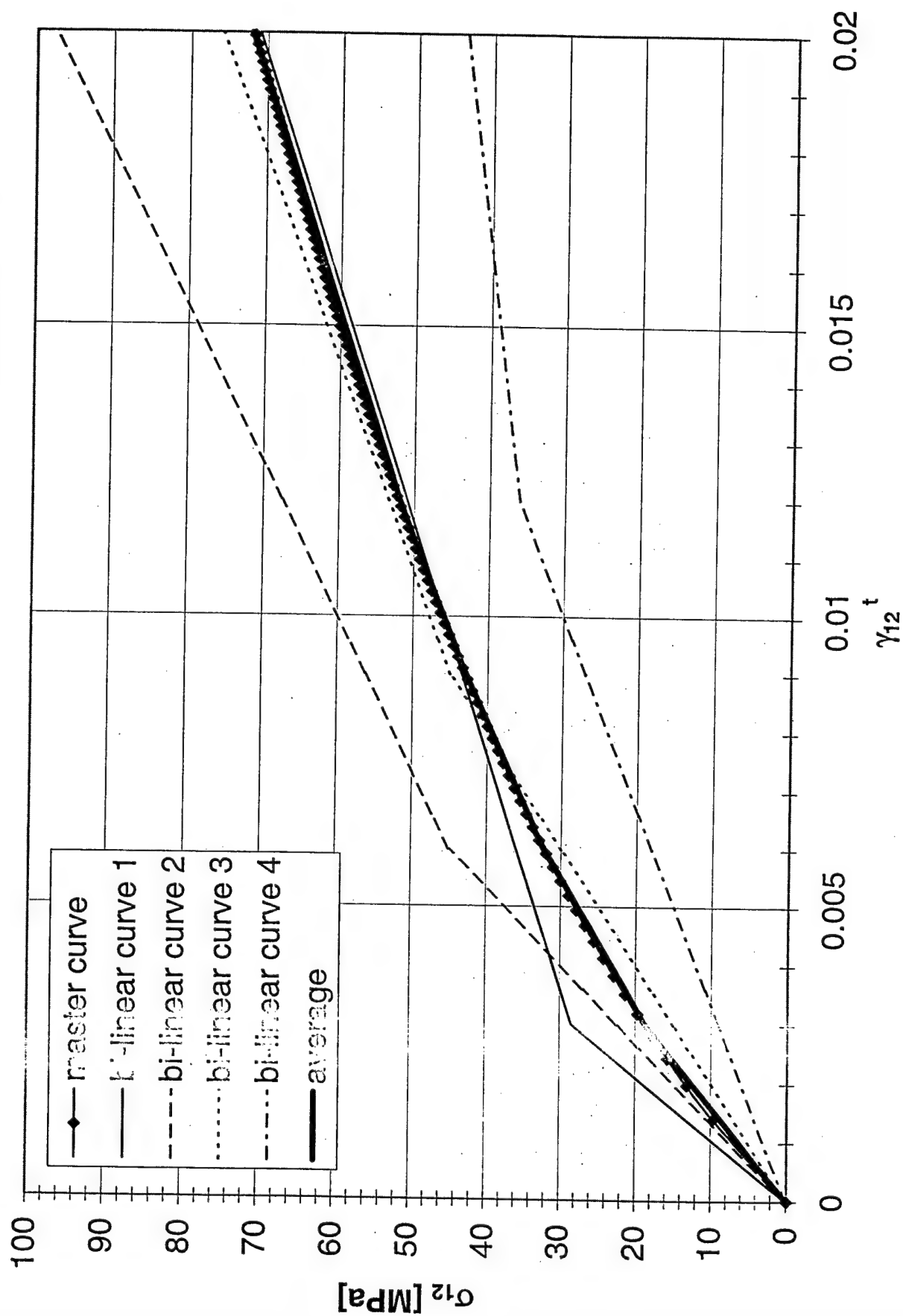
FIGURE 4

FIGURE 5

FIGURE 6
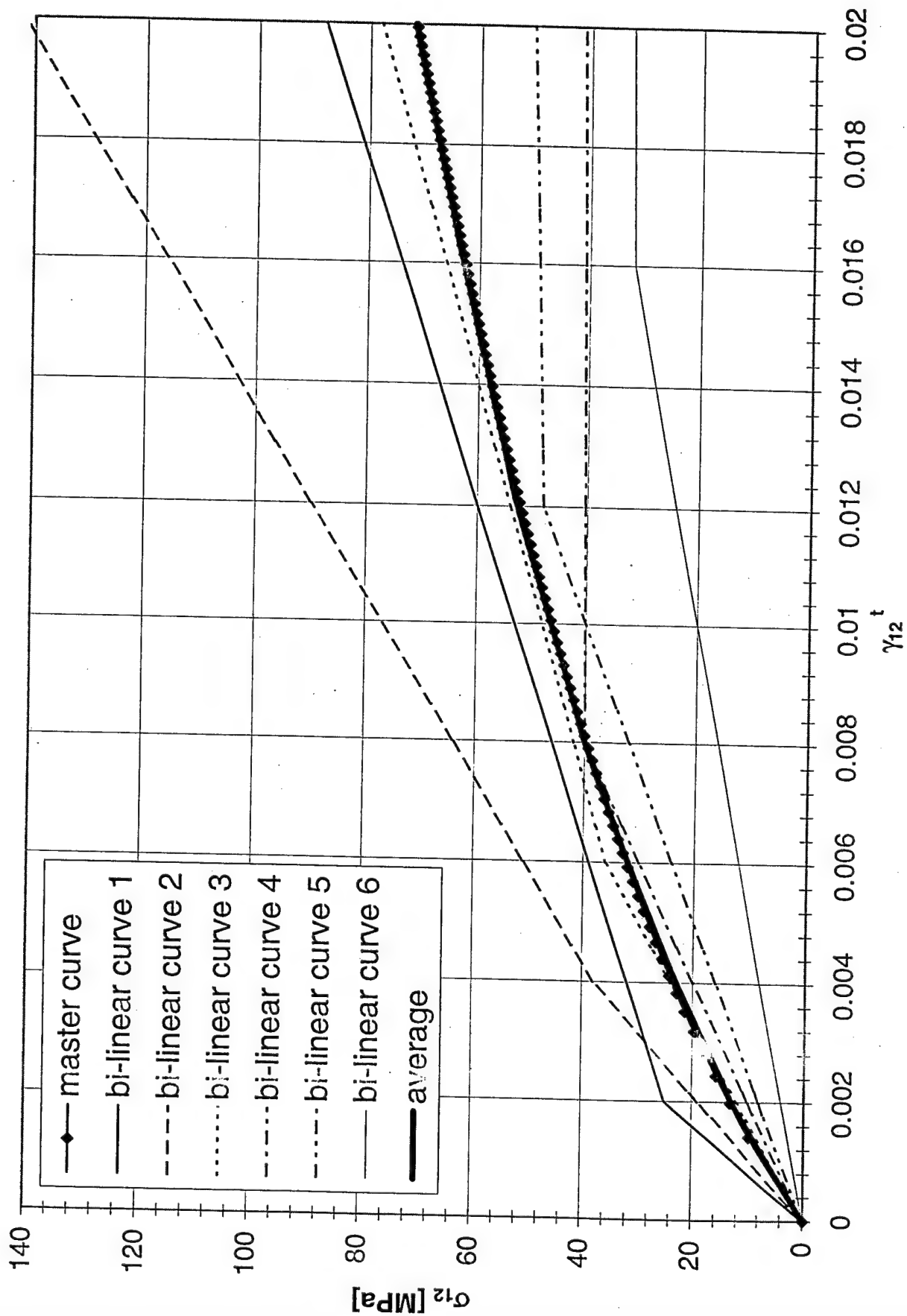
FIGURE 7
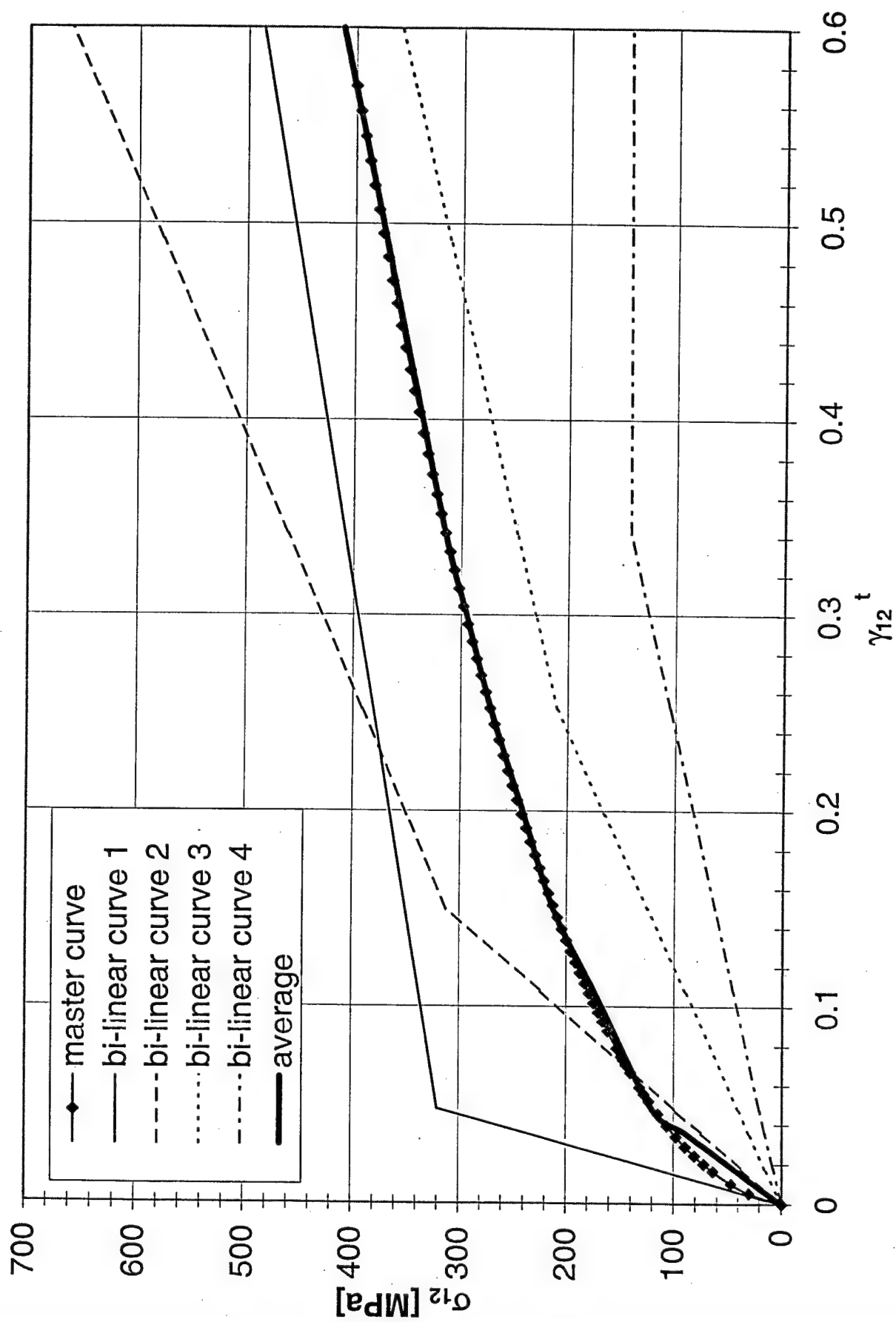
FIGURE 8
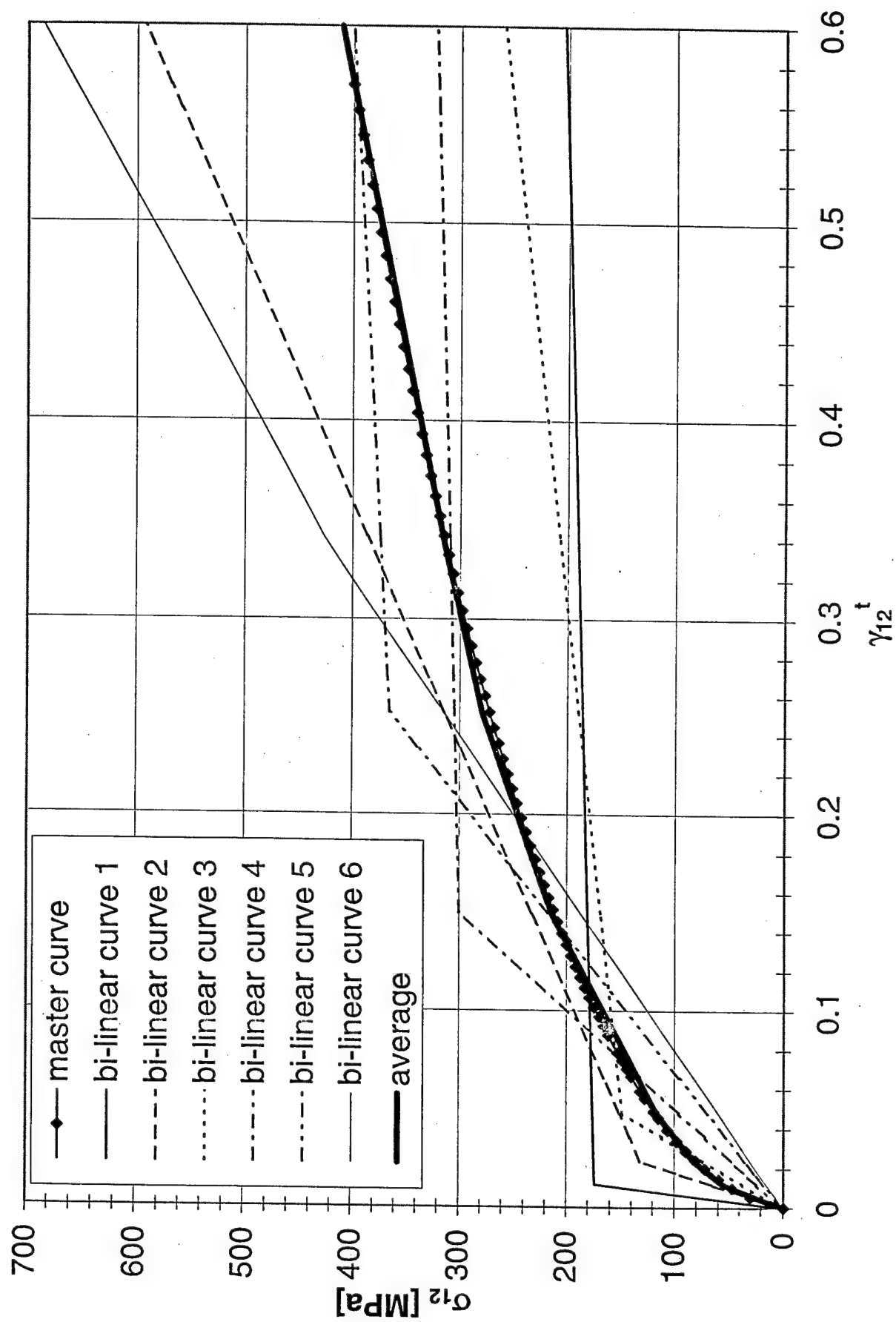
FIGURE 9
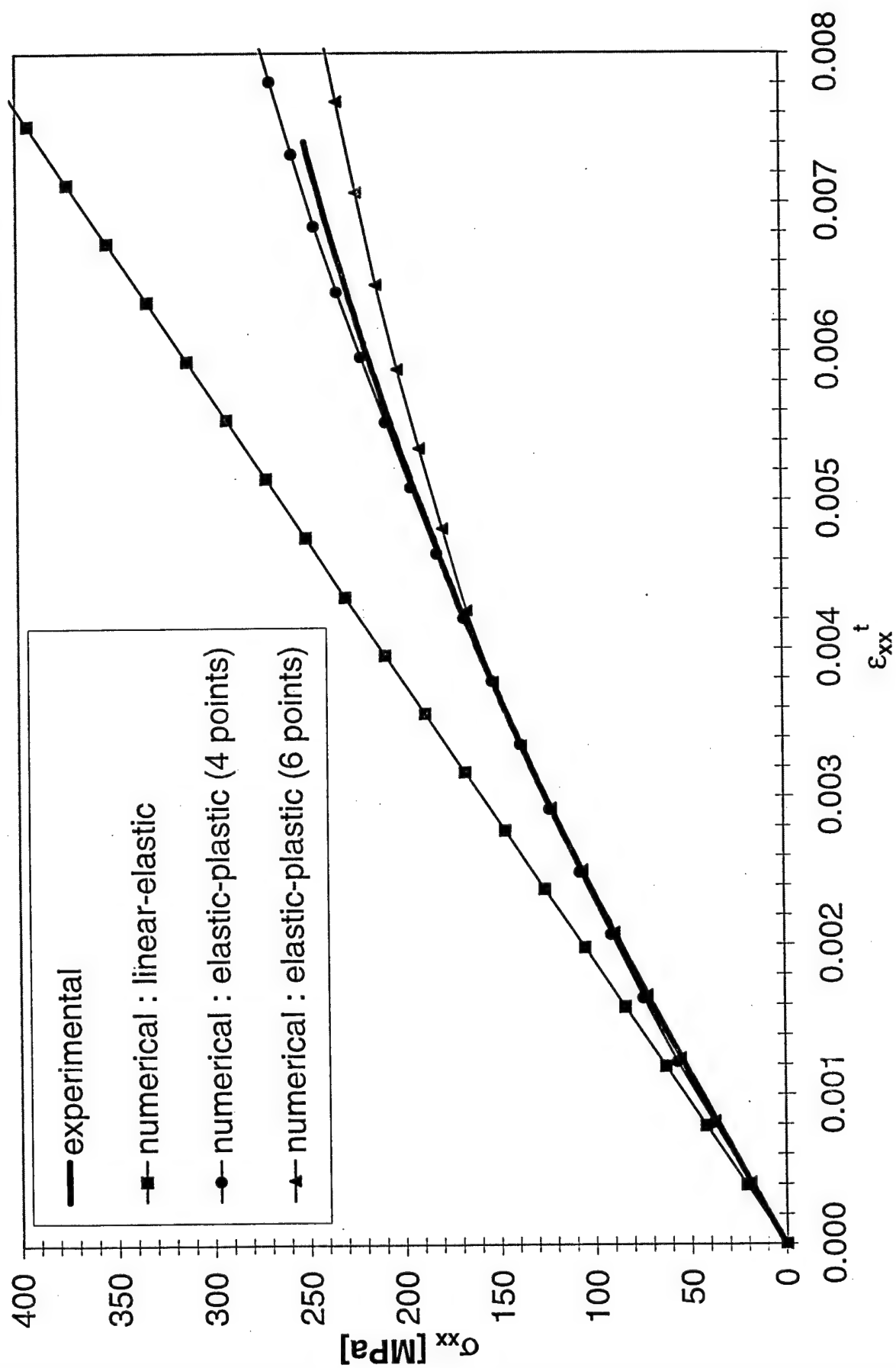
FIGURE 10
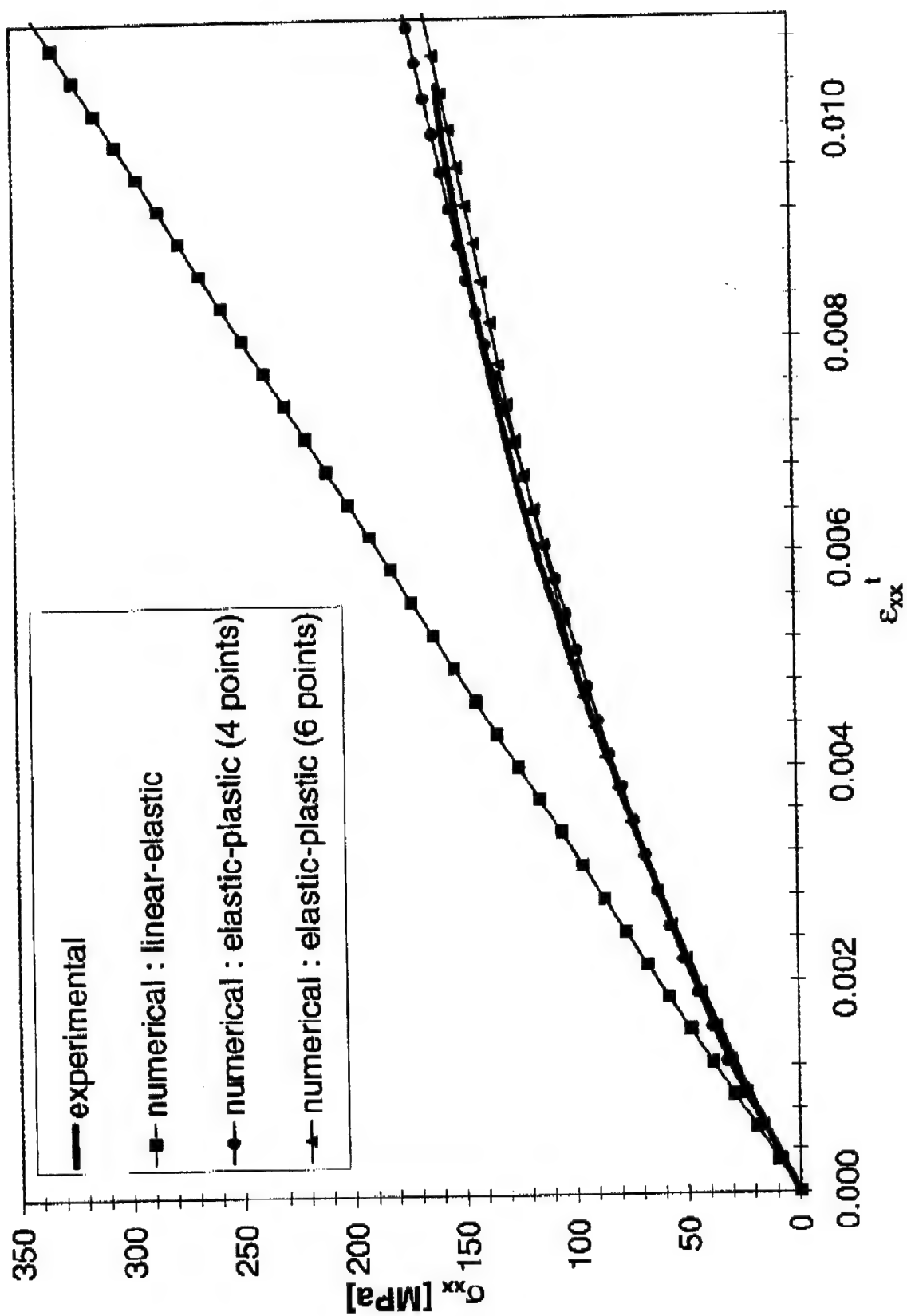
FIGURE 11

FIGURE 12

FIGURE 13

Shear Stress [MPa] (y-axis): 0, 200, 400, 600, 800, 1000, 1200, 1400, 1600, 1800

Fixture Displacement [mm] (x-axis): 0, 1, 2, 3, 4, 5, 6

Legend:
— experimental
— experimental
— numerical : linear-elastic
— numerical : elastic-plastic (4 points)
— numerical : elastic-plastic (6 points)

region of interlaminar damage propagation
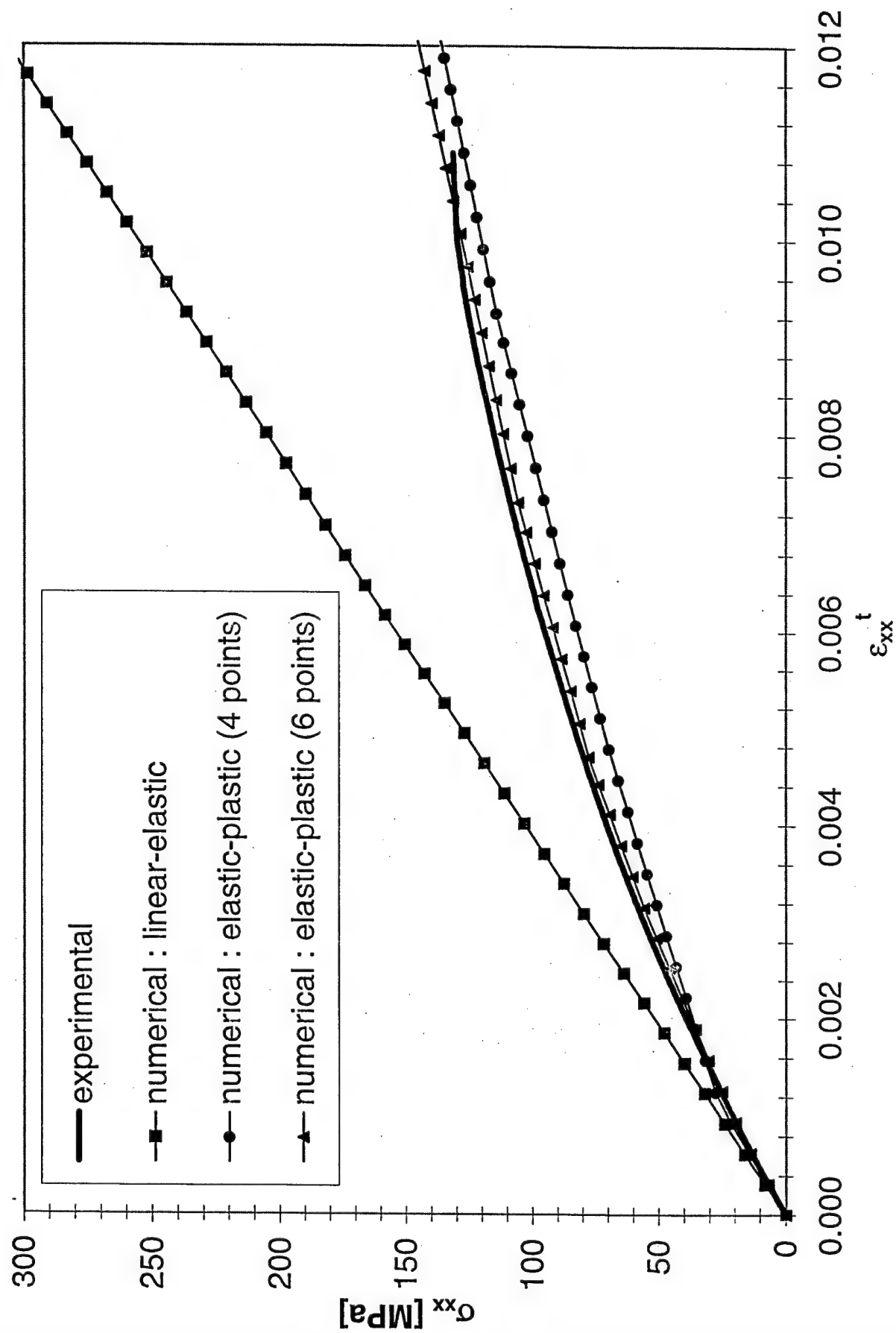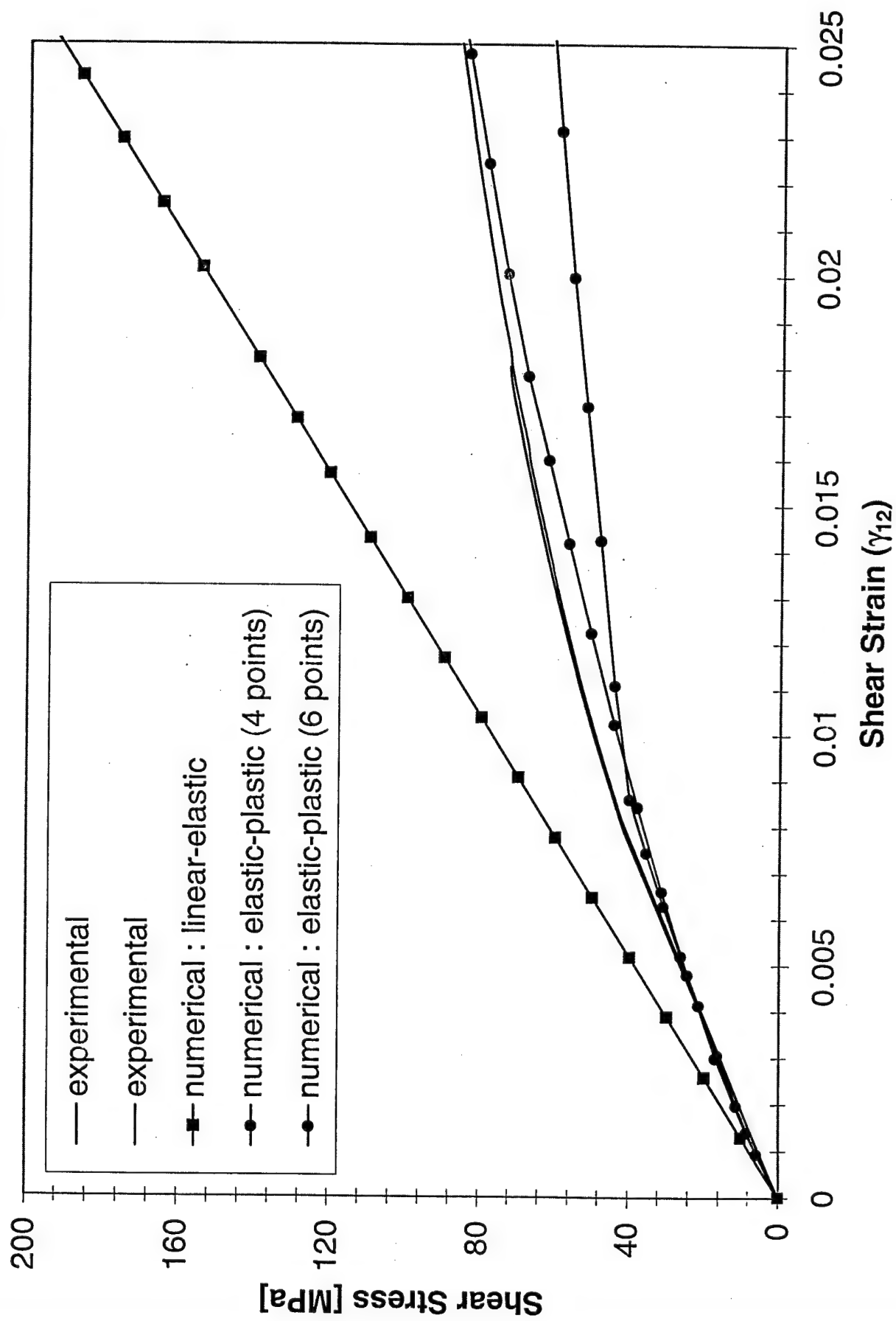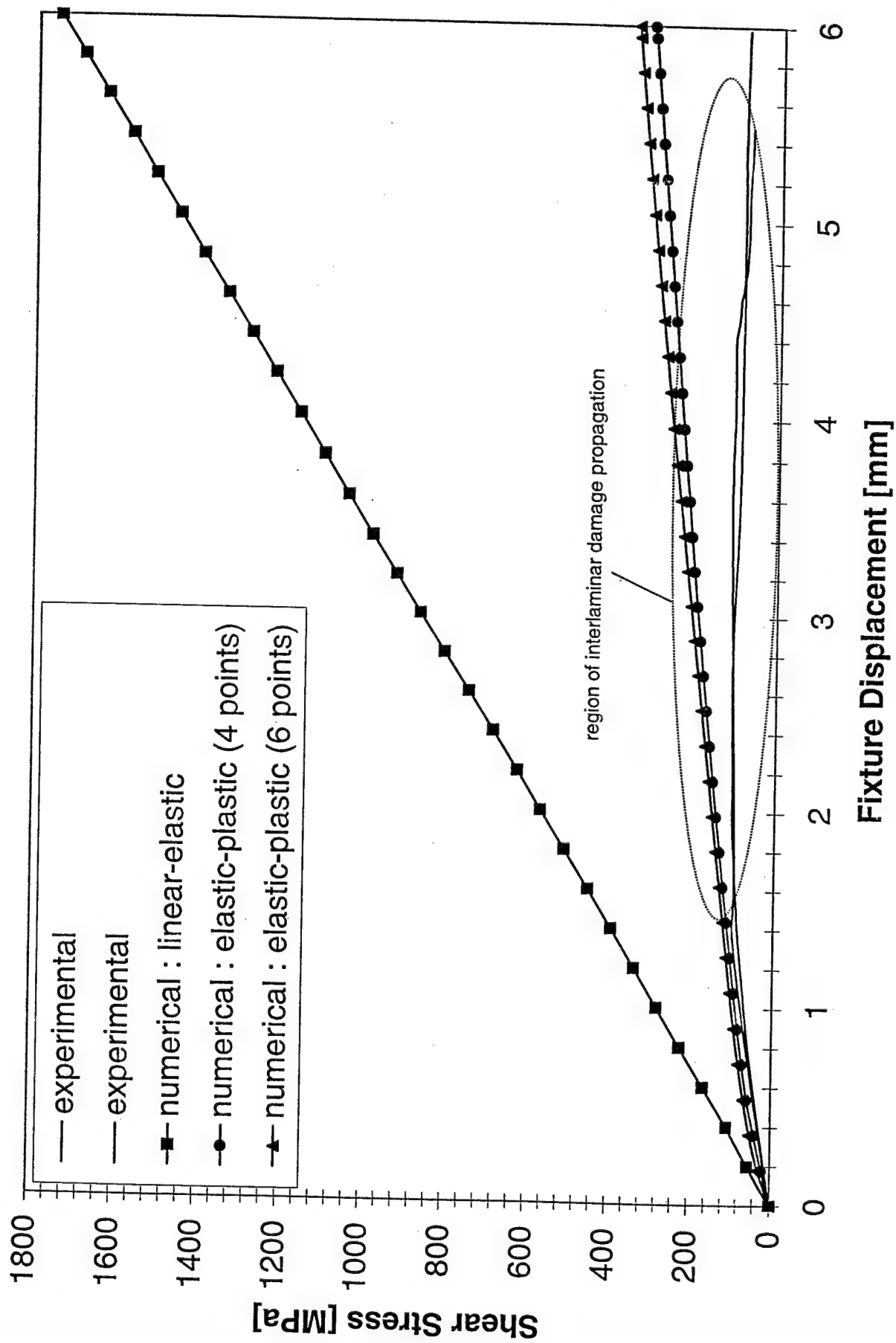
FIGURE 14

FIGURE 15

FIGURE 16 a
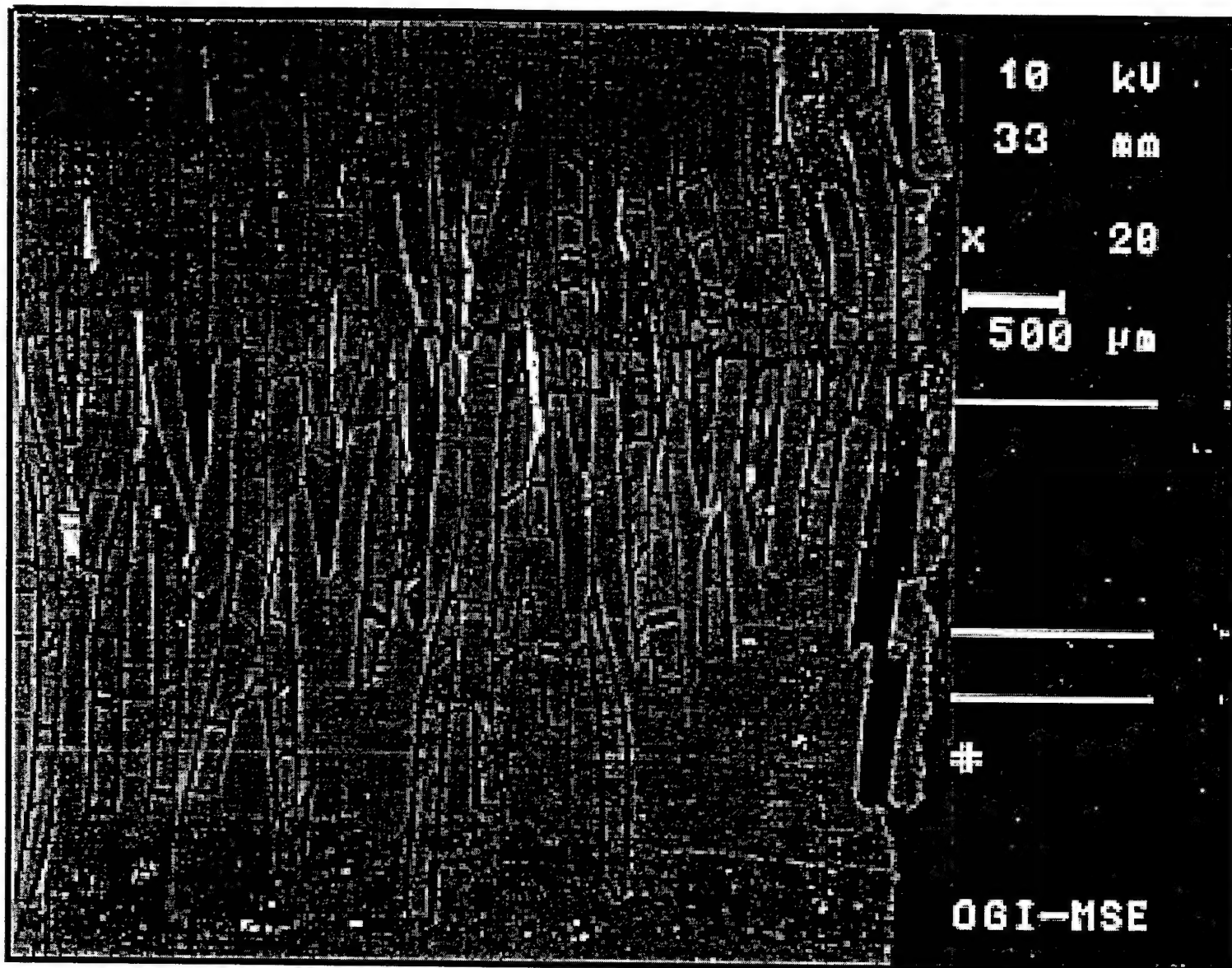
FIGURE 16 b

FIGURE 16 c

FIGURE 17
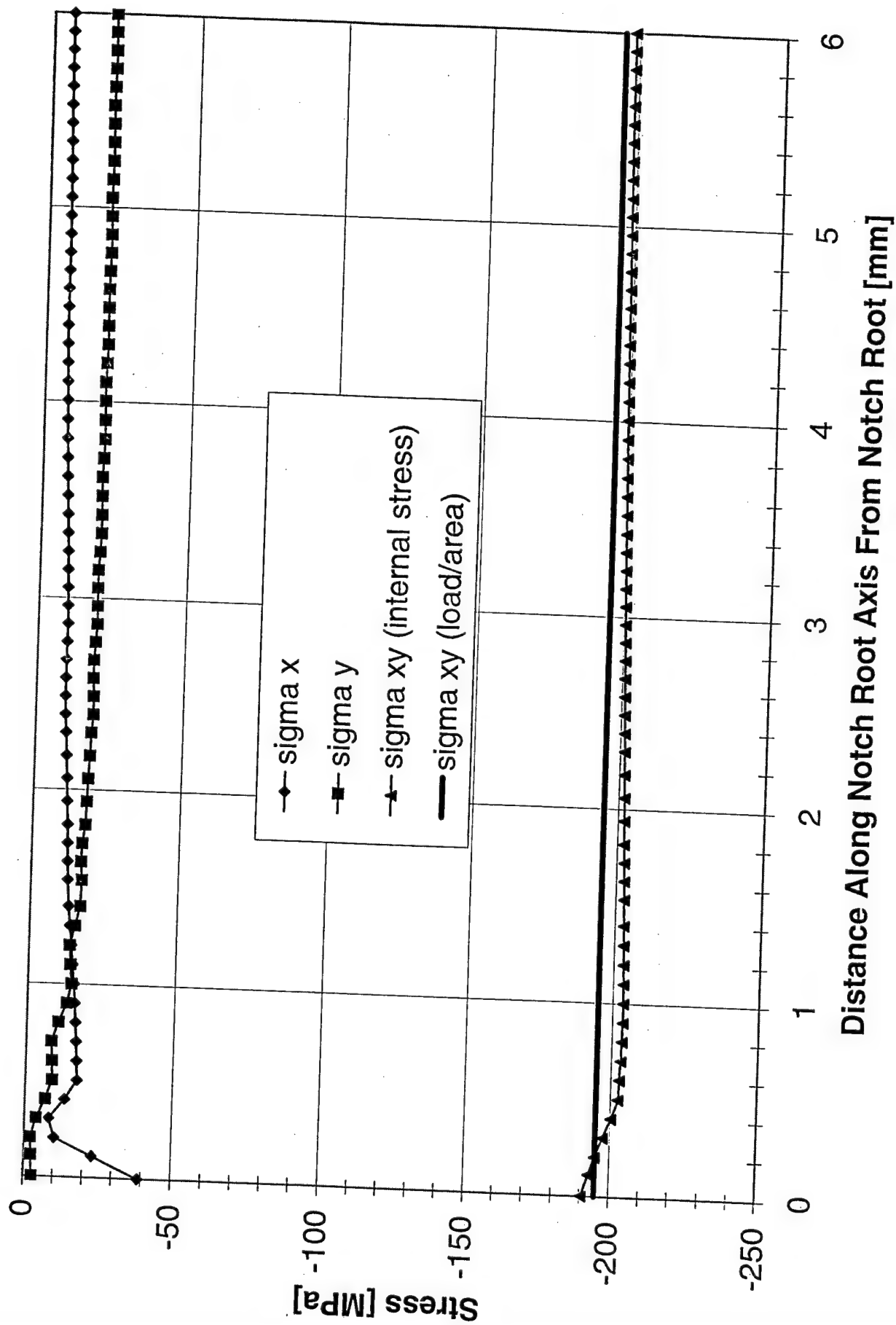
FIGURE 18

MICRO-AND MESOMECHANICS OF 8-HARNESS SATIN WOVEN FABRIC COMPOSITES: I – EVALUATION OF ELASTIC BEHAVIOR

K. Searles*, G. Odegard** and M. Kumosa**[1]

*Department of Materials Science and Engineering
Oregon Graduate Institute of Science and Technology
20000 N. W. Walker Rd., Beaverton, OR 97006-8921, USA

**Center for Advanced Materials and Structures
Department of Engineering
University of Denver
2390 South York, Denver, CO 80208, USA

Abstract

In Part I of this two-part paper, simplified two-dimensional micromechanics and mesomechanics models have been introduced to predict the elastic behavior of 8-harness satin (8HS) woven fabric composites. The woven warp and fill tows were independently treated as unidirectional composites and composite cylinder assemblage (CCA) theory was adopted to predict tow elastic properties from constituent fiber and matrix properties. Since evaluation of woven lamina stiffness requires an accurate description of tow geometry, a method was also developed to describe arbitrary tow geometries by mathematically fitting cubic splines and/or polynomials to micrographs of composite cross-sections. Finally, classical lamination theory was introduced to determine the overall elastic behavior of an n-layered composite laminate, assuming the woven lamina was a modified, two-layer laminate.

---

[1] To whom correspondence should be addressed.

The simplified mechanics model was evaluated using results from numerical strain energy and equivalent force approaches and results from a series of experimental Iosipescu shear tests and off-axis tensile tests on T650-35(3k), 8HS woven graphite-PMR 15 composites. Issues regarding exclusion of a matrix layer in the simplified, 2-layer laminate analysis were addressed in the strain energy analysis of an idealized 3-D, representative volume element. The mechanics model was found adequate in estimating the lower bounds of 8HS woven fabric, composite elastic properties. The model also provided a reasonable estimation of symmetric cross-ply composite properties.

1 INTRODUCTION

There has been a growing interest, particularly in the last 10 years, to use composite materials in structural component applications primarily within the military and aerospace sectors. Although these sectors drive the greatest use of composites on a percent weight basis, focus is shifting towards expanding use in commercial applications where higher strength-to-weight ratios, damage tolerance and near net-shapability are important considerations. Of the numerous classes of composite material systems employed for use in structural applications ranging from aircraft and space structures to automotive and biomedical applications, unidirectional (UD) composite systems have received the most treatment. However, UD composites are limited in applications requiring orthogonal reinforcement, increased intra- and interlaminar shear strength, better impact resistance and near net-shapability over complex geometries. Orthogonal woven fabric or textile composites overcome some of the aforementioned limitations found in UD composites.

Woven fabric composites are formed by the process of interlacing two individual fiber bundles or tows perpendicular to one another and impregnating with a matrix to form a layer. Each layer is stacked in some desired orientation and cured to form a laminate. The crosswise tows are referred to as fill or weft tows and the lengthwise weaver tows are referred to as warp tows. The pattern of interlacing warp tows with weft tows is fundamental in defining and classifying a two-dimensional (2-D) weave. In referring to a 2-D weave pattern, it is useful to describe the type of pattern by the number of weft tows interlaced (n_i-1) within a

2

given repeating unit or cell. Thus, a plain weave ($n_i = 2$) interlaces every other weft tow, a twill weave ($n_i = 3$) interlaces after every 2nd weft tow, a four-harness satin (4HS, $n_i = 4$) after every 3rd, a 5HS ($n_i = 5$) after every 4th and an 8HS ($n_i = 8$) after every 7th weft tow. There are several advantages associated with the tow interlacing such as increased intra- and interlaminar shear strength, impact resistance and near net-shape part production. The tradeoff with these benefits is the loss of in-plane strength and stiffness, which depends on the number of fibers aligned within the plane of interest. Obviously, when micro- and mesoscale geometric features and processing parameters contribute to the overall mechanical behavior of woven fabric composites, reasonable models are needed that account for this variation to provide sound design data.

The analytical and numerical treatments adopted for evaluating the performance of textile structural, reinforcing composite materials are not as well established compared to UD composite reinforcing materials. One reason the level of understanding has not reached the maturity that it has for UD composites is purely due to composite material and processing design evolution. Primarily though, a precise understanding of textile structural composite, thermomechanical behavior is tied directly to the level of complexity. Behavior of these composite architectures is dictated by a greater number of geometric and processing parameters vis-à-vis UD composite architectures. Parameters such as fabric lamina structure (weave style, tow density, fabric count, tow crimp, warp/fill tow characteristics) and fabric laminate structure (lamina sequence, lamina orientation, asymmetry, balance) greatly influence the composite behavior under multiaxial loading, in-service conditions. Under such conditions, these parameters may result in coupled interactions, thus complicating the nature of the problem. Therefore, it is necessary to either account for as many parameters as possible, or make reasonable assumptions/simplifications when developing analytical and numerical techniques to analyze woven fabric composite behavior. What follows is an account of analytical models found in the literature for analysis of woven fabric composite laminae.

Several researchers have addressed the need for computationally efficient analytical models to predict the elastic properties and overall mechanical behavior of woven fabric

composites, primarily plain weave composites. Ishikawa and Chou [1-3] have developed three models (later modified by Raju and Wang [4]), viz. the mosaic model, the crimp or fiber undulation model and the bridging model. The one-dimensional mosaic model idealized the fabric structure as an assemblage of asymmetric pieces of cross-ply laminates by omitting tow continuity and interlacing. Stiffness constants were evaluated based on the assumption of either isostrain (parallel) or isostress (series) conditions. Variation in stress and strain near the interlaced regions was neglected and the model provided reasonable upper and lower bounded solutions to in-plane stiffness constants.

The one-dimensional crimp or fiber undulation model extended the series mosaic model to include tow continuity and undulation, but only in the direction of applied load. The undulated tow was also treated as a single fiber, hence tow cross-sectional shape was excluded. This model was particularly suited for fabrics with a minimal number of fill tows per warp tow exchange (n_g), such as defined by a plain weave. The stiffness constants predicted by this model were lower than those predicted by the series mosaic model because transformed, reduced stiffness was evaluated as a function of the local off-axis angle in the filling direction. For satin weave architectures, the two-dimensional bridging model was proposed and this model was essentially a combination of the series and parallel models, again with continuity and undulation considered only in the direction of applied load. For this model, it was postulated that the regions immediately surrounding either end of the interlaced region acted as load bridges and regions immediately adjacent had the same average mid-plane strain and curvature. Comparisons made with experimental results for satin weave composites showed good agreement.

Naik *et al.* [5-8] developed a two-dimensional model to account for fiber continuity and undulation in both the warp and fill tow directions. The model idealized tow geometry with equations of periodic functions that constrained a tow to conform to the mutually orthogonal tow. For plain weaves with a closed architecture, i.e. adjacent tows in contact, the resemblance was a good match, however asymmetry resulted in open weaves if the gap was not taken into account. Woven fabric lamina in-plane, elastic constants were determined by

4

homogenization of through-thickness properties (from lamina slices cut off-axis or on-axis) and assembling slices in a series-parallel (SP) or parallel-series (PS) fashion. The upper bounded prediction of elastic moduli from the 2-D PS model was less than the parallel mosaic model and greater than the series mosaic model, while the lower bounded prediction from the 2-D SP model was less than the series mosaic model.

To more accurately represent both the open and closed plain weave geometries, Walsh and Ochoa [9] developed a revised set of three-dimensional shape equations. Their model did not constrain the tows to conform, thus the representation of the lamina by successive cross-sections was symmetric and correct for open weaves. However, the model did assume periodic functions and lenticular (idealized), cross-sectional tow shapes exhibiting two-axis symmetry. The mathematical moduli were homogenized with respect to the global coordinates by through-thickness integration and in-plane, average elastic properties were found by simultaneous solutions to homogenization processes along the fill and warp directions. Comparisons to experimentally determined apparent properties for S-RIM, plain weave composites showed quite good agreement.

1.1 One-Dimensional Characterization

The one-dimensional fiber crimp model considers continuity and undulation in the filling direction with a cross-sectional slice at $x = 0$ described by the shape functions due to Ishikawa and Chou (refer to Figure 1) as

$$h_1(y) = \left(\begin{array}{ccc} 0 & \leftarrow & \left(0 \leq y \leq a_0\right) \\ \left[1 + \sin\left\{\left(y - \dfrac{a}{2}\right)\dfrac{\pi}{a_u}\right\}\right]\dfrac{h_t}{4} & \leftarrow & \left(a_0 \leq y \leq a_2\right) \\ \dfrac{h_t}{2} & \leftarrow & \left(a_2 \leq y \leq \dfrac{n_g a}{2}\right) \end{array} \right)$$

(1)

$$\downarrow$$

$$h_2(y) = \begin{cases} \dfrac{h_t}{2} & \leftarrow & (0 \leq y \leq a_0) \\[2mm] \left[1 - \sin\left\{\left(y - \dfrac{a}{2}\right)\dfrac{\pi}{a_u}\right\}\right]\dfrac{h_t}{4} & \leftarrow & \left(a_0 \leq y \leq \dfrac{a}{2}\right) \\[2mm] -\left[1 + \sin\left\{\left(y - \dfrac{a}{2}\right)\dfrac{\pi}{a_u}\right\}\right]\dfrac{h_t}{4} & \leftarrow & \left(\dfrac{a}{2} \leq y \leq a_2\right) \\[2mm] -\dfrac{h_t}{2} & \leftarrow & \left(a_2 \leq y \leq \dfrac{n_g a}{2}\right) \end{cases}$$

The extension, extension-bending coupling and bending stiffness matrices, that is A_{ij}, B_{ij}, and D_{ij}, are evaluated by assuming that classical lamination theory is applicable to infinitesimal slices of d_y along the y-axis. This being the case, the extension stiffness matrix, as an example, is found by integrating the in-plane mathematical moduli for each constituent through-thickness. Over the range of $0 \leq y \leq \dfrac{a}{2}$, the summation of the average moduli with respect to the local off-axis angle ζ gives A_{ij} according to the following equation from [1-3]:

$$A_{ij}(y) = \int_{-\frac{h}{2}}^{h_1(y)-\frac{h_t}{2}} Q_{ij}^M \, dz + \int_{h_1(y)-\frac{h_t}{2}}^{h_1(y)} Q_{ij}^F(\zeta) \, dz + \int_{h_1(y)}^{h_2(y)} Q_{ij}^W \, dz + \int_{h_2(y)}^{\frac{h}{2}} Q_{ij}^M \, dz \qquad (2)$$

where the superscripts M, F and W denote the matrix, fill and warp constituents. The local off-axis angle is given by $\zeta(y) = \arctan(dh_1(y)/dy)$. The fill tow matrix of local mathematical moduli is expressed in terms of the undulation angle in the filling direction and the constituent tow elastic properties:

$$Q_{ij}^F(\zeta) = \begin{bmatrix} \dfrac{E_{xx}^F(\zeta)}{D_v} & \dfrac{E_{xx}^F(\zeta)v_{yx}^F}{D_v} & 0 \\[3mm] \dfrac{E_{xx}^F(\zeta)v_{yx}^F}{D_v} & \dfrac{E_{xx}^F(\zeta)}{D_v} & 0 \\[3mm] 0 & 0 & G_{xy}^F(\zeta) \end{bmatrix} \qquad (i,j=1,2,6) \qquad (3)$$

where the following relationship holds:

$$D_v = \frac{1-\left(v_{yx}^F(\zeta)\right)^2 E_{xx}^F(\zeta)}{E_{yy}^F(\zeta)} \tag{4}$$

Expressions in the manner of Eq. 2 can also be written for the extension-bending coupling and bending stiffnesses over all regions. The expressions for the A_{ij}, B_{ij}, D_{ij} stiffnesses can be expanded in terms of lamina thickness and explicitly stated for $0 \leq y \leq \frac{a}{2}$ as

$$A_{ij}(y) = Q_{ij}^M\left[h_1(y)-h_2(y)+h-\frac{h_t}{2}\right]+Q_{ij}^F(\zeta)\frac{h_t}{2}+Q_{ij}^W\left[h_2(y)-h_1(y)\right]$$

$$B_{ij}(y) = \frac{1}{2}Q_{ij}^F(\zeta)\left[h_1(y)-\frac{h_t}{4}\right]h_t + \frac{1}{4}Q_{ij}^W\left[h_2(y)-h_1(y)\right]h_t \tag{5}$$

$$D_{ij}(y) = \frac{1}{3}Q_{ij}^M\left\{\left[h_1(y)-\frac{h_t}{2}\right]^3 - h_2^3(y)+\frac{h^4}{4}\right\}$$
$$+\frac{1}{3}Q_{ij}^F(\zeta)\left[\frac{h_t^3}{8}-\frac{3h_t^2 h_1(y)}{4}+\frac{3h_t h_1^2(y)}{2}\right]+\frac{1}{3}Q_{ij}^W\left[h_2^3(y)-h_1^3(y)\right]$$

1.2 Two-Dimensional Characterization

The two-dimensional series-parallel (SP) and parallel-series models (PS) consider fiber continuity and undulation in both the warp and filling directions. Referring to the weave cross-sections (X-Z, Y-Z) shown in Figures 2 and 3, the regions a_1 to a_5 and b_1 to b_5 are given by Naik *et al.* as follows:

$$a_1 = \frac{1}{2}\left(a_{warp}-u_{fill}\right); \; a_2 = \frac{1}{2}a_{warp}; \; a_3 = \frac{1}{2}\left(a_{warp}+g_{warp}\right); \; a_4 = \frac{1}{2}\left(a_{warp}\right)+g_{warp}; \; a_5 = \frac{1}{2}\left(a_{warp}+u_{fill}\right)+g_{warp} \tag{6}$$

$$b_1 = \frac{1}{2}\left(a_{fill}-u_{warp}\right); \; b_2 = \frac{1}{2}a_{fill}; \; b_3 = \frac{1}{2}\left(a_{fill}+g_{fill}\right); \; b_4 = \frac{1}{2}\left(a_{fill}\right)+g_{fill}; \; b_5 = \frac{1}{2}\left(a_{fill}+u_{warp}\right)+g_{fill}$$

7

The two-dimensional shape equations are determined by taking through-thickness slices of a plain weave unit cell across the warp tow (Y-axis @ y = 0) and across the fill tow (X-axis @ x = 0). The shape equations are written to idealize the geometry of the on-axis fill tow or off-axis warp tow according to periodic functions in terms of the bounds described by regions in Eq. 6. The functions constrain the geometry of the on-axis tow to follow the off-axis tow, which is suitable for closed-gap architectures. These functions due to [6] are given by

$$
hx_1(x) = \begin{cases} \dfrac{h_{warp} - h_{fill}}{2} & \leftarrow & 0 \leq x \leq a_1 \\[2ex] \left[1 + \sin\left\{\dfrac{\pi(x - a_3)}{u_{warp} + g_{fill}}\right\}\right]\dfrac{h_{fill}}{2} + \dfrac{h_{warp} - h_{fill}}{2} & \leftarrow & a_1 \leq x \leq a_5 \\[2ex] \dfrac{h_{warp} + h_{fill}}{2} & \leftarrow & a_5 \leq x \leq \left(a_{fill} + g_{fill}\right) \end{cases}
$$

$$
hx_2(x) = \begin{cases} \dfrac{h_{fill} + h_{warp}}{2} & \leftarrow & 0 \leq x \leq a_1 \\[2ex] \left[\dfrac{h_{fill} + h_{warp}}{2} - hx_1(a_2)\right]\cos\left\{\dfrac{\pi(x - a_1)}{u_{warp}}\right\} + hx_1(a_2) & \leftarrow & a_1 \leq x \leq a_2 \\[2ex] -\left[\dfrac{h_{fill} + h_{warp}}{2} - hx_1(a_2)\right]\cos\left\{\dfrac{\pi(x - a_5)}{u_{warp}}\right\} + hx_1(a_2) & \leftarrow & a_4 \leq x \leq a_5 \\[2ex] -\dfrac{h_{fill} + h_{warp}}{2} & \leftarrow & a_5 \leq x \leq \left(a_{fill} + g_{fill}\right) \end{cases}
\tag{7}
$$

Since the geometry of mutually orthogonal tows of the plain weave are constrained to conform as given by Eq. 7, it is expected that the local off-axis angle of undulation for the warp tow is identical to the derivative of the fill tow undulation. With this, the local off-axis angle of undulation for the warp tow is given by

$$
\zeta_w(y) = \tan^{-1}\left\{-\dfrac{h_{fill}}{2}\left(\dfrac{\pi}{u_{warp}}\right)\sin\left[\dfrac{\pi(y - b_1)}{u_{warp}}\right]\right\} \qquad b_1 \leq y \leq b_2
\tag{8}
$$

$\downarrow$

8

$$\zeta_w(y) = \tan^{-1}\left\{-\frac{h_{fill}}{2}\left(\frac{\pi}{u_{warp}}\right)\sin\left[\frac{\pi\left(\dfrac{u_{warp}}{2}\right)}{u_{warp}}\right]\right\} \qquad b_2 \le y \le b_3$$

The extension, extension-bending coupling and bending stiffnesses are evaluated from the mathematical moduli for each constituent of the infinitesimal (dx or dy) slices, identical to the procedure outlined for one-dimensional characterization. The SP approach then adopts a two-step assembly scheme to determine the elastic constants of the plain weave, fabric lamina. First, all infinitesimal, through-thickness slices along the applied loading direction (on-axis) are assembled assuming an isostress condition. Second, all cross-sections on-axis are assembled assuming an isostrain condition. Accordingly, the average, in-plane compliances on-axis are found from [6]

$$\overline{a}_{ij}^f(y), \overline{b}_{ij}^f(y), \overline{d}_{ij}^f(y) = \left(a_{warp} + g_{warp}\right)^{-1} \int_0^{a_{warp}+g_{warp}} a_{ij}(x,y), b_{ij}(x,y), d_{ij}(x,y)\,dx \qquad (9)$$

giving an upper bounded approximation for each section. Here, the extension-bending coupling compliance is prescribed as zero for the plain weave architecture. The average, in-plane stiffness constants are found by integrating the inverted, average compliances from Eq. 9 with an isostrain condition according to

$$\overline{A}_{ij}^{fw}, \overline{B}_{ij}^{fw}, \overline{D}_{ij}^{fw} = \left(a_{fill} + g_{fill}\right)^{-1} \int_0^{a_{fill}+g_{fill}} \overline{A}^f_{\ ij}(y), \overline{B}^f_{\ ij}(y), \overline{D}^f_{\ ij}(y)\,dy \qquad (10)$$

where the integrands represented a lower bounded approximation due to the inversion of the upper bounded compliances. Likewise, the assembled extension-bending coupling stiffness is also prescribed as zero. Alternatively, the PS approach merely reverses the order of integration (assembly) in the SP scheme to determine the elastic constants.

1.3 Three-Dimensional Characterization

The main difference in the approach due to [9] is in defining the shape equations based on periodic functions that describe the tow centerline and tow perimeter explicitly, thus avoiding constrained tow geometries and asymmetry in open gap, plain weave architectures. Here, the gap defined by observations of micrographs from S-RIM composite cross-sections is accounted for in terms of the period of undulation given by an idealization of the mutual tow.

$$\psi_{fill} = 2\left(a_{warp} + g_{warp}\right)$$

$$\psi_{warp} = 2\left(a_{fill} + g_{fill}\right)$$

(11)

Since the period ψ of each tow undulation is independently defined in terms of the off-axis tow width a and gap g, the local off-axis angle of undulation for the warp tow is not identical to the derivative of the fill tow, hence the orthogonal tow geometries are not constrained to conform. In arriving at the shape equations that describe the upper and lower warp or fill tows independently of each other, the tow centerlines are modeled according to the prescribed height of the off-axis tow. The cosine functions describing the centerlines ξ_{fill} and ξ_{warp} are given by

$$\xi_{fill} = -\left(\frac{h_{warp}}{2}\right)\cos\left[\frac{2\pi(x - a_1)}{\psi_{fill}}\right]$$

$$\xi_{warp} = \left(\frac{h_{fill}}{2}\right)\cos\left[\frac{2\pi(y - b_1)}{\psi_{warp}}\right]$$

(12)

A comparable set of cosine functions, referenced from the centerlines, describe the orthogonal tow cross-sectional perimeters bounded by the regions 0 to (a_{warp} + g_{warp}) and 0 to (a_{fill} + g_{fill}). A process similar to that described for two-dimensional characterization is adopted for evaluating the elastic constants once the shape functions and local off-axis undulation angles have been established. As noted by Walsh, this method does not inadvertently force larger local angles of undulation for open architectures where increasingly smaller undulation angles

10

are expected due to the presence of a gap between adjacent tows. In other words, an open weave architecture is not prescribed to follow the same geometry as a closed weave architecture. Because of this, a more accurate estimation of the off-axis stiffness leads to greater accuracy in predicting the remaining in-plane, elastic constants for the plain weave laminae.

1.4 Numerical Schemes

Several numerical models have also been proposed to predict the elastic properties and overall mechanical behavior of plain weave fabric composites. Zhang and Harding [10] developed a model based on the finite element method for micromechanics analyses and principle of strain energy equivalence. Although the plain weave fabric lamina was modeled considering undulation in one direction, it was suggested that a two-dimensional case should be considered. A more representative case of the actual plain weave unit cell was developed by Blackketter *et al.* [11] The tow cross-sectional aspect ratio, obtained from micrographs, was included in the finite element model and the observed fiber volume fraction was obtained by iteration. Tows were assumed to conform perfectly to each other, resulting in a mathematically continuous model. An incremental iterative finite element algorithm was developed to analyze tensile loading responses, shear loading responses and estimate the effects of damage by stiffness reduction.

Extensive work on 2-D and 3-D finite element analyses of plain weave fabric composites has been done by Whitcomb *et al.* [12-14] A new 2-D finite macro element was developed and evaluated to account for element spatial variation of material properties. Detailed stress analyses of plain weave fabric composites were also performed using a global/local finite element method. It was found that surface stress distributions differed from internal stress distributions and failure behavior was influenced by a geometric feature defined as the tow waviness ratio. Effective elastic moduli were also found to be sensitive to the tow waviness ratio and increasing tow waviness in plain weave composites, subjected to uniaxial tensile loads, resulted in initial failure due to high transverse normal stress. In this case, the

11

particular failure mode was 0° fiber tow separation. When the tow waviness decreased, the initial failure mode was 0° fiber tow fracture from high longitudinal stress. The deformation behavior also tended towards that of cross-ply laminates.

The objectives of the current work are twofold: 1) develop a simplified two-dimensional micro-to-mesomechanics model suitable for estimating the elastic constants in 8-harness satin woven fabric composites, based on random tow cross-sectional shapes and tow arrangements lacking contiguity; 2) assess the validity of the simplified mechanics model by comparing the estimations to those obtained from 3-D finite element based, strain energy analyses and mechanical testing. The simplified mechanics model assumes that the woven 8HS fabric lamina may be treated as a 2-layered laminate if the micromechanics analysis is carried out using the woven fabric tow average V_f. The finite element model represents an idealized volume element (IVE) from a fabric unit cell and the IVE V_f is reached through an iterative process. A modified Iosipescu shear test [15-21] standard tension and off-axis tension tests [22] are used to determine the apparent composite elastic properties.

2 WOVEN 8HS GEOMETRY

As previously mentioned, there are several 2-D weave architectures for woven fabric composites. The simplest of patterns, the plain weave pattern, characterized by a one-over/one-under interlacing, reduces the composite stiffness and strength due to the frequent exchanges of tow positions from top to bottom. There are other patterns that reduce the number of exchanges and increase the length of the straight segments referred to as the "float". Of particular interest to the aerospace structural groups are the satin weave architectures, especially the eight-harness satin or 8-HS woven architecture. Since exchanges are minimal and the float is longer, the composite affords the opportunity to be formed into complex shapes (drape) while still providing a certain degree of mutually orthogonal reinforcement. A geometric feature unique to satin architectures is that of lamina asymmetry. There are predominantly warp tows on one side of the lamina while the other side is predominantly weft tows. The tow bends and interlace locations are also asymmetric, leading

12

to coupling between extension and bending as well as coupling between extension and in-plane shear, i.e. $B_{ij}/D_{ij} \neq 0$. Laminate symmetry and quasi-isotropic laminate behavior may be ascertained depending on the number of laminae considered and desired orientation during the layup sequence.

2.1 Examination of Lamina Geometry

Most textile processes produce patterns that are periodic in nature. That is, the patterns of interlaced tows or yarns repeat in one or two directions. The geometry and periodicity of a textile is conveniently described in terms of unit cells. What is unique in this definition is that the stress and strain distribution in a periodic textile composite is also periodic, provided the external loading conditions are uniform. When the external loads are not uniform, periodicity in the stress and strain distributions no longer exists. The term unit cell, borrowed from crystallography, defines the requirement that the complete textile pattern can be constructed from spatially translated copies of the unit cell without rotating or reflecting. The unit cell representation for an 8-HS woven fabric lamina is shown in Figure 4. Examination of the 8HS unit cell reveals that even further simplification is possible, leading to the smaller repeat unit sub-cell shown in Figure 5. In the course of analyzing the composite lamina behavior, it is commonplace to choose a modified square boundary of equivalent area to the hexagonal boundary for simplicity of calculation. By adopting the notation of Chou [23], the equivalent sub-cell major dimensions are given as:

hexagonal dimensions: **(3a) x (3a)**

simplified square dimensions: **($\sqrt{8}$a) x ($\sqrt{8}$a)**

where **a** is the width of the warp or weft tow. In addition to boundary generalizations, calculations are often reduced by assuming tow cross-sections of the following shapes: rectangular, perfectly elliptical and lenticular, i.e. shaped like a biconvex lens. The strain energy analyses presented in this paper assume the <u>model</u> geometry within the larger repeat unit, but the simplified mechanics approach <u>does not idealize</u> the tow cross-sectional shape as lenticular and symmetric. The model geometry is employed using the simplified dimensions only to facilitate ease in application of suitable prescribed displacement boundary conditions.

13

2.2 Woven Tow Cross-Section

Evaluation of woven composite lamina and laminate stiffness requires an accurate description of the woven tow geometry, including both the woven tow cross-section and tow centerline. Rather than assuming an idealized geometry described in terms of complimentary functions that force contiguity between the warp and fill tows, the particular shape of the 8HS woven tow cross-section observed in SEM micrographs (Figure 6) may be described by specific rational B-splines and polynomial functions where z = f(x or y), depending on the tow considered. If a given threshold[2] level is applied to the micrograph of the lamina cross-section, a binary image can be rendered that separates the tows from the matrix sufficiently to allow for boundary digitizing. As shown successively in Figures 7a and 7b, this technique permits an accurate tow rendition and recording of coordinate pairs ([x, z] or [y, z]) of points selected around the perimeter of the tow. The mathematical representation of the particular shape of a reproduced tow cross-section retains somewhat better accuracy if the perimeter is halved about an imaginary axis through the geometric center or centroid as given by

$$\overline{X} = \frac{\int_A x \, dA}{\int_A dA} \qquad \overline{z} = \frac{\int_A z \, dA}{\int_A dA} \qquad (13)$$

where $\overline{x}$ represents the x-coordinate of the warp tow centroid and the numerators are formulations of the "first moment" of the area element dA about the z and the x axes, respectively. The relationship is similar for locating the fill tow centroid.

Once the coordinate pairs are established for the upper and lower half of the tow cross-section (with respect to the centroid), the points can be joined using a piecewise polynomial interpolation method such as spline interpolation. The simplest continuous

---

[2]

 Thresholding implements an algorithm to select all regions of pixels having similar contrasts and applies the same color level to these regions, either black or white in the case of a binary threshold. Levels of threshold are determined by locations on a histogram range from 0-255.

polynomial approximation would be by piecewise linear functions. However, corners would exist that are not representative of the actual tow cross-sectional shape. More practical, natural-ended, cubic splines $p(x)$ are adopted to join the points along the perimeter and are given by cubic polynomials of the following form:

$$p_j(x) = a_{j0} + a_{j1}(x - x_j) + a_{j2}(x - x_j)^2 + a_{j3}(x - x_j)^3 \tag{14}$$

Cubic splines on an interval $a \leq x \leq b$ corresponding to the space between two points or nodes have, by definition, continuous first and second derivative everywhere in that interval. The cubic polynomial coefficients are determined using Taylor's formula to obtain

$$a_{j0} = p(x_j) = f_j$$

$$a_{j1} = p'_j(x_j) = k_j$$

$$a_{j2} = \frac{1}{2} p''_j(x_j) = \frac{3}{h^2}(f_{j+1} - f_j) - \frac{1}{h}(k_{j+1} + 2k_j) \tag{15}$$

$$a_{j3} = \frac{1}{6} p'''_j(x_j) = \frac{2}{h^3}(f_j - f_{j+1}) + \frac{1}{h^2}(k_{j+1} + k_j)$$

The strain energy minimization by using splines to fit curves through points is proportionate to the square of the second derivative of the spline. Curve fits chosen by natural splines result in a linear graph of the interval endpoints because natural splines are functions that result in the integral tending towards zero as follows:

$$\int_a^b p''(x)^2 \, dx \to 0 \tag{16}$$

2.3 Woven Tow Centerline

The geometric description of the warp or fill tow centerline is approached in the same manner

15

as the description of the tow cross-section. An appropriate threshold level is applied to an SEM micrograph of the lamina or laminate edge (see Figure 8a), rendering a binary outline of the woven tow path as it passes over or under a mutually orthogonal tow (fill). To arrive at coordinate pairs for points representing the tow centerline, the path thickness represented by Figure 8b must be divided evenly along the path with respect to an imaginary axis through the geometric center of the orthogonal tow. By advancing in increments along the path and determining the new centroid at each increment, the difference between z-coordinates of the upper and lower digitized points (path perimeter) yields a new point that coincides with the centroid. Necessarily, the tow centerline and geometric center of the tow should be identical. Piecewise polynomial approximations for natural-ended splines that satisfy Eq. 16, as previously described, are also used to connect the centerline points in a continual fashion.

2.4 Woven Tow Surfaces

Once the particular geometry of the woven tow cross-sections and centerlines is known, upper and lower tow surfaces may be accurately described by two-dimensional approximations in terms of $z = f(x, y)$. Additionally, rendition of tow volumes is possible by extruding either the warp or fill tow cross-section along the path defined by its mutually orthogonal centerline. At this stage, it also possible to delineate the adjacency of neighboring tows in both closed and open weave architectures and characterize the requisite lamina and laminate volume fractions. Figure 9 displays such an arrangement of upper fill tow surfaces created from two-dimensional, piecewise approximations with the local off-axis angle of undulation given as ζ and in-plane dimensions defined according to reduction of the 8HS woven unit cell.

The simplest case of describing the lamina geometry assumes that the lower fill tow surfaces are reflections of the upper fill tow surfaces along the z-axis, and the resulting set of fill tow volumes is a reflection of the mutual warp tow volumes rotated 90° about an imaginary z-axis (through the interlace). Although it is certainly plausible that variations in tow cross-sections arise from the manufacturing process, inaccuracies in lamina stiffness

16

calculations are trivial compared with those stemming from discrepancies in constituent properties and volume fractions.

3 MICROMECHANICS APPROACH

A suitable laminate analysis for carbon fiber based, woven fabric composites distinctly emerges from three structural scales due to inherent differences between constituent material properties and lamina architectures. At the micromechancs scale, it is beneficial to analyze the interactions between individual fibers, fiber bundles and the surrounding matrix. Composite Cylinder Assemblage (CCA) theory is usually employed and affords simple, closed-form solutions to predict effective elastic properties at this scale by treating the constituent phases as transversely isotropic. At the mesomechanics scale, the complex lamina geometry is either simplified to facilitate the ease of computations or the geometry is represented by periodic shapes and trigonometric functions. Judicious use of classical lamination theory is applicable at the mesoscale to homogenize through-thickness properties and arrive at Cartesian planar stiffness constants in terms of thickness cross-sections, i.e. mathematical moduli - Q_{ij}'s. Average laminae compliances or stiffnesses are found, depending on the order of integration, by assuming isostress and isostrain conditions during the assembly of infinitesimal thickness slices. Prediction of macroscale laminate elastic properties involves application of classical lamination theory an additional time to homogenize mesoscale, lamina properties in terms of the total composite laminate thickness. The macroscale elastic behavior of the laminate is dependent on the ply arrangement and the values obtained at this scale can equally be compared to the apparent, experimental elastic properties.

3.1 Evaluation of Woven Tow Properties

A woven fabric lamina may be considered as a "composite within a composite" with the bundled tows, surrounded by a matrix, forming the 1st composite material and the woven lamina, surrounded by a matrix, forming the 2nd composite material. The least complicated approach to take in evaluating the elastic properties of the 8HS woven fabric tow, is to treat

17

individual tows as unidirectional composites composed of continuous arrays of fibers and surrounding matrix. In practice, the fiber-to-fiber "lattice" spacings and diameters are highly irregular, so it does not make much sense to evaluate fiber volume fraction based on the argument of maximum 2-D circle packing density (analogous to the Kepler Conjecture) with regular tessellations of the form

$$V_f^{hexagonal} = \frac{\pi}{2\sqrt{3}} \left(\frac{r}{R} \right)^2$$

$$V_f^{square} = \frac{\pi}{4} \left(\frac{r}{R} \right)^2$$

(17)

where $\mathbf{R}$ is half the center-to-center spacing of fibers and $\mathbf{r}$ is half the fiber diameter. Instead, it is more practical to evaluate fiber volume fraction based on observations and measurements of scanning electron micrographs taken from actual laminate cross-sections. Analyses of SEM images taken from several cross-sections lead to measured binary ratios (normalization of the number of white pixels to the total image area in pixels) in the range of 0.71/1.00 to 0.74/1.00 as shown in Figure 10 for the composites considered here. The measured binary ratios or area fractions can be considered to be an equivalent representation of the measured tow volume fractions if the phases are assumed to be infinitely long and continuous and if variations in tow-to-tow cross-sections are considered negligible. Once the ranges of measured volume fractions of fibers and constituent material properties are determined, CCA theory can be applied successfully to calculate the equivalent elastic properties, in the principal material directions, of the unidirectional composite laminae (warp and fill tows). Subsequently, classical lamination theory may also be applied to evaluate lamina and laminate properties.

3.2 Composite Cylinder Assemblage

The CCA model due to Hashin and Rosen [24-26] gives closed-form, analytical expressions for the effective elastic constants of a UD lamina where the transversely isotropic (assumed) fiber and matrix are modeled as concentric cylinders. The longitudinal Young's modulus $\mathbf{E_{11}}$

of the UD composite lamina is given by

$$E_{11} = E_{11}^f V_f + E_{11}^m V_m + \frac{4V_f V_m \left(v_{12}^f - v_{12}^m\right)^2}{\dfrac{V_m}{k_f} + \dfrac{V_f}{k_m} + \dfrac{1}{G_{23}^m}} \tag{18}$$

where the sub- and superscripts **f** and **m** denote material properties of the constituent fiber and matrix phases, respectively. The subscript 1 refers to the longitudinal fiber direction and the subscripts 2 and 3 refer to the directions transverse to the fiber. The matrix volume fraction is $V_m = (1 - V_f)$. The transverse Young's modulus E_{22} is a bounded solution and the bounds are given by

$$E_{22}^{UB} = \frac{4k_t^* G_t^{*UB}}{k_t^* + G_t^{*UB}\left(1 + \dfrac{4k_t^* v_{12}^2}{E_{11}}\right)} \tag{19}$$

$$E_{22}^{LB} = \frac{4k_t^* G_t^{*LB}}{k_t^* + G_t^{*LB}\left(1 + \dfrac{4k_t^* v_{12}^2}{E_{11}}\right)} \tag{20}$$

where the superscripts UB and LB are the upper and lower bounds of the solution to the transverse Young's modulus. Both the upper bounded and lower bounded solutions for E_{22} are dependent on the transverse bulk modulus k_t^* of the UD lamina and a bounded solution for the transverse shear modulus G_t^* as well.

$$k_t^* = \frac{k_m\left(1 - V_f\right)\left(k_f + G_{23}^m\right) + k_f V_f \left(k_m + G_{23}^m\right)}{\left(1 - V_f\right)\left(k_f + G_{23}^m\right) + V_f \left(k_m + G_{23}^m\right)} \tag{21}$$

Although more accurate solutions for G_t^* have been developed based on equivalent, homogeneous composite properties (single fiber surrounded by an equivalent composite instead of constituent matrix material), the concise forms are given as

19

$$G_t^{*UB} = G_{23}^m \left[1 + \frac{V_f \left(1 + \beta_m \right)}{\left(\dfrac{\gamma + \beta_m}{\gamma - 1} \right) - V_f \left(1 + \dfrac{3V_m^2 \beta_m^2}{V_f^3 \alpha + 1} \right)} \right] \qquad (22)$$

$$G_t^{*LB} = G_{23}^m + \frac{V_f}{\dfrac{1}{G_{23}^f - G_{23}^m} + \dfrac{V_m \left(k_m + 2G_{23}^m \right)}{2G_{23}^m \left(k_m + G_{23}^m \right)}} \qquad (23)$$

The bounds given by Eqs. 22 and 23 are acceptable solutions when the fiber transverse shear modulus is larger than the transverse shear modulus of the matrix and the fiber bulk modulus is larger than the matrix bulk modulus, that is when $G_{23}^f > G_{23}^m$ and $k_f > k_m$. If the opposite conditions exist, then the upper and lower bounds for the transverse shear modulus of the UD lamina are given by

$$G_t^{*UB} = G_{23}^m + \frac{V_f}{\dfrac{1}{G_{23}^f - G_{23}^m} + \dfrac{V_m \left(k_m + 2G_{23}^m \right)}{2G_{23}^m \left(k_m + G_{23}^m \right)}} \qquad (24)$$

$$G_t^{*LB} = G_{23}^m \left[1 + \frac{V_f \left(1 + \beta_m \right)}{\left(\dfrac{\gamma + \beta_m}{\gamma - 1} \right) - V_f \left(1 + \dfrac{3V_m^2 \beta_m^2}{V_f^3 \alpha + 1} \right)} \right] \qquad (25)$$

In either case, the following relationships hold for the fiber and matrix transverse bulk moduli with the fiber transverse bulk modulus defined as

$$k_f = \left(\frac{4}{E_{22}^f} - \frac{4\nu_{12}^{f2}}{E_{11}^f} - \frac{1}{G_{23}^f} \right)^{-1} \qquad (26)$$

20

and the matrix transverse bulk modulus defined as

$$k_m = \left(\frac{4}{E_{22}^m} - \frac{4v_{12}^{m2}}{E_{11}^m} - \frac{1}{G_{23}^m} \right)^{-1} \tag{27}$$

while relationships between the fiber and matrix transverse bulk and shear moduli are given as the following:

$$\beta_f = \frac{k_f}{k_f + 2G_{23}^f}, \quad \beta_m = \frac{k_m}{k_m + 2G_{23}^m} \tag{28}$$

$$\alpha = \frac{\beta_m - \gamma\beta_f}{1 + \gamma\beta_f} \qquad \gamma = \frac{G_{23}^f}{G_{23}^m} \tag{29}$$

The longitudinal shear modulus G_{12} and Poisson's ratio v_{12} of the UD composite lamina are

$$G_{12} = G_{12}^m \left(\frac{V_m G_{12}^m + G_{12}^f \left(1 + V_f\right)}{G_{12}^m \left(1 + V_f\right) + V_m \left(G_{12}^f\right)} \right) \tag{30}$$

$$v_{12} = v_{12}^f V_f + v_{12}^m V_m + \frac{V_f V_m \left(v_{12}^f - v_{12}^m\right)\left(\dfrac{1}{k_m} - \dfrac{1}{k_f}\right)}{\dfrac{V_m}{k_f} + \dfrac{V_f}{k_m} + \dfrac{1}{G_{23}^m}} \tag{31}$$

If the transverse Poisson's ratio v_{23} of the UD composite is desired, then a bounded solution can be given in terms of the upper or lower derivations of the transverse shear modulus as

$$v_{23} = \frac{E_{22}}{2G_t^*} - 1 \tag{32}$$

3.3 Strain Energy Equivalence

Accurate application of numerical methods to validate the elastic properties determined from the CCA model involves the analysis of a representative volume element (RVE). The RVE is modeled based on a periodic fiber packing sequence, and although the ideal square or hexagonal packing model given by Eq. 17 is chosen for simplicity, the numerical fiber volume fraction is made equivalent, by iteration, to the actual fiber volume fraction determined from SEM cross-sections. From a numerical standpoint, it is important that the RVE accurately represents periodicity and the accompanying periodic boundary conditions. Without such accuracy, the RVE elastic constants predicted will <u>not</u> be representative of the composite. If the proper choices are made for a periodic geometry and boundary conditions, the stress and strain states should also be periodic even though they are not necessarily uniform as in homogenous materials. By assuming strain energy equivalence, it can be shown (see Sun and Vaidya [27]) that subjecting the periodic RVE to appropriate surface tractions or displacements that would produce uniform stresses in a homogenous medium is valid here.

Macro-stress and strain, based on classical lamination theory pertaining to average moduli of homogenous media, are derived via an average of the stress and strain tensor over the RVE volume as follows where the average stress is given as

$$\sigma_{ij}^{ave} = \frac{1}{V} \int_V \sigma_{ij}(x,y,z)dV \tag{33}$$

and the average strain is given as

$$\varepsilon_{ij}^{ave} = \frac{1}{V} \int_V \varepsilon_{ij}(x,y,z)dV \tag{34}$$

According to strain energy equivalence criteria, the strain energy **U'** is stored in the heterogeneous RVE with a potential equivalent to external work **W'** done by a force acting

on the volume. It can be assumed that the difference in this strain energy and that of the homogeneous volume (U) yields the following relationship:

$$U'-U = \frac{1}{2} \int\limits_V \frac{\partial}{\partial x_j} \left[\sigma_{ij} \left(u_i - u_i^{ave} \right) \right] dV \tag{35}$$

where u_i represent boundary displacements. If the volume is discretized in such a manner that produces a large number of elements and nodes, the use of Eq. 35 becomes somewhat unwieldy to manage. In the place of the volume integral, the divergence theorem of Gauss can be applied to convert the volume integral into a surface integral by

in general

$$\iiint\limits_T div\, \mathbf{F}\ dV = \iint\limits_S \mathbf{F} \bullet \mathbf{n}\ dA \tag{36}$$

$$\iiint\limits_T \left(\frac{\partial F_1}{\partial x} + \frac{\partial F_2}{\partial y} + \frac{\partial F_3}{\partial z} \right) dx\, dy\, dz = \iint\limits_S \left(F_1 \cos\alpha + F_2 \cos\beta + F_3 \cos\gamma \right)\ dA$$

where $\mathbf{T}$ is a closed and bounded region in space whose boundary is a piecewise smooth surface S. If $\mathbf{F}(x, y, z)$ is a vector function that is continuous and has continuous first partials in the T domain, then $\mathbf{n}$ is the outwardly normal unit vector of S. Therefore, Eq. 35 becomes

$$U'-U = \frac{1}{2} \int\limits_S \sigma_{ij} \left(u_i - u_i^{ave} \right) n_j dS \tag{37}$$

Similarly, Gaussian divergence theorem may also be applied to the volume integral given in Eq. 34 to yield a relationship for tensorial strain in terms of a surface integral as given by the following:

$$\varepsilon_{ij} = \frac{1}{2V} \int\limits_S \left(u_i n_j + u_j n_i \right) dS \tag{38}$$

23

where V is the RVE volume, S is the boundary RVE surface, $\mathbf{u_i}$ is the ith component of displacement and $\mathbf{n_j}$ is the jth component of the outwardly normal unit vector. From Eq. 38, displacements can be prescribed on the boundary surface and tractions can be determined from resulting surface reactions to prescribed displacements. In all cases, it is assumed that the Cartesian and principal material coordinate systems are coincident.

Uniaxial Tensile Case (E_{xx}) - For the case of axial loading, a ¼ symmetry RVE can be modeled to determine the longitudinal tensile elastic modulus. The following boundary conditions are imposed (with node matching) on the finite element model shown in Figure 11:

$$\delta_x(0, y, z) = 0$$

$$\delta_x(0.5a, y, z) = \text{constant}$$

Clearly, Eq. 38 reduces to the more apparent definition of strain as given by

$$\varepsilon_{xx}^{ave} = \frac{1}{V} \int_S u_x n_x dS = \frac{\delta_x}{0.5a} \tag{39}$$

The average stress in the RVE can be determined by equating the external work to the strain energy stored within the RVE and solving [27]:

$$\frac{1}{2} P_x \delta_x = \frac{1}{2} \sigma_{xx}^{ave} \varepsilon_{xx}^{ave} V \tag{40}$$

therefore

$$\sigma_{xx}^{ave} = \frac{P_x}{(0.5b)(0.5c)} \tag{41}$$

Finally, the longitudinal tensile modulus and Poisson's ratio are obtained as follows, assuming a prescribed displacement (δ_x) of unity:

$$E_{xx} = \frac{P_x}{(0.5c)} \quad \text{and} \quad v_{xy} = -\left(\frac{\delta_y}{\delta_x}\right) \tag{42}$$

This is based on the premise that $a = b$ and P_x is the resultant surface reaction derived from the prescribed boundary conditions.

Transverse Tensile Cases ($E_{yy} = E_{zz}$) - Similarly, the transverse tensile elastic moduli E_{yy} and E_{zz} can be calculated, based on the above derivations, and by assuming that the following boundary conditions apply to the ¼ symmetry finite element model shown in Figure 11:

$$\delta_y(x, 0, z) = 0$$
$$\delta_y(x, 0.5b, z) = \text{constant}$$

$$E_{yy} = \frac{P_y}{(0.5a)} \quad \text{and} \quad \nu_{yz} = -\left(\frac{\delta_z}{\delta_y}\right) \tag{43}$$

$$\delta_z(x, y, 0) = 0$$
$$\delta_y(x, y, 0.5c) = \text{constant}$$

$$E_{zz} = \frac{P_z}{(0.5b)} \quad \text{and} \quad \nu_{zx} = -\left(\frac{\delta_y}{\delta_z}\right) \tag{44}$$

Longitudinal Shear Case (G_{xy}) - The case of longitudinal shear loading requires more specific boundary conditions imposed on a full representation of the square array, i.e. no planes of symmetry are assumed. Since this type of loading is independent of the long axis (axis parallel to the fiber), boundary conditions must be such that both the Y-Z planes at $x = 0$ and $x = 1.0a$ displace identically to each other. Ideally, this also implies that nodes on opposing faces share the same planar locations. To satisfy this requirement, the following boundary conditions are applied to the finite element model in Figure 12:

$$\delta_x(x, 0, z) = \delta_y(x, 0, z) = \delta_z(x, 0, z) = 0$$
$$\delta_x(x, 1.0b, z) = \text{constant}$$
$$\delta_y(x, 1.0b, z) = 0$$

To assure that both Y-Z planar surfaces at $x = 0$ and $x = 1.0a$ displace by an identical amount at every point on each surface, the additional prescribed boundary conditions are:

25

$$\delta_x(0, y, z) = \delta_x(1.0a, y, z)$$
$$\delta_y(0, y, z) = \delta_y(1.0a, y, z)$$
$$\delta_z(0, y, z) = \delta_z(1.0a, y, z)$$

As in the previous cases of deriving the axial and transverse tensile elastic constants, a similar solution for the longitudinal shear modulus is adopted from Sun and Vaidya and shown as well. Again, application of Gaussian divergence theorem to the RVE yields the following relationship for average, equivalent shear strain γ_{xy}:

$$\gamma_{xy}^{ave} = \frac{2}{V} \int_V \varepsilon_{xy} dV = \frac{1}{V} \int_S (u_x n_y + u_y n_x) dS \tag{45}$$

Accordingly, by equating the external work to the strain energy stored within the RVE [27] and reducing Eq. 45 according to prescribed boundary conditions:

$$\gamma_{xy}^{ave} = \frac{\delta_{xy}}{(0.5b)(0.5b)} \quad \text{and} \quad \frac{1}{2} P_{xy} \delta_{xy} = \frac{1}{2} \sigma_{xy}^{ave} \gamma_{xy}^{ave} V$$
$$\downarrow \tag{46}$$
$$\sigma_{xy} = \frac{P_{xy}}{2(0.5a)(0.5c)}$$

therefore, the longitudinal shear modulus is given by

$$G_{xy} = P_{xy} \Big/ (0.5c) \tag{47}$$

based on the premise that $\mathbf{a} = \mathbf{b}$ and $\mathbf{P_{xy}}$ is the resultant surface reaction derived from the prescribed boundary conditions. This analysis can also be employed for the case of transverse shear (G_{yz}) similarly. An alternate set of boundary conditions are imposed to deform the RVE (Figure 12) in a manner such that it forms an unrestricted parallelepiped about the fiber axis:

$$\delta_x(x, y, 0) = \delta_x(x, y, 1.0c) = \delta_x(x, 0, z) = \delta_x(x, 1.0b, z) = 0$$
$$-[\delta_y(x, y, 0)] = \delta_y(x, y, 1.0c) = \text{constant}$$
$$-[\delta_z(x, 0, z)] = \delta_z(x, 1.0b, z) = \text{constant}$$

26

4 MESOMECHANICS APPROACH

At the mesoscale, classical lamination theory is considered applicable for evaluating the equivalent elastic properties of the woven fabric lamina. Several mathematical models [1-9] have previously been proposed to account for the woven fabric geometry in evaluating elastic properties, particularly for the plain, open and closed weave architectures. For satin weaves specifically, Ishikawa and Chou proposed the bridging model which was necessarily a combination of their series and parallel models. The 2-D bridging model treats the non-interlacing tows surrounding the interlaced region as an assemblage of cross-ply laminates that act as load bridges. Tow undulation is considered only in the loading direction while the cross-sectional geometry and orthogonal undulation are not considered. In this work, a simplified 2-D model is proposed for the 8HS woven architecture that accounts for actual undulation of mutually orthogonal tows and actual tow cross-sections, including random variation.

4.1 Evaluation of Woven Lamina Properties

The basic premise of the simplified 2-D model considers the 8HS, woven fabric lamina as a laminate having two layers and a V_f equivalent to that of the woven fabric tows. From the digitized reproduction of the tow centerlines and tow cross-sections by cubic spline interpolation, m^{th}-order polynomials are fitted according to the method of least-squares approximation. As an example, consider a straight line $z = a + bx$ or $z = c + dy$ (consistent with the previously established coordinate system) fitted through the given points $(x_1, z_1), \ldots, (x_n, z_n)$ or $(y_1, z_1), \ldots, (y_n, z_n)$ so that the sum of the squares of the distances of those points from the straight line is a minimum, where the distance is measured from the z-direction. The point ordinate $a + bx_j$ or $c + dy_j$ corresponds to an abscissa x_j or y_j. Therefore, the distance from (x_j, z_j) and (y_j, z_j) is $|z_j - a - bx_j|$ and $|z_j - c - dy_j|$, respectively. In general, a polynomial of degree **m** is given by

$$p(x) = b_0 + b_1 x + \cdots + b_m x^m \quad ; \quad m \leq n\text{-}1 \tag{48}$$

and the sum of the squares of the distances **q** takes the form given by

$$q = \sum_{j=1}^{n} \left(z_j - p(x_j) \right)^2$$

(49)

$$\frac{\partial q}{\partial b_0} = 0, \quad \cdots, \quad \frac{\partial q}{\partial b_m} = 0$$

where q depends on (m + 1) parameters b_0, ..., b_m and there are (m +1) conditions or minimums which give a system of (m + 1) normal equations. Upon extending the example for the case of a 2nd order, least-squares polynomial approximation with a quadratic polynomial of the following form

$$p(x) = b_0 + b_1 x + b_2 x^2$$

(50)

where the normal equations (summation from 1 to n implied) are given by

$$b_0 n \quad + b_1 \sum x_j + b_2 \sum x_j^2 = \sum z_j$$

$$b_0 \sum x_j + b_1 \sum x_j^2 + b_2 \sum x_j^3 = \sum x_j z_j$$

(51)

$$b_0 \sum x_j^2 + b_1 \sum x_j^3 + b_2 \sum x_j^4 = \sum x_j^2 z_j$$

This system is symmetric and solution to the unknowns b_0, b_1 and b_2 is accomplished by one of the more commonly used numerical methods such as Gauss elimination, Gauss-Seidel iteration or LU-factorization. A modified method of Gauss elimination with LU-factorization is employed to solve the system of normal equations for the unknowns in mth-order polynomial fits of the upper and lower tow cross-sectional perimeters and tow centerline as illustrated by Figures 13 and 14. The success criterion used for determining the appropriate polynomial order of fit is a coefficient of determination $R^2 \geq 0.95$.

4.2 Compliance Transformation

The equivalent elastic properties of the warp and fill laminae can be determined by evaluating the average, reduced compliance for the local off-axis angle of undulation. The local off-axis angle of undulation for the warp and fill tows is given by

$$\zeta_w(x) = \tan^{-1}\frac{\partial}{\partial x}[z = p(x)]$$

(52)

$$\zeta_f(y) = \tan^{-1}\frac{\partial}{\partial y}[z = p(y)]$$

where ζ is the local off-axis angle as represented in Figure 9 and z is given in terms of x or y and is equivalent to the least-squares polynomial approximation for either the warp or fill tow centerlines (defined by Eq. 48 for a mth-order polynomial). The particular off-axis angle reduces the effective elastic constants with respect to the Cartesian (global) coordinate directions. Solution to derivatives in (52) are the slopes of secant lines that approximate lines tangent to any segment of the least-squares polynomials. Unlike numerical integration which is a smoothing process, differentiation is much less accurate since the derivative is the limit of the difference quotient. The forward difference quotient tends to underestimate the derivative and the backward difference quotient tends to overestimate the derivative. The symmetric difference quotient provides the best approximation to the slope of the tangent line as Δx becomes smaller as is given by (example: warp tow centerline)

$$\frac{dz}{dx} = \lim_{\Delta x \to 0}\left[\frac{p(x + \Delta x) - p(x - \Delta x)}{2\Delta x}\right]$$

(53)

From Hooke's law, the constitutive relations of a UD lamina which relate strain to stress in terms of the compliance matrix S_{ij} can be expressed in the generalized form with contracted notation

29

$$\varepsilon_i = \sum_{j=1}^{6} S_{ij}\sigma_j \tag{54}$$

where i, j = 1, ..., 6 in reference to the material principal coordinate system x_1 - x_2 - x_3. For a UD lamina with fibers oriented at an angle ζ with respect to the Cartesian reference axis (see Figure 15), the generalized form of the constitutive relations in terms of the transformed reduced compliance matrix $\bar{S}_{ij}$ can be expressed as

$$\begin{bmatrix} \varepsilon_x \\ \varepsilon_y \\ \gamma_{xy} \end{bmatrix} = \begin{bmatrix} \bar{S}_{11} & \bar{S}_{12} & \bar{S}_{16} \\ \bar{S}_{12} & \bar{S}_{22} & \bar{S}_{26} \\ \bar{S}_{16} & \bar{S}_{26} & \bar{S}_{66} \end{bmatrix} \begin{bmatrix} \sigma_x \\ \sigma_y \\ \tau_{xy} \end{bmatrix} \tag{55}$$

In this case, the transformed reduced compliance constants $\bar{S}_{ij}$ where i, j = 1, ..., 6 can be written for the transversely isotropic warp or fill tows as follows (after [28]):

$$S_{11}(\zeta) = \frac{\cos^4(\zeta)}{E_{11}} + \left(\frac{1}{G_{12}} - \frac{2v_{12}}{E_{11}}\right)\cos^2(\zeta)\sin^2(\zeta) + \frac{\sin^4(\zeta)}{E_{22}}$$

$$S_{22}(\zeta) = \frac{1}{E_{22}}$$

$$S_{66}(\zeta) = \frac{\cos^2(\zeta)}{G_{12}} + \frac{\sin^2(\zeta)}{G_{23}} \tag{56a-e}$$

$$S_{12}(\zeta) = \frac{v_{21}\cos^2(\zeta)}{E_{22}} + \frac{v_{23}\sin^2(\zeta)}{E_{22}}$$

$$v_{21} = \frac{E_{22}}{E_{11}}v_{12}$$

The effective elastic properties for the equivalent warp and fill laminae are determined by

30

inverting the averaged local, transformed compliance. The average compliance is the mean integral value of the local compliance given as

$$\bar{S}_{ij}^{ave} = \frac{1}{\phi} \int_0^{\phi} \bar{S}_{ij}(\zeta) \, d\zeta \qquad (57)$$

where the limit of integration φ is defined as the maximum off-axis angle of warp or fill tow undulation. The maximum off-axis angle may be stated as

$$\phi_w = \max\left[\tan^{-1} \frac{\partial}{\partial x}[z = p(x)] \right]$$

$$\phi_f = \max\left[\tan^{-1} \frac{\partial}{\partial y}[z = p(y)] \right] \qquad (58)$$

and determined for the warp or fill tow centerline by utilizing techniques to sort the local off-axis angles into ascending order by numerical methods such as straight insertion, quicksort and Shell's method.

4.3 Application of Classical Lamination Theory

The elastic properties of the woven fabric lamina can be evaluated using classical lamination theory (CLT). Knowing the effective elastic properties of the warp and fill laminae, the lamina can typically be treated as a 3-layered laminate and evaluated at the V_f of that specific lamina. It is also proposed that the lamina can be treated as a 2-layered laminate and evaluated at a V_f equivalent to an average value for the woven warp and fill tows. Under the assumptions of the Kirchhoff conjecture for thin plates, the constitutive relations, in condensed form, are given as [23]

$$\left\{ \begin{array}{c} N \\ M \end{array} \right\} = \left[\begin{array}{c|c} A & B \\ \hline B & D \end{array} \right] \left\{ \begin{array}{c} \varepsilon_0 \\ \kappa_0 \end{array} \right\} \qquad (59)$$

31

where N and M are membrane stress and moment resultants, respectively. The strain and curvature of the laminate midplane are ε_o and κ_o. The [A], [B] and [D] (extensional, extensional-bending coupling, bending) stiffness matrices are evaluated accordingly by

$$\left[A_{ij},B_{ij},D_{ij}\right] = \sum_{k=1}^{n} \int_{h_{k-1}}^{h_k} \left(1,z,z^2\right)\left[\overline{Q}_{ij}\right]_k dz \quad (i,j=1,2,6)$$

$$\downarrow$$

$$\left[A_{ij}\right] = \sum_{k=1}^{n} \left(h_k - h_{k-1}\right)\left[\overline{Q}_{ij}\right]_k$$

$$\left[B_{ij}\right] = \sum_{k=1}^{n} \frac{1}{2}\left(h_k^2 - h_{k-1}^2\right)\left[\overline{Q}_{ij}\right]_k$$

$$\left[D_{ij}\right] = \sum_{k=1}^{n} \frac{1}{3}\left(h_k^3 - h_{k-1}^3\right)\left[\overline{Q}_{ij}\right]_k$$

(60a-c)

where $\left[\overline{Q}_{ij}\right]_k$ are the reduced mathematical moduli of the laminate k^{th}-layer corresponding to the lamina defined by a thickness $(h_k - h_{k-1})$. On the basis of assuming that the equivalent, 2-layered laminate is composed of UD laminae with transformed tows (fibers) in the x and y directions, the non-vanishing stiffness constants are given as

$$A_{11} = A_{22} = \frac{\left(E_{11} + E_{22}\right)h}{2D_v}$$

$$A_{12} = \frac{v_{12}E_{22}h}{D_v}$$

$$A_{66} = G_{12}h$$

$$B_{11} = -B_{22} = \frac{\left(E_{11} - E_{22}\right)h^2}{8D_v}$$

$$D_{11} = D_{22} = \frac{\left(E_{11} + E_{22}\right)h^3}{24D_v}$$

$$D_{12} = \frac{v_{12}E_{22}h^3}{12D_v}$$

$$D_{66} = \frac{G_{12}h^3}{12}$$

(61a-f)

where the following relationship is applies:

$$D_v = 1 - v_{12}v_{21}$$

In Eqs. 61a-f, E_{11} and E_{22} are the Young's moduli, G_{12} is the in-plane shear modulus and v_{12} is the Poisson's ratio determined from inversion of the averaged compliance given by Eq. 57.

In reference to the geometrical midplane of the 2-layered laminate, the total laminate thickness **h** is determined by evaluating the average warp and fill tow thicknesses $\mathbf{h_w}$ and $\mathbf{h_f}$. The average tow thicknesses can be determined by analysis of the least squares polynomial approximations **p(x, y)** to the perimeter of the tow cross-sections. Given a maximum tow width of **a**, the mean value of thickness $\pm\dfrac{h}{2}$, in reference to the midplane, is found by

$$h_w = \int_0^a p(x)\,dx = p(x^*)(a - 0)$$
$$\downarrow$$
$$\frac{1}{a-0}\int_0^a p(x)\,dx = p(x^*)$$

(62)

Assuming the polynomials were approximations to points defining the upper and lower perimeter about the geometric center of the respective tow (Eq. 13), then the thickness represents the sum of mean values evaluated by Eq. 62.

4.4 Numerical Strain Energy Method

With reference to the numerical strain energy approach adopted for verification of the micromechanics solution, a similar numerical analysis can also be employed to verify the results obtained from the simplified 2-D mesomechanics model. The 8HS woven fabric lamina repeat volume element is simplified to an idealized volume (IVE) having planar dimensions as suggested by Ishikawa and Chou [23]. Under presumptions similar to those for the treatment of thin homogeneous plates, the top and bottom lamina surfaces are left free of tractions, i.e. a single ply analysis. Lamina elastic constants are evaluated by prescribing linearly independent displacements suitable for the requisite state of deformation. As with the numerical verification of woven tow properties, a direct frontal or wavefront solver is used in the finite element analysis to compute macrostress components obtained from averaging

33

forces on IVE faces in the directions of interest. As an example, the macrostress component σ_{xx} in the Cartesian coordinate system can be obtained by

$$\sigma_{xx} = \frac{1}{\left(\sqrt{2}\,a\right)\left(h_t\right)} \sum_n F_R^{\{n\}}\left(x_1 = x = \sqrt{2}\,a,\ x_2 = y,\ x_3 = z\right) \tag{63}$$

where $F_R^{\{n\}}$ is the nodal reaction at the nth node on the face normal (at $x_1 = \sqrt{2}a$) and summation occurs over all nodes on that face. It is worthwhile to note that use of Eq. 63 in the manner presented is equivalent from a numerical perspective to the use of Eq. 33. Evolution of the IVE from the RVE is shown in Figure 16 where the lamina thickness (h_t) given above is influenced by the exact V_f determined from an iterative process.

In general, the equations for solving static and linear finite element analyses are of one of the following forms [29]:

$$[K]\{u\} = \{F\}$$

$$[K]\{u\} = \{F^a\} + \{F^r\} \tag{64}$$

where [K] represents the total stiffness matrix, $\{u\}$ is the nodal degree of freedom (DOF) vector and $\{F\}$ is decomposed into the applied load vector $\{F^a\}$ and the nodal reaction load vector $\{F^r\}$. The total applied load vector is the sum of the applied nodal load vector $\{F^n\}$ and total of all element load vector effects $\{F^e\}$. Nodal DOF values on every node can be obtained if boundary conditions are sufficient to guarantee a unique solution to Eq. 64. The nodal reaction load, i.e. the $\sum F_R^{\{n\}}$ in Eq. 63 considered for all pertinent DOF's where only the loads at imposed DOF are output can be written as

$$\{F^R\} = [K]\{u\} - \{F^n\} - \{F^e\} \tag{65}$$

Displacement boundary conditions are imposed on the lateral faces of the IVE in a manner that would produce uniform strains in an equivalent homogeneous medium. For instance, a uniform strain state in the warp direction (ε_{xx} in reference to the model shown in

34

Figure 17) implies that the following boundary conditions are applicable:

$$(\delta_x (0, y, z) - \delta_x (\sqrt{8}a, y, z) = \text{const.}) \qquad (\delta_x (x, 0, z) - \delta_x (x, \sqrt{8}a, z) = 0)$$

$$(\delta_y (0, y, z) - \delta_y (\sqrt{8}a, y, z) = 0) \qquad (\delta_y (x, 0, z) - \delta_y (x, \sqrt{8}a, z) = 0)$$

$$(\delta_z (0, y, z) - \delta_z (\sqrt{8}a, y, z) = 0) \qquad (\delta_z (x, 0, z) - \delta_z (x, \sqrt{8}a, z) = 0)$$

For the remaining planar states of deformation, the non-zero boundary conditions are

ε_{yy} $\qquad (\delta_y (x, 0, z) - \delta_y (x, \sqrt{8}a, z) = \text{const.})$

γ_{xy} $\qquad (\delta_x (x, 0, z) - \delta_x (x, \sqrt{8}a, z) = \text{const.}) \quad (\delta_y (0, y, z) - \delta_y (\sqrt{8}a, y, z) = \text{const.})$

5 EXPERIMENTAL

In this investigation, an experimental procedure was adopted to determine the apparent on-axis and off-axis elastic properties of 8-harness satin, woven fabric composites using the tensile and off-axis tensile tests (ASTM Standard D 3039-76: Standard Test Method for Tensile Properties of Fiber-Resin Composites) and a modified, Iosipescu shear test (ASTM Standard D 5379-93: Standard Test Method for Shear Properties of Composite Materials by the V-Notched Beam Method). Three different composite systems, based on woven graphite fabric, reinforced polyimides were tested. Four graphite-PMR15 composite plaques were fabricated at the NASA Lewis Research Center per the following specifications:

- Fiber / Fabric: T650-35 / 3k, 8HS cloth
- Matrix: PMR-15 (f.m.w. 1500)
- Laminate sequence: $[0°]_{16S}$, floating undulations
- Cure method: simulated autoclave and postcure (G. E. specifications)
- Q/A: C-SCAN showing varying attenuation only at edges
- Plaque dimensions: 305 mm x 305 mm x (4.82, 5.15, 5.50, 5.38 mm)
  [12.0 in x 12.0 in x (0.19, 0.20, 0.22, 0.21 in)]

Two graphite-Avimid R composite systems with different ply orientations were also submitted by Pratt & Whitney. The plaques were fabricated at DuPont per the following specifications:

35

- Fiber / Fabric: T650-35 / 3k, 8HS cloth

- Matrix: Avimid-R (dianhydride-diamine monomers)

- Laminate sequence: system 1 - $[0°]_{10S}$, floating undulations

- Ply arrangement: system 2 - $[0°/90°]_{10S}$

- Cure method: simulated autoclave and postcure

- Q/A: C-SCAN showing varying attenuation only at edges

- Plaque dimensions: 305 mm x 305 mm x 3.92 mm {12.0 in x 12.0 in x 0.15 in)

5.1 Off-axis Tensile Testing

For the static tensile and off-axis tensile tests, a total of 15 specimens was prepared predominantly from the graphite-PMR 15 composite plaques at angles of 0°, 15°, 30°, 45° and 90°. The tests were performed at room temperature on a MTS 880 servo hydraulic machine with pressure controlled grips and serrated wedge inserts. Under monotonic, displacement controlled conditions, a crosshead displacement rate of 0.5 mm (0.02 in) per minute was used. Specimen dimensions were maintained according to ASTM standard specifications and aluminum tabs with an included 10° taper were used to prevent crushing by the serrated inserts. For tests where a predominant failure stress was of interest, hardened steel pins were employed to prevent slipping within the grips. Loads, displacements and strains were recorded digitally and strains were measured with rectangular, 3-element rosettes (Measurements Group WK-06-060WR-350 series).

The ply-level stresses in the off-axis tensile specimens with tows oriented at an angle β to the principal loading axis were determined using the established transformation equations. In referring to the schematic of a loaded off-axis specimen shown in Figure 18:

$$\sigma_{11} = \sigma_x \cos^2 \beta$$

$$\sigma_{22} = \sigma_x \sin^2 \beta \qquad (66)$$

$$\tau_{12} = \sigma_x \sin \beta \cos \beta$$

The ply-level strains in the off-axis specimens were evaluated based on strain gages having elements oriented at 0°, 45° and 90°. In such as case, the shearing strain was interpreted from the gages as $\gamma_{xy} = (-\varepsilon_x + 2\varepsilon_{45} - \varepsilon_y)$. Therefore, the strains in the material coordinate system, in terms of the gage strains and off-axis angle were determined using

$$\varepsilon_{11} = \varepsilon_x \cos^2 \beta + \varepsilon_y \sin^2 \beta + \left(\left(-\varepsilon_x + 2\varepsilon_{45} - \varepsilon_y\right)\sin \beta \cos \beta\right)$$

$$\varepsilon_{22} = \varepsilon_x \sin^2 \beta + \varepsilon_y \cos^2 \beta - \left(\left(-\varepsilon_x + 2\varepsilon_{45} - \varepsilon_y\right)\sin \beta \cos \beta\right) \qquad (67)$$

$$\gamma_{12} = \left(-\varepsilon_x + \varepsilon_y\right)\sin 2\beta + \left(\left(-\varepsilon_x + 2\varepsilon_{45} - \varepsilon_y\right)\cos 2\beta\right)$$

5.2 Biaxial Shear Testing

For the static shear dominated, biaxial tests, a total of 20 specimens was prepared from all of the composite plaques. The shear test fixture used was specially designed to permit the testing of Iosipescu shear specimens at a variety of angles α (max ± 45°) to the axis of applied load as illustrated by the schematic in Figure 19. It has been used on numerous occasions for the purposes of investigating the failure behavior of composite materials under shear dominated, biaxial loading conditions [15-20]. The fixture accommodates different loading block designs including the ASTM standard geometry. In this investigation, the original loading blocks were used which allow for Iosipescu specimen dimensions of 80 mm x 20 mm (3.15 in x 0.79 in). All shear tests were performed at room temperature on both the MTS 880 and Instron 1230-20 machines for the purposes of comparison. Under monotonic loading conditions, these tests maintained the same control and rate as in the tensile tests. Loads, displacements and gage strains (2-gage, back-to-back) were also recorded digitally and strains were measured using the same WK series rosettes.

The apparent shear stress in the modified Iosipescu specimens was determined by the following relationship in terms of the notch root axis and width:

$$\tau_{12} = \frac{P_\alpha}{A} = \frac{P\cos(\alpha)}{(w)(t)} \qquad (68)$$

37

where P is the externally applied load, α is the orientation of the notch root axis to the loading axis, w is the distance between notches and t is the "as received" plaque thickness. For calculating the apparent shear modulus, α was taken to be zero. The strains were evaluated by rotating the rosette so the elements were oriented at +45°, 0° and -45° with 0° being parallel to the Iosipescu specimen notch root axis. The primary reason this was done was to monitor the amount of transverse compression produced by different loading block configurations. Given this, the shear strain was calculated from average readings of the pair of rosettes mounted on each side using the relationship

$$\gamma_{12} = \left(\varepsilon_{-45} - \varepsilon_{+45} \right) \tag{69}$$

6 RESULTS AND DISCUSSION

A simplified 2-D model has been presented for the on-axis and off-axis elastic analyses of 8HS woven fabric composites. At the microscale, the model employs CCA theory to predict woven tow elastic properties over a range of constituent carbon or graphite fiber and polyimide matrix properties. The mutually orthogonal warp and fill tows are treated as UD composites and the mesoscale model considers the real, random geometry of tow cross-sections and undulations based on digitized scanning electron images. Model validity is scrutinized with finite element analysis and a series of standard experimental tests to determine apparent elastic properties. An extensive finite element analysis is performed at both scales to verify tow elastic properties predicted by CCA and composite elastic properties predicted by the simplified model. An assumption is made that the woven lamina may be treated as a 2-layered laminate if evaluated at the equivalent tow V_f. This assumption is studied by comparing model results based on the tow and laminate V_f with 3-D FEA results that include the matrix and V_f representative of a woven lamina having matrix rich regions. Equivalent numerical elastic properties are determined by dividing the applied strains from prescribed displacements into the average stresses from nodal reactions. These results are verified by equating the external work done to internal strain energy.

38

The ranges of constituent properties for the graphite or carbon fibers and polyimide matrices considered in this investigation are presented in Table 1. With reference to this table, all subsequent results presented are in terms of a composite system. As an example, system F-c[H] refers to a composite possessing the upper limit of reported values for T650-35 (3k) fiber properties combined with the upper values for PMR-15 matrix properties. The F-b[H] and F-c systems are used here extensively for comparison as they are more representative of an average of constituent properties for the composite materials tested in the experimental program. It is seen from Table 1 that the reported range for fiber-based properties varies significantly, particularly in the transverse directions. Graphite and carbon-based fibers exhibit highly anisotropic behavior so this is not entirely unexpected, particularly considering the difficulty in obtaining or estimating these values.

On the basis of CCA theory, Table 2 presents the results for several composite systems having various combinations of constituent properties. Upper and lower bounds for the transverse tensile and shear elastic properties are shown in accordance with the bounded CCA prediction. The {H} represents an upper bound where the transverse shear modulus of the fiber is much greater than the matrix shear modulus, while the lower bound {L} represents the opposite. As expected, the greatest difference between the upper and lower bounds occurs with the greatest range between fiber transverse and matrix shear moduli exhibited by system B-b. The F-c[H] system appears to maintain the best balance of longitudinal and transverse properties. Clearly, Table 2 also shows that intralaminar and transverse shear behaviors are influenced more by the elastic properties of the matrix than of the fibers. CCA theory provides a simple closed-form expression for the equivalent composite shear modulus in terms of the matrix shear modulus and rule-of-mixtures ratio. Therefore, a nominal increase of 12% in fiber shear properties results in a 5% increase of equivalent shear properties while the same increase in matrix shear properties adds an additional 5 or 6%.

Linear elastic finite element results for the micromechanics analysis of woven tow properties from the example composite system F-b[H], as a function of V_f, are provided in Figures 20-24. For the periodic geometry of a ¼ symmetry, square array RVE, fiber diameter

was held constant at 7.37 μm (0.29 mils) and requisite volume fractions of surrounding matrix were achieved by numerical iteration. The apparent elastic moduli were determined using two approaches: 1) averaged stress – applied strain (dividing the equivalent force from summed nodal reactions by the normal area), and 2) strain energy principles (equating the external work to internal strain energy). Comparisons of the present results were made with the analytical micromechanics solutions of Hashin and Rosen (CCA) [24 -26], Halpin-Tsai [32] and Chamis [33]. For the longitudinal tensile modulus E_{11}, agreement between the numerical and closed-form solutions is excellent as shown in Figure 20. Although the practical range of V_f approximately varies from 0.3 to a theoretical maximum of 0.8, the entire range from absolute matrix to absolute fiber is shown for the purpose of comparison. It is evident from Figure 21 that the numerical solution for the transverse tensile modulus E_{22} tends to converge on the lower CCA bound near a V_f of 0.45 and the upper CCA bound near 0.65. Beyond this, the current model predicts slightly larger values for E_{22} compared with the closed-form solutions. Within the useful range, the numerical solution for the intralaminar shear modulus G_{12} predicts values near the model presented by Chamis for highly anisotropic materials such as carbon-based fibers. As seen from Figure 22, the FE model suggests an average approximation that falls within the bounds provided by the analytical micromechanics solutions as the V_f approaches 0.65. At a V_f between 0.7 and 0.8, the FE model suggests an upper bound approximation to the shear modulus.

The results for the longitudinal Poisson's ratio v_{12} and transverse Poisson's ratio v_{23} are presented in Figures 23 and 24. The analytical approaches essentially predict a linear reduction in v_{12} with increasing V_f, the exception being a minor inflection in the CCA solution near 0.4. The FE model transitions from an underestimate to an overestimate in the range of 0.4 to 0.5. The reasons for such a trend are twofold: first of all, a somewhat linear declination in the longitudinal Poisson's ratio with increasing V_f is expected due to a reduction in the amount of transverse straining possible from contraction. This depends not only on the degree of anisotropy of the fiber, but also on the fiber volume fraction, constituent Poisson's ratios and constituent plain strain bulk moduli. Here, the difference in magnitudes of relative transverse straining occurring in the fiber and matrix for a given applied longitudinal strain

40

govern the slope of the line over the range of V_f considered. Secondly, the transition in v_{12} between 0.4 and 0.6 as seen in Figure 23 seems to be highly dependent on the FE discretization procedure. The ¼ symmetry RVE, constructed for the longitudinal and transverse tensile load cases, used 159 10-node, isoparametric tetrahedral elements (354 nodes) while the full RVE, constructed for the longitudinal and transverse shear loading cases, used 1049 10-node, isoparametric tetrahedral elements (1768 nodes). Further mesh refinement, particularly in the thickness direction, tended to result in both Poisson's ratios converging on the solution predicted by the theories. For v_{12}, the trending line became more linear and any inflection was less evident. Changes in the solution for v_{23} shown in Figure 24 subsequent to further through-thickness mesh refinement were similar. Under the auspices for calculating the transverse Poisson's ratio according to the relationship $v_{23} = (E_{22}/2G_{23})-1$, the trend in behavior with increasing V_f appears to be a consequence of the larger or smaller difference in increasing transverse tensile stiffness of the equivalent composite relative to transverse shear about the fiber axis. Given this, the magnitude of change in stiffness behavior in transverse tension and shear seems equivalent within the ranges of 0 to 0.4 V_f and 0.6 to 0.8 V_f.

Based on the same requisite volume fractions as considered in the tow analysis, Table 3 compares the non-zero extension, extending-bending coupling and bending compliance solutions for 8HS woven laminae having the same T650-35 fiber properties, but different polyimide matrix properties. These values are compared with a baseline solution for a lamina having no undulations, essentially a UD cross-ply. If differences in non-zero terms are compared for each lamina, it is clearly suggested that variation in properties of the matrix influence the diagonal {66} and off-diagonal {12} terms to a greater extent. Upon closer scrutiny, it is found that these terms diminish by some 20-30% when matrix elastic properties are augmented by approximately 40%, implying enhanced stiffnesses. The present model also suggests an inverse behavior when comparisons are made between both lamina architectures. That is, a significant increase occurs in diagonal extension and bending {11} terms when local off-axis undulation angles ranging from 10-12.3° (using quick-sort and Shell's methods) are considered, as observed for the 8HS architectures in this investigation. Contrarily, the

41

extension-bending coupling terms reduce to 18% of their baseline value while very little finite change is evident for the diagonal {66} terms. Variations in extension and extension-bending coupling compliances with local angle of undulation are shown in Figures 25 and 26. The ranges indicated are for a woven lamina with a system of type F-b[H] having a measured tow V_f of 0.72. Two important indices are evident from these range charts: 1) constituent elastic properties, and 2) angle of undulation. It appears that the present model would predict maximum extension $\{A_{11,22}\}$ terms and minimum extension-bending coupling $\{B_{11,-22}\}$ terms near an undulation angle of 16°. This seems reasonable for the case of a plain weave architecture ($n_i = 2$) depending on the size of the gap between adjacent tows.

The macroscale laminate solutions for several of the composite systems are provided in Table 4 on the basis of results from the mesoscale predictions carried over from CCA (see Table 2). The composite laminate elastic properties are based on a 16-layer laminate having a total thickness of 5.00 mm (0.20 in), representative of the composite plaques tested in tension, off-axis tension and shear. In comparing the macroscale results with the range of apparent elastic properties determined experimentally and given in Table 5, it can be seen that the model tends towards underestimating the mean of E_{11} and E_{22} by 7.5% and v_{12} by 14%, while overestimating the mean of G_{12} by 21% for the F-c[H] system. Additionally, the gap would increase by 15% for E_{11} and E_{22} of the F-b[H] system, but G_{12} would be underestimated by 7%. This suggests that either the actual matrix properties lie in between the b and c constituent system properties or the simplified model predicts average diagonal $[A_{ij}]^{-1}$ terms greater than what is to be expected. However, considering the range in measured apparent composite elastic properties, the model provides reasonable, bounded approximations.

Structure-performance maps for evaluating the composite off-axis elastic behavior, in terms of constituent system properties, are shown in Figures 27-29. In total, the off-axis performance of six systems was determined, five in the type A, B, C, F systems and the composites from the experimental program. Relationships between the longitudinal/transverse tensile moduli, intralaminar shear modulus and longitudinal Poisson's ratio were established over off-axis angles (β) ranging from 0° to 45° according to the transformation expressions

$$E_x = E_{11}(\beta) = \left[\frac{1}{E_{11}} \cos^4 \beta + \left(\frac{1}{G_{12}} - \frac{2v_{12}}{E_{11}} \right) \sin^2 \beta \cos^2 \beta + \frac{1}{E_{22}} \sin^4 \beta \right]^{-1}$$

$$E_y = E_{22}(\beta) = \left[\frac{1}{E_{11}} \sin^4 \beta + \left(\frac{1}{G_{12}} - \frac{2v_{12}}{E_{11}} \right) \sin^2 \beta \cos^2 \beta + \frac{1}{E_{22}} \sin^4 \beta \right]^{-1}$$

(70)

$$G_{xy} = G_{12}(\beta) = \left[2 \left(\frac{2}{E_{11}} + \frac{2}{E_{22}} + \frac{4v_{12}}{E_{11}} - \frac{1}{G_{12}} \right) \sin^2 \beta \cos^2 \beta + \frac{1}{G_{12}} \left(\sin^4 \beta + \cos^4 \beta \right) \right]^{-1}$$

$$v_{xy} = v_{12}(\beta) = E_{11}(\beta) \left[\frac{v_{12}}{E_{11}} \left(\sin^4 \beta + \cos^4 \beta \right) - \left(\frac{1}{E_{11}} + \frac{1}{E_{22}} - \frac{1}{G_{12}} \right) \sin^2 \beta \cos^2 \beta \right]$$

where the engineering constants refer to Cartesian x-y axes not aligned with the principal material coordinate x_1-x_2 system. For the range of angles considered, agreement between the various systems and the experiments seems to be quite agreeable. Presumably, the remaining angles in the 2nd half of the quadrant should result in identical curves since reinforcement is mutually orthogonal. In this work, it was initially assumed that this was the case and subsequently verified through experimentation. In instances where curves would not match would tend to indicate the extent of unbalanced properties, i.e. more orthotropic than quasi-isotropic (0/90° vs. warp-aligned). The usefulness of the structure-performance maps lies in the ability to tailor the architecture and constituent properties to suit a desired off-axis elastic behavior with some degree of certainty. From these maps, knowledge of the complete range of in-plane, elastic response is only a matter of measuring a particular elastic constant for a given system once relationships are firmly established.

The relevant metrics presented in Table 6 for the 8HS woven composite architectures considered were determined by image analysis of SEM micrographs and C-SCAN data. This information was passed into the simplified, mesoscale model as well as the woven tow and lamina FE models. From this table, an average fiber diameter of 7.37 µm (0.29 mils) was used in the micromechanics FE models as previously described. These solutions to the woven tow

43

elastic properties were passed into the mesomechanics IVE model having a major tow width of 1393.60 μm (54.87 mils). The resulting tow aspect ratio of 8.3:1 and corresponding volume fraction of matrix were correctly established by numerical iteration. Analytical and numerical elastic analyses of the F-b$^{(H)}$ and F-c$^{(H)}$ composite systems evaluated at the equivalent tow and laminate V_f were compared to the experimentally obtained properties. The results from these comparisons are presented in Table 7. The composite elastic properties obtained from the present analytical approach are in agreement with the composite elastic properties obtained from the finite element analyses for both systems and fiber volume fractions under consideration. Additionally, when compared with the apparent elastic properties presented in Table 5, the results in Table 7 tend to reiterate the notion that the actual range of constituent properties for the composite materials tested lie somewhere in between those assumed for F-b$^{(H)}$ and F-c$^{(H)}$. It is also suggested that assuming the tow V_f in the simplified, 2-layer lamina model serves as a much better lower bound approximation to experimentally determined elastic properties than assuming the laminate V_f when considering the F-b$^{(H)}$ system. Mostly, the predicted and experimental elastic properties tend to converge on the F-c$^{(H)}$ system with the exception of the intralaminar shear modulus, which is slightly overestimated.

7 CONCLUSIONS

1. A simplified micro-to-mesoscale analytical model has been presented for evaluating the elastic behavior of 8HS woven fabric composites. The model assumes that random variation in geometries of the tow cross-sections and undulations can be adequately described by cubic splines and fitted mth-order polynomials. The model also assumes that warp/fill tows can be considered UD composite materials and the 8HS woven lamina considered as a 2-layered laminate. Results for n-layered composite laminate properties show good agreement with experimentally obtained apparent elastic properties for the range of constituent properties studied. In comparison, the model suggests that the composite plaque constituent properties lie between those given for the F-b$^{(H)}$ and F-c$^{(H)}$ systems.

44

2. Evaluation of lamina compliances using the SMM model suggests a range of extension and extension-bending coupling constants for the composites considered. According to the model results, the limiting cases are shown to exist at local, off-axis undulation angles of $0°$ and $16°$ approximately. It seems that these angles are practical lower and upper bounds for UD and plain weave composite materials, respectively.

3. A 3-D finite element model was also presented to verify the predictions from the mechanics model. The idealized volume element simplified the 8HS representative volume element to facilitate appropriate use of prescribed displacement boundary conditions. The model used the measured tow aspect ratio and volume fraction arrived at through numerical iteration. Elastic properties were calculated from force equivalence and strain energy methods. The results compare favorably with both the analytical model and the experiments. It is suggested that the tow fiber volume fraction is more appropriate when the 8HS woven fabric lamina is evaluated in the manner presented and compared with apparent elastic properties.

4. Off-axis composite elastic behavior was evaluated through the use of the familiar equations of transformation. Structure-performance maps were introduced for several of the composite systems considered to show relationships between off-axis behavior and constituent properties. Comparison between the predicted and experimental off-axis properties was favorable, but more importantly, the maps appear to serve as a possible guide for constituent composite material selection.

ACKNOWLEDGMENTS

REFERENCES

1. Ishikawa, T., and T. W. Chou. "Stiffness and strength behavior of woven fabric composites." *Journal of Materials Science* 17 (1982): 3211-20.

2. Ishikawa, T., and T. W. Chou. "Nonlinear behavior of woven fabric composites." *Journal of Composite Materials* 17 (1983): 399-412.

3. Ishikawa, T., M. Matsushima, and Y. Hayashi. "Experimental confirmation of the theory of elastic moduli of fabric composites." *Journal of Composite Materials* 19 (1985): 443-58.

4. Raju, I. S., and J. T. Wang. "Classical laminate theory models for woven fabric composites." *Journal of Composites Technology & Research* 16 (1994): 289-303.

5. Naik, N. K., and V. K. Ganesh. "Prediction of on-axis elastic properties of plain weave fabric composites." *Composites Science and Technology* 45 (1992): 135-52.

6. Naik, N. K., and P. S. Shembekar. "Elastic behavior of woven fabric composites: I - lamina analysis." *Journal of Composite Materials* 26 (1992): 2196-2225.

7. Shembekar, P. S., and N. K. Naik. "Elastic behavior of woven fabric composites: II - laminate analysis." *Journal of Composite Materials* 26 (1992): 2226-46.

8. Naik, N. K., and P. S. Shembekar. "Elastic behavior of woven fabric composites: III - laminate design." *Journal of Composite Materials* 26 (1992): 2522-41.

9. Walsh, T. J., and O. O. Ochoa. "Analytical and experimental mechanics of woven fabric composites." *Mechanics of Composite Materials and Structures* 3 (1996): 133-52.

10. Zhang, Y. C., and J. Harding. "A numerical micromechanics analysis of the mechanical properties of a plain weave composite." *Computers and Structures* 36 (1990): 839-44.

11. Blackketter, D. M., D. E. Walrath, and A. C. Hansen. "Modeling damage in a plain weave fabric-reinforced composite material." *Journal of Composites Technology & Research* 15 (1993): 136-42.

12. Woo, K., and J. D. Whitcomb. "Global/local finite element analysis for textile composites." *Journal of Composite Materials* 28 (1994): 1305-20.

13. Whitcomb, J. D., K. Woo, and S. Gundapaneni. "Macro finite element for analysis of textile composites." *Journal of Composite Materials* 28 (1994): 607-17.

14. Woo, K., and J. D. Whitcomb. "Three-dimensional failure analysis of plain weave textile composites using a global/local finite element method." *Journal of Composite Materials* 30 (1996): 984-03.

15. Broughton, W. R. "Shear properties of unidirectional carbon fibre composites." Ph.D. Dissertation, University of Cambridge, 1989.

16. Broughton, W. R., M. Kumosa, and D. Hull. "Analysis of the Iosipescu shear test as applied to unidirectional carbon-fiber reinforced composites." *Composites Science and Technology* 38 (1990): 299-325.

17. Bansal, A., and M. Kumosa. "Experimental and analytical studies of failure modes in Iosipescu specimens under biaxial loadings." *Journal of Composite Materials* 29 (1995): 334-58.

18. Kumosa, M., K. H. Searles, and G. Odegard. "Biaxial Failure Analysis of Graphite Reinforced Polyimide Composites." *HITEMP Review 1997* (1997), Paper 18: 1-11.

19. Odegard, G., K. Searles, and M. Kumosa. "A critical examination of the Iosipescu shear test as applied to 0° unidirectional composite materials." *submitted for publication in Mechanics of Composite Materials and Structures* (1998).

20. Searles, K., G. Odegard, M. Castelli, and M. Kumosa. "Failure investigation of graphite-polyimide fabric composites at room and elevated temperatures using the biaxial Iosipescu test." *accepted for publication in Journal of Composite Materials* (1998).

21. Standard Test Method for Shear Properties of Composite Materials by the V-Notched Beam Method. ASTM Standard D 5379-93, *American Society for Testing and Materials* (1993).

22. Standard Test Method for Tensile Properties of Fiber-Resin Composites. ASTM Standard D 3039-76, *American Society for Testing and Materials* (1976).

23. Chou, T. W. *"Microstructural Design of Fiber Composites."* Cambridge Solid State Science Series, Ed.: R. W. Cahn, E. A. Davis and I. M. Ward, Cambridge University Press, G. B. (1992).

24. Hashin, Z., and B. W. Rosen. "The elastic moduli of fiber reinforced materials." *Journal of Applied Mechanics* 31 (1964): 223-32.

25. Hashin, Z. "Analysis of properties of fiber composites with anisotropic constituents." *Journal of Applied Mechanics* 46 (1979): 543-50.

26. Hashin, Z. "Analysis of composite materials - A survey." *Journal of Applied Mechanics* 50 (1983): 481-505.

27. Sun, C. T., and R. S. Vaidya. "Prediction of composite properties from a representative volume element." *Composites Science and Technology* 56 (1996): 171-9.

28. Lekhnitskii, S. G. *"Theory of Elasticity of an Anisotropic Body."* Holden-Day, San Francisco, CA. (1963).

29. ANSYS Inc. *"Analysis Tools: 15.12 Solving for Unknowns and Reactions."* ANSYS Theory Reference, Ed.: P. Kohnke, Swanson Analysis System Inc., Houston, P. A. (1994).

30. Mirzadeh, F., and K. L. Reifsnider. "Micro-deformations in C3000/PMR15 woven composite." *Journal of Composite Materials* 26 (1992): 185-205.

31. Alif, N., L. A. Carlsson, and J. W. Gillespie, Jr. "Mode I, mode II, and mixed mode interlaminar fracture of woven fabric carbon/epoxy." *Composite Materials Testing and Design, Thirteenth Volume*, ASTM STP 1242 (1997): 82-106.

32. Halpin, J. C., and S. W. Tsai. *"Environmental factors in composite materials design."* Air Force Materials Laboratory Technical Report AFML-TR-67-423 (1967): 67-423.

33. Chamis, C. C. *"Simplified composite micromechanics equations for hygral, thermal and mechanical properties."* NASA TM-83320. NASA Lewis Research Center, Cleveland OH. (1983).

List of Tables

List of Figures

12. 3-D FE model assumed for the analysis of tow longitudinal and transverse shear elastic properties.

13. 4th-order polynomial fits to the upper and lower woven tow cross-section perimeters halved about the respective tow centroid.

14. 4th-order polynomial fit to the woven tow undulation centerline with respect to the centroid of the mutually orthogonal tows.

15. Definition of the off-axis angle of undulation for evaluation of average transformed reduced compliance relative to the principal material coordinates.

16. Evolution of the idealized volume element FE model from the representative volume element.

17. 3-D FE model assumed for the analysis of 8HS woven fabric composite elastic properties.

18. Representation for evaluating ply-level elastic behavior in the off-axis tensile composite specimens.

19. Representation for evaluating ply-level elastic behavior in the biaxial Iosipescu shear composite specimens.

20. Comparison between the FE analysis and micromechanics solutions for the woven tow longitudinal tensile modulus E_{11} over the range of V_f from 0 to 1.

21. Comparison between the FE analysis and micromechanics solutions for the woven tow transverse tensile modulus E_{22} over the range of V_f from 0 to 1.

22. Comparison between the FE analysis and micromechanics solutions for the woven tow longitudinal shear modulus G_{12} over the range of V_f from 0 to 1.

23. Comparison between the FE analysis and micromechanics solutions for the woven tow longitudinal Poisson's ratio ν_{12} over the range of V_f from 0 to 1.

24. Comparison between the FE analysis and micromechanics solutions for the woven tow transverse Poisson's ratio ν_{23} over the range of V_f from 0 to 1.

25. Variation in 8HS woven fabric lamina extensional compliances over the range of local angles of undulation from $0°$ to $16°$ as predicted by the current model.

26. Variation in 8HS woven fabric lamina extension-bending coupling compliances over the range of local angles of undulation from $0°$ to $16°$ as predicted by the current model.

27. E_x/E_y-G_{xy} chart mapping the off-axis elastic behavior for several composite systems considered against experimental data.

28. ν_{xy}-G_{xy} chart mapping the off-axis elastic behavior for several composite systems considered against experimental data.

29. ν_{xy}-E_x/E_y chart mapping the off-axis elastic behavior for several composite systems considered against experimental data.

Table 1

System	Ref	Fibers	E_{11} GPa (Msi)	E_{22} GPa (Msi)	G_{12} GPa (Msi)	G_{23} GPa (Msi)	v_{12}	v_{23}
A	30	C3000	234.5 (34.0)	13.8 (2.0)	11.4 (1.7)	4.8 (0.7)	.20	.25
B	31	IM7*	276.0 (40.0)	56.0 (8.1)	28.0 (4.1)	16.7 (2.4)	.25	----
C	27	AS4	235.0 (34.1)	14.0 (2.0)	28.0 (4.1)	----	.20	.25
D	6	T-300	230.0 (33.4)	40.0 (5.8)	24.0 (3.5)	14.3 (2.1)	.26	----
E	11	AS4	221.0 (32.1)	13.8 (2.0)	13.8 (2.0)	5.5 (0.8)	.20	.25
F	†	T650-35 (3k)[a]	243.4 (L) 258.6 (H) (37.5)	40.0 (5.8)	25.0 (3.6)	14.0 (2.0)	.20 .26	.25

System	Ref	Matrix[b]	E_{11} GPa (Msi)	G_{12} GPa (Msi)
a	30	PMR-15	3.3 (0.48)	1.2 (0.17)
b	†		3.24 (0.46)	1.2 (0.17)
c	†† †		4.0 (L) 4.5 (H) (0.65)	1.5 1.7 (0.25)
d	†††	Avimid-R	3.6 (0.5)	1.4 (0.2)

*Constituent property maxima.
[a]Tow density.
[b]Isotropic.
†NASA LeRC and Amoco Corp.
††ASM Engineered Materials Handbook, Vol. 1: Composites.
†††DuPont-AMS.

Table 2

Micromechanics Analysis of Woven Tows

Composite System[†]	E_{11} GPa (Msi)	E_{22} {H} GPa (Msi)	E_{22} {L} GPa (Msi)	G_{12} GPa (Msi)	ν_{12}	G_{23} {H} GPa (Msi)	G_{23} {L} GPa (Msi)
A-a	169.8 (24.6)	9.2 (1.3)	8.8 (1.3)	4.6 (0.67)	0.24	3.1 (0.45)	2.9 (0.42)
B-b	199.6 (28.9)	16.6 (2.4)	14.2 (2.1)	5.9 (0.86)	0.28	5.8 (0.84)	4.7 (0.68)
C-c [(L)]	170.4 (24.7)	10.1 (1.5)	9.7 (1.4)	7.0 (1.0)	0.25	3.7 (0.54)	3.5 (0.51)
D-d	166.6 (24.2)	16.0 (2.3)	14.3 (2.1)	6.4 (0.93)	0.29	5.8 (0.84)	4.9 (0.71)
E-a	160.1 (23.2)	9.1 (1.3)	8.6 (1.2)	4.9 (0.71)	0.24	3.4 (0.49)	3.1 (0.45)
F-c [(L)]	176.4 (25.6)	17.3 (2.5)	15.4 (2.2)	6.8 (0.99)	0.24	6.1 (0.88)	5.2 (0.75)
F-c [(H)]	187.5 (27.2)	18.4 (2.7)	16.6 (2.4)	7.4 (1.1)	0.29	6.5 (0.94)	5.6 (0.81)
F-d [(H)]	187.2 (27.2)	16.2 (2.3)	14.5 (2.1)	6.5 (0.94)	0.29	5.8 (0.84)	4.9 (0.71)

[†]Denotes fiber and matrix constituents.

Note: Properties indicated by {H} or {L} represent bounds, i.e. $G_{23}^{f} \gg G^{m}$ or $G_{23}^{f} \ll G^{m}$.

Composite system (F-b)[(tt)] assumed for mesomechanics and macromechanics analyses.

Table 3

Composite Lamina (8HS-weave)	$[A_{11}, A_{22}]^{-1}$ {H} x10^{-4}	$[A_{66}]^{-1}$ {H} x10^{-3}	$[A_{12}]^{-1}$ {H} x10^{-3}	$[B_{11}, -B_{22}]^{-1}$ {H} x10^{-5}	$[D_{11}, D_{22}]^{-1}$ {H} x10^{-8}	$[D_{66}]^{-1}$ {H} x10^{-6}	$[D_{12}]^{-1}$ {H} x10^{-6}
F-b [H]	0.594	0.653	0.940	0.117	0.997	0.110	0.158
F-c [H]	0.526	0.504	0.775	0.106	0.883	0.085	0.127
F-d [H]	0.562	0.581	0.862	0.112	0.944	0.098	0.145

Composite Laminate* (Cross-ply)	$[A_{11}, A_{22}]^{-1}$ {H} x10^{-4}	$[A_{66}]^{-1}$ {H} x10^{-3}	$[A_{12}]^{-1}$ {H} x10^{-3}	$[B_{11}, -B_{22}]^{-1}$ {H} x10^{-5}	$[D_{11}, D_{22}]^{-1}$ {H} x10^{-8}	$[D_{66}]^{-1}$ {H} x10^{-6}	$[D_{12}]^{-1}$ {H} x10^{-6}
F-b [H]	0.367	0.652	0.854	0.650	0.617	0.109	0.143
F-c [H]	0.360	0.502	0.701	0.660	0.605	0.084	0.118
F-d [H]	0.365	0.579	0.788	0.650	0.613	0.097	0.132

*Comparison made equivalent considering the 8HS as a "2-ply" laminate.
*Cross-ply interpreted as a 1st order polynomial fit.
Note: Units are consistently SI with [A B D]$^{-1}$ in terms of (MPa • mm)$^{-1}$.
    {H} indicates upper-bounded elastic constants.

Table 4

Properties of Woven 8 HS N-Layered Laminate
(from Mesomechanics Analysis)

Composite System[†]	E_{11} {H} GPa (Msi)	E_{11} {L} GPa (Msi)	E_{22} {H} GPa (Msi)	E_{22} {L} GPa (Msi)	G_{12} {H} GPa (Msi)	G_{12} {L} GPa (Msi)	ν_{12} {H}	ν_{12} {L}
A-a	51.7 (7.49)	51.4 (7.45)	51.7 (7.49)	51.4 (7.45)	4.5 (0.65)	4.4 (0.64)	.047	.042
B-b	66.7 (9.67)	65.1 (9.44)	66.7 (9.67)	65.1 (9.44)	5.9 (0.86)	5.8 (0.84)	.065	.050
C-c [(L)]	61.6 (8.93)	61.3 (8.89)	61.6 (8.93)	61.3 (8.89)	6.8 (0.99)	6.8 (0.99)	.044	.041
D-d	62.6 (9.08)	61.4 (8.91)	62.6 (9.08)	61.4 (8.91)	6.4 (0.93)	6.3 (0.91)	.068	.057
E-a	51.5 (7.47)	51.2 (7.43)	51.5 (7.47)	51.2 (7.43)	4.8 (0.70)	4.8 (0.70)	.042	.038
F-c [(L)]	66.3 (9.62)	65.1 (9.44)	66.3 (9.62)	65.1 (9.44)	6.8 (0.99)	6.7 (0.97)	.063	.052
F-c [(H)]	71.5 (10.37)	70.3 (10.19)	71.5 (10.37)	70.3 (10.19)	7.4 (1.07)	7.4 (1.07)	.070	.060
F-d [(H)]	66.8 (9.69)	65.6 (9.51)	66.8 (9.69)	65.6 (9.51)	6.4 (0.93)	6.4 (0.93)	.065	.054

[†]Denotes fiber and matrix constituents.

Note: Properties indicated by {H} or {L} represent bounds, i.e. $G_{23}^{f} \gg G^{m}$ or $G_{23}^{f} \ll G^{m}$.

N-layered laminate assumed with N = 16, thickness of 5.0 mm and V_f = 0.72 (tow equivalent).

Table 5

Experimental Test	Apparent Elastic Properties			
	E_{11} GPa (Msi)	E_{22} GPa (Msi)	G_{12} GPa (Msi)	ν_{12}
On-Axis / Off-Axis Tension	76.9 ± 6.2 $(11.1 \pm .9)$	76.9 ± 6.2 $(11.1 \pm .9)$	6.0 ± 0.5 $(.9 \pm .07)$	$.08 \pm .03$
Biaxial Iosipescu Shear			6.1 ± 1.6 $(.9 \pm .2)$	

Table 6

Metric	Geometric Scale			
	Fiber µm (mils)	Tow µm (mils)	Lamina µm (mils)	Plaque mm (in)
Diameter	7.37 (0.29)	----	----	----
Major Width	----	1393.60 (54.87)	4180.80 (164.60)	304.80 (12..00)
Major Thickness	----	167.70 (6.60)	301.25-392.00 (11.86-15.43)	3.92-5.50 (0.15-0.22)
V_f	----	0.71-0.74	0.68-0.72	0.58-0.62

Table 7

V_f	System	Model	E_{11} GPa (Msi)	E_{22} GPa (Msi)	G_{12} GPa (Msi)	v_{12}
0.72	F-b$^{(H)}$	SMM	62.70 (9.09)	62.70 (9.09)	5.70 (0.83)	0.06
	F-b$^{(H)}$	FE	63.90 (9.27)	63.90 (9.27)	5.00 (0.73)	0.13
	F-c$^{(H)}$	SMM	71.00 (10.30)	71.00 (10.30)	7.40 (1.07)	0.07
	F-c$^{(H)}$	FE	73.60 (10.67)	73.60 (10.67)	6.90 (1.00)	0.14
0.62	F-b$^{(H)}$	SMM	50.60 (7.34)	50.60 (7.34)	4.30 (0.62)	0.06
	F-b$^{(H)}$	FE	54.70 (7.93)	54.70 (7.93)	3.70 (0.54)	0.13
	F-c$^{(H)}$	SMM	58.50 (8.48)	58.50 (8.48)	5.70 (0.83)	0.06
	F-c$^{(H)}$	FE	63.50 (9.21)	63.50 (9.21)	5.10 (0.74)	0.14

Note: SMM refers to the present analytical simplified mechanics model.
FE refers to the equivalent force and strain energy finite element models.
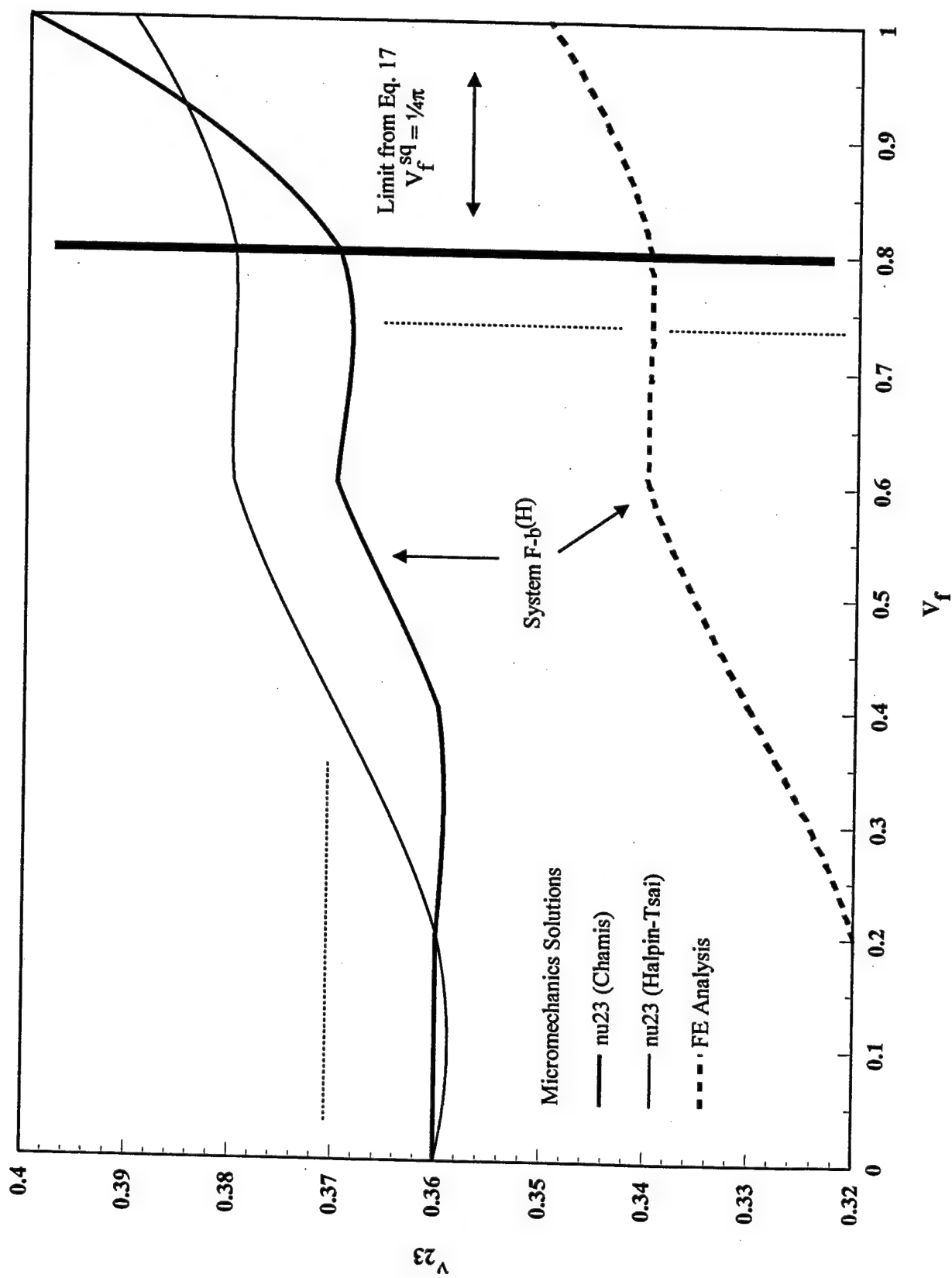
Figure 1

Figure 2

Figure 3

8HS WOVEN UNIT CELL

Z

X

Y

a

WARP TOWS

WEFT (FILL) TOWS

FUNDAMENTAL
RUC

Figure 4

WARP

FILL

FUNDAMENTAL
RUC

PLAN VIEW OF 8HS
WOVEN ARCHITECTURE

3a

2a

SIMPLIFIED REPEAT ELEMENT

$\sqrt{8}$ a

$\sqrt{8}$ a

Figure 5

(PIXELS)

(PIXELS)

Figure 6

(PIXELS)

(PIXELS)

Figure 7a

Image Origin

Calibration Scale
0.339 pixels/micron

Centroid Coordinates: (648.97, 259.59)
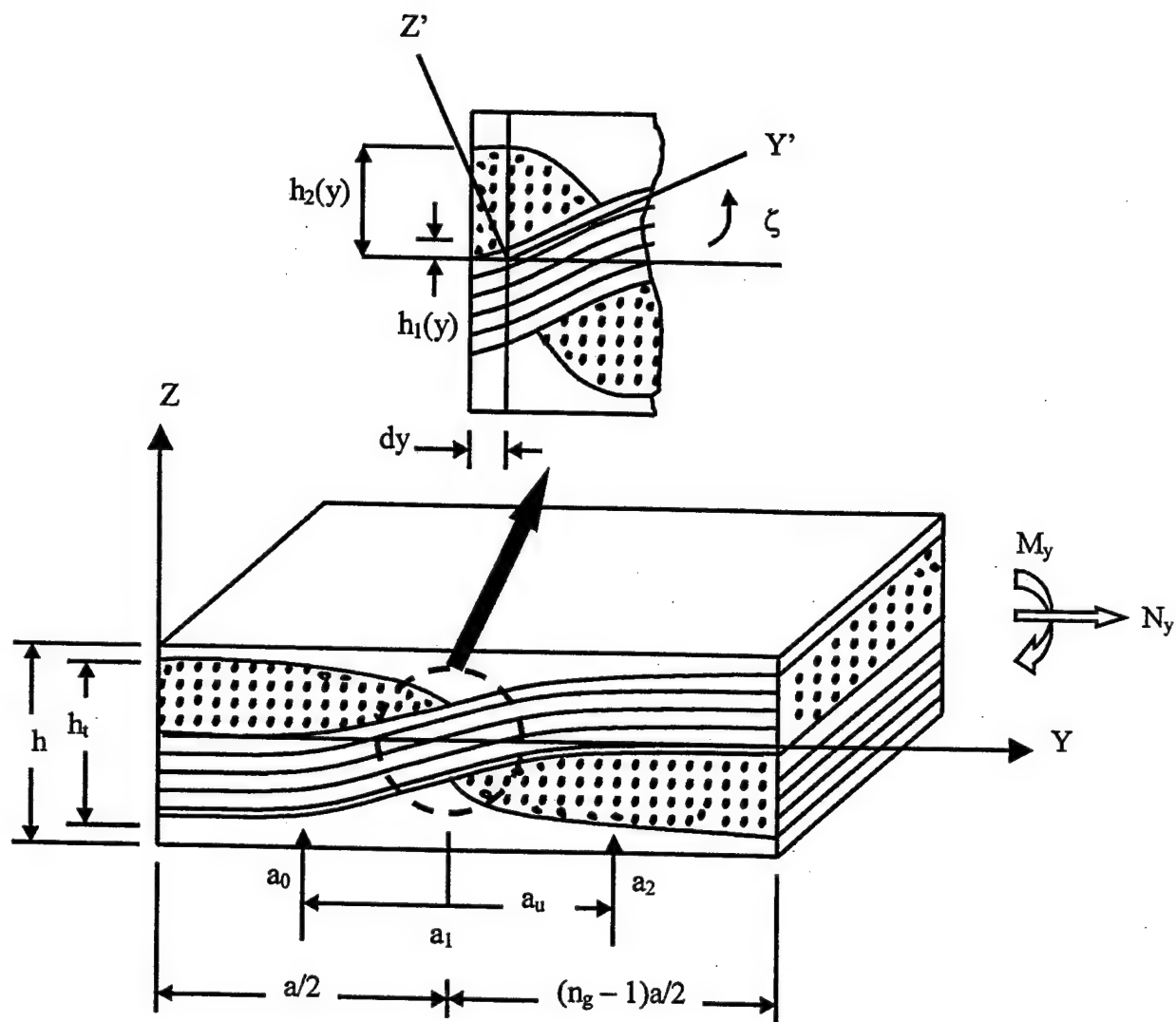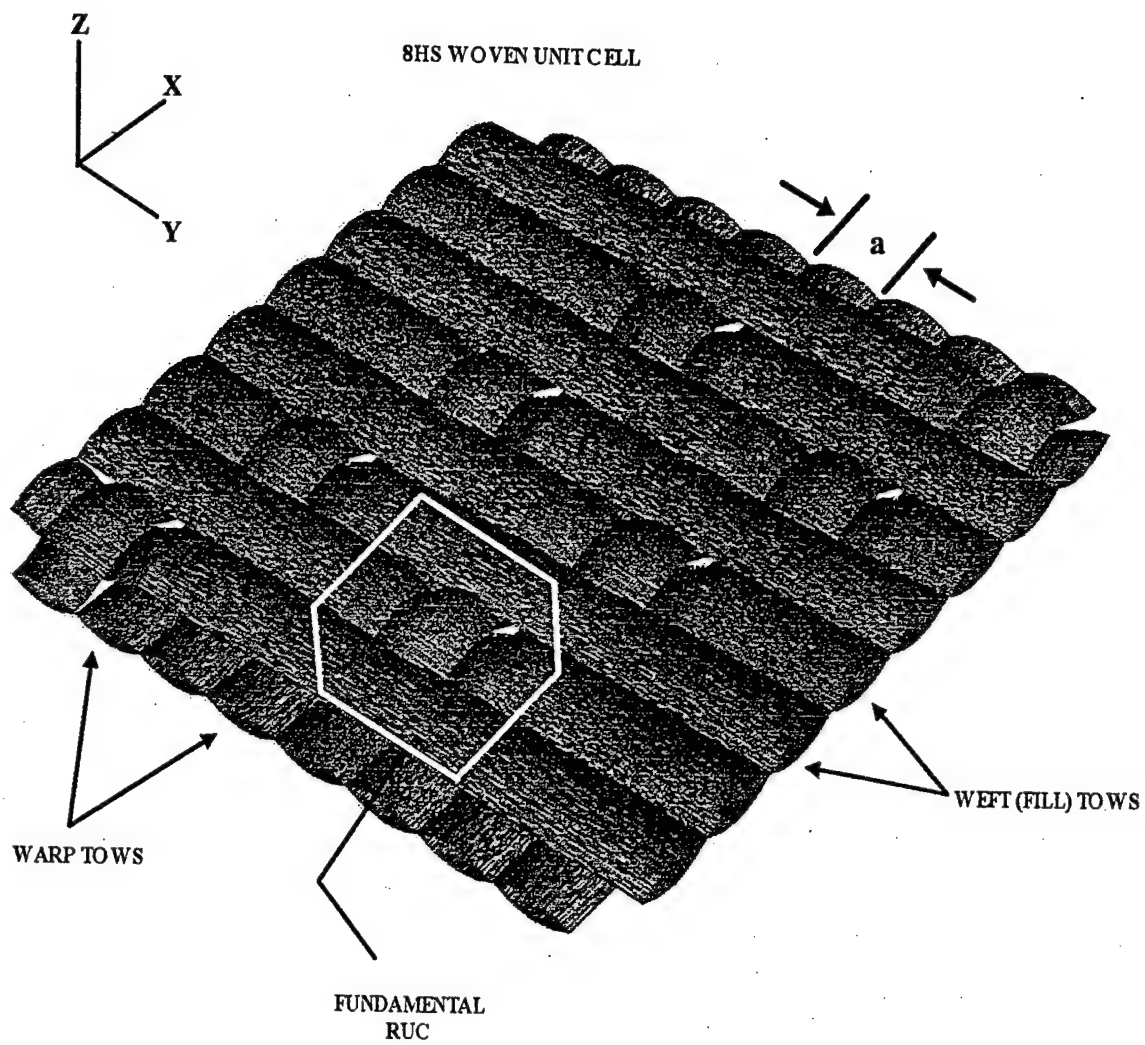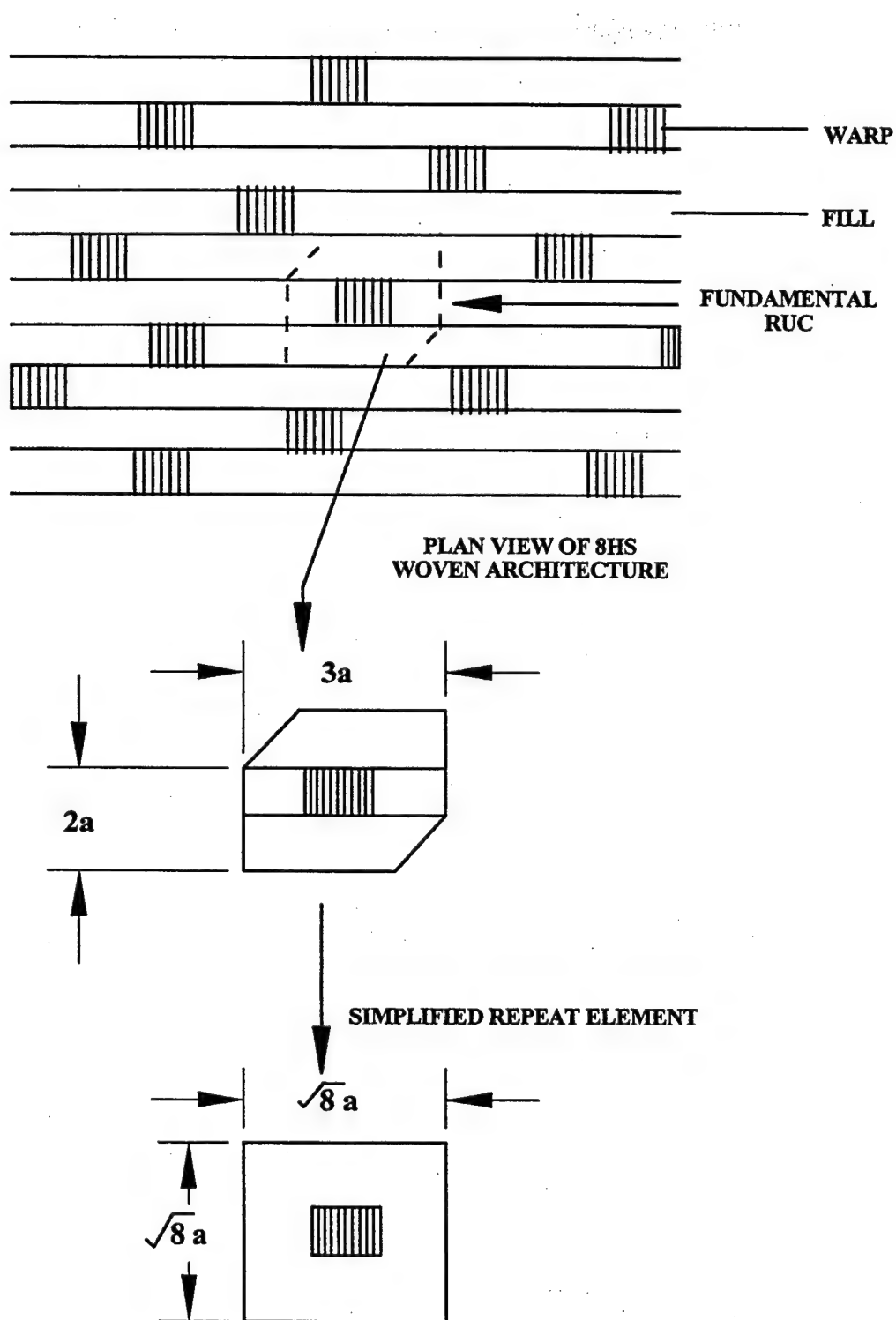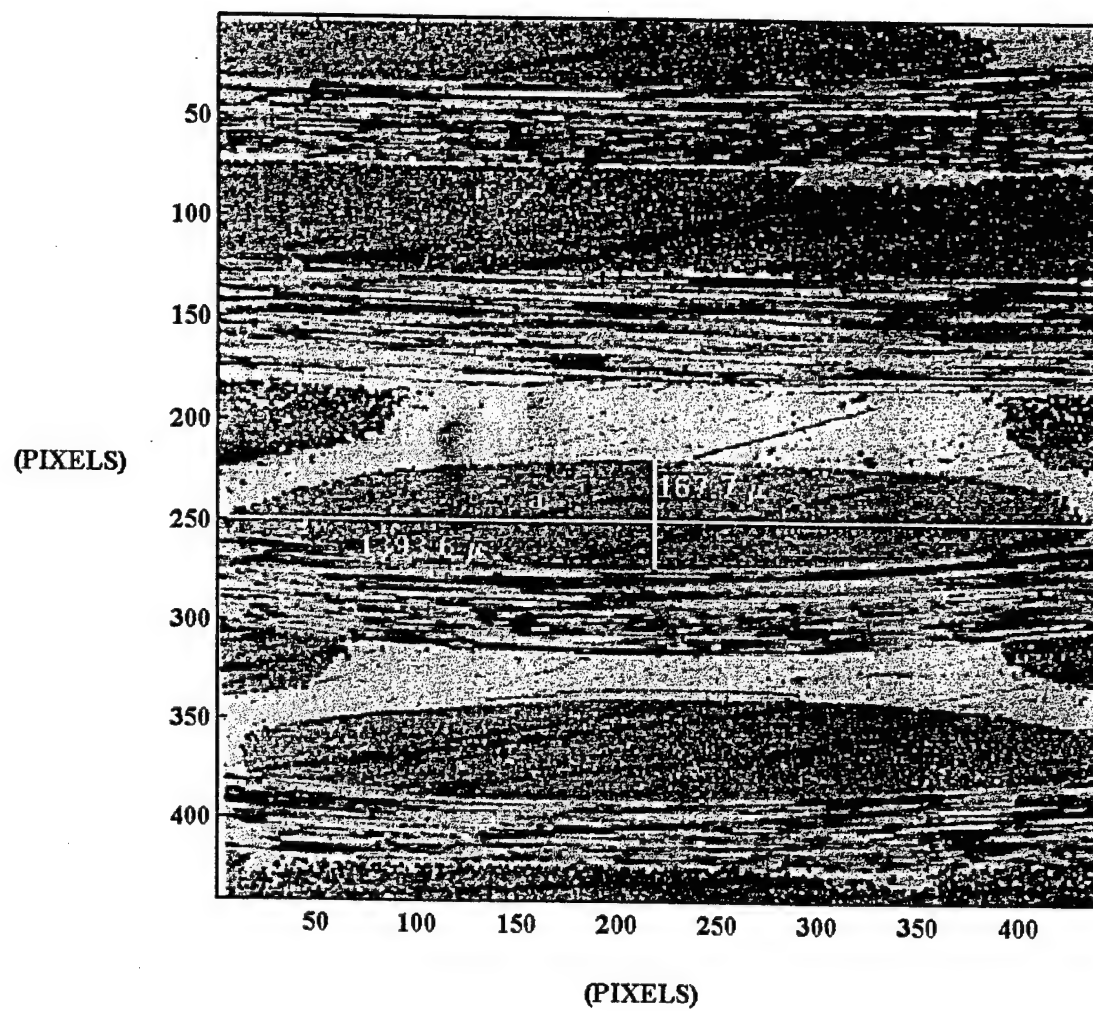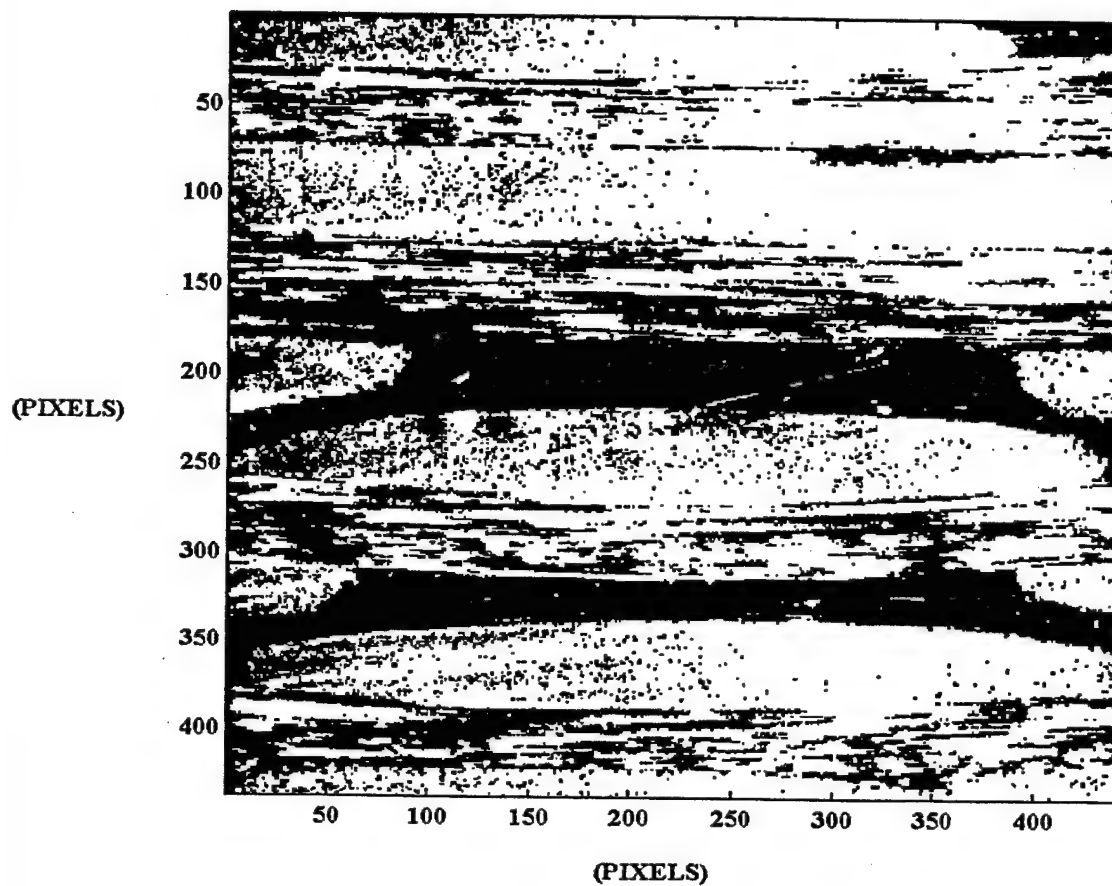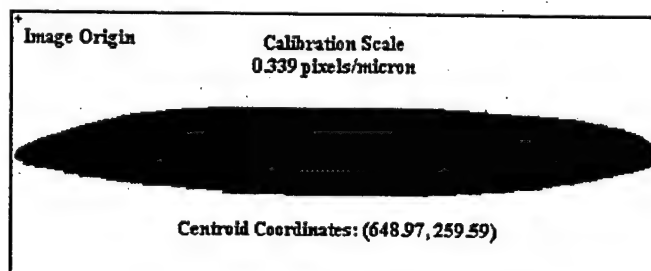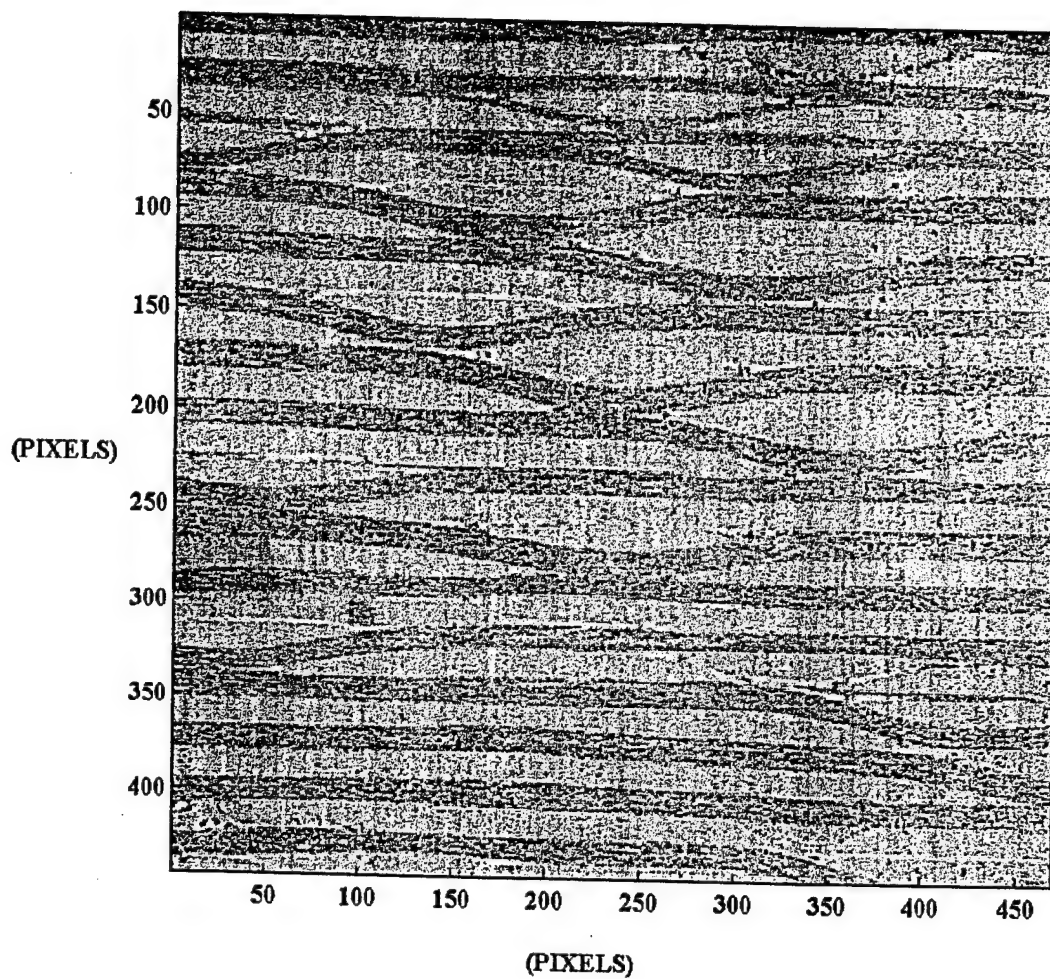
Figure 7b

Figure 8a

Figure 8b

Figure 9

Figure 10

Figure 11

Z

X   Y

FULL (UD) TOW
RVE

1.0c

1.0b   1.0a
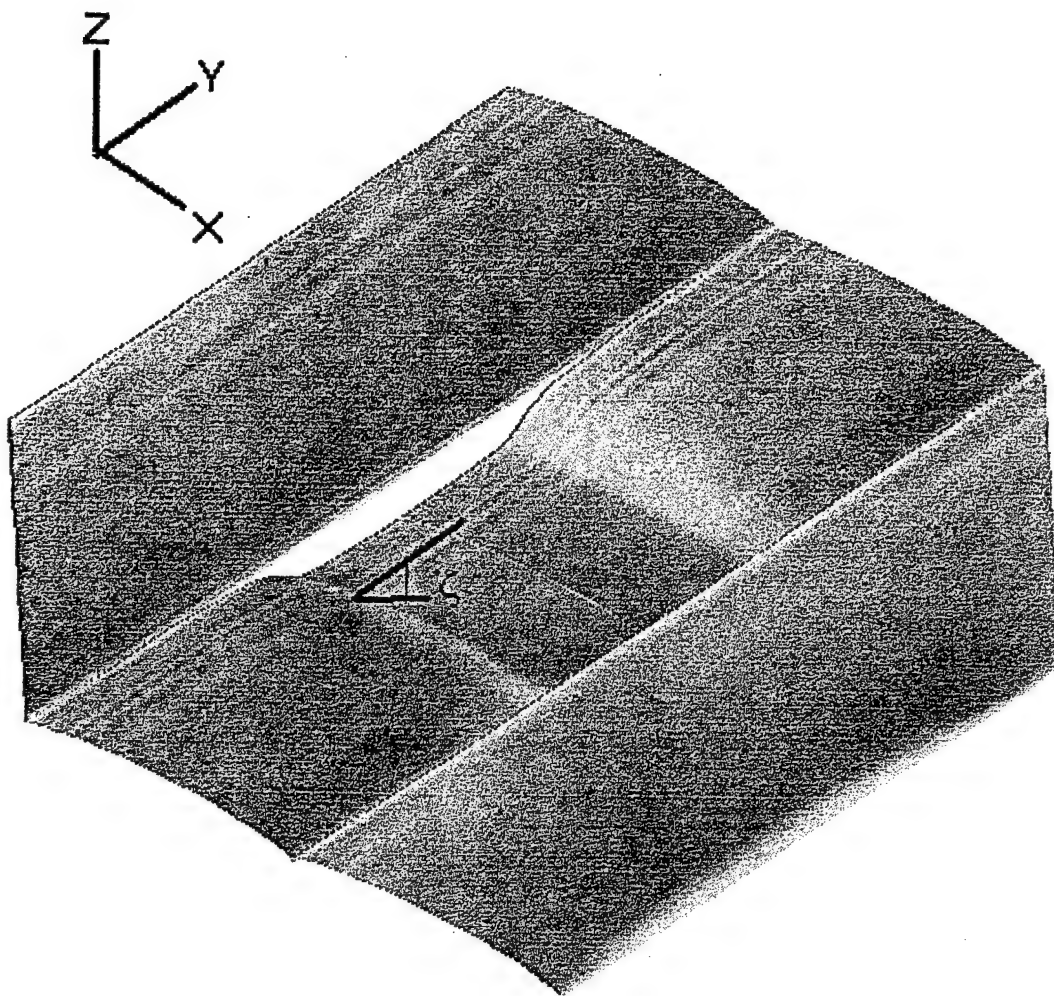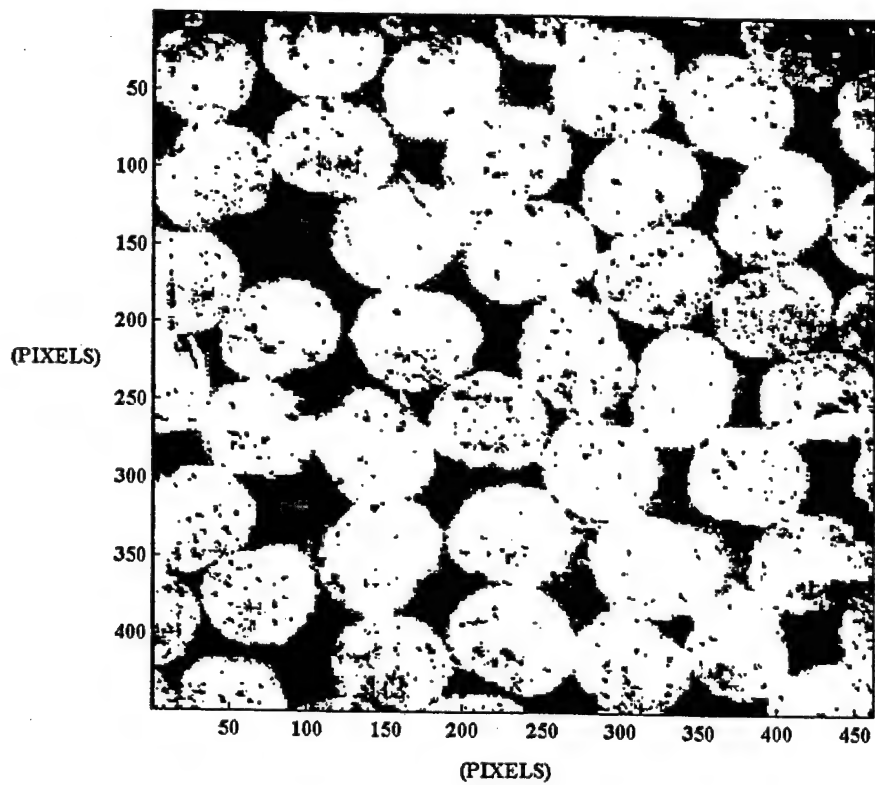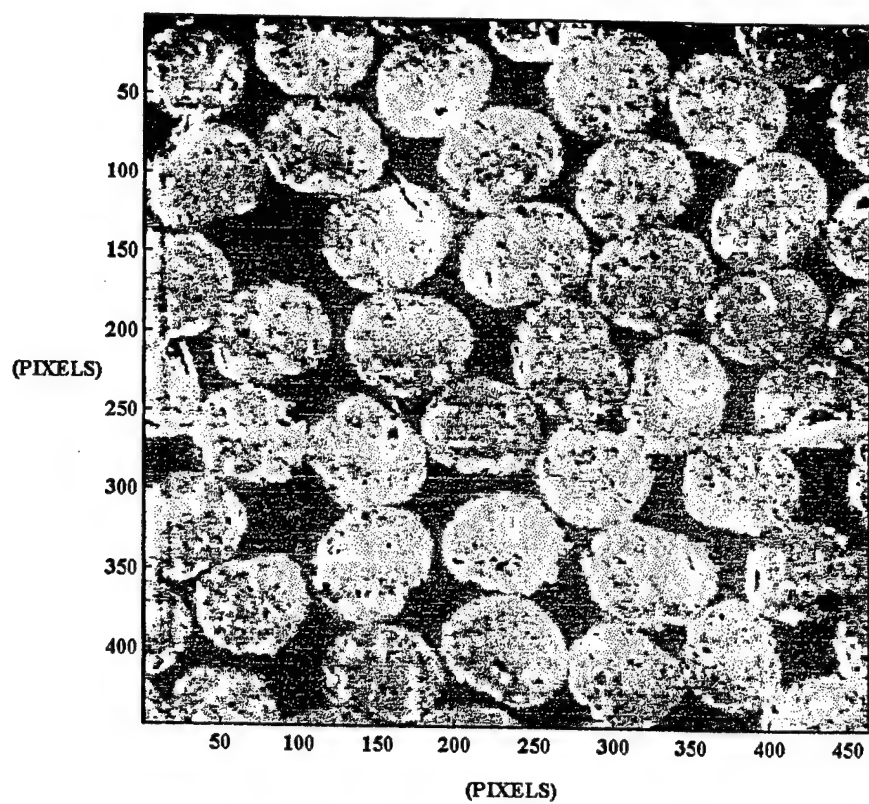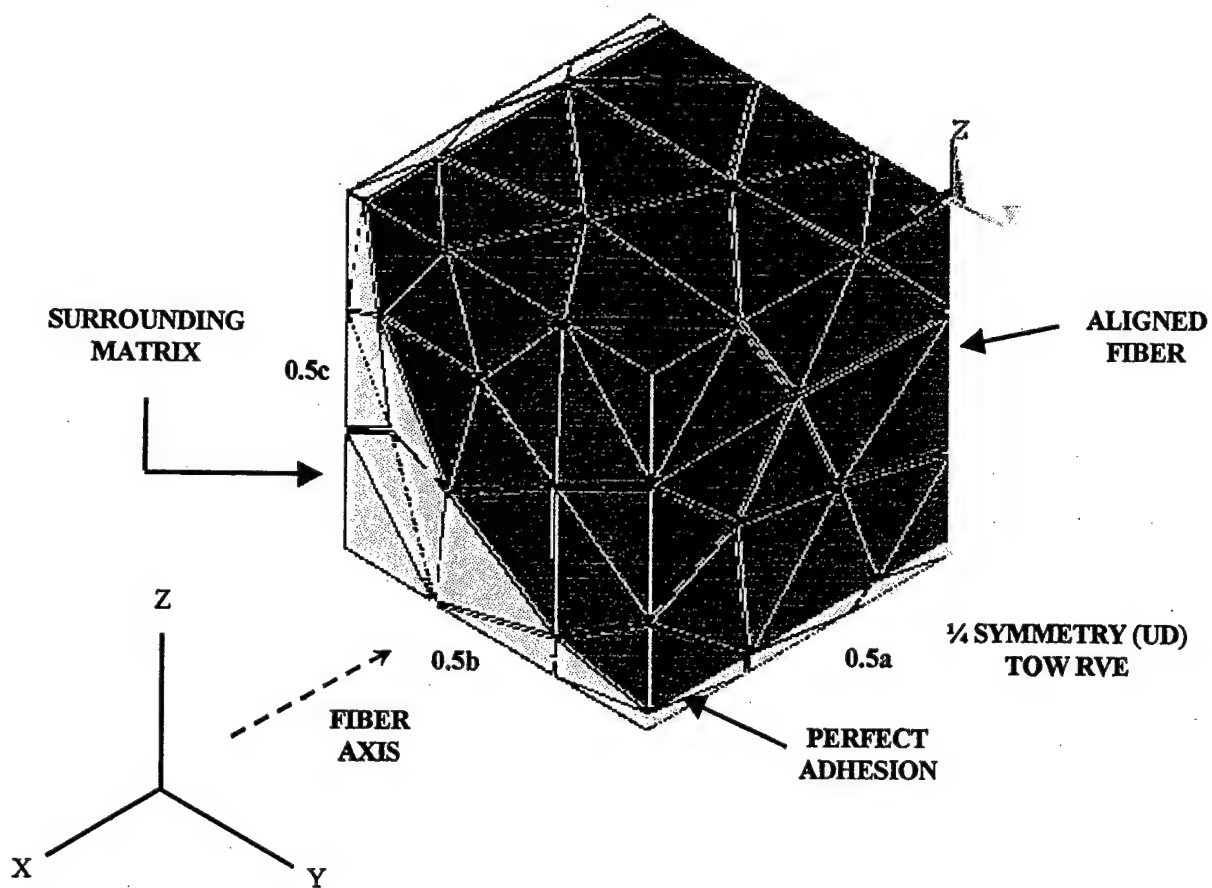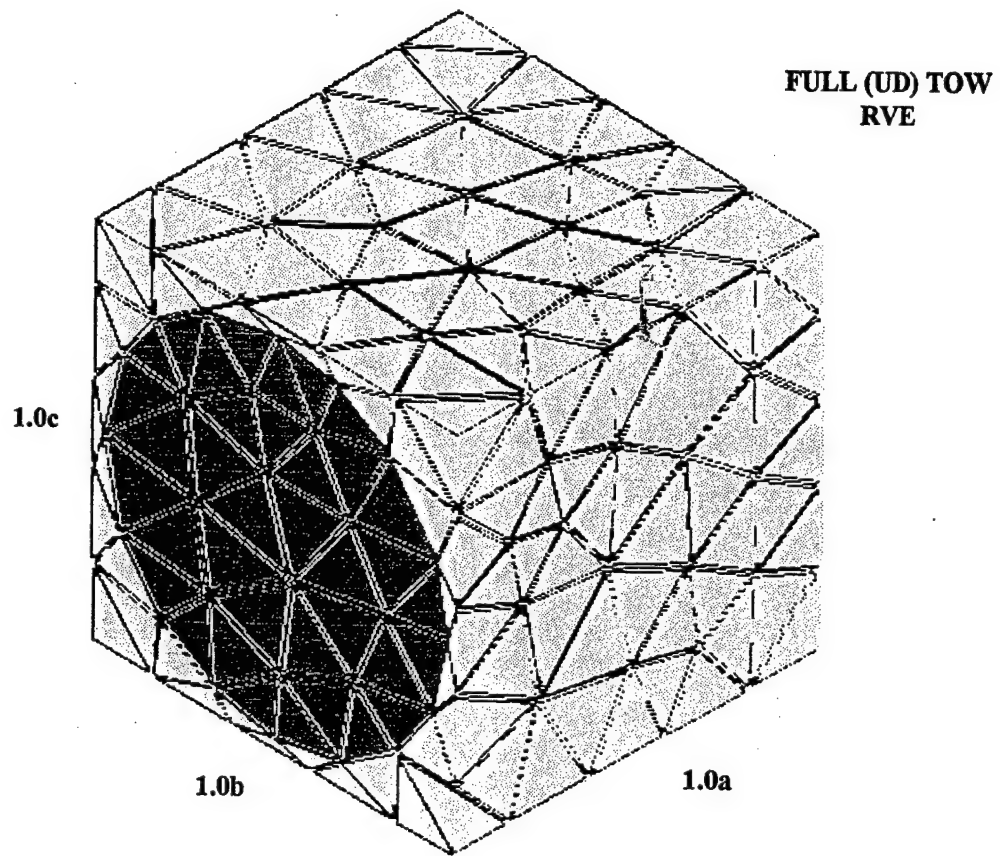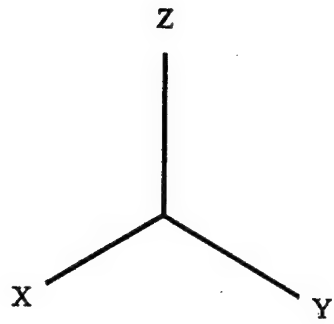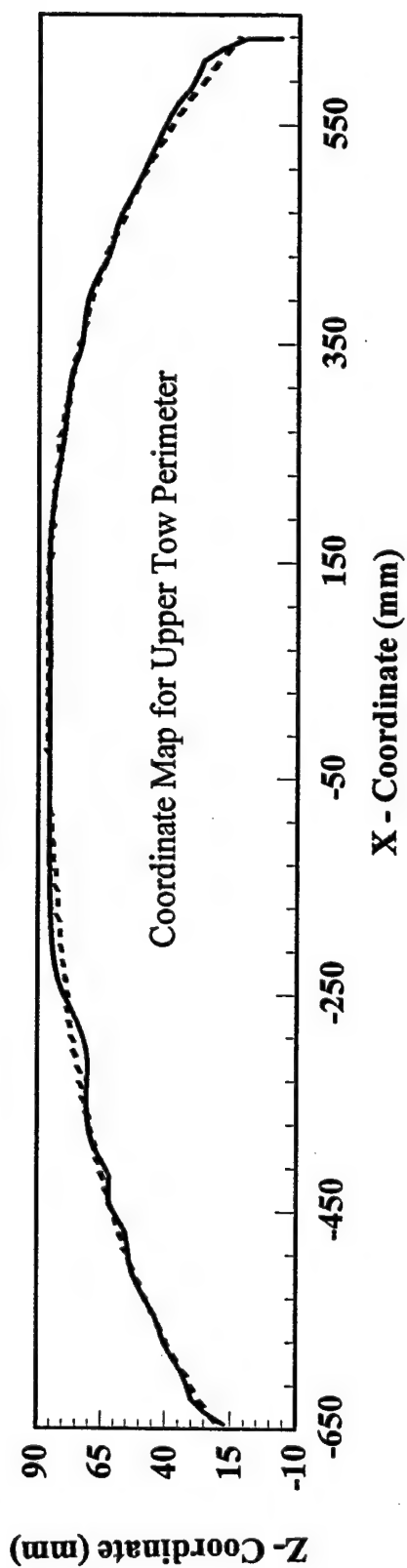
Figure 12

Upper Polynomial

$$y = -2E-10x^4 - 5E-08x^3 - 8E-05x^2 + 0.0109x + 86.37$$

$$R^2 = 0.987$$

Lower Polynomial

$$y = 5E-10x^4 - 4E-08x^3 + 1E-06x^2 + 0.0046x - 86.693$$

$$R^2 = 0.9866$$

Figure 13

Coordinate Map for Tow Undulation Path

Y - Coordinate (mm)

Z - Coordinate (mm)
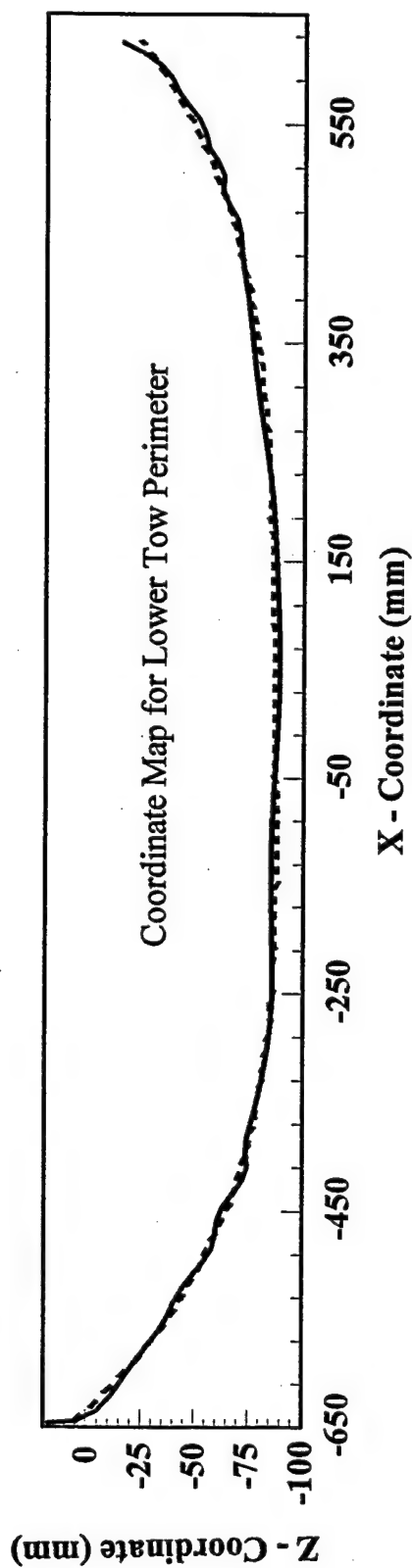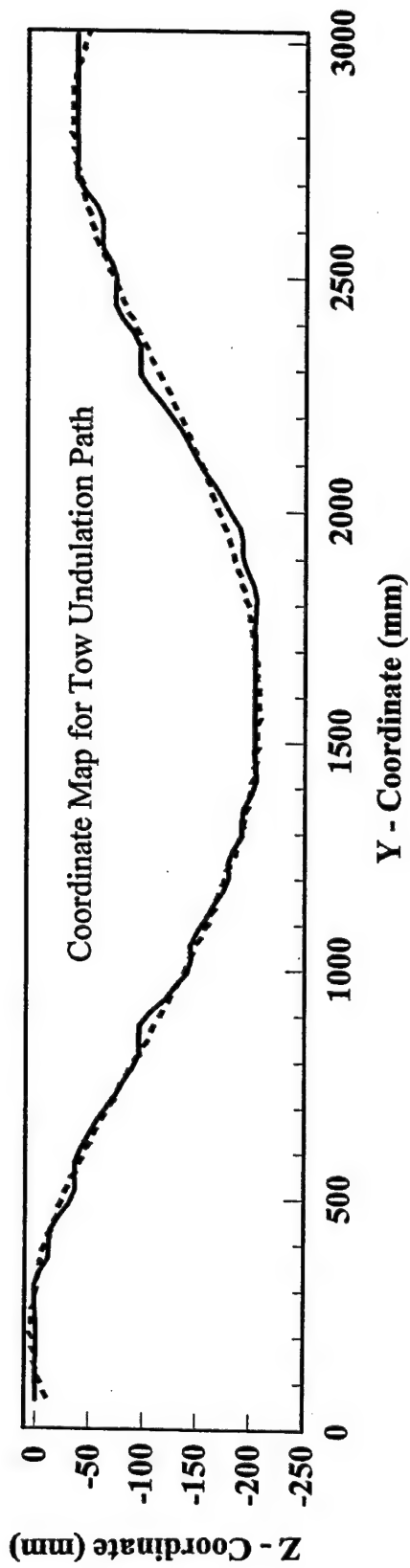
Tow Undulation Path Polynomial

$y = -6.6E-11x^4 + 4.1E-07x^3 - 7.2E-04x^2 + 2.7E-01x - 24.2$

$R^2 = 0.9929$

Figure 14

Figure 15

$$A_{RVE} = (3a)^2 - (a)^2$$

8HS WOVEN
RVE

FILL TOWS

WARP TOWS

Z

Y   X

8HS WOVEN
IVE

$$A_{IVE} = \left(\sqrt{8}a\right)^2$$
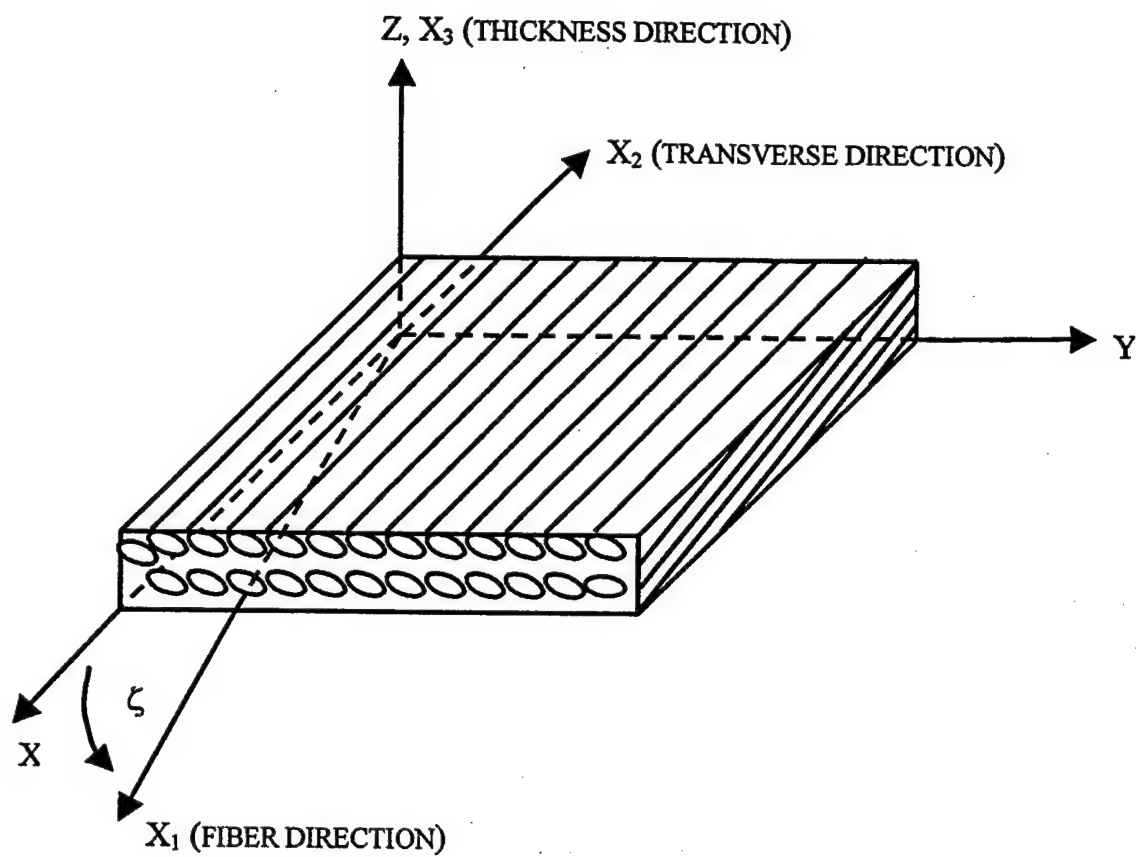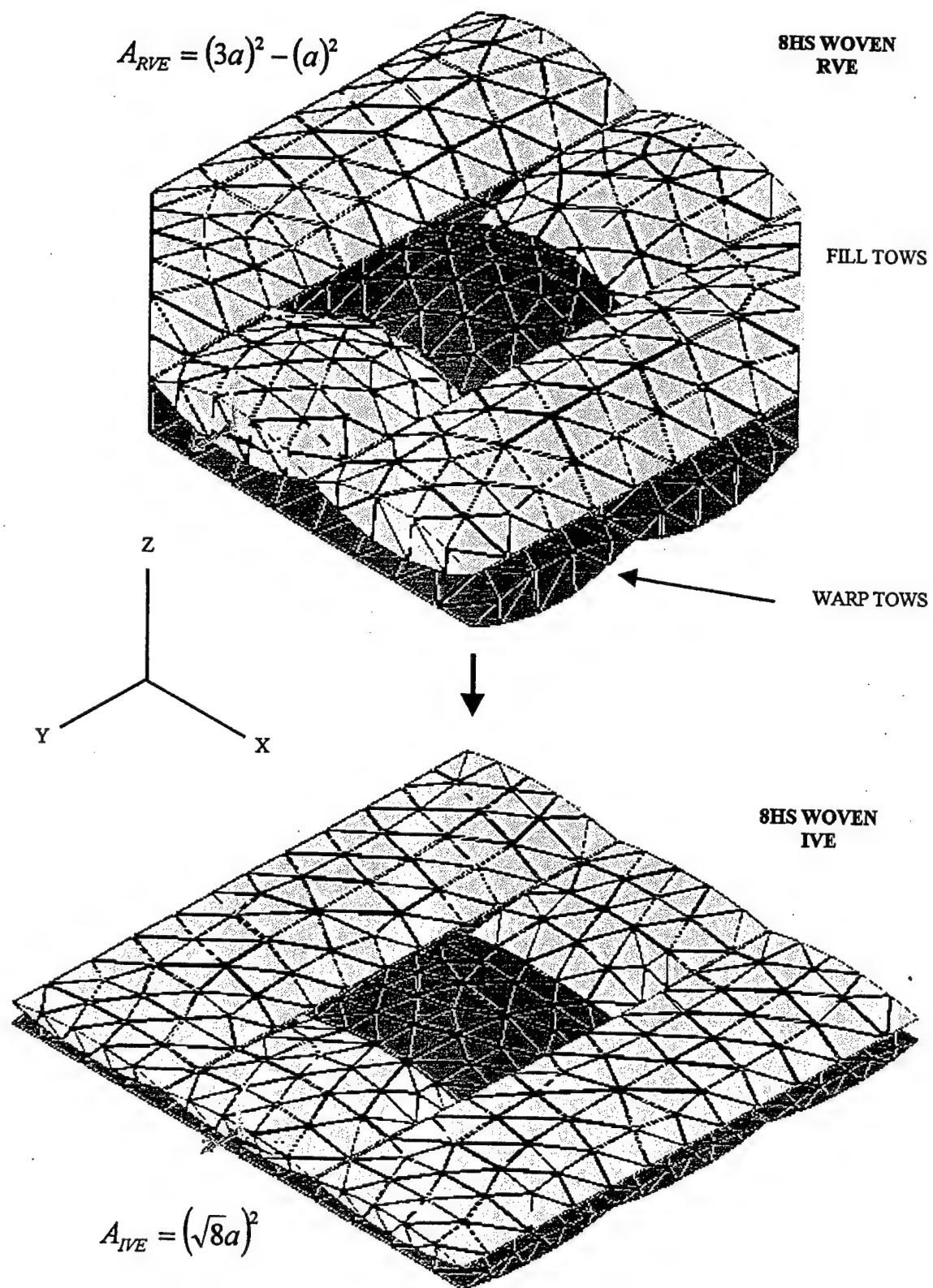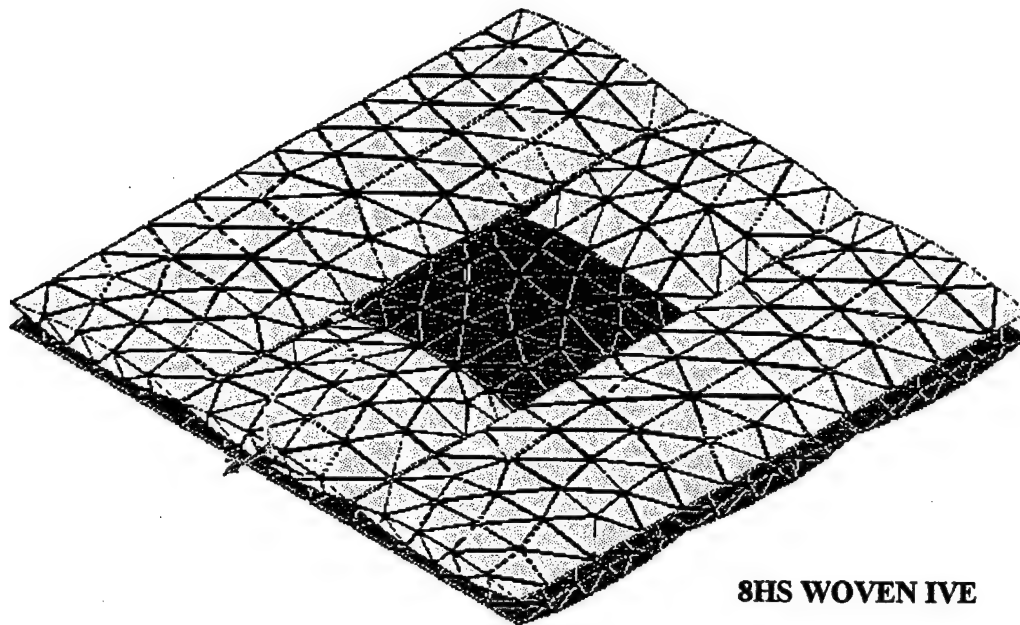
Figure 16
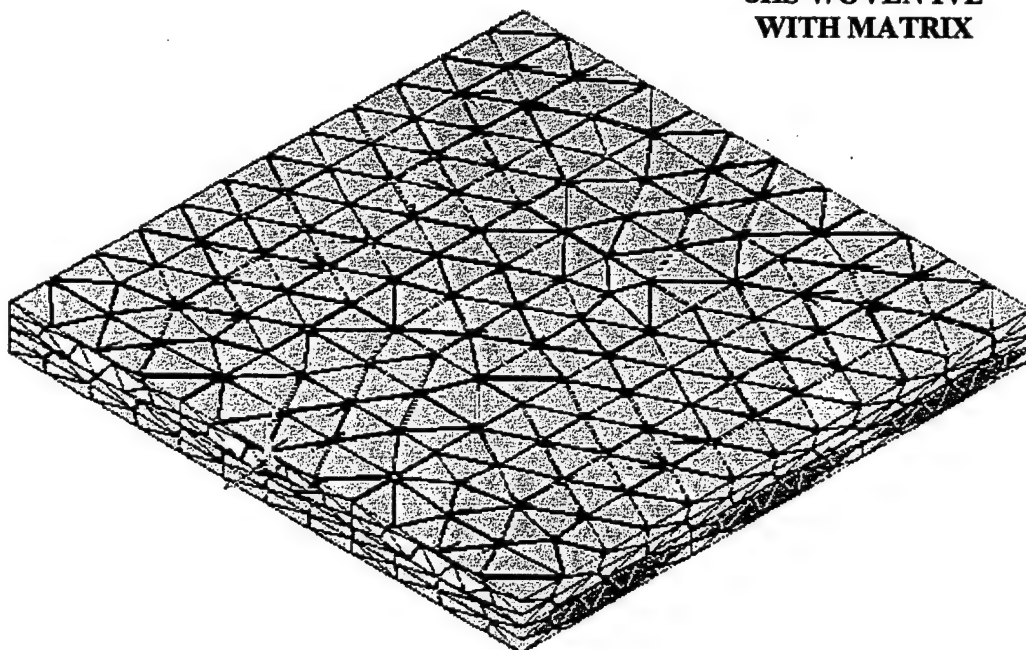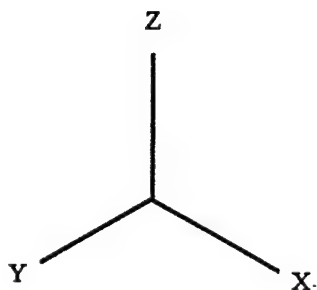
8HS WOVEN IVE

8HS WOVEN IVE
WITH MATRIX

Figure 17
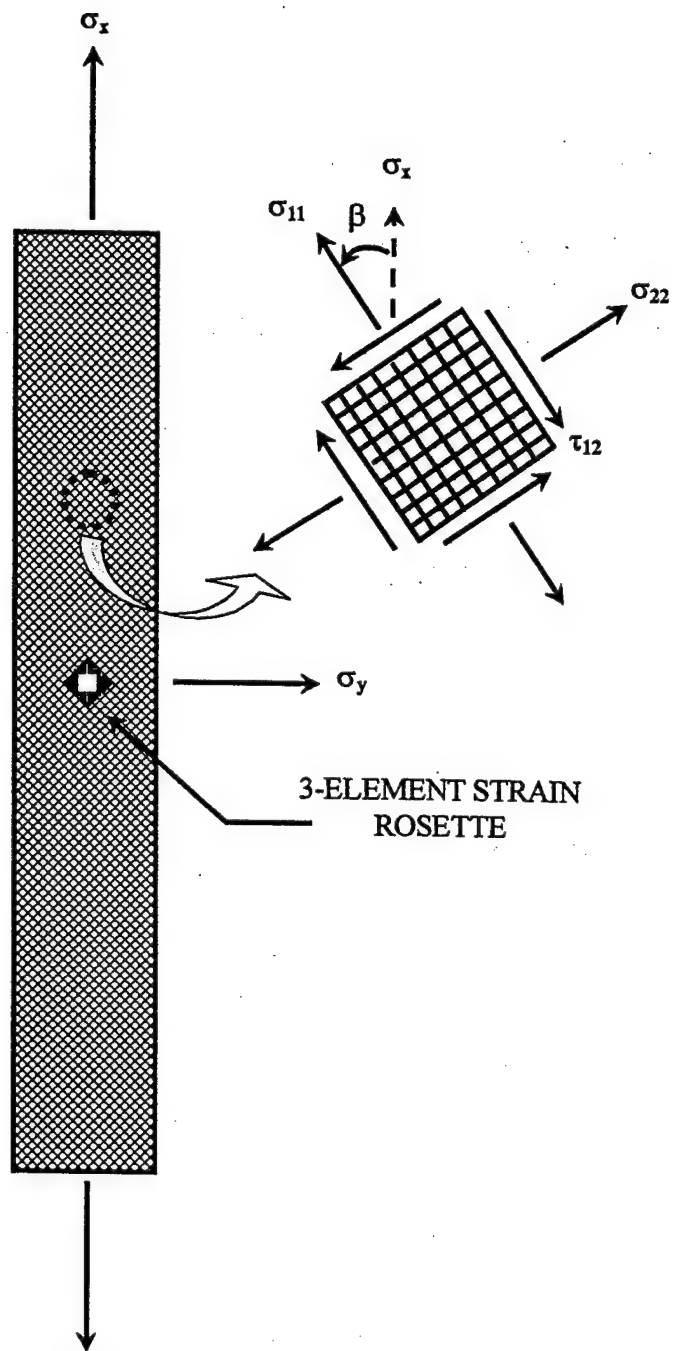
Figure 18
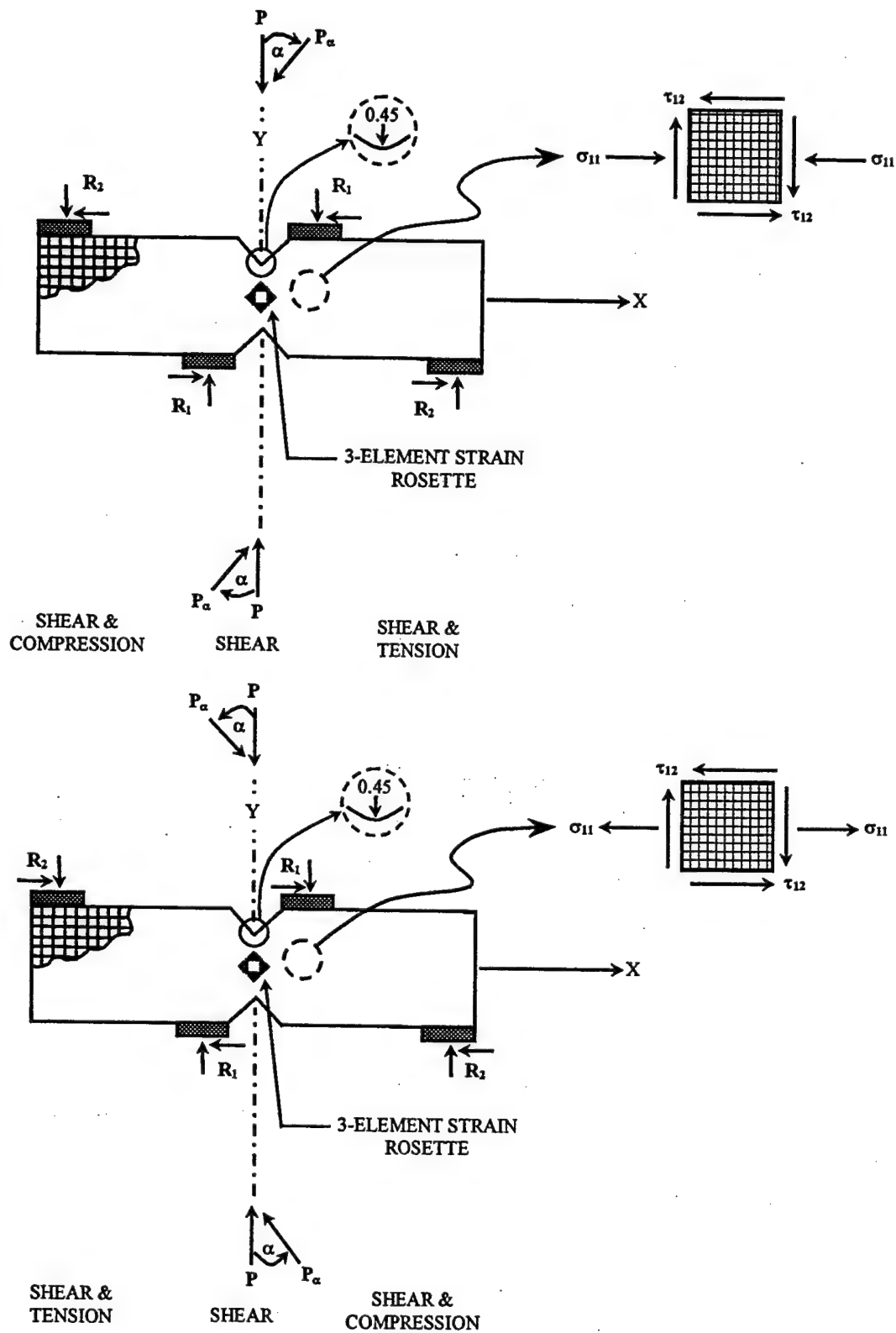
Figure 19
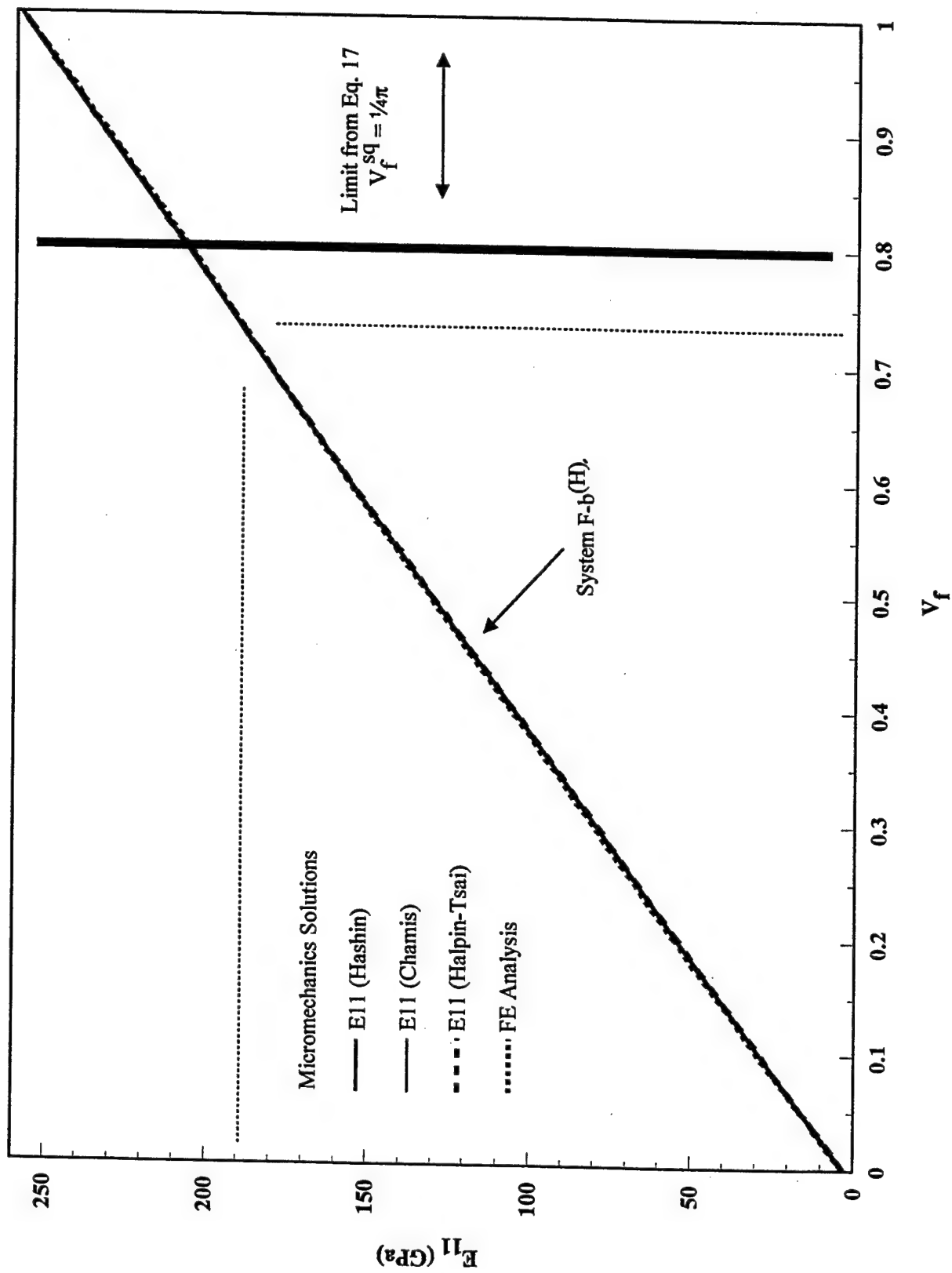
Figure 20
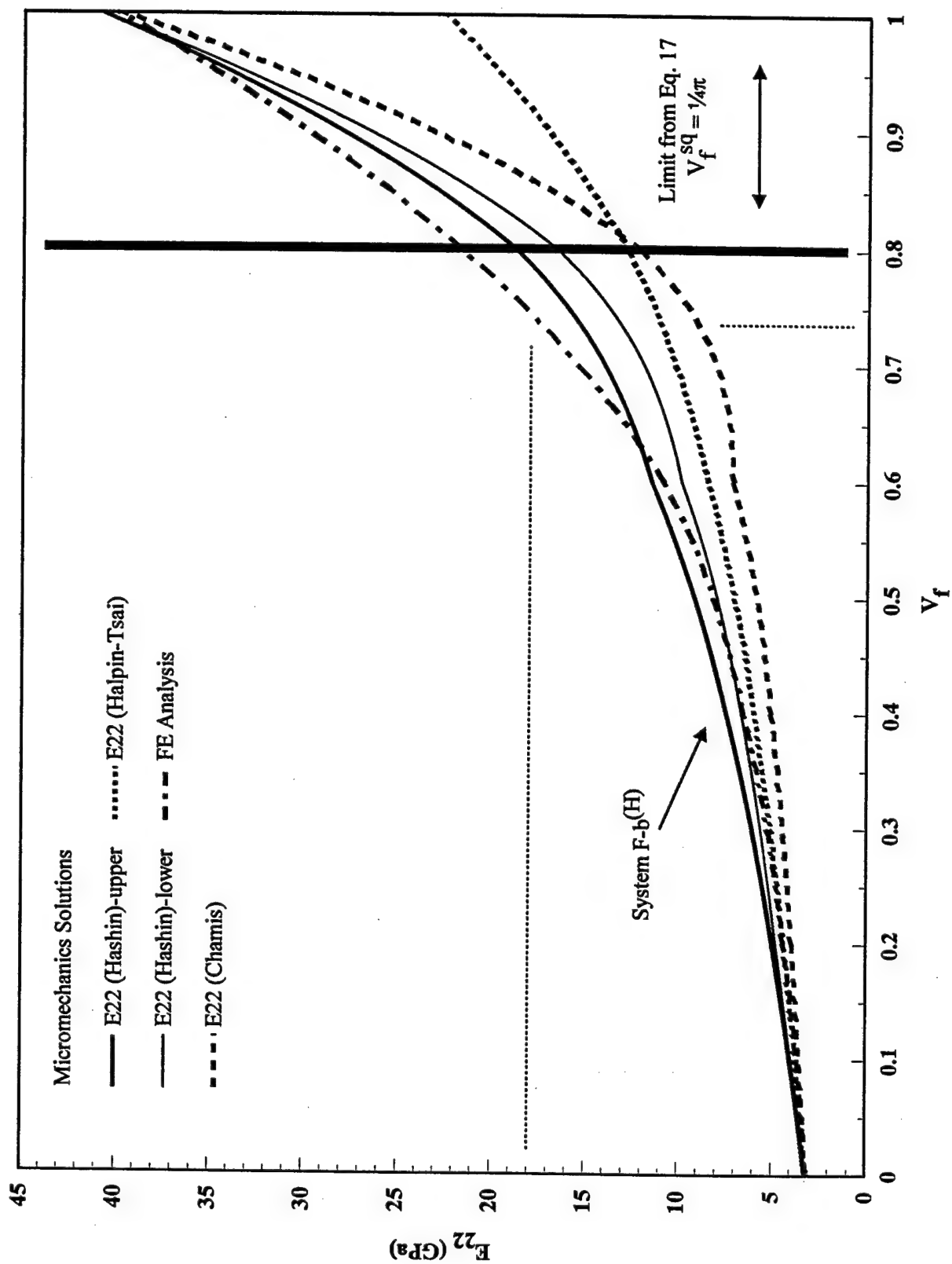
Figure 21
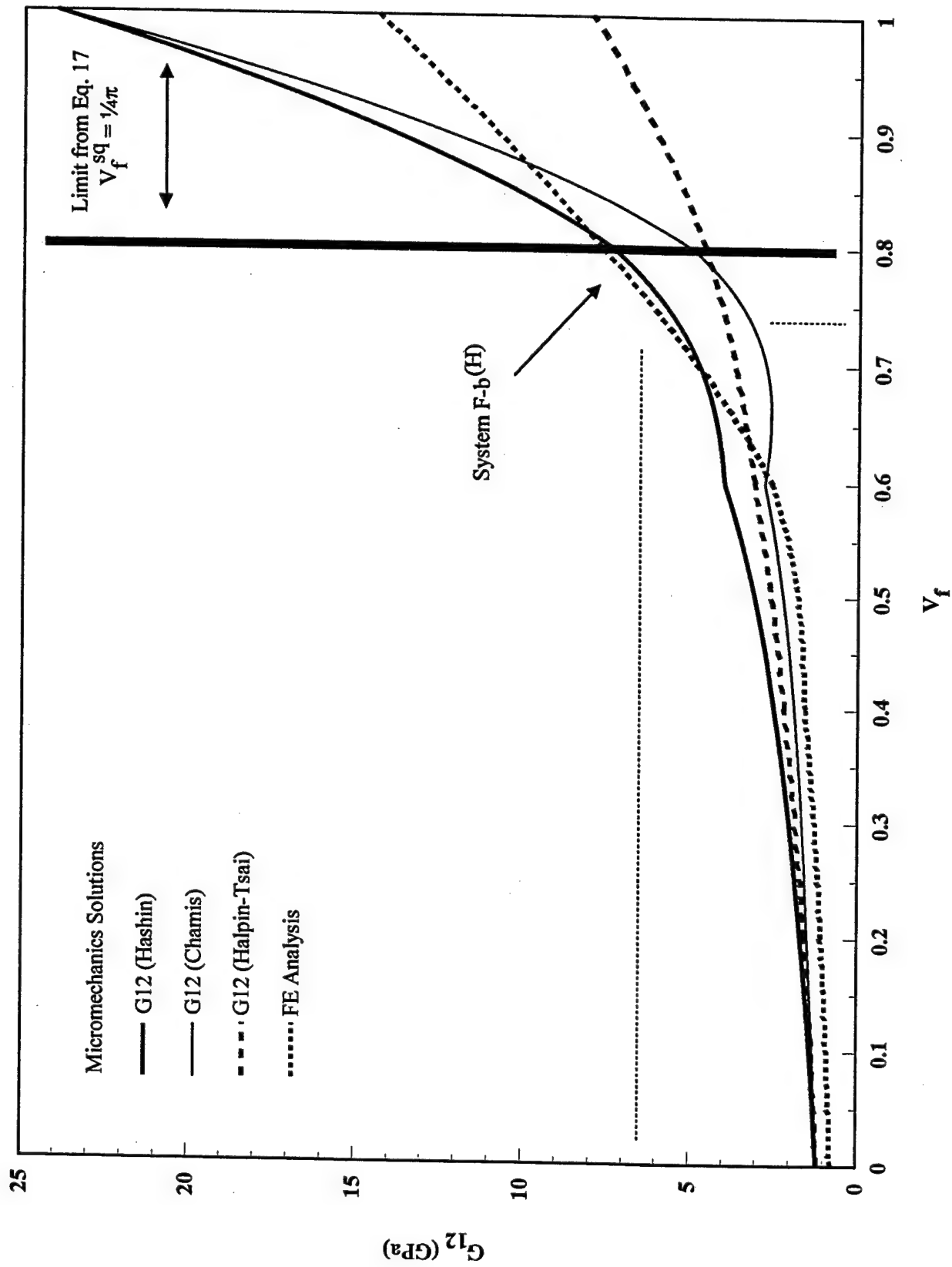
Figure 22
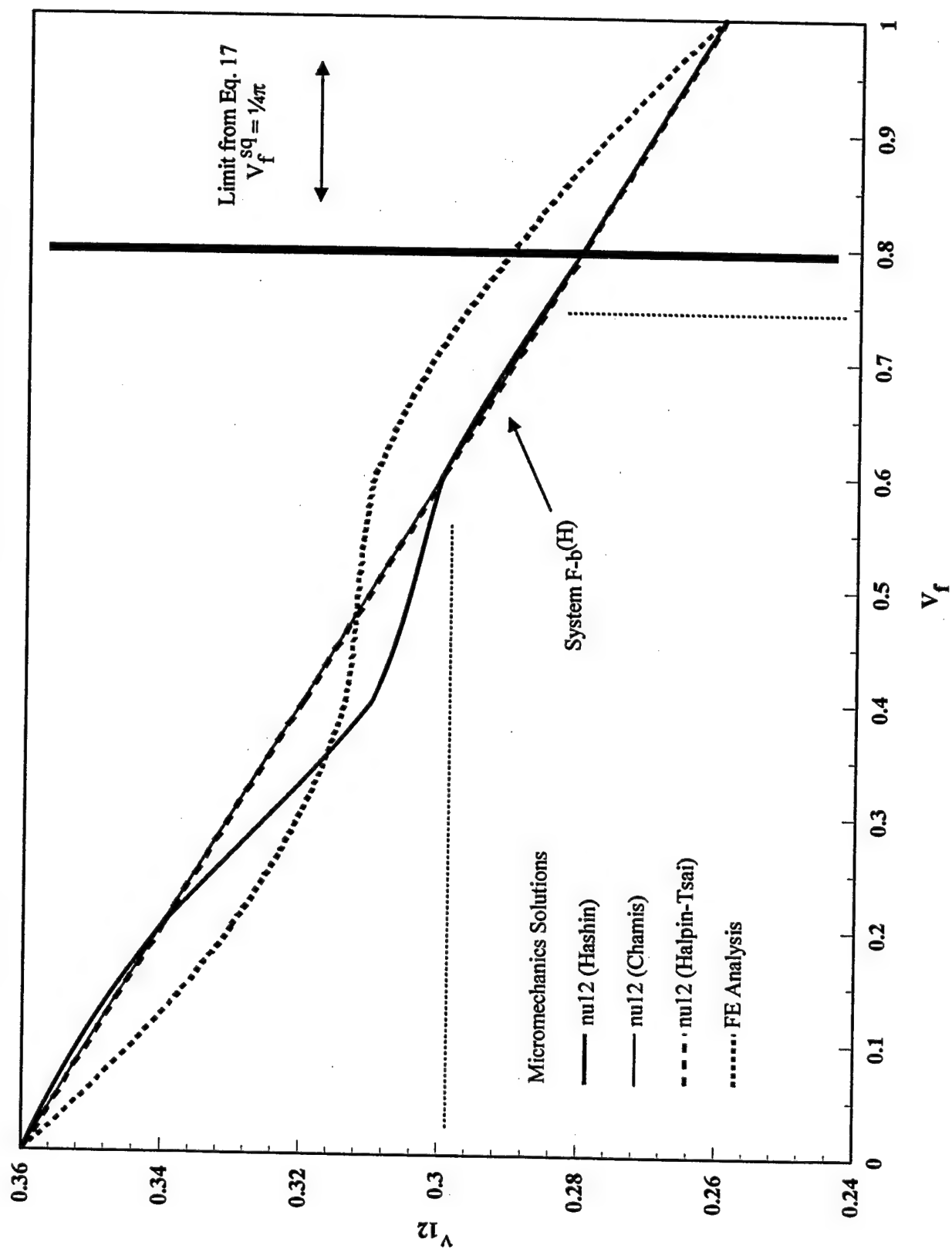
Figure 23

Figure 24
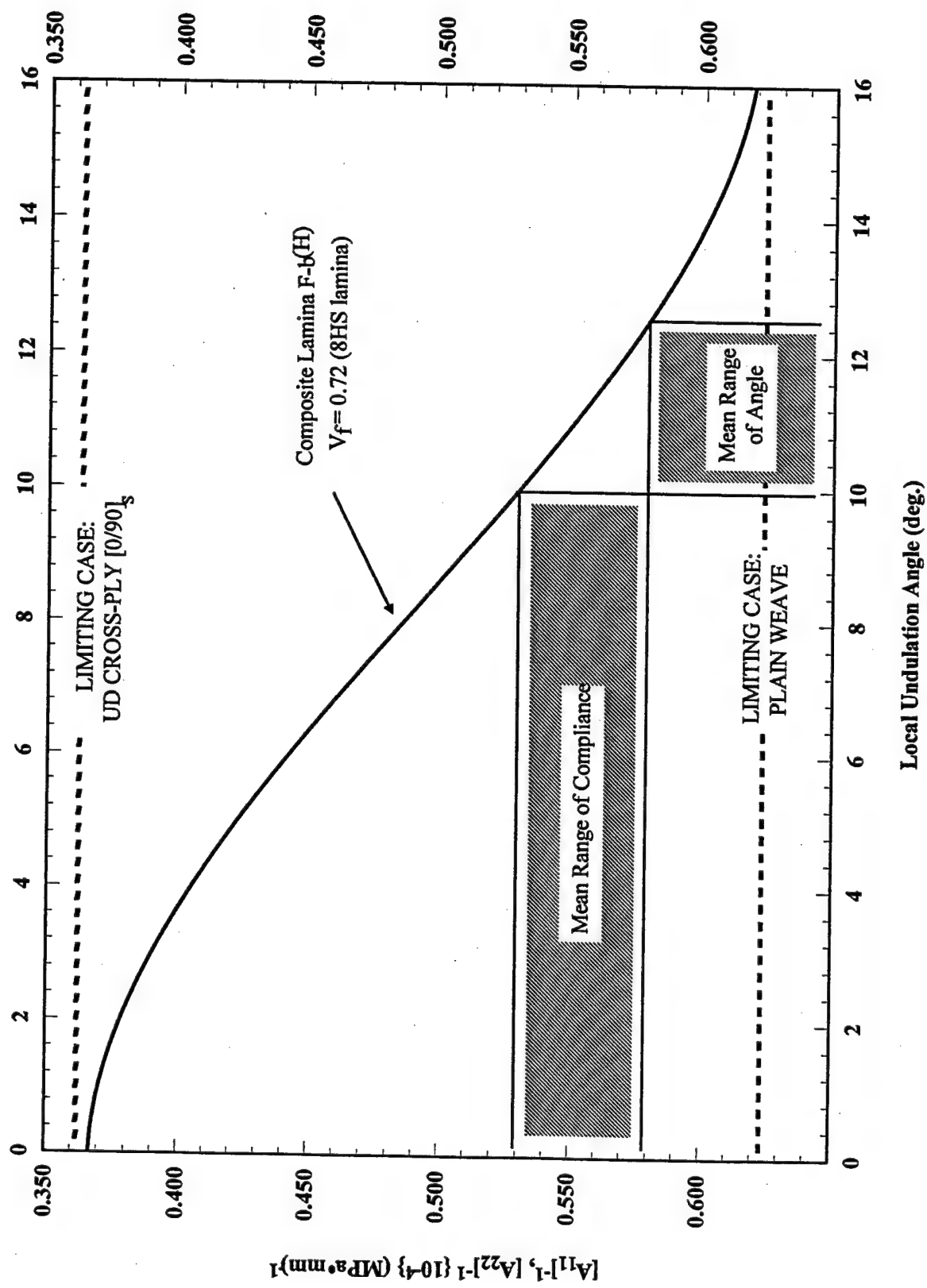
Figure 25

Figure 26

Figure 27

Figure 28

Figure 29